Mars in the Visible to Near Infrared:

Two Views of the Red Planet

by

Danika Wellington

A Dissertation Presented in Partial Fulfillment
of the Requirements for the Degree
Doctor of Philosophy

Approved June 2018 by the
Graduate Supervisory Committee:

James F. Bell III, Chair
Philip R. Christensen
Mark S. Robinson
Thomas G. Sharp
Christy B. Till

ARIZONA STATE UNIVERSITY

August 2018

ABSTRACT

Remote sensing in visible to near-infrared wavelengths is an important tool for identifying and understanding compositional differences on planetary surfaces. Electronic transitions produce broad absorption bands that are often due to the presence of iron cations in crystalline mineral structures or amorphous phases. Mars' iron-rich and variably oxidized surface provides an ideal environment for detecting spectral variations that can be related to differences in surface dust cover or the composition of the underlying bedrock. Several imaging cameras sent to Mars include the capability to selectively filter incoming light to discriminate between surface materials.

At the coarse spatial resolution provided by the wide-angle Mars Color Imager (MARCI) camera aboard the Mars Reconnaissance Orbiter (MRO), regional scale differences in reflectance at all wavelengths are dominated by the presence or absence of Fe^{3+}-rich dust. The dust cover in many regions is highly variable, often with strong seasonal dependence although major storm events can redistribute dust in ways that significantly alter the albedo of large-scale regions outside of the normal annual cycle. Surface dust reservoirs represent an important part of the martian climate system and may play a critical role in the growth of regional dust storms to planet-wide scales. Detailed investigation of seasonal and secular changes permitted by repeated MARCI imaging coverage have allowed the surface dust coverage of the planet at large to be described and have revealed multiannual replenishing of regions historically associated with the growth of storms.

From the ground, rover-based multispectral imaging acquired by the Mastcam cameras allows compositional discrimination between bedrock units and float material encountered along the Curiosity rover's traverse across crater floor and lower Mt. Sharp units. Mastcam spectra indicate differences in primary mineralogy, the presence of iron-bearing alteration phases, and variations in iron oxidation state, which occur at specific locations along the rover's traverse. These changes represent differences in the primary depositional environment and the action of later alteration by fluids circulating through fractures in the bedrock. Loose float rocks sample materials brought into the crater by fluvial or other processes. Mastcam observations provide important constraints on the geologic history of the Gale Crater site.

DEDICATION

To Mars – To explore another world is the greatest adventure I have ever undertaken. Thank you for the joy of discovery.

To Curiosity – thanks for teaching me that even if I land in a hole, to set my sights on the nearest mountain.

ACKNOWLEDGMENTS

None of this would have been possible without the help of so many people, both here at ASU and elsewhere. Nathan Williams and Kristen Bennett were the source of much helpful information and advice in my early graduate school years. Thanks to Austin Godber for fixing my problems, listening to my ranting, and just in general being someone I still look up to. Thanks to the rest of the group for all the good time office shenanigans – Hannah, Jake, Pepé, Andy, Steven, Kristen, Tanya, Gen, Teagan, Sammie, SAMMIE, Stephanie, Kai, Nathan, Ernest, Judy, Trudy, and all the undergraduate student workers who have supported what we do. SESE, and the friends I have made here – thank you. Thanks to Scott Smas for his selfless support of my baking habits. I need to acknowledge my housemates as well, for putting up with me (although I think I'm fairly easy to put up with!) – Heather Meyer, Anna Brunner, Bhavin Joshi, and Sean Peters. Heather, I definitely downloaded your dissertation just to see what one should look like, done right. Thanks to my friends outside of ASU as well – moles, other Techers, my gaming buddies and their consistently dark humor and on point metaphors for graduate school, and anyone else I've left out.

Thanks to the MSL Team, especially all the science and operations folks I had the honor to work with. Lauren Edgar, for explaining the tactical timeline to me after Jim threw me in over my head. Craig Hardgrove, I'll never forget the epic Mastcam-DAN collaboration of Yellowknife Bay. Thanks to all the other people I've worked closely with on Mastcam analysis, especially Jeff Johnson and Melissa Rice for consistently good advice and helpful suggestions. Thanks to the operations team at MSSS, especially Jason Van Beek and the other Mastcam PULs for their patience in dealing with multispectral requests from me.

Almost forgot my family! Thanks Mom & Dad! You are the best. That being said, if any of my brothers are reading this (presumably from a position of lower educational attainment) – stop now. There's nothing here for you. You won't find any grammatical, analytical, or scientific errors within…because there are none.

Back to ASU, special thanks to Rick Hervig for letting me ambush him at Planetary Seminar and agreeing to be on my exam committee when I was just weeks out from my qualifying exam and still needed one more faculty member.

And of course, last but *definitely* not least, my thesis committee – Phil Christensen, Mark Robinson, Tom Sharp, Christy Till, and especially my advisor Jim Bell, who gave me lots of advice but the only piece of it that I remember[1] was his first riddle: “What is the most important thing to get out of grad school?”

Me. I’m getting myself out.

[1]Not true actually, I remember all kinds of useless formatting and slide numbering advice

TABLE OF CONTENTS

Page

LIST OF TABLES

LIST OF FIGURES

Figure Page

LIST OF ACRONYMS AND ABBREVIATIONS

CCD ------- Charge-coupled device, a modern digital imaging sensor

CRISM ---- Compact Reconnaissance Imaging Spectrometer for Mars, aboard MRO

DN --------- Data (or Digital) Number, the raw values recorded in uncalibrated data products

EDR ------- Experimental Data Record, low-level product commonly with data in DN

FOV-------- Field-of-view, the angular extent that an instrument can see at one time

GIS--------- Geographic information system, a system of spatial data analysis, often as software

IAU--------- International Astronomical Union, authority for designations applied to celestial bodies

L_s ---------- Areocentric solar longitude, an angular measure of orbital position (and hence season)

JMARS---- Java Mission-planning and Analysis for Remote Sensing, planetary GIS software

JPL--------- Jet Propulsion Laboratory, NASA center for robotic spacecraft engineering/operations

MARCI ---- Mars Color Imager, a wide-angle multi-filter camera on MRO

MC --------- Mars Chart, USGS 1:5,000,000-scale map series of Mars

MER ------- Mars Exploration Rover, twin rover missions that landed on Mars in 2004

MER-A ---- The Spirit rover (also, MER-2) sent to Gusev Crater, Mars (2004-2010)

MER-B ---- The Opportunity rover (also, MER-1) sent to Meridiani Planum, Mars (2004-present)

MGS ------- Mars Global Surveyor, a spacecraft that functioned in Mars orbit 1997-2006

MOC ------- Mars Orbiter Camera, an instrument aboard the now-defunct MGS

MRO ------- Mars Reconnaissance Orbiter, a spacecraft orbiting Mars (2006-present)

MSL-------- Mars Science Laboratory, NASA Mars mission with rover Curiosity (2012-present)

MSSS ----- Malin Space Science Systems, a space camera company that contracts with NASA

MY --------- Mars Year, numbering scheme of individual Mars years, see Clancy et al. (2000)

NASA------ National Aeronautics and Space Administration, US federal space agency

OMEGA--- Observatoire pour la Minéralogie, l'Eau, les Glaces et l'Activité, on Mars Express

PDS-------- NASA’s Planetary Data System, an online archive of planetary mission data

RAT-------- Rock Abrasion Tool, a arm-mounted tool on MER for grinding rock surfaces

RDR ------- Reduced Data Record, data product with some calibration/transformation applied

RGB ------- Red, green, and blue; commonly describes an image taken through a Bayer filter

ROI -------- Region of interest, spatial area designated for closer inspection or data extraction

SIS --------- Software Interface Specification, a document that describes data products

USGS ----- United States Geological Survey, US government scientific agency

VNIR------- The visible and near-infrared portion of the electromagnetic spectrum

WAC------- Wide Angle Camera, name for the wide FOV camera of several instruments

MSL HARDWARE ABBREVIATIONS

APXS---------Alpha-Particle X-Ray Spectrometer, an arm-mounted geochemistry instrument

LIBS ----------Laser-Induced Breakdown Spectrometer, part of the ChemCam suite

MAHLI--------Mars Hand Lens Imager, an arm-mounted color camera

Mastcam-----The Mast Camera instrument suite, located on the RSM

M-34 ----------The left, 34-mm focal length Mastcam instrument

M-100 --------The right, 100-mm focal length Mastcam instrument

“Caltarget”---Abbreviated form of “calibration target”

ChemCam---Chemistry & Camera instrument, geochemistry instrument with LIBS laser

CheMin ------Chemistry & Mineralogy instrument, an internal sample analysis suite

CHIMRA -----Collection and Handling for Interior Martian Rock Analysis, sieving/portioning unit

DRT----------Dust Removal Tool, an arm-mounted wire brush for removing surface dust coatings

PADS---------Powder Acquisition Drill System, device for acquiring powdered rock sample

RSM ----------Remote Sensing Mast, where Mastcam, ChemCam and other cameras are located

SA/SPaH ----Sample Acquisition, Processing, and Handling rover subsystem

SAM ----------Sample Analysis at Mars, internal analysis suite for volatile and organic compounds

XRD X-Ray Diffraction, CheMin technique to identify crystalline mineral phase

PREFACE

This dissertation is the culmination of six years' effort that began in August 2012; coincidentally, around the same time that Curiosity landed in Gale Crater. I wasn't involved with MSL's Science Team at that point, just one of many people who tuned in to watch its incredible landing. I'd seen Curiosity once about a year before that, through a window into a clean room at JPL where I was an intern in the summer of 2011. (At that point, there wasn't much to see; the rover was fairly well bundled up to be shipped out to the Cape.) And of course I'd watched the launch, remotely, the following November, while I was still an undergraduate at Caltech.

But I started graduate school working on MRO MARCI data, an enormous, unwieldy, and for these reasons, terribly underused orbital imaging dataset. MARCI captures Mars's day-to-day weather patterns, and, relevant for purposes here, changes in the surface that result from dust being picked up and moved around. These are the kind of data that, the longer you look at them, the more patterns are apparent. Mars has an amazing regularity on small scales, but also curious departures that leave the impression that something important is being missed. Figuring out how to efficiently process, display, and analyze these data was a challenge, however, and this project was as much an exercise in juggling computing resources and managing my own time as it was data analysis. (For perspective, we had originally planned to submit to a special issue of Icarus, "Dynamic Mars from long-term observations", which the manuscript (Chapter 2) would have been singularly well-suited for, with a submission deadline of November 2013!)

Part of the delay was that I was being pulled between many projects at that point, most especially as a new MSL Science Team collaborator, trying to make some sense of the Mastcam multispectral dataset. The state of the in-flight calibration, at that point, was poor; because MSL didn't land clean like the MER rovers had, the reflectance of the calibration target needed to be adjusted for the layer of dust that had been kicked up onto the rover deck by the retrorockets from the start (and later, that settled onto the deck from the atmosphere). We were saved by a model developed by Kjartan Kinch (U. Copenhagen) who had done this same correction for MER Pancam, but the in-flight data still needed extensive amount of work both to validate that the calibration was producing sensible and consistent results, and to extract calibration target image

values that would allow further refinements to the dust model. These were corrections that could be applied across the entire dataset to bring previous versions of a calibrated image product up to par; other issues discovered in early mission data required urgent adjustments to operational standards to avoid an irrevocable loss of science value. Over some wavelengths, the contrast between certain light-toned materials (like calcium-sulfate veins, or small piles of drill fines) is large enough, and the features small enough, that the autoexposure algorithm can fail to set the image exposure time appropriately, and image DN values over these surfaces flirt with the nonlinear portion of CCD response, or are badly saturated. At present, the state of the *I/F* data is reasonably good, as determined by comparisons of the calibrated data against laboratory spectra of calibration target materials and other hardware (with reasonable allowances for the influence of dust) as well as results from comparable data acquired by ChemCam in its passive mode of operation, although a few challenges remain.

In addition to the scientific work presented below, a major goal of my work here has been to enable further scientific analyses by others. To that end, the two chapters that are either published (Chapter 3) or at least submittable (Chapter 2) have ancillary material associated with them that are easily available. The initial multispectral work (Chapter 3) is published open-access and includes supplemental files containing all the spectra presented in the paper as .csv files. The calibrated RDR files used for Chapters 3-5 are not part of the MSL releases to the PDS, but are generated at ASU using the improved in-flight calibration pipeline as discussed and referenced in those chapters. As part of a project funded through NASA's Planetary Data Archiving, Restoration, and Tools (PDART) program, I and others are working to make those data widely accessible to the planetary community, along with the documentation that will enable them to be understood and used correctly. With regards to MARCI, that manuscript includes a large amount of supplementary information, as well as a lengthy appendix (included with this dissertation), in order to allow the text to be more easily understood and better referenced to the supporting data, and to facilitate any follow-on investigation by interested readers. We will make the mosaic data files available online as well.

It is my hope that some of the effort I've put into working with these datasets can "feed forward" to aid further related remote sensing work. The process of calibrating data for an ongoing rover mission has emphasized to me the importance of rapid tactical turnaround from the receipt of uncalibrated data files to the production of calibrated products and accompanying scientific interpretation. The cadence of rover drives and limited mission resources is unforgiving to the sort of missed opportunities that can occur when the scientific follow-up is slow. As such, some significant amount of time I've spent here has been devoted to turning around data faster, to produce standard sets of spectral parameters that can provide a quick look at the content of a multi-filter sequence, and to advocate tactically for additional multispectral observations when recent data warranted that approach, sometimes in limited filter sets to allow for either more spatial coverage, or to fit into a limited tactical downlink volume. The Mars2020 mission will include the Mastcam-Z instrument, with very similar capabilities to MSL Mastcam. That camera should prove to be a valuable remote sensing tool for the furtherance of the scientific goals of the mission, and from that, our understanding of Mars itself.

- Danika W., June 2018

CHAPTER 1

INTRODUCTION

Mars shines in reflected light. No other planet is so well known by its color, and no other planet's visible appearance has driven human imagination and exploration to the degree that the Red Planet has. Over a hundred years ago, telescopes trained on Mars saw a world that was more familiar than it was alien; close enough that, pushing our technology just a bit further, we could reach out to it. Remote sensing chose Mars as the most compelling destination for the ultimate and enduring adventure of interplanetary exploration: the search for life.

Mars' relationship with humanity's desire to find other environments that might support life today, or could have done so in the past, has been complex. Its dynamic surface features and the obvious presence of a volatile species forming the polar caps led to the rise of infamously wrong hypotheses in the late 19th and early 20th century on the nature of the surface and the possibility for extant life. As a result of spacecraft observations, we understand today that the surface of Mars is composed of regional scale reddish dust deposits, which take their color from the presence of iron oxides; dark expanses of predominantly basalt or basaltically-derived bedrock and sand; and, bright CO_2 and H_2O polar ice deposits. Outside of the polar regions, major changes in the planet's surface appearance result from a large scale redistribution of thin layers of dust by seasonal and storm-driven surface winds. A study of these changes is then fundamentally a study of Mars' present-day atmosphere, even as advancements in our understanding of Mars have pushed the search for life into the planet's past. Observations of these changes, however, have important implications for our ongoing efforts to understand the geologic history of the planet from orbit and the ground, for operational considerations of present and future robotic and human exploration, and for our fundamental understanding of atmospheric physics and modeling. Chapter 2 presents a detailed study of surface dust changes conducted at relatively high temporal resolution from Mars Color Imager (MARCI) observations, a camera on the Mars Reconnaissance Orbiter (MRO) that images the majority of the planet nearly every single day, and has done so for more than twelve Earth years.

Dust is Mars' present, but the rock it obscures is the planet's past. In many ways, then, dust is "the enemy" in trying to understand the planet's history. Even thin layers can obscure spectral signatures of the underlying bedrock; bedrock that records the conditions under which it was created and the extent to which it has been since altered by interactions with aqueous fluids. From orbit, detailed spectroscopic work must be conducted over areas that are relatively clear of dust, restricting our ability to inspect extensive areas of the planet that could hide geologic evidence of a warmer, wetter past. These orbital studies form the basis of scientific support for landed missions, including the Mars Science Laboratory (MSL) Curiosity rover. From the ground, rovers like Curiosity are able to interrogate the local stratigraphic rock record in vastly more detail than possible from space, though often with instrumentation designed to analyze or sample over small footprints in the rover workspace. Hence remote sensing instruments are important to rover missions as well, including multispectral cameras designed to capture not only morphology and stratigraphy of bedrock and other materials, but also clues to composition that can be gleaned from properties of the surface reflectance.

Quantitative measurements of light reflected off of a surface often rely on silicon-based detectors, which are sensitive to light from approximately the visible (400-700 nm) to the 1 μm portion of the near-infrared. The wavelength-dependence of the reflected light can be resolved by either diffracting or filtering the light to allow a specific wavelength range to reach elements of the detector. What are sought in reflectance spectra are absorption features - losses of incident light over particular wavelengths that provide clues to composition. At these wavelengths, such features are commonly the result of electronic processes (as opposed to, e.g., vibrational or rotational transitions which occur, generally speaking, at longer wavelengths). The strength and position of the resulting absorption bands depends on the electronic configuration of the constituent ions or ionic groups and the nature of their surrounding crystal field environment, including the coordination states and symmetries of the sites (Bell et al., 1975; Burns, 1993a).

Electronic transitions of core electrons are typically too high-energy to produce features in the visible and near-infrared. Perhaps surprisingly, the relatively low-energy transitions that do extend to the visible are, in terms of natural occurrence, overwhelmingly due to the presence of

cations of a single element, iron (Fe). A transition element, iron possesses partially filled 3d orbitals which, while energetically degenerate in the case of an isolated Fe atom or ion, split into different energy levels in the presence of neighboring atoms and ionic groups which are present in its surrounding environment in a regular way in a crystalline mineral structure. A major element in many common rock types, iron cations are incorporated into the structure of primary silicate minerals as well as oxides, sulfates, and phyllosilicates. The presence of ferrous (Fe^{2+}) iron, the dominant cation in unaltered igneous rocks, and/or its ferric (Fe^{3+}) oxidative weathering products give rise to a variety of spectral absorption bands in reflectance spectra, including the visible wavelength features (color) that give Mars its well-known appearance.

Curiosity's mast-mounted color imaging cameras (the Mastcams) don't capture the surface reflectance to the same spectral resolution that laboratory spectrometers typically do, but image instead at "multispectral" resolution - sampling the reflectance over twelve unique regions of the spectrum using filters designed to discriminate between surface materials over wavelengths where they are most likely to show differences from one another. Surface mission cameras have advantages over space-based measurements: they can distinguish features that cannot be resolved from orbit, including small, sloped facets of rock surfaces, on which the dust thickness can be considerably lesser, and take advantage of fresh materials produced by the deliberate action of hardware on the surface (brushing, grinding, drilling, etc.) or incidentally by the rover body or landing system (rocks broken by wheels, dust removed by retrorocket fire, etc.). In addition, observations of well understood onboard calibration materials can better characterize and remove variations in measured radiance that are due to changes in the incident illumination (light which, for surface-based measurements, must only traverse the atmosphere once before being registered).

The interpretation of visible-to-near-infrared spectra can be challenging, due to the nonlinear manner in which spectral features of multiple component mixtures combine. Strongly absorbing species can dominate the reflectance over particular wavelength ranges, masking the presence of even more abundant phases. In addition, because reflectance depends in a significant way on the particle size (or size distribution) of the various phases that are present,

qualitative comparisons of band depth between samples do not reliably correlate to relative abundances. For these reasons, comparisons of the reflectance data to results obtains from other on-board instruments can be helpful to constrain hypotheses for the origin of various reflectance characteristics. Chapter 3 debuts the Mastcam multispectral reflectance dataset, recently calibrated using a high fidelity version of the calibration pipeline, and draws such comparisons to demonstrate the variation of spectral reflectance with measured differences in mineralogy and chemistry. This highlights Mastcam's utility as a reconnaissance instrument, including its ability to provide a first-pass characterization and classification of the surface by its spectral reflectance, a topic explored in more detail in Chapter 4. Finally, Chapter 5 addresses a particular spectral class of exogenous material detectable by surface multispectral imaging, Fe-Ni meteorites, which have survived on the planet's surface for some unknown amount of time, and explores what may be learned from inter-comparisons of the abundance of these materials across different rover landing sites.

From orbit to the ground, the instruments on whose data the conclusions presented in each chapter are based are nestled within a growing history of Mars exploration, with heritage based on previous flight instruments and a legacy in those that are in development or will be called for in future proposal solicitations. Because of this, the studies presented here will be expandable in obvious ways, as our understanding of Mars increases beyond what we have gleaned from the sliver of time and small scraps of ground we've observed. Mars science has a growing need for integrating results from many different missions and instruments into a cohesive whole. These chapters suggest that such opportunities, although barely touched on here, are many.

CHAPTER 2

PATTERNS OF SURFACE ALBEDO CHANGES FROM MARS RECONNAISSANCE ORBITER MARS COLOR IMAGER (MARCI) OBSERVATIONS

This chapter is a manuscript in preparation for submission to Icarus. It is included here with permission of coauthor Jim Bell III.

2.1 Introduction

The global pattern of surface albedo on Mars is maintained and modified by aeolian processes that influence the distribution of bright, reddish dust over the underlying darker-toned substrate. Large regions of high or low albedo are known to have persisted since early telescopic observations, giving Mars its familiar appearance (e.g., (Antoniadi, 1930; Flammarion, 1892; Slipher, 1962). In spite of this, frequent and sometimes large-scale changes in the surface albedo have been documented by repeat observations made by telescopes and orbiting spacecraft (e.g., (Bell III et al., 1999; Geissler, 2005; Martin et al., 1992; Sagan et al., 1972). These changes are part of the system of interactions between the surface and the atmosphere that lifts, transports, and redeposits fine-grained material and represents an important part of the martian climate system (e.g., (Kahn et al., 1992). In-situ data on near-surface wind conditions are available from only a few specific locations that have been investigated by landed spacecraft and rovers, several of which are within the topographically-influenced sub-environment of a crater. Therefore, our understanding of present-day global wind and weather patterns is primarily inferred from the effect that these processes have on the large-scale distribution of movable fine particles, the results of which can be observed from orbit. Repeated observations can reveal the seasonal or interannual variability of surface changes, their frequency and extent, and the presence or absence of specific weather events or patterns in association with dust removal or deposition.

NASA's Mars Reconnaissance Orbiter (MRO) has been in orbit around Mars since 2006, and continues to operate at the time of this writing. MRO maintains a near-circular sun-synchronous orbit, passing from south to north over the martian equator at approximately 3:00 pm local time on the sunlit side of the planet (Zurek and Smrekar, 2007). This allows for repeated imaging of the same surface regions under similar illumination approximately once per sol (a sol

is a martian day), with very similar viewing geometry after several sols. These characteristics are conducive to global-scale mapping, which is obtained as near-daily coverage by the Mars Color Imager (MARCI). With a 180° field-of-view, MARCI has been able to acquire approximately 50,000 imaging observations to date, each covering an over 1000 km wide longitudinal swath of the planet, since the beginning of the primary science phase in November 2006. This relatively high temporal resolution imaging allows dynamic processes, including dust transport, to be characterized at spatial scales that are not achievable from ground-based or Earth orbital telescopic monitoring. In this study we investigate surface albedo changes captured by the MARCI instrument over five-and-a-half Mars years of observation in order to better understand the relationship between the variable surface dust cover and seasonal, annual, and decadal-scale changes in the climate of modern-day Mars.

2.2 Background & Motivation

The study of surface changes on Mars has a long history, some of which pre-dates the era of spacecraft, modern digital imaging, and our understanding of the physical nature of differences in regional albedo. Early descriptive studies of albedo changes based on telescopic observations were limited to observations acquired near opposition, when the relative positions of Mars and Earth afforded sufficient spatial resolution for detailed observations of latitude regions favored by the planet's relative orientation towards Earth at that time. This fragmentary observation record made it difficult to constrain the timing of many past surface changes, and while some observers reported a seasonal appearance to some surface features (e.g., (Antoniadi, 1930; Slipher, 1962) and global seasonal darkening trends (e.g., (Dollfus, 1961; Focas, 1962; Pollack et al., 1967), most changes to the surface have been described as less predictable in occurrence or appearance ("secular" changes, e.g. (Baum, 1974; Martin et al., 1992). Despite the long-term apparent stability of the general configuration of large regions of high or low albedo, some observed secular variations have been dramatic, affecting hundreds of thousands of square kilometers (e.g., changes in Daedalia-Claritas, Laocoontis-Alcyonius, and Cerberus; (Capen, 1976; James et al., 1996; Slipher, 1962). Certain regions of Mars have been historically noted to be more variable than others (in terms of the frequency, spatial extent, and/or

magnitude of albedo changes), including Syrtis Major and regions of southern Utopia Planitia to the north and east, the Solis Lacus region, Pandorae Fretum, and others (e.g., (Antoniadi, 1930; Slipher, 1962). Many of these features were targeted by repeated Mariner 9 orbital observations as part of a deliberate variable features campaign (Sagan et al., 1973, 1972), which, together with earlier Mariner IV images (Salisbury, 1966) and later Viking Orbiter and Viking Lander observations (Arvidson et al., 1989; Kieffer et al., 1977; Thomas and Veverka, 1979; Veverka et al., 1977), confirmed the particulate nature of bright surface deposits and aeolian activity as the primary cause of surface changes.

In recent decades, a series of orbiters have provided nearly uninterrupted imaging capabilities at Mars, starting with the arrival of Mars Global Surveyor (MGS) in 1997. MGS Mars Orbiter Camera (MOC) Wide Angle Camera (WAC) (Malin and Edgett, 2001) observations have shown extensive changes in the surface since the Viking Orbiter observations, as well as frequent changes that took place during the mission itself, especially subsequent to the large 2001 storm (Geissler, 2005; Geissler et al., 2016; Szwast et al., 2006). Some, but not all, of the observed changes correspond well in time and location to tabulations of dust storm activity (Geissler et al., 2016), which is known to have a seasonally variable occurrence in different regions (Cantor et al., 2001; Wang and Richardson, 2015). The surface of Mars continues to be monitored by spacecraft that are active at the time of this writing, returning measurements of surface albedo from instruments on Mars Odyssey (e.g., (Edwards et al., 2011; Kieffer et al., 2006), Mars Express (Vincendon et al., 2015), and MRO (Calvin et al., 2017, 2015). These measurements are supplemented by broadband observations of the surface acquired by rover cameras at landing sites (Bell III et al., 2008), Rice et al., in press) as well as narrowband multispectral imaging from the Hubble Space Telescope in Earth orbit (e.g., (Bell III et al., 1999; James et al., 1996).

Surface albedo is a good proxy for surface dust cover (Ruff and Christensen, 2002; Szwast et al., 2006) due to the significantly higher reflectance of martian dust at red and near-infrared wavelengths versus less oxidized basaltic materials. Dust influences the thermal properties of the surface (and atmosphere directly, when lifted) and as such is an important variable in Mars climate studies (e.g., Kahn et al., 1992; Read et al., 2015). Previous studies have

shown that observed albedo changes result in significant daytime temperature differences in model results (Kahre et al., 2005a) and orbital temperature measurements (Smith, 2004). The surface dust reservoir may play an important role in the interannual variability of the dust cycle and the generation of large storms, although as yet those phenomena have been difficult to reproduce accurately in global climate models (e.g., (Kahre et al., 2005b; Mulholland et al., 2013; Newman et al., 2002; Newman and Richardson, 2015). Simulations of the martian dust cycle can be compared to imaging observations to assess the performance of the models in accurately reproducing the timing and spatial pattern of dust lifting, as has been done previously for certain regional and local scale models (Fenton et al., 2005; Spiga and Forget, 2009; Toigo et al., 2002).

Understanding the interaction of surface dust reservoirs with the atmosphere and how this varies across the surface of Mars is also relevant in a practical sense, both for robotic and potential future human exploration. Dust obscuration negatively impacts visible to infrared remote sensing observations aimed at investigating the composition of underlying bedrock or other materials (e.g., (Johnson et al., 2002; Johnson and Grundy, 2001a). Surface missions spend operational resources mitigating this issue by brushing, grinding, or otherwise disturbing the surface to reveal fresher materials underneath. Dust settling on the body of a surface rover or lander also presents challenges by reducing the efficiency of solar panel arrays, clinging to the windows of cameras and other sensors, and obscuring on-board remote sensing calibration targets (e.g., (Kinch et al., 2015; Landis and Jenkins, 2000). Human missions to the surface of Mars will have to contend with the challenges posed by dust settling on and infiltrating equipment and habitats, and potentially acting as an irritant or other health concern (e.g., (Kerschmann, 2017; Rucker, 2017). For these reasons, a detailed understanding of the martian dust cycle also has the potential to allow improved future mission planning to Mars.

2.3 Methodology

This study focuses on orbital observations of surface albedo changes from the Mars Reconnaissance Orbiter (MRO) Mars Color Imager (MARCI) (Bell III et al., 2009). MARCI is a wide-angle CCD camera capable of push-frame imaging in five visible to near-infrared channels, plus two additional ultraviolet bands for ozone measurements occupying a separate set of optics.

Over this wavelength range, higher signal and greater contrast imaging between areas of high and low dust cover is achieved at longer wavelengths, due to the strongly reddish spectral slope of dustier regions compared to the darker substrate (e.g., (Singer et al., 1979). For this reason, and because multi-band color information is not necessary for the goals of this study, we focus exclusively on the longest-wavelength, 718 nm MARCI band (band 5). Raw MARCI images are processed to separate the individual color frames and are decompanded, flat-fielded, and radiometrically-calibrated to radiance factor (*I*/*F*, where *I* is the observed radiance-on-sensor, and πF is the solar spectral irradiance at the top of the martian atmosphere at the time of the observation) via the pipeline described by Bell et al. (2009). The *I*/*F* values are further divided by the cosine of the incidence angles to derive an approximate (i.e., no atmospheric or detailed photometric corrections) Lambert albedo.

Calibrated observations are map-projected and mosaicked in time-steps of 20° of aerocentric solar longitude (L_s, an angular measure of orbital position such that a martian year is 360° in length and northern hemisphere martian spring begins at L_s = 0°). The choice of 20° L_s bins is a compromise between temporal resolution and imaging coverage that provides enough overlap to minimize seams and gaps. The overlap is resolved by selecting the lowest value pixel at each location in the projected image. This method of choosing the lowest valid pixel values minimizes the influence of atmospheric phenomena in the final mosaic by preferentially selecting lower opacity observations within each time-step. It also favors the higher-resolution center track of each MARCI image, with the result that the final mosaic is near the approximate 1 km/pixel scale of the image swath center. This method does occasionally result in the inclusion of shadows within the final mosaic (from clouds or a Phobos transit, for example), but as transient features these do not confuse the identification of surface dust cover changes. For computational efficiency, and to allow different regions of Mars to be viewed with minimal map distortion, the mosaics are produced as twenty-eight separately projected maps, using the USGS cartographic Mars Chart (MC) quadrangles for latitude and longitude bounds (e.g., Batson et al., 1979). We avoid the polar regions (> 65° latitude) due to seasonal obscuration and the predominance of the effect of ice over dust on the surface albedo.

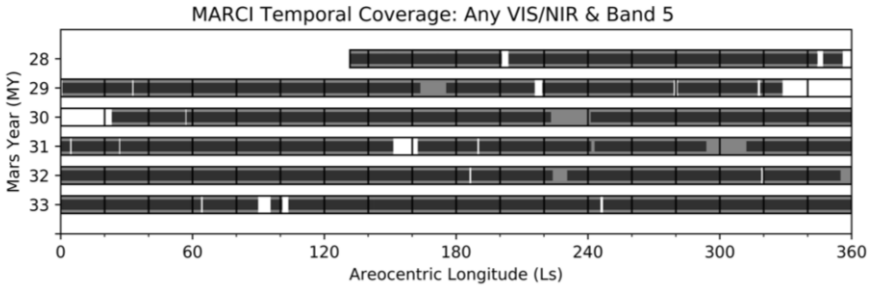

Figure 2.1: Timeline of MARCI imaging coverage in any visible/near-infrared band (light gray), and MARCI band 5 (inner dark gray). Boxes show the 20° L_s range over which each mosaic was produced (see supplemental information for animated mosaics over this time period). Gaps in coverage indicate either operational decisions or spacecraft malfunction. The large gap in late MY 29 and early MY 30 corresponds to a major MRO safing that occurred between August and December 2009.

The temporal coverage of MARCI imaging, and band 5 imaging specifically, is shown in Figure 2.1, along with the intervals of time-steps used to construct the mosaics themselves. MRO's primary science phase began in November 2006, corresponding to Mars Year (MY) 28 by the Mars year numbering convention of Clancy et al. (2000) and an L_s of approximately 130°. These units are more convenient for comparing the seasonal timing of events in different martian years than terrestrial dates and will be used throughout this paper. While the MRO mission is still ongoing at the time of this writing, for the purposes of this study we consider only MARCI data through the end of MY 33 (to early May of 2017), with one exception (MY 34 data in Section 2.4.1.2) that is relevant to investigating the behavior of a region-specific multi-annual pattern. As can be seen in Figure 2.1, several significant gaps within the span of MARCI coverage occur, including a large gap in MY 29-30 that results in no data for two 20° L_s intervals. The lack of data within that time frame is due to the spacecraft entering and remaining in safe mode for an extended period between August and December of 2009. Several additional smaller gaps occur, but do not have as significant an effect on our ability to constrain the timing of surface changes.

As mentioned above, the approximate Lambert albedos depicted in subsequent figures and supplementary files fully include the contribution from the atmosphere, which is often significant; we do not attempt any correction for suspended dust or ice particles. Characterizing differences in surface albedo therefore requires care in avoiding confusion with differences in atmospheric opacity, the latter of which can dominate absolute differences between successive

time-steps. We have found that many surface changes, especially surface darkenings, produce a difference in the surface patterning of albedo boundaries that are often sharply delineated by contrast with the neighboring terrain. In these cases, the change in apparent albedo cannot be ascribed to differences in atmospheric opacity, and the reality of an actual surface change is clear on inspection.

More difficult to characterize well by visual identification are surface brightenings resulting from the deposition of suspended dust, which is generally laid down gradually and evenly across large areas as it settles out of the atmosphere. In these cases, as shown in subsequent plots, we compare the apparent albedo of a surface with a nearby region whose albedo is at some point(s) in time close in value with that surface. Atmospheric variations due to general dustiness can be expected to affect nearby regions similarly; whereas differences between the albedo of the two regions will reflect actual surface change.

When discrete (not gradual) albedo changes are identified in the mosaics, a more precise characterization of the timing of individual changes is made by examining individual calibrated, map-projected near-daily images of those regions. We constrain the timing by identifying the latest image in which the surface can be seen clearly without any change from its previous state, and the earliest image in which the surface change is clearly visible. Because many changes are small, sufficient resolution for identifying these differences often requires an observation whose center passes relatively close (often within a few degrees of longitude) to the feature itself. In most cases the difference between the before and after observation is a few sols, although in some cases atmospheric obscuration or a lack of imaging data due to operational reasons can cause the timing to be less well constrained. These changes are listed in Appendix A.

2.4 Results

We present our observations of MARCI surface albedo changes in approximate order of increasing eastward longitude (with some significant deviations to allow regions with related behaviors to follow consecutively), choosing arbitrarily to begin with Syrtis Major. Appendix A includes the pre- and post-observation image IDs that constrains the timing of individual discrete changes, and an approximate latitude and longitude for each of the changes. The text below

provides clarity on the extent and seasonal repeatability of these changes, and additionally discusses surface changes that are too gradual or too frequent to include in the appendix. Animations of quadrangles covering the regions discussed below are available online as supplementary material; full resolution mosaic data will eventually be archived with the NASA Planetary Data System.

Nomenclature for the regions discussed below is predominantly drawn from IAU-approved albedo feature names, although in some cases we also use additional names that have appeared in scientific literature whose meaning is clearly understood. One of the best resources for understanding the identity and extent of names applied to albedo features, including historical names that may appear in older literature, is a map by Ebisawa (1960). However, to avoid any confusion, Figure 2.2 shows a map with the feature names used in the text and appendix. Finally, geomorphic names are sometimes used to describe groups of features that share similar behavior or are strongly topographically associated with a particular feature (e.g. a volcano) or larger region; these are shown in Figure 2.2 as well.

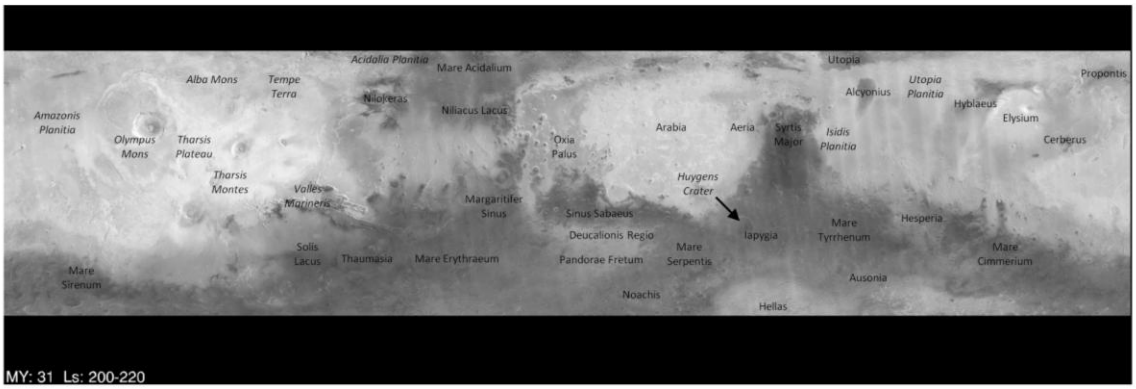

Figure 2.2: MARCI band 5 (718 nm) global mosaic produced from observations within MY 31 L_s 200-220° (Nov.-Dec. 2012), annotated to show the locations of features discussed in the text. Names in italics represent regional topographic feature names, not albedo feature names, which are useful for referencing the locations of changes.

2.4.1 Syrtis Major

2.4.1.1 Syrtis Major: Interior

The low albedo Syrtis Major feature has historically been noted to be a region of frequent albedo changes (e.g., (Antoniadi, 1930; Capen, 1976; Christensen, 1988; Dollfus, 1961), and indeed, numerous changes can be seen over the span of MARCI mosaic coverage as well (the

reader is referred to the online supplemental data files for an animation). Many of these changes are part of a regular seasonal cycle of dust deposition and erosion, modulated by the atmospheric dust load in the southern spring/summer dusty season. Dust is deposited on the surface in Syrtis Major during seasonal declines in atmospheric opacity in late northern autumn and winter, raising the albedo of portions of the interior to an intermediate value that is greater than unaffected dark-toned areas in the region but less than neighboring terrain in Isidis and Aeria. This is more apparent in the southeast and south-central regions of Syrtis Major (broadly, the vicinity of 10°N, 75°E), but lengthening crater lee dust deposits suggest that dust was deposited across the region wherever it could not be immediately swept away by the wind. In the areas where it does linger, the dust is removed slowly and unevenly over the following months, reducing the albedo of the surface to baseline values by late northern spring to early summer. This is shown in Figure 2.3(a-d). In Figure 2.3d, we plot the mean mosaic albedo values of two ROIs in Syrtis Major (whose locations are shown in Figures 2.3b and 2.3c), one situated within a region of central Syrtis that visual examination of the mosaics suggests experiences clearly this pattern of dust deposition and removal, and another to the northwest, in a region where the dust deposition is less and of similar albedo to the former at certain times of year. These two regions are close enough that we do not expect regional atmospheric opacity variations or latitude-dependent photometric effects to affect the regions differently to any significant degree. Variations that both regions display are due largely to differences in atmospheric dust opacity, and to a lesser extent, seasonal differences in illumination; meanwhile, seasonal differences in surface dust cover between regions are apparent where the two curves diverge. Further evidence that these changes are occurring on the surface can be seen in Figure 2.3b-c, which shows portions of two mosaic time-steps for east-central Syrtis Major. In Figure 2.3b, the region has just received a fresh dust coating; in Figure 2.3c, this region that was previously homogenous in albedo is now irregularly toned in clear relation to the local topography, especially to the east where the terrain slopes into low-lying Isidis Planitia. Interannual variations in this cycle are caused by differences in the seasonal atmospheric dust load during the dusty season. In MY 28, the occurrence of major dust lifting at multiple sites around Mars (i.e., the global 2007 storm (Cantor et al., 2014; Wang and Richardson, 2015))

resulted in higher than normal subsequent deposition in this region (as in many other regions) compared to later years. In all years, the gradual and annually repeatable pattern of dust removal makes clear that seasonal wind erosion is responsible for the post-deposition cleaning, rather than local storms.

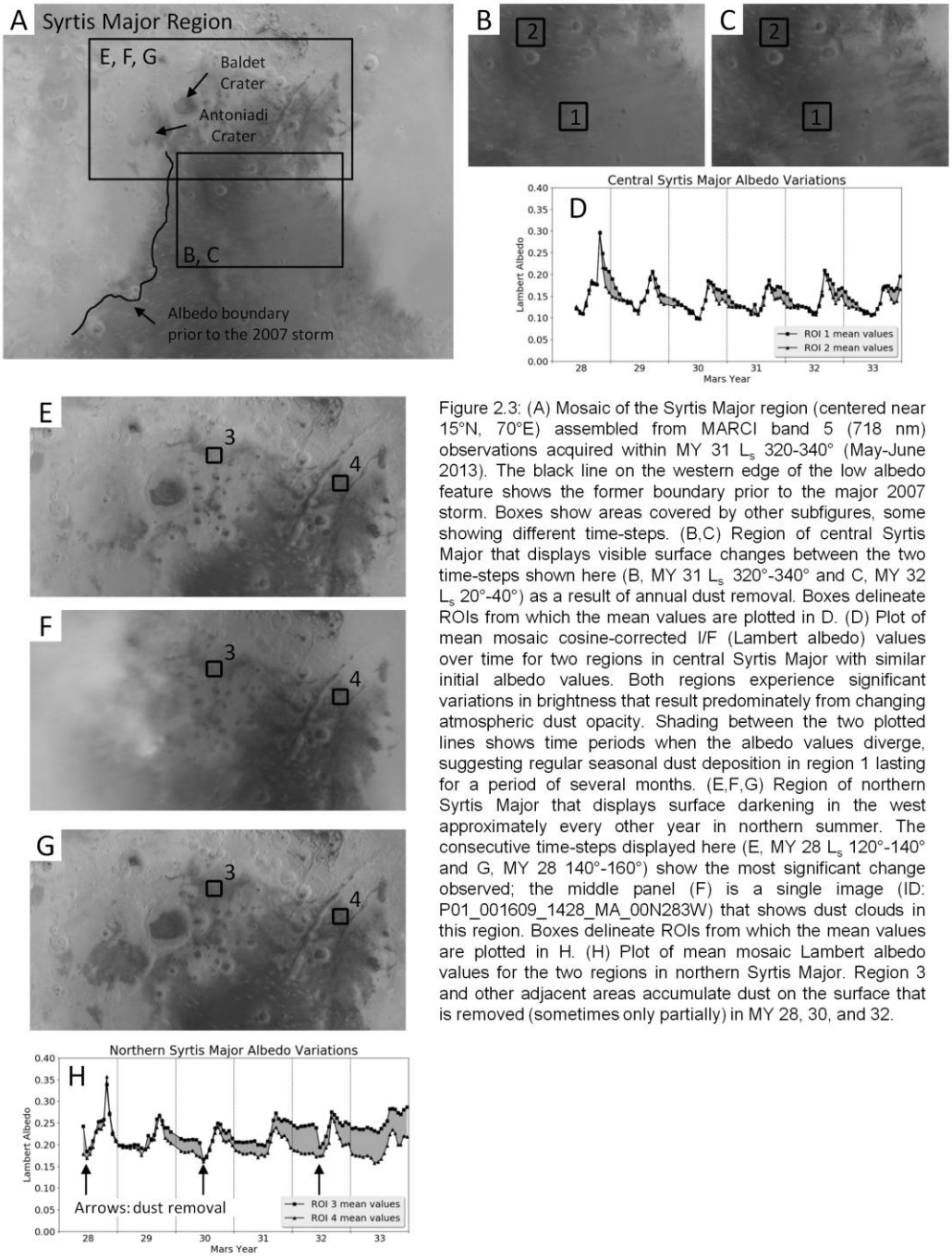

Figure 2.3: (A) Mosaic of the Syrtis Major region (centered near 15°N, 70°E) assembled from MARCI band 5 (718 nm) observations acquired within MY 31 L_s 320-340° (May-June 2013). The black line on the western edge of the low albedo feature shows the former boundary prior to the major 2007 storm. Boxes show areas covered by other subfigures, some showing different time-steps. (B,C) Region of central Syrtis Major that displays visible surface changes between the two time-steps shown here (B, MY 31 L_s 320°-340° and C, MY 32 L_s 20°-40°) as a result of annual dust removal. Boxes delineate ROIs from which the mean values are plotted in D. (D) Plot of mean mosaic cosine-corrected I/F (Lambert albedo) values over time for two regions in central Syrtis Major with similar initial albedo values. Both regions experience significant variations in brightness that result predominately from changing atmospheric dust opacity. Shading between the two plotted lines shows time periods when the albedo values diverge, suggesting regular seasonal dust deposition in region 1 lasting for a period of several months. (E,F,G) Region of northern Syrtis Major that displays surface darkening in the west approximately every other year in northern summer. The consecutive time-steps displayed here (E, MY 28 L_s 120°-140° and G, MY 28 140°-160°) show the most significant change observed; the middle panel (F) is a single image (ID: P01_001609_1428_MA_00N283W) that shows dust clouds in this region. Boxes delineate ROIs from which the mean values are plotted in H. (H) Plot of mean mosaic Lambert albedo values for the two regions in northern Syrtis Major. Region 3 and other adjacent areas accumulate dust on the surface that is removed (sometimes only partially) in MY 28, 30, and 32.

2.4.1.2 Syrtis Major: Northwest

The northwestern portion of the Syrtis Major albedo feature participates, to a degree, in the cycle of seasonal changes discussed above, but has its own additional and unique pattern of

darkening that takes place in northern summer. The affected region includes the interiors of the craters Antoniadi and Baldet, and areas to the east, southeast, and south in the vicinity of 25°N, 68°E to 22°N, 70°E, 19°N, 66°E, and 18°N, 60°E. The approximately 200-km wide swath between the rim of Baldet Crater and the low albedo region of central Syrtis Major to the southeast was in a partially bright, dust-covered state at the beginning of the MARCI dataset. This dust appears to be a remnant of the extensive brightening that took place across much of northern Syrtis Major as a result of the 2001 (MY 25) major dust storm (Geissler et al., 2016). In MY 28, the region darkened substantially between L_s 139.8° and L_s 144.9°. This seasonal timing is not characteristic of the global pattern of northern hemisphere mid-latitude storms, which reach their most southerly extent in northern autumn and winter (Cantor et al., 2014, 2001), nor is this location along the major storm tracks (e.g. (Wang and Richardson, 2015). A closer examination of individual MARCI images showed that the changes occurred in a series of steps, often in association with local dust clouds. Some darkening in the interior of Antoniadi Crater and the area southeast of Antoniadi, for example, occurred by L_s 141.8°, although images do not confirm Antoniadi has reached its final darkened state until L_s 143.4°. Meanwhile, the portion of this area that is east of Baldet Crater was unchanged by L_s 142.8° but darkened between then and L_s 144.9°. Before and after mosaics of these changes, as well as an individual MARCI observation showing local dust lifting, is shown in Figure 2.3(e-g).

While the most extensive darkening took place in MY 28, the region underwent darkening again in subsequent Mars years with a similar seasonal occurrence. The major dust storm of MY 28 deposited dust in this area (although not to the extent that it reversed the darkening earlier in that year), as did the dusty season of MY 29. Darkening occurred in MY 30 between L_s 134.7° and L_s 136.7°, and again between L_s 140.2° and L_s 143.3°, the former event mostly restricted to Antoniadi Crater and the expansion of a small low-albedo spot to the southwest of the crater, but the latter involving Baldet and much of the surrounding area as well. The next major darkening in this region took place in MY 32, during which the region darkened between L_s 145.8° and L_s 146.3°, continuing what appears to be a biennial pattern of change. This pattern can be seen in a plot of average ROI values across the individual mosaics shown in Figure 2.3h, where arrows on

the plot show the dip in albedo values post-darkening. In other years (MY 29, MY 31, MY 33) any surface darkening appears to be either very minor (in MY 29, spatially minor dust removal, likely in response to the global storm, occurred between L_s 146.2° and 148.8° but is not covered by the ROI whose mean values are shown in Figure 2.3h) or entirely not apparent in MARCI images.

To investigate whether this pattern holds in preceding Mars years, we additionally consulted daily global MOC mosaics produced by Helen Wang (Wang and Ingersoll, 2002) and provided through JMARS, a GIS software application developed by the Mars Space Flight Facility (Christensen et al., 2009). At approximately 7.5 km/pixel (Malin and Edgett, 2001), these daily global observations are lower in spatial resolution than the MARCI observations, but nevertheless are sufficient for assessing the presence or absence of changes that affect areas of several tens of kilometers or more. In MY 27, no changes in the mosaic are apparent in this region between R23:26 (i.e., the twenty-sixth day of mission subphase R23) and S03:04, a period of time that spans from approximately L_s 120°-155°. Darkening within and near Antoniadi Crater takes place between R02:02 and R03:31 (MY 26, approx. L_s 130°-160°). Previous years at this seasonal time pre-date the MY 25 global storm, and this region of northwest Syrtis Major is extensively dark.

While our data analysis nominally covers through only MY 33, for the sake of further investigating this apparent pattern we delved into the MY 34 observations that cover the time period that surrounds the darkening events noted above. However, the changes in MY 34 are not consistent with the previous two-year “pattern”; while minor darkening occurs within Baldet Crater, no noticeable changes occur in the surrounding terrain, and the magnitude and extent of difference is more in accordance with previous odd-numbered mars years, despite the availability of dust in the surrounding area. The changes within this region of northwestern Syrtis Major, then, are not entirely regular, which is more in line with other regions whose variability is driven by dust storm events.

2.4.1.3 Syrtis Major: Western Boundary

Seasonally regular and multiannual cycles of dust deposition and removal are not the only variations that affected the Syrtis Major region over the span of MARCI observations. As mentioned above, dust fallout following the decay of the 2007 (MY 28) planet-encircling storm

had a significant effect on the albedo of this feature; however, in addition to the subsequent enhanced deposition in the interior, dust was also removed from portions of this feature as a consequence of this storm. A comparison of before and after time-steps (see supplemental material) shows that the western boundary of Syrtis Major expanded westward during the storm by approximately 100 km from around 5°N to 18°N (this difference can also be seen in Figure 2.3a by comparing the low albedo feature to the solid black line, which depicts the old boundary). It is difficult to constrain the exact timing of the change due to the high atmospheric opacity, but comparisons of individual images suggest that this took place between L_s 269.5° and L_s 273.4°. This western edge was affected by the post-storm deposition like much of the region, so the net effect of the storm was to bring the surface to a mid-tone. Subsequent seasonal cleaning darkened it along with the areas that had belonged to the low albedo feature from the beginning of the dataset. By the end of the MY 33, the boundary has somewhat receded, but has still not returned to its pre-storm appearance.

2.4.1.4 Syrtis Major: Eastern Boundary

Other changes affect the eastern boundary of the Syrtis Major region. Within the MARCI dataset, darkening from these events occurs in the vicinity of a low albedo streak extending to the northeast into Isidis in the vicinity of 12°N, 82°E. At the beginning of the dataset, this extension is very faint, although some minor darkening may occur over the span of the major MY 28 storm. In MY 29, a small streak darkens between L_s 220.5° and 224.3°; more significant darkening occurs later, between L_s 303.7° and 310.4°. To the north, near 15°N, 80°E, faint changes take place in MY 30 (L_s 333.2°-336.0°) and again in MY 31 (L_s 202.8°-209.6°), while the main streak to the south again darkens in MY 32 (L_s 214.3°-218.0°). The broadly seasonal but less regular occurrence of these changes in northern autumn and winter and the proximity of eastern Syrtis to the Utopia storm track (e.g. Wang and Richardson, 2015) suggests that these changes may be related to passing storms. This is confirmed by the observation that the timing of the darkening events in MY 29 correspond well with that of storms that passed south through Utopia Planitia (see 4.2 and 4.3); the same is true of the changes in MY 30, MY 31, and MY 32.

2.4.2 Alcyonius & Hyblaeus

Southern Utopia Planitia is host to two isolated regions of low albedo referred to as Alcyonius (30°N, 95°E) and Hyblaeus (25°N, 125°E). Both of these are subject to variations that are often clearly associated with dust storm activity (Figure 2.4a-c), most significantly in conjunction with the 2007 storm (see online supplementary files for an animation). Prior to that dust storm beginning in earnest, a portion of Hyblaeus lengthened by a diffuse (i.e., without a sharp boundary) 100 km-long dark extension forming near 21°N, 122°E between L_s 205.7° and 218.9°, and the feature at large darkened again between L_s 233.0° and 233.6°, in each case with bounding or intervening observations displaying dense clouds of dust. Over the course of the high dust opacity of the MY 28 global storm, Hyblaeus lengthened dramatically by nearly a thousand kilometers, extending itself southwest to the equator. This can be seen in Figure 2.5(a-b), which shows a pair of global mosaics assembled from observations acquired before and after the global storm. The darkening in Hyblaeus suggests that it was one of several regions that acted as a net source for dust during the storm. Alcyonius darkened to a much lesser extent over that same time period, but by comparison of before and after mosaics and images bounding the high opacity, the southern end can be seen to have expanded westward, somewhat diffusely, by tens of kilometers.

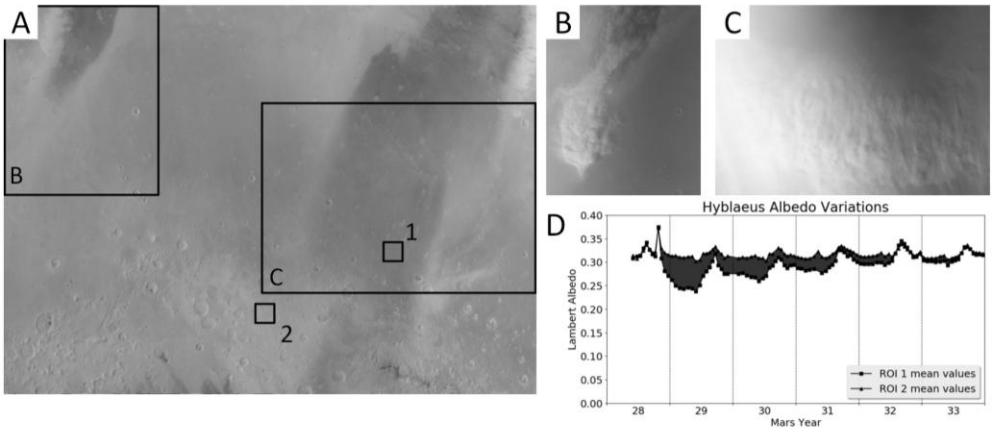

Figure 2.4: a) Mosaic of the Amenthes quadrangle (0-30°N, 225-270°W) assembled from MARCI band 5 (718 nm) observations acquired within the MY 29 L_s 120°-140° time-step (August-October 2008). Two variable dark features are found in this region, Alcyonius (upper left) and Hyblaeus (right). b,c) Dust storms over southern Alcyonius (b, B11_013950_3055_MA_00N258W) and Hyblaeus (c, P07_003651_2336_MA_00N228W), coinciding with darkening of the respective features. d) Plot of cosine-corrected I/F values (Lambert albedo) for two regions, one in the extension of Hyblaeus that darkened over the span of the 2007 global storm (1) and a nearby region (2) included to control for atmospheric fluctuations. Shading between the two plotted lines shows time periods when the albedo values diverge, showing that region 1 has been gradually re-acquiring dust since its initial darkening.

In subsequent years, Hyblaeus does not experience as extensive changes as in MY 28, and the principal change is a gradual fading of the previous southwesterly expansion (Figure 2.4d). Both features, however, do experience a few additional darkening events, predominantly in northern winter. In MY 29, Alcyonius broadens to the west (L_s 304.9°-307.4°) and later in the year, lengthens by up to 100 km between L_s 326.8° and L_s 24.5°, although this latter is poorly constrained in time due to the major MRO safe mode over that interval. This southerly dark extension fades over later years. Other minor changes take place in the northern end of this feature, which gains dust during several dusty seasons, moving the northern boundary southward by tens of kilometers over the course of the dataset (though the brightened areas still contrast weakly with terrain to the north). To the east, minor darkening of a small portion of Hyblaeus near 25°N, 124°E takes place in MY 30 (L_s 332.6°-337.6°) and somewhat more extensively in MY 32 (L_s 327.4°-329.7°), again in association with dust clouds. Other, more subtle darkening in this same vicinity can be seen in the mosaics, likewise in northern fall or winter. The consistent appearance of nearby dust clouds in time with sudden, discrete changes in the surface indicates that the darkening events are dust lifting directly associated with these passing storms; subsequent slow fading that most of the darkened regions experience is consistent with gradual dust settling from the general seasonal opacity cycle of the atmosphere. A timeline plot of these changes, together with similarly timed darkening events in eastern Syrtis Major (2.4.1.4) and northwestern Elysium (2.4.5) is shown in Figure 2.6a.

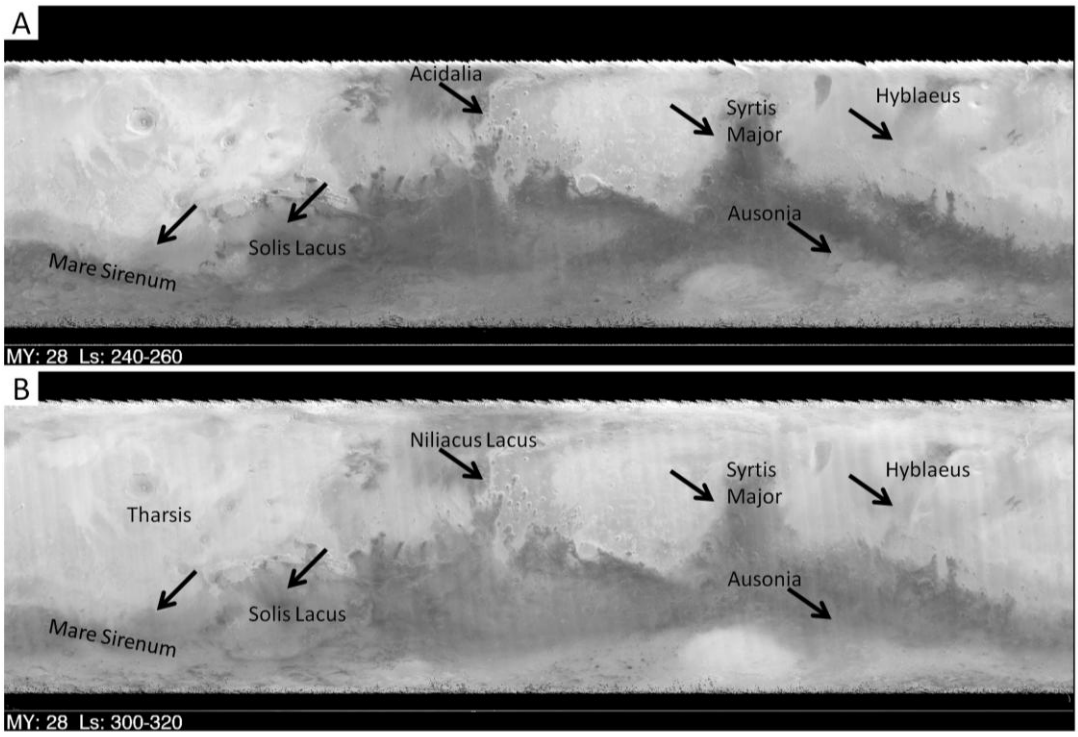

Figure 2.5: Global mosaics composed of images acquired before (A) and after (B) the 2007 global storm that took place in MY 28 between L_s 260°-300°. Large portions of the surface brighten noticeably, especially in the southern hemisphere. During the storm, specific areas experience a net darkening, including Ausonia, western Syrtis Major, Hyblaeus, northern Solis Lacus, southeastern Niliacus Lacus, Tharsis, and eastern Mare Sirenum.

2.4.3 Mare Serpentis , Pandorae Fretum, and Iapygia

Areas to the far south and west of Utopia Planitia were affected by some of the same storm events that caused darkening in those previously discussed locations, as well as other disturbances arising in the southern hemisphere. In this region, cross-equatorial and other large storms produced some of the most spatially extensive discrete surface changes of significant magitude anywhere on Mars outside of the major 2007 storm. These changes sometimes affect tens to hundreds of thousands of square kilometers in an area we will refer to as Mare Serpentis, although some of the changes also affect regions that may be referred to as Pandorae Fretum, or the adjacent brighter terrain of Deucalionis Regio and Noachis. Some of this darkening additionally affected regions to the east, to the vicinity of Huygens Crater, in Iapygia. These storms do not show up in supplementary mosaics due to deliberate efforts to combine mosaics to exclude atmospheric effects (see Section 2.3, above), but can easily be found in individual images acquired within the bounding time frame of large-scale changes discussed below (see

Appendix A or the timeline plot Figure 2.6b). Storm tracking is not a goal of this study, so to provide context in this region where dust storm provenance can be particularly ambiguous, we consulted daily global mosaics produced by Malin Space Science Systems (MSSS) (Malin et al., 2007). The region's extensive variability appears to result in large part from its position at the confluence of several significant storm tracks.

In MY 29, a storm moving south from Utopia Planitia appears to either turn abruptly west when it reaches northern Hellas, or else triggers additional storms that move west and significantly darken Mare Serpentis/Pandorae Fretum between L_s 309.3°-311.1°. This is the same storm sequence that caused darkening in Alcyonius (2.4.2) and eastern Syrtis Major (2.4.1.4). In MY 31, a cross-equatorial storm passed south through eastern Syrtis Major to Hellas before expanding to the southwest, darkening around 2 million km^2 from Iapygia to Mare Serpentis (L_s 207.9°-209.1°). This change is so large it is easily visible in a global map (Figure 2.7). Likely owing to the path of the storm, little change was produced in the Utopia Planitia albedo features, although the timing corresponds well, again, with changes on the eastern edge of Syrtis Major (2.4.1.4). Further extensive changes took place the following year (MY 32 L_s 218.8°-222.0°) that are either related to storms that can be seen moving through Utopia Planitia at this time, or else originated in the vicinity of northern Hellas.

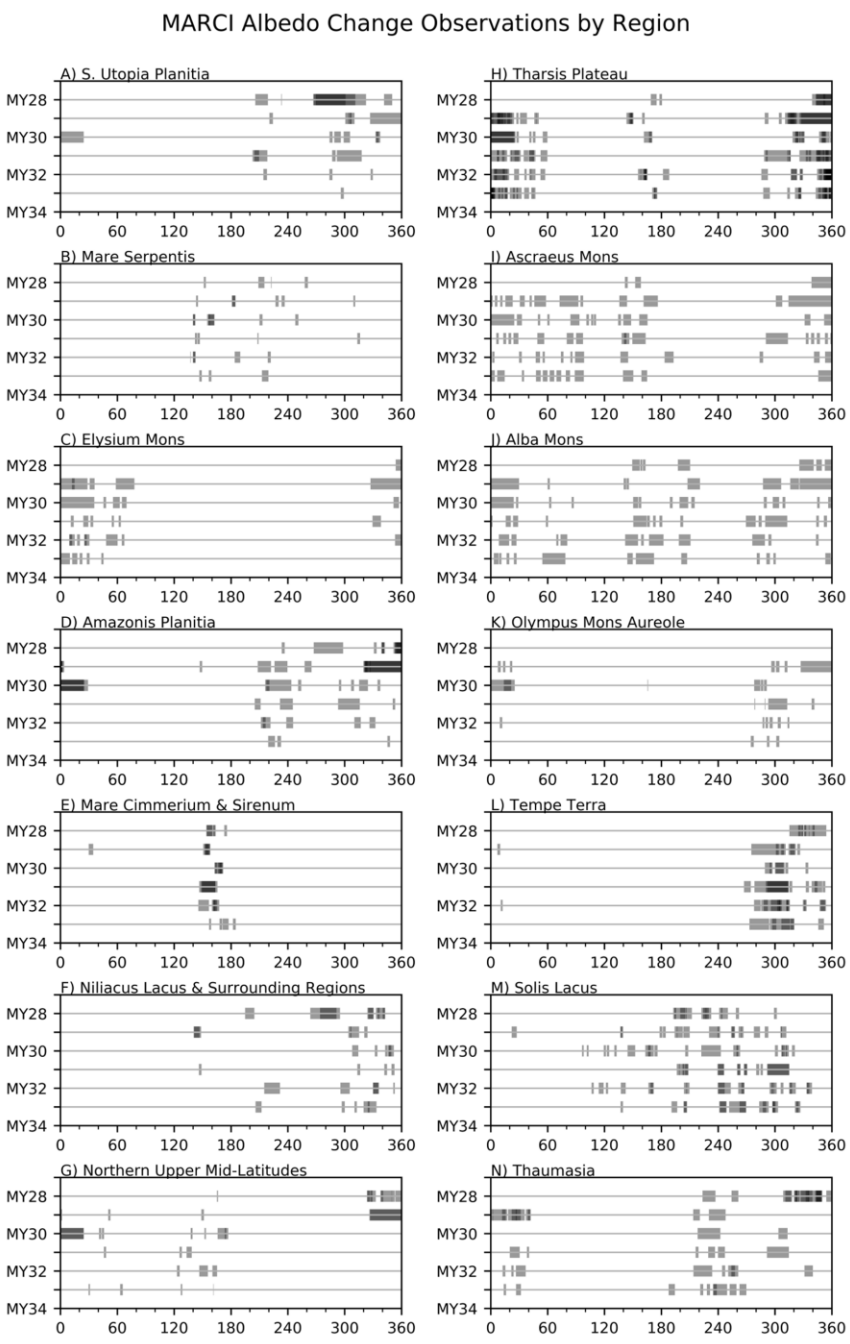
MARCI Albedo Change Observations by Region
A) S. Utopia Planitia
H) Tharsis Plateau
B) Mare Serpentis
I) Ascraeus Mons
C) Elysium Mons
J) Alba Mons
D) Amazonis Planitia
K) Olympus Mons Aureole
E) Mare Cimmerium & Sirenum
L) Tempe Terra
F) Niliacus Lacus & Surrounding Regions
M) Solis Lacus
G) Northern Upper Mid-Latitudes
N) Thaumasia
MY28
MY30
MY32
MY34
0
60
120
180
240
300
360

Figure 2.6 (previous page): Summary timeline plots showing the occurrence of discrete changes in individual regions or related regions of the martian surface. Shaded bars begin and end at L_s values corresponding to pre- and post-change observations, respectively, as listed in Appendix A. Darker segments represent multiple changes that overlap in time. Regions are those as stated above the plots, with a few grouped as follows: (A) S. Utopia Planitia includes E. Syrtis, Alcyonius, Hyblaeus, and N. Elysium; (D) Amazonis Planitia includes Amazonis, Propontis, and W. Propontis; (F) Niliacus Lacus & Surrounding Regions includes that feature plus Nilokeras and Oxia Palus; (G) the "Northern Upper Mid-Latitudes" includes Utopia, Ismenius Lacus, Acidalia Planitia, and Mare Acidalium.

Storms arising near Hellas account for a few of the larger instances of darkening that took place as a result of southern hemisphere storms. In MY 28, a large storm can be seen northeast of Hellas that passed over this region between L_s 222.2°-222.9°, which produced darkening in Mare Serpentis on a scale similar to that of the cross-equatorial storms. Smaller-scale darkening also resulted from a Hellas-spawned storm in MY 29 (L_s 181.4°-182.0°), while in MY 33, very extensive darkening affecting the entire region followed significant regional storm activity (L_s 215.8-219.6). Additional darkening events occurred in the southern winter in all years in the southernmost portion of the Sabaeus quadrangle, affecting the Noachis/Pandorae Fretum region. This darkening is generally relatively minor in spatial extent and took place within L_s 135°-160° (see Appendix A). These events are also associated with southern hemisphere dust storms that either move north into the region, or else arise locally.

Somewhat surprisingly, given the penchant of this region to undergo dramatic changes in response to major storms and the dust lifting that took place to the north and east along the Utopia storm track, the 2007 global storm did not darken the region, and in fact it experienced significant net deposition over that time period (L_s 260°-300°) that reversed much of the darkening from a previous lesser storm. The brightening affected the region much more extensively than dust accumulation after more typical seasonal opacity highs. In following months to a martian year following the storm, numerous episodic cleaning events redarkened portions of Mare Serpentis, as well as the southern edge of Sinus Sabaeus, which had also experienced significant brightening. These events are numerous enough that we do not include them in

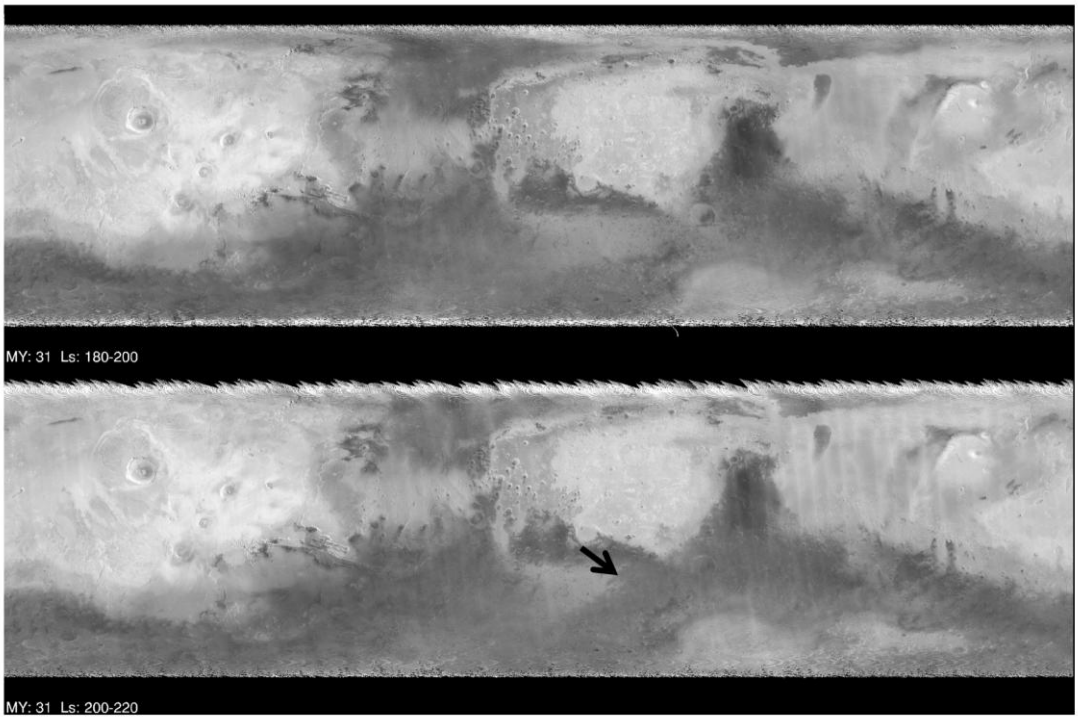

Figure 2.7: Before and after global mosaics of Mars in the time period MY 31 L_s 180°-200° and 200°-220° (September-December 2012). Darkening occurs in Mare Serpentis (arrow) affecting millions of square kilometers that is easily visible even at this scale. This represents the single most significant change that occurred within the dataset outside of the MY 28 global dust storm and occurred as the result of a cross-equatorial storm that travelled south from Utopia.

Appendix A, but most take place the following southern summer and fall. Additional seasonally repeating frequent changes take place in southern Sinus Sabaeus (especially near 12°S, 10°E) in southern fall, sometimes continuing into southern winter, more noticeably in the two years following the MY 28 global storm.

2.4.4 Mare Tyrrhenum and neighboring regions

Like many of the extensive low albedo regions on Mars, Mare Tyrrhenum is host to discrete changes, as well as the gradual brightening that the southern summer dusty season provides. Extensive changes took place during the 2007 storm, which affected both the boundaries of this feature with the higher albedo features to the north, as well as the interior and neighboring bright regions. Dust lifting during this major storm produced the significant darkening near 3°S, 105°E and 0°N, 108°E in the north (L_s 270.0°-282.9°), but most of the region was affected to different degrees. The decay of the storm deposited dust across much of the region, although Ausonia to the south experienced a net darkening (see Section 2.4.16); in total, the

region had less contrast as a result of the 2007 storm. Post-storm, the dust was gradually removed, including in Hesperia to the extent that it no longer formed a clear boundary between Mare Tyrrhenum and Mare Cimmerium to the east. Hesperia became more distinct in MY 30, as a result of preferential dust removal from the adjacent dark regions following southern summer brightening. In MY 32, a large storm from the south darkened a region in northern Mare Tyrrhenum near the northwestern boundary of Mare Cimmerium around 3°S, 105°E between L_s 146.7° and L_s 157.9°; areas to the south and west were affected as well. Other changes to the boundaries of this low albedo region occur within the dataset but are comparatively minor. The interior of Mare Tyrrhenum does not experience regional differences of seasonal change that are quite as sharply contrasting as in Syrtis Major to the northwest, but does appear to vary seasonally and unevenly in response to dust deposition.

2.4.5 Elysium

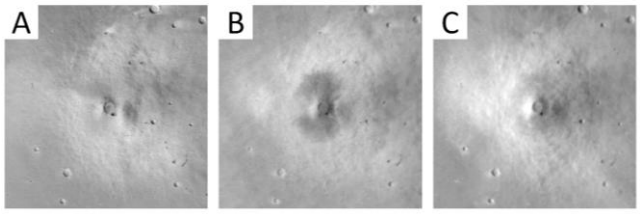

Figure 2.8: Slope darkening on Elysium Mons presented as three separate time-steps: a) MY 28 L_s 340-360°, before the appearance of changes, b) MY 29 L_s 60-80°, near maximum slope darkening, and c) MY 29 L_s 140-160°, after significant fading. Images is approximately 280 km across and is centered on the volcano (near 25°N, 147°E).

The slopes of Elysium Mons have a simple pattern of darkening that takes place predominantly in the northern spring season. Beginning near the very end of MY 28 and the start of MY 29, and continuing through early MY 29, darkening spreads from near the summit of the volcano to a distance of about 50 km, favoring the northern and southern slopes. Darkening is complete by about L_s 80°, after which the streaks fade until the next Mars year (see Figure 2.8). The rate at which the streaks fade is difficult to ascertain due to cloudiness and changes in atmospheric dust opacity, but appears to occur not long after the darkening ceases; in mosaics the contrast between the slopes and surrounding terrain seems greatly diminished by the L_s 140°-160° time-step. Little change occurs for the remainder of the year, until the following spring when

the slopes begin to re-darken. The cycle repeats for the duration of the MARCI dataset with very little variation from year to year (see Figure 2.6c for a plot of all changes).

Some small-scale darkening also takes place lower on the Elysium rise to the northwest, in the vicinity of 27°N 142°E. This forms in patches in northern winter, before the slopes of Elysium Mons begin to darken, and appears to fade more quickly. To the north (near 30°N, 142°E), faint darkening takes place in that creates streaks within a brighter-toned fringe of material to the north of Elysium Mons that are of a similar albedo to material higher on the rise. Like the darkening on the edifice of the volcano itself, these changes are highly repeatable in timing and location, with only minor year-to-year variation.

To the northwest of Elysium (and immediately to the east of Hyblaeus) is a light-toned fringe of material that undergoes occasional expansion (i.e., brightening of the neighboring regions), followed by gradual darkening, unlike most of the albedo changes we describe. The MY 28 dust storm fades this region, but it re-brightens and spreads to the east in the first half of MY 29. In subsequent years, the area fades in the latter half of the martian year and rebrightens again in predominantly the northern spring, although in some years (as in MY 29, perhaps because of the preceding global storm) changes also take place in late winter or summer. The creeping spread of this material suggests it may be of a coarser particle size than the globally-distributed dust that is carried in suspension.

2.4.6 Cerberus

"Cerberus" is a low albedo feature name that describes a formerly extensive dark region to the southeast of Elysium Mons. Easily recognizable in maps spanning decades of both Earth-based and orbital imaging (de Mottoni Y Palacios, 1975; Slipher, 1962), this low albedo feature had faded by the time Hubble observed Mars during the 1995 opposition (James et al., 1996). At the beginning of the MARCI dataset, this area is occupied by several separate dark spots, each around 100 km or more in longest extent, located around 15°N, 159°E; 13°N, 161°E; and 9°N, 149°E; this last in the lee of a 50-km unnamed crater. Over the span of the MARCI dataset to the end of MY 33, the primary change in the feature is a continued brightening of this remnant albedo feature, predominantly affecting mid-toned regions around the outer edges of the remaining

spots. Most of this brightening takes place in MY 30-33 (Figure 2.9); it is not a result of the MY 28 dust storm. Rather, some modest darkening of the dark spots takes place as a result of the MY 28 storm, especially near 13°N, 158°E, and near 11°N, 159°E in late MY 29 following a dust storm. Both of these instances of darkening are reversed by the dust deposition in the following years.

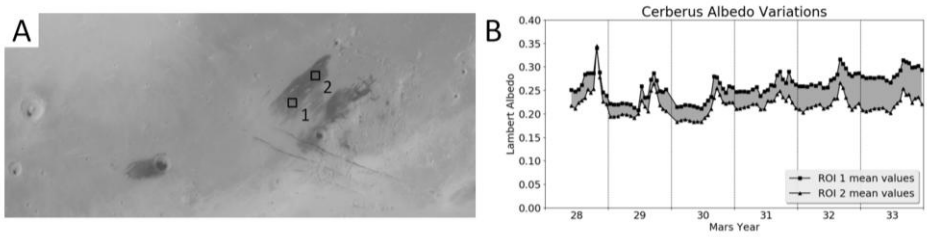

Figure 2.9: A) Portion of Elysium Planitia with remnants of the low albedo feature known as Cerberus (mosaic, MY 28 L_s 340-360° MARCI band 5 (718 nm) observations). Prior to its post-Viking era fading, the dark-toned region would have extended east-west across much of the surface shown here (for scale, around 1600 km across). B) Two portions of one of the remnant dark splotches showing post-GDS darkening following by gradual brightening, especially within ROI 1 to the southwest.

2.4.7 Propontis

Propontis is a low albedo feature that can be seen in early MARCI data near 38°N, 180°E. This prominent dark spot is the eastern portion of a previously more latitudinally extensive feature (Szwast et al., 2006) whose western remnant can be seen to about 170°E. Dust deposition from the atmospheric opacity decline following the major 2007 storm modestly brightened the dark region, but Propontis recovered by early MY 29, with noticeable darkening between MY 28 L_s 330.9°-333.7° and 339.8°-342.5°, as well as smaller changes near the end of MY 28 (Appendix A). Dust storms are common at this latitude and season and frequently appear in MARCI images with timings consistent with many of the surface changes, including very minor changes. The most significant variation happened late in MY 29, just prior to the major MRO safe mode. Between L_s 322.0° and 327.2° of MY 29, the feature nearly disappeared – the entire region suddenly became significantly brighter, similar to (though still weakly darker than) the adjacent terrain. This change has been previously noted by Lee et al. (2014) in MARCI data and by Vincendon et al. (2015) in contemporary OMEGA data. Intervening observations strongly suggest that large-scale dust storms moving through the region are the source for the new surface deposit, unusual in the context of previous and subsequent storms that were associated with

erosion of dust. A few minor instances of re-darkening affect the western edge and regions adjacent to the formerly dark region in MY 29, 31 and 32, but these do not affect the bulk of the interior, and Propontis remains largely buried by the end of MY 33.

2.4.8 Amazonis

Amazonis Planitia is host to a high albedo deposit near 30°N, 200°E that contrasts even with the surrounding darker, but still relatively light-toned terrain. The southern end of this high albedo feature undergoes irregular changes in predominantly the northern fall and winter, including the formation of kilometer-wide curvilinear streaks, darker than their surrounding terrain, that extend hundreds of kilometers in length (see Figure 2.10). These are the “mesoscale linear streaks” described by Thomas et al. (2003). Contrary to many other regions of Mars, discrete brightening events are seasonally quite common here, in the form of changes in the boundary of this high albedo patch. The mosaic time series (see supplemental files) show that the bright material is intermittently spread across scales of tens of kilometers or more, generally to the south or southwest, rather than being disseminated widely by the atmosphere. This suggests that this material is of a coarser particle size than the fine-grained dust whose removal causes the more typical discrete darkening events observable widely across the planet. Sudden changes in the boundaries of the albedo features are often accompanied by visible dust clouds, including storms that appear directly related to the formation of the streaks, as in Figure 2.10b.

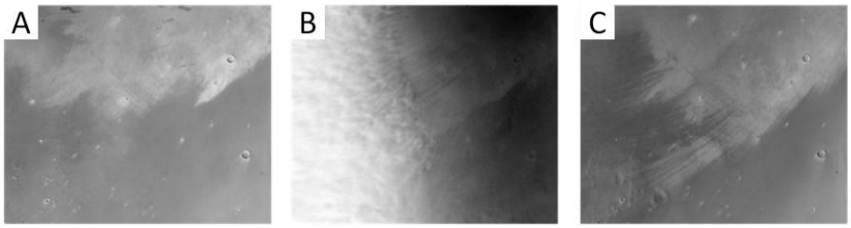

Figure 2.10: A) Mosaic of a portion of Amazonis Planitia (centered near 26°N, 200°E; view is approximately 800 km across) showing variability in the bright-toned deposit and associated mesoscale linear streaks. The mosaic is of band 5 (718 nm) MARCI observations within L_s 300-320° of MY 29. This and the other subfigures have been contrast-stretched relative to most other images and supplemental data to better bring out the features. B) A single MARCI observation showing new streaks that have formed behind billowing dust storm clouds. Image is B12_014368_3243_MA_00N150W, band 5 (MY 29 L_s 324.3°, between the time that images in mosaics A and C were acquired). C) As in A, but several time-steps later (MY 30 L_s 20-40°, after the major MRO safe). The streaks that can be seen forming in B are no longer visible, but new ones have appeared.

At the beginning of the dataset, well-defined streaks can be seen near 30°N, 190°E curving from west to northwest, in addition to a fainter, straight streak patch running NE-SW near 29°N, 199°E that merges into the adjacent darker terrain. Bright patches in the lees of several small craters, higher in albedo than the “bright deposit” itself, grow during northern summer, most noticeably near the small crater at 31.1°N, 199.7°E. The bright deposit itself expands slightly from L_s 233.5° to 236.7°, and then much more significantly over the course of the 2007 storm, in places by over 100 km. The region is modified during the subsequent year, including the formation of streaks around 29°N, 200°E over MY 29 L_s 208.3-222.2°, which partially disappeared by L_s 232.4° and more completely by L_s 239.6°, to be replaced by other streaks with a more southwesterly than westerly orientation. These are themselves again overwritten by southwest-oriented streaks in the lee of a large storm captured by the camera at L_s 324.3°. In the west, near 27°N, 194°E, a MARCI observation caught new streaks between two large storm clouds at L_s 322.6°. Finally, the camera loses sight of the surface completely during the major MRO safe, acquiring the next images in early MY 30, at which point the surface can be seen to have been further modified with long, dark arcuate streaks that formed in the vicinity of 23°N, 200°E (Figure 2.10c).

Later Mars years are similar in behavior, although the changes are generally less extensive than the active MY 29 season. As above, the region is characterized by ongoing seasonal modification of the bright region by changes in its boundary and occasional formation of sets of mesoscale streaks. A catalogue of changes is recorded in Appendix A as for other regions, while a timeline plot of changes in this region and nearby Propontis is shown in Figure 2.6d. Of particular note is a large change in MY 32 that results in the formation of an invading dark region near 27°N, 195°E between L_s 221.5° and L_s 221.7°. This region is erased in a stepwise manner by the bright material over the MY 32-33 fall and winter seasons. Not listed in the table are some minor and gradual variations that include seasonal lengthening of bright (even compared to the “bright” region) crater lee deposits, as mentioned above for MY 28; this appears to be a seasonally repeatable northern summer pattern. By the end of MY 33, the region is substantially different in appearance than the beginning of the dataset; the bright region has been

displaced from its original position and extends far further to the south, by approximately 200 km in places. It is unclear from the span of the data if this is part of an ongoing, long-term trend, or simply a fluctuation around an average position whose current configuration may be the result of interannual variability in storm frequency and intensity.

2.4.9 Mare Cimmerium and Mare Sirenum

The southern hemisphere low albedo features of Mare Cimmerium and Mare Sirenum stretch more than a quarter of the way longitudinally around the planet. Terrain just to the north, included in the discussion here as well, includes two rover landing sites (Gale and Gusev Craters). The interiors of these great dark regions experience a seasonal cycle of dust deposition and removal, as many of the low albedo features on Mars can be seen to do. The timing is different from that of Syrtis Major, discussed in 2.4.1.1. In these regions, dust is deposited on the surface in southern spring, and is removed by southern summer. Compared to Syrtis Major, the dust deposits appear less evenly laid down across these features, likely due in part to the rougher large scale topography of the cratered highlands. The MY 28 dust storm deposits dust in the region as well, but perhaps on account of the seasonal timing, the brightening is less dramatic than certain other regions of the planet.

The major MY 28 storm did, however, produce significant changes in the boundaries of Mare Cimmerium and Mare Sirenum, as it did in many other regions on Mars. The storm darkened areas along the boundary between Mare Cimmerium and the high albedo terrain to the north, and additionally darkened crater streaks and isolated patches that lie in the mid-toned region between the dark features to the south and the northern bright plains. Along the northern boundary of Mare Cimmerium, the most dramatic changes occurred in the vicinity of Hadley and Graff craters, near 20°S, 155°E, northwest to 16°S, 148°E; in some of these regions, the dark area expanded north by around 50 km or more. Southeast of this region, to Ma'adim Vallis, dust removal and deposition resulted in intermediate-toned regions with different boundaries than before the storm (some of this region then darkened again early the following year). The global storm changes also affected the dark streak south of Gale Crater, which expanded eastward by tens of kilometers, and coincided with the darkening of large numerous intracrater dark deposits

or erosional streaks and neighboring dark areas, including those within Gusev Crater, within and to the south of Boeddicker Crater, as well as other named and unnamed craters in the region, and dark patches in the vicinities of 19°S, 164°E and 19°S, 167°E. In Mare Sirenum, the 2007 storm darkened a region in the northeastern end of this feature, near 28°S, 220°E. This region did not participate in seasonal re-darkening that affects the main body of these dark features and faded over subsequent martian years.

Outside of the planet-encircling MY 28 storm, changes in the boundaries of these regions, and sometimes the interiors as well (especially in Mare Sirenum), occur seasonally in conjunction with local or regional storm activity, although they are generally relatively subtle. In Mare Cimmerium, minor darkening occurred in MY 28 near 23°S, 169°E (L_s 154.2°-162.9°). While not an impressive change on its own, the seasonal timing coincided with later changes, suggesting that this region experiences a broadly similar timing to changes each year with year-to-year variations in amount of dust removed (Figure 2.6e). To the east, changes took place in Mare Sirenum with similar seasonal timing (L_s 154.2°-175.7°), affecting regions along with albedo border to the northeast of Dejnev Crater and south of Bernard Crater. In MY 29, the darkening along northern Mare Cimmerium and Sirenum is much more extensive (L_s 150.8°-158.2°), affecting the northern border most noticeably from approximately 145°E to 170°E and 195°E-215°E, and additionally expanding the dark patches within Gusev Crater. In MY 30 changes in Mare Cimmerium are largely restricted to the east, including the northern boundary of Mare Cimmerium near Ma'adim Vallis (L_s 162.8°-165.5°), as well as the interior of Gusev Crater (L_s 168.3°-171.1°) and possibly cotemporal changes in nearby craters at 16.5°S, 166.5°E and 17°S, 169°E (L_s 167.8°-170.6°); changes also take place in Mare Sirenum, most notably east of Bernard Crater (L_s 162.7°-168.8°). MY 31 changes in the boundary are weak, but the region does experience some minor darkening, including north of Graff Crater (L_s 146.5°-163.6°), as well as north of Dejnev and east of Bernard (L_s 148.5°-165.7°). In MY 32, these seasonal changes are again much more noticeable, with darkening observable again near Graff (L_s 145.6°-156.7°) and near the albedo boundary in vicinity of longitude 165°E, including the dark patches near 19°S, 164°E and 19°S, 167°E and within and south of Boeddicker Crater (L_s 161.1°-163.8°), as well as

along the northern border of Mare Sirenum from 195°E-215°E (L_s 159.9°-167.6°). MY 33 changes favor the region near the base of Ma'adim Vallis (L_s 167.9°-170.7°), and all along northern Mare Sirenum within L_s 156.9°-185.0°. These seasonal, storm-driven boundary changes thus apparently occur every year, though variable in extent. The brightening of these regions is not apparent as a sudden change and they instead seem to fade, pointing to gradual dust fallout "resetting" these areas. Hence, there is little net change that occurs over the entire period of observation.

2.4.10 Tharsis

The greater Tharsis region – including the Tharsis Montes and nearby volcanic edifices, Olympus Mons, and Alba Mons, and the interlying plains – is one of the most dynamic regions of the planet for discrete surface changes, albeit most or all of the changes that contribute to the regular, seasonal, and strongly topographically-influenced variability of these areas contrast only weakly with the surrounding terrain. Regional and local aeolian environments across this broad plateau can be expected to vary considerably with proximity to the large volcanoes and other topography arising from the region's volcanic and tectonic history. In addition, Tharsis covers such a large portion of the planet that distant regions may be expected to experience different regimes of the global-scale circulation. For this discussion, we divide Tharsis into the following regions: the plateau consisting of the low-latitude plains, the steep-sloped volcanic edifices, the more gradually sloped region around Alba Mons and the northern portions of the Olympus Mons aureole, and the area in and around Tempe Terra to the east of Alba Mons, each of which exhibits somewhat different albedo change behavior. The high elevation terrain of Syria, Sinai, and Solis Planum to the southeast is covered in the following section (2.4.11) on Solis Lacus.

2.4.10.1 Tharsis Plateau

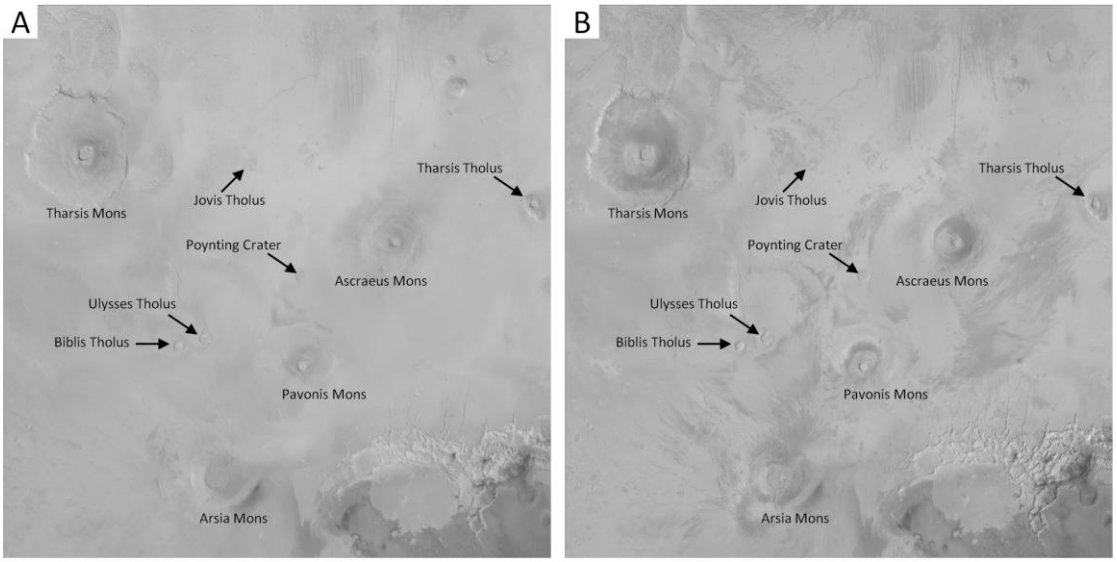

Figure 2.11: a) MARCI band 5 mosaic of the Tharsis plateau, created from images acquired in MY 28 L_s 320-340°. Features mentioned in the text are labeled. b) The same, for MY 29 L_s 20-40°. Regions of the plains surrounding the major volcanoes have darkened, as well as areas on the volcanic edifices themselves.

Extensive regions of the Tharsis plateau are linked by a shared seasonal cycle of change. Portions of this region undergo two distinct periods of darkening in a martian year, affecting specific areas of the plains around the major volcanoes (darkening on the slopes of the large volcanoes themselves is covered in the next subsection). These regions are approximately as follows: (see Figure 2.11 as well): to the north and west of Ascraeus Mons, to the southwest between Ascraeus and Pavonis Mons, to the south and east of Ascraeus to the vicinity of Tharsis Tholus, east of Pavonis, west and northwest of Pavonis including southeast of Biblis and Ulysses Tholus, between those tholi and Poynting Crater to the northeast, from Jovis Tholus northwest to approximately 30°N, 230°E, and north, west, and southwest of Arsia Mons. Each is characterized by one or more small darkening events that affect similar regions around the three large volcanoes. The most significant darkening occurs in late northern winter and early spring (Figure 2.6h), with much of the change occurring between L_s 340° and L_s 20° (see supplemental mosaics as well). A second darkening usually occurs in late northern summer (within approximately L_s 140°-180°), although there is significant interannual variation in the areal extent of these changes, which is less than the winter/spring events. Dust storms were not observed in

before and after image pairs. Together with the high frequency and regularity of the surface changes, this suggests that seasonal wind erosion is the cause of the surface darkening.

At the beginning of the dataset, the darker patches around the major volcanoes are barely visible against the surrounding plains. A small patch west of Ascraeus Mons and approximately 270 km north of the crater Poynting darkens between L_s 168.9°-175.1°. While small, the darkening is consistent in seasonal timing with other changes, sometimes minor in extent, that take place in subsequent years. In the following time-steps, little surface change is apparent (although of course, the atmospheric opacity increases significantly for the duration of the MY 28 storm), until about L_s 339.1°. After this point, comparing almost any two pairs of images covering the same location reveals successive changes across the Tharsis plateau, suggesting that within this time frame, wind stresses capable of lifting dust must be a near-daily occurrence. The darkening continues to at least L_s 24.6° of MY 29 and affects hundreds of thousands of square kilometers. After this point, the dark patches fade gradually, until suddenly redarkening between L_s 143.3°-162.5°. This late summer darkening is much more extensive than in MY 28, affecting many of the same regions that were darkened in the late winter/early spring events; and as with those darkenings, these occur, again, as a series of smaller changes. The following MY 29 winter darkening begins earlier than in the previous year, with small changes noticeable as early as L_s 289.2-293.0°. Much further darkening occurs over the major MRO safe mode; and, when MARCI observations resume in MY 30, the surface is extensively darkened in a manner similar to its appearance at this time in early MY 29.

Interestingly, while the position and extent of the dark patches are similar between early MY 29 and early MY 30, the latter also has bright regions that are higher in albedo than both the darkened areas and the majority of the unaffected plains. A comparison with MY 28 mosaics suggests that these had been bright at the beginning of the dataset as well and that Tharsis lost dust from these regions as a result of the 2007 storm; this is consistent with the behavior of the region in the response to the 2001 storm, in which it also darkened (Geissler et al., 2016; Szwast et al., 2006).

The behavior of this region in later years is consistent with the pattern of timing described above. In MY 30 between L_s 161.6° and 172.7°, isolated portions of the region redarken after fading between the intervening period along with the previous changes. Here, the seasonal summer darkening is significantly greater than in MY 28 but less than the equivalent MY 29 season. In MY 31, however, it is entirely absent. Repeated seasonal winter/spring darkenings occur regularly in all Mars years to the end of MY 33, and subsequent years display the late summer changes as well, which are easily apparent in the supplemental mosaic data in MY 32 and MY 33.

2.4.10.2 Tharsis Montes and Olympus Mons

The steep-sloped Tharsis volcanoes undergo a seasonal pattern of changes that is similar, but with somewhat extended seasonal duration, compared to that of the surrounding region. This manner of darkening affects the slopes of Olympus Mons and the three Tharsis Montes volcanoes Ascraeus, Pavonis, and Arsia Mons. The annual cycle of slope darkening begins in late northern winter/early spring, with similar timing to the changes that take place on the surrounding plains (previous section).The darkening begins midway up each volcano and spreads downslope and then upslope, darkening to the summit by late northern spring. The darkened surfaces often have the appearance of a dark collar around each mountain (see Figure 2.11), but in some cases, especially on Olympus Mons, individual dark slope streaks can be seen. The mountains fade but undergo a minor re-darkening in northern summer that is often very apparent on Olympus and Ascraeus Mons, but may not occur on Pavonis (or is much more subtle). For brevity, we record these changes for Ascraeus Mons only in Figure 2.6i and Appendix A; the timings for the other large volcanoes in the region are similar. The darkening in Tharsis is much more extensive than what takes place on the slopes of Elysium Mons (2.4.5), where the summer re-darkening is entirely absent.

The majority of these changes, like the changes on the plateau below, are seasonally regular and incremental, and clearly associated with the extreme topography that drives significant diurnal slope winds (e.g., (Magalhães and Gierasch, 1982; Toyota et al., 2011)). We do occasionally see, in individual MARCI frames, evidence of local-scale convective dust lifting,

which include predominantly small plumes, although it is not clear the extent to which these may contribute to the visible surface changes driven by topographic winds. Over Arsia Mons, a comparatively large (10s of km) dust-lifting storm often forms around the southern spring equinox; the resultant shadow cast by this storm is often visible in our mosaics (see supplemental files). This seems to be a regular or at least semi-regular event.

2.4.10.3 Western Alba Mons

In northern Tharsis, Alba Mons dominates the regional geography in the form of a broad topographic bulge, although it lacks the sharply-defined edifices of the taller volcanoes to the south. As is the case with the other large Tharsis volcanoes, dark patches form seasonally on the plains surrounding the base of the mountain. While these share some similarity with the Tharsis plateau streaks, they have sufficiently different behavior, especially in the late northern summer and early autumn, as to merit their own discussion.

At the beginning of the MARCI dataset, the plains to the west and southwest of Alba Mons are in a relatively bright, dusty state. After L_s 149.3° of MY 28, dark streaks appear on the upper slopes of the volcanic rise below the main edifice (near 38°N, 243°E) and progressively darken the area near that elevation and some of the lower slopes until at least L_s 210.4°. As in regions of Tharsis to the south, there is a second annual darkening near the northern spring equinox. In this case, the darkening favors regions lower on the slope than the changes that occurred prior to and just after the fall equinox. The changes, which begin around L_s 325.7°, are mostly complete by MY 29 L_s 29.8°, but there is a “last gasp” of small-scale darkening that takes place late in northern spring (L_s 60.1-62.3°) in the southernmost portion of this area, near 31°N, 245°E. In MY 29, thin dark streaks again appear on the upper slopes in northern summer (beginning L_s 140.3-142.8°), followed by darkening of the lower slopes in autumn. The winter-spring darkening begins earlier, with changes discernible by L_s 290.5°; later years suggest this is a more typical pattern, with MY 28 unusual likely because of the major dust storm. As in other years there is a modest north to south trend to the darkening (or, darkening progressively towards the north, and then later to the south), perhaps due in large part to the higher topography to the south. As in the previous year, the last bit of darkening occurs over a spatially small region in the

south, this time as late as L_s 85.4-87.7°. Other years are similar in the appearance, timing, and progression of the changes, demonstrating that this is a regular seasonal pattern in this region. Compared to the lower latitude Tharsis region, not only is the summer-autumn darkening more regular in extent, but the timing of the changes in both seasons is not the same, as can be seen in Figure 2.6j. Particularly, the changes in Alba Mons occupy a significantly larger extent of the year, and sometimes include “pauses”, such as the hiatus in darkening that takes place in most years around the L_s 320-340° time-step, visible in the supplemental mosaic animations in MY 30-33.

To the west and south of the Alba region, isolated darkening takes place with similar timing, essentially as an extension of the previous region’s behavior. These areas are smaller and skirt the base of regional topographic boundaries formed by the northern portions of the Olympus Mons aureole and other regional highs, near 33°N, 214°E, and from 37°N, 217°E northeast to 40°N, 223°E (and from there, joining the region around Alba Patera), and in the east in the vicinity of 32°N, 228°E. The darkening favors the northern winter-early spring season (see Figure 2.6k) and typically begins with the lower elevation regions, with the area around 32°N, 228°E continuing to darken into the early spring. Interestingly, the area at 33°N, 214°E also undergoes sudden, discrete brightenings, something that appears to be true for only a few regions on Mars. One such example occurs in MY 32 (L_s 313.3-315.1°), during which the middle of the region that had just darkened (in several steps, but e.g. L_s 290.0-292.6° broadened the dark region) becomes suddenly bright, with sharp boundaries to the adjacent dark areas. These changes can be seen in the mosaic animations provided as supplemental files (for this example, the brightening appears in the following L_s 320-340° time-step, because the mosaicking favors darker pixels in a given time range).

2.4.10.4 Eastern Alba Patera region and Tempe Terra

To the east and southeast of Alba Patera, including the eastern slopes of the volcano itself and as far east as the Tempe Terra region (between approximately 28-45°N, 250-290°E), is an area that also undergoes seasonal and frequent changes that suggest a regular cycle of dust deposition and removal by seasonally variable winds. These changes are listed in Appendix A

under the name “Tempe Terra.” Unlike the region west of Alba Patera and much of Tharsis to the southwest, darkening occurs seasonally only once per Mars year, almost exclusively in the northern winter. As can be seen in Figure 2.6L, MY 28 is somewhat unusual in that visible darkening is delayed to after the global-scale storm, either because earlier darkening is obscured or erased by the storm, or because of the influence of the heightened atmospheric dust opacity on dust lifting in this region. The MY 28 storm deposits dust that is rapidly removed during the remainder of the northern winter season. In all years smaller-scale winter storms are commonly seen down to around 45°N, although they do not appear to be connected to most instances of darkening that occur on the surface here. There are, however, a few exceptions, in which visible dust clouds occur in convincing association with surface changes. These occur predominantly in the eastern portion of the region, where Tempe Terra abuts the Acidalia storm track, and seem to occur predominantly in the mid-late winter season. Also seen in the eastern portion of this region are occasional discrete brightenings, similarly in northern winter, that suggest some of the lighter-toned material is capable of being redistributed by aeolian forces without being broadly disseminated as lifted dust frequently is.

2.4.11 Solis Lacus and Thaumasia

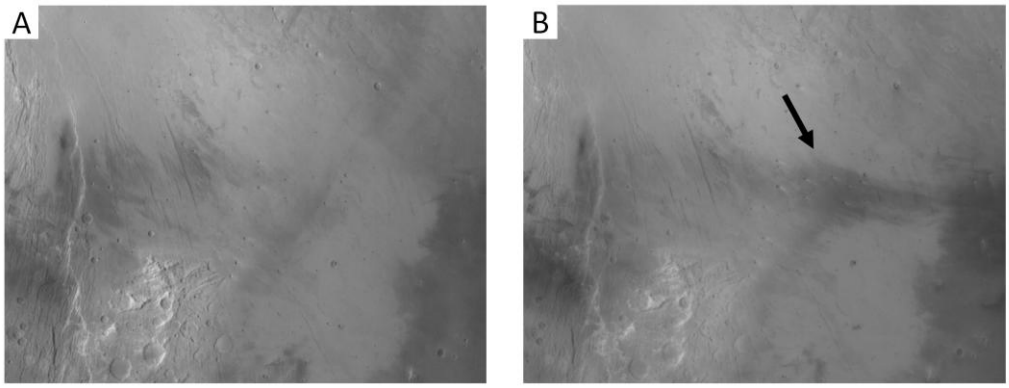

Figure 2.12: a) A MARCI band 5 mosaic of southwestern Solis Lacus (centered near 24°S, 260°E; view is approximately 1000 km across) in MY 29 L_s 200-220°. b) The same region within MY 29 L_s 300-320°, showing the appearance (arrow) of a low albedo streak. The feature is seasonal and redarkens every southern spring and summer.

Solis Lacus (located broadly at 25°S, 270°E) has been widely reported to be a site of significant albedo variation (Antoniadi, 1930; Sagan et al., 1973). MARCI data show that this

region participates in many different modes of variation, including both seasonal and secular changes, that have likely contributed to its historical reputation.

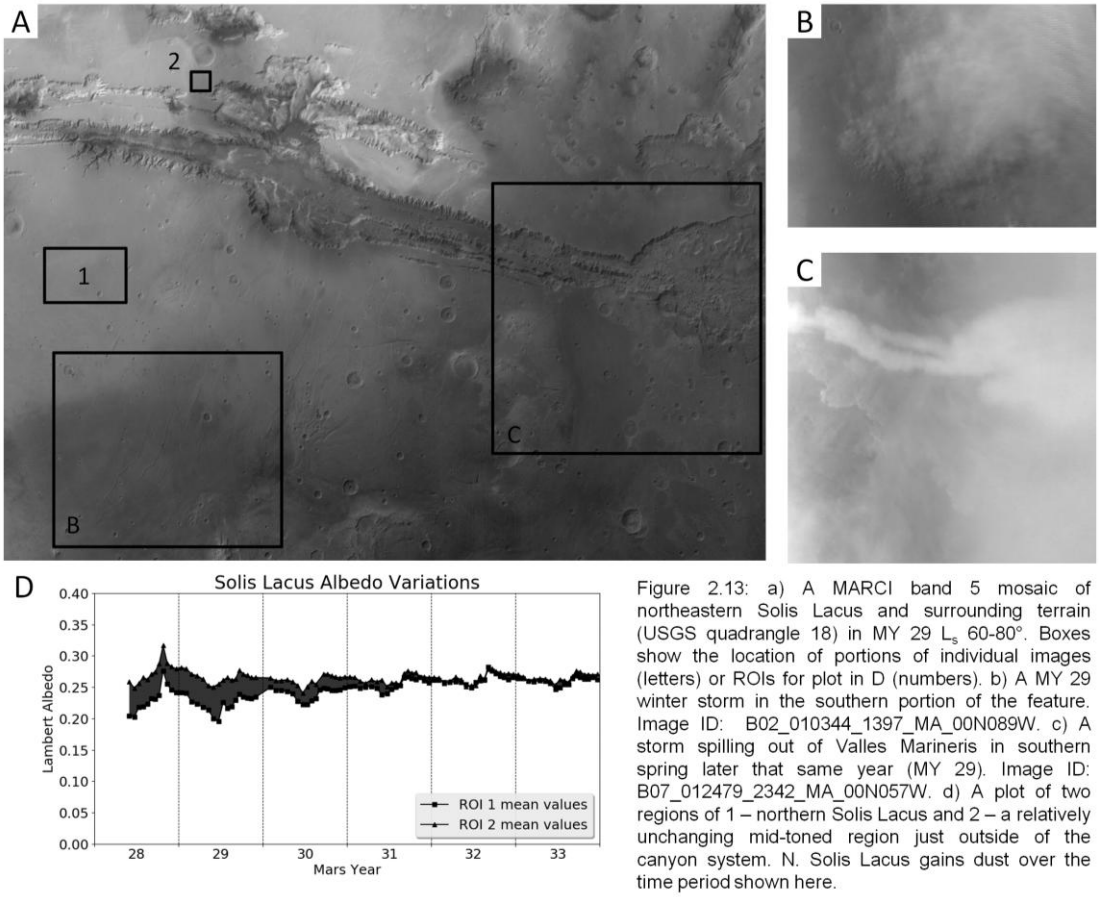

Figure 2.13: a) A MARCI band 5 mosaic of northeastern Solis Lacus and surrounding terrain (USGS quadrangle 18) in MY 29 L_s 60-80°. Boxes show the location of portions of individual images (letters) or ROIs for plot in D (numbers). b) A MY 29 winter storm in the southern portion of the feature. Image ID: B02_010344_1397_MA_00N089W. c) A storm spilling out of Valles Marineris in southern spring later that same year (MY 29). Image ID: B07_012479_2342_MA_00N057W. d) A plot of two regions of 1 – northern Solis Lacus and 2 – a relatively unchanging mid-toned region just outside of the canyon system. N. Solis Lacus gains dust over the time period shown here.

In the southern portion of Solis Lacus, an irregular dark patch forms (or re-darkens) seasonally every year in southern spring to midsummer. This feature is located between 260°E to 275°E and is centered at approximately 24°S. This darkening is composed of numerous individual changes, sometimes as elongate east-west streaks that curve slightly northwest/southeast, especially near 24°S, 266°E. The difference in albedo is relatively low in contrast against the surrounding terrain, particularly in MY 28 before the global storm, but can be seen to repeat every year (see Figure 2.12, as well as supplemental mosaics for quadrangles 17 and 18). The formation of this dark patch is likely related to the larger scale topography; the area is a regional low compared to Syria Planum to the northwest and higher topography to the south

and southwest. Many of these changes, together with other changes discussed below, are listed in Appendix A and shown in Figure 2.6M.

Certain changes in the area can be seen to be directly associated with storm clouds. This includes regions to the south, east and northeast of the region discussed above, which are affected by storms that leave both large and small changes in their wake. The global storm of MY 28 affected the entire area significantly; darkening portions of the region hundreds of kilometers across around, e.g., 16°S, 264°E and 26°S, 276°E but raising the albedo in southwestern Solis Lacus and Thaumasia to the east. Other storms occur in this region throughout much of the year. In southern winter, they may move into the southern portions of Solis Lacus from the south, while in southern spring and summer, many appear to come from the northeast. To the east, Thaumasia Planum and surrounding regions are affected by numerous changes, sometimes associated with storms, with similar seasonal timing. In that region, however, changes can extend into southern autumn as well, as shown in Figure 2.6N. Examples of such storms are shown in Figure 2.13.

In the northern portion of the region, within or near Sinai Planum, other secular changes take place over the MARCI dataset that are not related to the 2007 storm. As shown in Figure 2.13, this region gains dust from MY 28 to MY 33. Most of this brightening appears to take place in MY 30 and MY 31. By the end of MY 33, the region is substantially different than at the start of the MARCI dataset.

2.4.12 Niliacus Lacus and neighboring regions

The region in and around Niliacus Lacus (southern Mare Acidalium and surrounding areas, essentially) experienced numerous changes that affected the interior and boundaries of this low albedo feature, as well as the low albedo terrain to the southeast in Oxia Palus, including nearby crater streaks. Images acquired by MARCI in the intervals within which observations constrain the timing of discrete changes very frequently contain dust clouds (see Figure 2.14). These changes occur predominantly as darkening events at several specific seasonal times, most occurring within approximately the following intervals: northern mid-summer, L_s 140°-150°; northern early-to-mid autumn, L_s 190°-220°, and northern mid-to-late winter, L_s 290°-355°.

Common areas where changes occur include in the boundaries around an isolated, 350-km (east-west) wide high albedo spot near 29°N, 335°E, the southeast border of Niliacus Lacus or terrain between it and Oxia Palus near 15°N, 340°E, and western Niliacus Lacus around 27°N, 320°E. Changes in this latter region tend to be lower in contrast than others, as they occur within already relatively dark terrain, and appear restricted to the northern winter season.

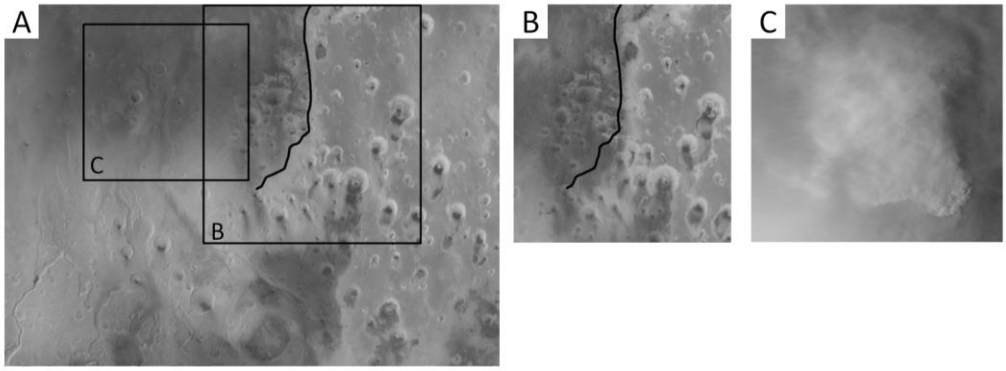

Figure 2.14: a) A mosaic covering portions of Niliacus Lacus and Oxia Palus (0-30°N,0-45°W), composed of MARCI band 5 (718 nm) images acquired within L_s 120-140° of MY 28. Outlines show the locations of the areas in b) and c). B) The southeastern boundary of Niliacus Lacus at MY 33 L_s 340-360°. The low albedo region has expanded southeast relative to its position at the beginning of the dataset, shown by the black line. C) An individual MARCI band 5 image showing a northern summer storm moving through the area. Image ID: B02_010447_1437_MA_00N021W.

Of particular note are secular changes that occur along the eastern and southeastern boundary of Niliacus Lacus, and the bordering fringe of light-toned material, as well as between Niliacus Lacus and Oxia Palus to the southeast. Over the course of the MY 28 global dust storm, this area changed significantly; both the light-toned border and the low albedo terrain behind it advanced to the east and southeast along its border with the intermediate-toned terrain to the east, occurring from at least 31°N, 348°E along the albedo boundary to 12°N, 338°E. Changes can also be seen either within or in the dark streak that appears to emanate from almost every crater in the mid-toned terrain in this region, as a darkening that is in many places accompanied by a small bordering light-toned fringe (see supplemental material). This affects dozens of craters within 0-23°N and 325-15°E (i.e., many of those within the intermediate albedo terrain between Niliacus Lacus, and Margaritifer Sinus and Sinus Meridiani to the south and southeast). In addition to the global storm changes, comparatively minor year-to-year differences can be seen in the position of the east and southeast boundary of Niliacus Lacus that tend to extend the low

albedo feature, and the leading bright fringe, to the east and south. In MY 28 and 33 such changes additionally and noticeably affect the regional broad crater streaks in a similar manner. The magnitude of the shift in the boundary of eastern Niliacus Lacus from the beginning of the dataset to the end of MY 33 is a few 10s of km (see Figure 2.14a-b), although it is difficult to measure precisely because the boundary is generally not sharp and the shift is not the same along the entire length. However, each change represents the same tendency to enlarge this feature, and this secular trend is continued in the north as well (see 2.4.15).

To the west, changes take place in areas within and surrounding Nilokeras, the dark terrain that occupies the distal portion of Kasei Vallis near 27°N, 300°E. These changes occur overwhelmingly in mid-to-late northern winter, often with visible dust clouds. The highest contrast changes are darkenings that followed the MY 28 storm, which deposited dust in the region. Changes take place in nearby mid-to-light-toned terrain as well, including to the west near 28°N, 289°E, and in Lunae Palus to the south. A few of these changes are brightenings, for example, very noticeably near 28°N, 291°E between L_s 351.3° and L_s 352.9°, and earlier, immediately to the southeast, on the southern side of the northern Kasei channel between L_s 330.0° and L_s 336.1° of the same year, MY 32. The timing of all changes is shown in Figure 2.6F and listed in Appendix A as well.

2.4.13 Mare Erythraeum and Margaritifer Sinus

Across the equator south from Mare Acidalium and Niliacus Lacus is a vast low albedo region that is occupied by Margaritifer Sinus (to the west and southwest of Sinus Meridiani) and, further south and southwest, Mare Erythraeum. These dark features are often not well separated by dustier regions, giving the appearance of an uninterrupted dusky highlands terrain that stretches from equatorial latitudes into the mid-latitudes. These regions cycle dust extensively with the atmosphere, gaining significantly following atmospheric opacity highs and rapidly losing the deposited dust the following Mars year. The 2007 global storm significantly, if unevenly, raises the albedo across extensive portions of this region; the region recovers early in MY 29 in a “patchwork” manner, as dark regions with sharply-delineated albedo boundaries appear and spread across the aforementioned brightened terrain. This pattern recurs in the following years,

although less dramatically than following the global dust storm fallout. These cleanings, while occurring as discrete darkening events, are so widespread and numerous across the region during the southern fall that we do not tabulate all the individual changes. There is an additional period of seasonal darkening occurs in mid-late southern spring that is easily visible in the mosaics (see supplemental material) because of the uneven albedo values of the surface at regional scales.

In addition to the changes described above, which affect the bulk of the low albedo terrain in this region, there are also changes that affect small regions to the east and southeast of Margaritifer Sinus at later seasonal times. These affect the area between Dollfus and Newcomb Craters (near 21°S, 358°E), as well as the variably-toned terrain that separates Margaritifer Sinus from Sinus Meridiani (near 15°S, 355°E), between approximately L_s 130°-160° (mid-late southern winter). Small dust clouds are occasionally seen around this time, but it is not clear from the observations that these changes are due to such storms, or if these are simply late seasonal changes caused by locally gusting winds following the earlier changes to the west.

2.4.14 Arabia

The high albedo terrain of Arabia is arguably one of the most static large-scale regions of the planet. This feature covers most of its eponymous quadrangle (see supplemental files), and the lack of any significant changes in the light-toned terrain is clear from the animation. Transient dark patches are shadows of clouds or, on occasion, a shadow of the moon Phobos. The 2007 dust storm produces changes in intracrater and adjacent dark patches in the terrain to the west, which is Oxia on albedo maps, but no changes to the boundary of Arabia and darker-toned regions to the west. To the east, where Arabia (or Aeria in that location) meets Syrtis Major, variability with that dark feature's western border is as discussed in the section on Syrtis Major, 2.4.1.3.

2.4.15 Northern mid-latitudes

The upper portions of the northern mid-latitudes (50-65°N, the most northerly extent of our analysis) are seasonally obscured by the polar hood and the low light conditions of near polar night, and portions are covered by seasonal ice from the encroaching polar cap in winter and

early spring. Significant obscuration is visible in the mosaics in time-steps from L_s 180°-340°, and the retreating cap is still quite visible in northern portion of the mosaics in the subsequent two time-steps (L_s 340°-20°). This limits our ability to constrain the timing of dust-cover changes that occur along the boundary and within the interior of northern upper mid-latitude low albedo features (In this section, we refer to these large albedo features themselves broadly as Mare Acidalium and Utopia, the latter not to be confused with Utopia Planitia, the low-lying plains that extend to the south.) Comparison of before and after time-steps confirms that most of the change that takes place in the albedo boundaries occurs over the span of the seasonal obscuration. Many of these changes are spatially minor and may represent a fluctuation around some approximate “average” configuration where the dark features meet the bright plains to the south (this appears to be more true of Utopia than Mare Acidalium, see below). At some longitudes, and perhaps most visibly where there is more dust cover in this latitude band (such as near 240°E), some changes in the north may be the beginning of a seasonal darkening that otherwise largely takes place when the surface is hidden from the camera’s view. Several instances of change that occur outside of the northern fall and winter obscuration are included in Appendix A and shown in Figure 2.6g. These occur in mid/late northern summer and early/mid spring, and are very often accompanied by dust storm clouds. The season of the 2007 dust storm caused significant changes in some places in the northern mid-latitudes and little to none in others. In particular, the ~500 km dark patch near 44°N, 63°E gained an extensive amount of dust over the course of the global storm, as did a portion of Utopia to the east around 47°N, 108°E; both of these regions largely recovered during the following northern winter season.

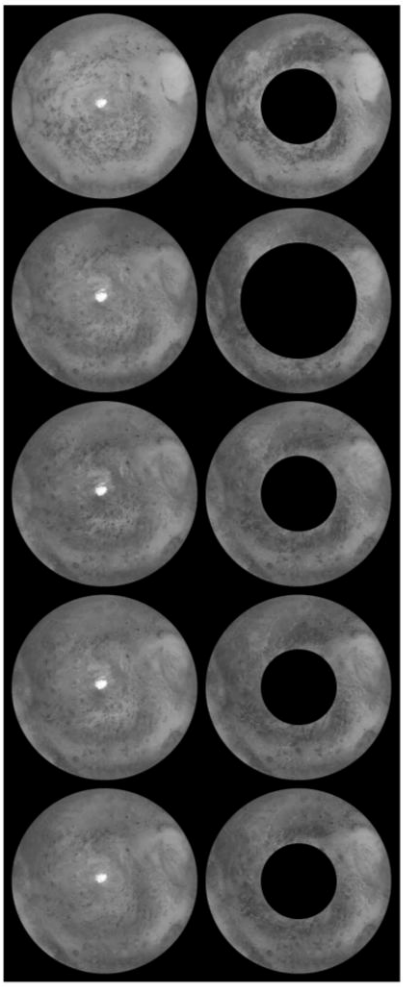

Figure 2.15: Five pairs of MARCI band 5 azimuthal mosaics centered on the south pole of Mars, composed of images acquired within (left column) L_s 320-340° of MY 28-32 (ordered top to bottom), and (right column) L_s 0-20° of MY 29-33, except for MY 30 (second from top) which is L_s 20-40°, due to an MRO safe. Time-steps in the right column do not show all latitudes to the pole due to high solar incidence angles. Darkening concentrated near 55°S occurs between each mosaic pair.

Along the eastern edge of Mare Acidalium, there is a bordering region of relatively higher albedo separating the low albedo feature from the intermediate-toned terrain to the southeast. This bright-toned fringe, and in places the dark region behind it, expanded to the southeast over the span of the MARCI data examined. This takes place while the surface is seasonally difficult to observe. Changes contributing to this secular variation appear to have occurred in most years, although the changes in MY 31 are more noticeable than other years. The changes appear to be the northerly portion of an expansion that is also occurring to the south, along southeastern Niliacus Lacus (see section 2.4.12). Possibly related as well is apparently secular darkening that takes place over the fall/winter season to the northeast of Mare Acidalium, darkening to an intermediate or dark tone a latitudinal band near 50°N from 10°E to 30°E over the several martian years of observation. The net effect of these changes, combined with those to the south, is a secular expansion of the greater Mare Acidalium region.

2.4.16 Southern Mid-Latitudes

The southern mid-latitudes (30-65°S) suffer from the same viewing challenges, at the opposite seasons, as the mid-latitude regions of the northern hemisphere. Unlike the northern hemisphere, however, which has regions of high and low albedo with what are often well-defined boundaries, the southern mid-latitudes are variably-toned and composed of diffuse or patchy albedo differences, sometimes in relationship to local or regional topography. Albedo variations in the south are substantially different than the other hemisphere, with significant seasonal and

interannual variability. The MY 28 storm deposited dust that raised the albedo extensively throughout the southern mid-latitudes, especially below around 40°S latitude, although much of the region appears to gain dust following other lesser opacity increases as well. At higher latitudes, dust is removed every year in early southern fall as the polar cap and hood expand northward (Figure 2.15). This change is especially noticeable in a dark-toned ring that circles that southern cap at around 55-60°S, more so at particular longitudes that include across portions of Mare Chronium (at this latitude band between around 120°E and 180°E), and broadly around both 15°E (southwest of Hellas Basin) and 250°E (southwest of Solis Lacus). In the northern portions of these latitudes, changes occur that are often southerly extensions of variability described elsewhere in this paper. These include the spatially extensive changes that take place as a result of storms crossing Noachis (2.4.3), changes in the southeastern portion of Mare Sirenum (2.4.9), and in the southernmost portions of Solis Lacus (2.4.11).

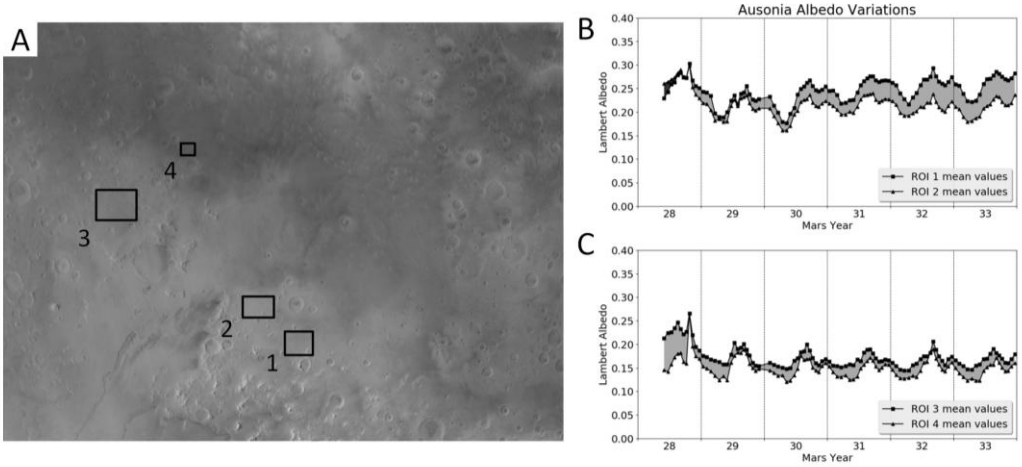

Figure 2.16: a) Mosaic of the region between Hellas and Mare Tyrrhenum (40-10°S, 230-275°W) assembled from MARCI band 5 (718 nm) observations acquired within the MY 28 L_s 180°-200°. ROIs show the locations from which the mean mosaic values are plotted in b) and c). b) A plot of two regions in Ausonia labeled 1 and 2 in a). Both regions lose dust as a consequence of the MY 28 global storm, with significant recovery shown by ROI 1. c) A plot of another region of Ausonia (ROI 3) and a relatively stable area of Mare Tyrrhenum (ROI 4). It is clear that the region of Ausonia represented by ROI 3 does not recover the dust it lost following the MY 28 storm (in all plots, the occurrence of the storm is the peak value in MY 28).

To the east and northeast of Hellas Basin, there is a region, Ausonia (near 30°S, 105°E), that darkened noticeably following the 2007 global storm (see Figure 2.5). This difference was also reported by Vincendon et al. (2015, §4.4.2) in OMEGA data. Portions of this region, especially in the southeast, recovered some of the dust lost to the storm; however, it is clear that

some regions did not (Figure 2.16) as of the end of MY 33. This contrasts noticeably with Hellas itself, which gained dust following the 2007 storm, and appears to lose much of this over the following year. Hellas is seasonally difficult to observe but does appear to show some annual changes, especially in southern autumn near the margins of this feature, and also maintains some albedo difference within its interior that may be related to topography.

Other interannual changes in the southern mid-latitudes appear to be fluctuations around an average configuration of boundaries of lighter and darker toned regions across a range of spatial and magnitude scales. Regional scale albedo features maintain their average identities through latitude and longitude dependent seasonal dust cleaning despite undergoing extensive changes in albedo that are large compared with the albedo contrast with neighboring regions. Lower contrast differences within large regions fluctuate in value as well. Crater interiors generally follow the regional behavior, although a number of craters also have intracrater dark areas and/or may have influences of local topography on km-scale albedo differences.

2.5. Discussion

The MARCI dataset shows that large regions of the planet are expressive of near-surface wind events in the form of albedo changes that result from the removal or deposition of surface dust. Many of these changes are seasonally timed and annually repeatable, occurring each year with different degrees of regularity in form and extent. Numerous changes coincide, unsurprisingly, with storm activity that is frequently captured by the high temporal resolution imaging that MARCI provides. The observation that much of the sudden changes caused by storms are associated with darkening of the surface, and only rarely with brightening, suggests that dust removed by storm activity is typically disseminated widely by the atmosphere before being re-deposited on the surface. In regions where changes are frequent and repeatedly observed without accompanying storm clouds, we suspect a more gradual erosion of dust by seasonal winds that intermittently reach a threshold for dust lifting. This manner of dust lifting may act across much of the martian surface, although such removal generally does not produce the sharp albedo boundary differences that are more characteristic of the storm-driven changes, making them more challenging to extract from temporal and regional differences in atmospheric

opacity. Exceptions to this occur in areas with significant topography, such as near the bases of the large Tharsis volcanoes, where variations in aeolian dust removal result in clear albedo differences over relatively small (10s of km) scales; in eastern Syrtis Major, where the sloping terrain between Syrtis and Isidis allows for irregular removal of dust; and around other topographic features as well. Annually recurring declines of atmospheric opacity during and following the southern summer dusty season play an important role in recharging regions with dust.

Many of the larger surface changes discussed above are similar to those that have been recorded in the literature for prior Mars years, suggesting that specific patterns of change within the MARCI dataset are likely representative of the typical modern day martian climate cycle of dust removal and deposition. For example, MARCI observations of seasonal dust deposition and erosion in east/central Syrtis Major correspond well with descriptions and drawings of the behavior of this region over the last ~50 Mars years or more (e.g., Antoniadi, 1930, 1916; Capen, 1976). Changes in the Mare Serpentis or Pandorae Fretum regions of Mars occur frequently in the MARCI dataset due to occasional large, sometimes cross-equatorial storms and are often of sufficient size to be easily visible in Earth-based telescopes. Such variations in this region are indeed well-recorded in historical observations (e.g., Slipher, 1962).

Other examples of historical changes can be said to be not well represented within the MARCI dataset, or to have affected specific regions to a much greater magnitude than observed in present times. Dramatic changes to the extent that occurred in the early to mid 20th century to the east of Syrtis Major (de Mottoni Y Palacios, 1975; Slipher, 1962), during which a large area was substantially darkened relative to present-day Mars, have no parallel in MARCI or any other orbiting spacecraft imagery. MARCI observations show that the changes in this region that occur in the present day, while significantly lesser in spatial extent, are overwhelmingly due to dust storm activity (as are most observed changes that significantly alter albedo boundaries). Indeed, this region of southern Utopia is within one of three topographically-controlled northern hemisphere storm tracks that extend longitudinally across the equator from the large northern basins of Utopia, Acidalia, and Arcadia (Cantor et al., 2001; Hollingsworth et al., 1997, 1996).

MOC and MARCI observations have shown that martian dust storms favor the Acidalia storm track, at a rate of about three times that of Utopia for storms lasting five sols or more (Wang and Richardson, 2015). The expansion of the low albedo terrain in eastern Mare Acidalium and Niliacus Lacus which has been observed by both MARCI (Section 4.12, 4.15) and MGS MOC (Geissler, 2005; Geissler et al., 2016), and the current absence of the kinds of historical variability seen previously in southern Utopia, could be a response to decadal (or longer) timescale variations in dust storm activity along these tracks.

Other secular changes observed on Mars might similarly be related to decadal timescale differences in storm frequency. For example, the fading of the Cerberus feature appears to have occurred gradually (James et al., 1996), suggesting that in the present climate regime the region's low albedo surfaces are not in equilibrium against atmospheric dust fallout. It is possible that the previously darker, more extensive form may have been maintained by more frequent storm activity, either in this region or from global-scale storm events, by analogy with the spatially limited darkening observed by MARCI following the 2007 storm (Section 2.4.6). Previous observations of variability in the extent and position of Cerberus that occurred while it was still a large dark region (Chaikin et al., 1981) may indicate the effect of storms not observed before the present era of orbital monitoring.

The above examples show how long-term monitoring of Mars can inform our understanding of to what extent, and on what timescales, the martian dust cycle is 'closed'. In other words, how long does it take for regions which undergo a change in surface dust cover to revert to their previous state, and by what processes, thus maintaining the long-term configuration of albedo patterns on Mars? Many regions on Mars acquire and lose dust cover on timescales shorter than the secular changes discussed above. Within individual Mars years, MARCI has seen that for many regions there is a tendency for new dust that has settled onto a surface to be removed, and for darkened regions to reacquire dust deposits seasonally, preventing any gradual change in regional albedo from one year to the next. In some cases the seasonal variations in wind stress may allow dust to accumulate and remain on the surface for months, such as is the case most prominently in eastern and central Syrtis Major (see Section 2.4.1.1 above), while in

other dark regions, seasonal winds appear to be persistent enough to prevent significant dust accumulation, such as in the interiors of perennial dark features like Mare Acidalium and Sinus Sabaeus. Over sub-annual timescales, many regions in the mid-latitudes maintain a dynamic equilibrium between seasonal storm removal and atmospheric settling. In the southern hemisphere, these changes are more regular, and also more noticeable (such as along the northern boundaries of Mare Cimmerium and Mare Sirenum, and more poleward southern latitudes; see Sections 2.4.9 and 2.4.16), perhaps a result of the relative timing of the annual opacity decline of the atmosphere and the latitudinal occurrence of cap-edge storms. Globally, the most significant atmospheric opacity decline occurs in late southern summer, when southern mid-latitude storms have retreated poleward with the shrinking cap, while northern mid-latitude storms have advanced (Cantor et al., 2014, 2001). This may allow more dust to accumulate on the surface before being seasonally removed. The larger seasonal solar forcing in the southern hemisphere may also contribute directly to this pattern, promoting stronger seasonal control on surface albedo than in the northern hemisphere.

Seasonal variations, together with the less regular local and regional dust storm removal, may represent the ordinary behavior of large portions of the martian surface. Other changes, spanning multiple Mars years or perhaps even decades, may contribute significantly to the martian climate system as well. Of particular interest is to what extent the depletion and recovery of dust reservoirs might drive the significant variability in the occurrence of planet-encircling dust storms. That such dust deposits should be a major factor in the genesis of global storms has been suggested by multiple authors (e.g., Haberle, 1986; Pankine and Ingersoll, 2004; Szwast et al., 2006), but characterizing and predicting the specific circumstances that give rise to such events is challenging. In MARCI data, large areas of the post-storm surface acquired new dust deposits from the storm's decay; in contrast, a few specific areas experienced net dust removal as a result of the storm. This is consistent with the primary effect of a "global" storm being to spread dust across the surface from spatially smaller reservoirs. In subsequent months and years after such a storm takes place, this dust must make its way back to these source regions to close the cycle. MARCI data show that the darkened areas in southern Utopia, Syria Planum, Solis

Lacus, and portions of Ausonia have been gradually (re-)accumulating dust in the post-storm years. By the end of MY 33, some of these regions had recovered or nearly recovered to their pre-storm values, raising the question of whether this is an indication that Mars may be ready for another planetary scale storm. Unfortunately, MARCI has had the opportunity to observe only one such global storm before the end of MY 33, and so caveats should be placed on the conclusions on global storm occurrence that can be drawn from these data alone. However, even as we write, a new planet-encircling dust storm has arisen on Mars in MY 34. The full extent of the changes wrought by this storm event will not be apparent until the atmosphere has cleared, but we anticipate that further studies will explore the sources and sinks of this latest development in the planet's modern climate.

From previous orbital observations and historical telescopic observations, different location(s) of onset and growth for global storms have been observed (Martin and Zurek, 1993; Strausberg et al., 2005; Zurek, 1982), hence separate regional dust sources may be implicated in different global storm years. Nevertheless, we suspect that certain broadly defined regions may have particular importance in the generation of these storms. The critical regions are most likely either those neighboring the lower latitudes of cross-equatorial storm tracks, into which such storms may expand and relay on these dust deposits for further growth, or else likewise for portions of the southern hemisphere into which these storms move laterally, especially regions which albedo changes suggest have been net dust sources. It seems unlikely that southern latitudes poleward of around 50-55°S serve as multi-annually variable dust reservoirs significant to the triggering of large storms, because these regions appear to be net sinks following such events, and are cleaned relatively quickly by seasonal storms (Section 4.16). Areas in and around Solis Lacus, or Hellas, are of particular interest with regards to the previous two global storms. Darkening occurred in the greater Solis Lacus area subsequent to both the 2007 global dust storm and the 2001 storm (Geissler et al., 2016; Szwast et al., 2006), although the extent and location of the darkening were different between those two storms. The bright deposit in Ausonia seems to have originated, at least in part, from the fallout of the 2001 storm (Szwast et al., 2006), however, to become a net source region for the 2007 storm. It is clear that multiple different

configurations of these dust deposits can give rise to global storms; however, it is not apparent from these data what constitutes sufficient dust concentrates in which regions to prime the planet for a global storm. An extension of these analyses, covering both the MOC WA and MARCI datasets, could potentially provide more insight than the qualitative discussion here; fortuitously, Mars has just provided another opportunity in the form of the MY 34 storm to understand the processes and conditions that give rise to these events, while the MARCI investigation is still ongoing.

From a remote sensing standpoint, surface changes on Mars represent both opening and closing opportunities for visible to infrared spectroscopic observations of the underlying surface. Improvements in spatial and/or spectral resolution have greatly enhanced our understanding of Mars through improved knowledge of mineral assemblages suggesting diverse ancient environmental conditions, but unfortunately large portions of the surface are too dusty to enable valuable remote sensing scientific results. Locally, some areas can be found within these dust-covered provinces that are amenable to spectroscopic investigation, in regions where the local wind environment has produced either sufficiently clean bedrock surfaces, or, in other cases, fine materials in the interiors of craters that are presumed to be locally derived (e.g., Lai et al., 2017, (Mangold et al., 2010; Stockstill-Cahill et al., 2008). MARCI observations suggest that for certain areas, careful timing of planned future observations based on seasonal opportunities for low surface dust cover, or a coordinated response to dust cover change from ongoing surface monitoring, may enable or enhance the science return of a spectroscopic observation (for example, dust removal by large-scale storms may uncover regions that have never been spectrally characterized). MARCI observations also show that storms that produce regional darkening can also affect the interiors of some impact craters (true of many areas in the southern hemisphere), which could be attractive future destinations for surface missions. These opportunities arise from a greater consideration of the dynamic nature of the surface dust cover than is commonly applied to remote sensing of Mars.

2.6 Summary

Albedo changes on Mars represent a dynamic interplay between the settling of dust from the atmosphere and its subsequent removal from the surface. Surface changes are very common across much of the planet. In some regions, such as Tharsis and Syrtis Major, the changes are regular enough to produce a seasonal appearance (with some interannual variation); other regions are too variable in extent and precise location to create recognizable seasonal patterns. Although the exact appearance of many features may be variable, the timing of changes in regions that do exhibit seasonal variability is broadly consistent from year-to-year, such that characteristic patterns for different areas can be described. For some regions, such as Mare Serpentis, the seasonality of surface changes is as broad as half the martian year and irregular in occurrence within that interval, while in other areas, such as northwestern Syrtis Major, surface changes are tightly constrained in time to a period of only 10-15° in L_s. In MARCI observations, dust clouds are often either imaged in close association in time and space with darkening of the surface, or else are conspicuously absent, given MARCI's high temporal resolution. In the latter case, the surface darkening from prevailing winds is generally far more frequent within the seasonal window, and the net darkening is apparently formed by many smaller events. In places, dust-cloud-free darkening is morphologically distinct from the irregularly-shaped storm-induced changes. For example, in Solis Lacus, wind erosion across this plateau produces elongated thin streaks, while in Tharsis and Syrtis Major the surface darkening is more strongly affected by significant local topography. Many of the regular changes produced by the cycle of erosion and deposition contrast with the surrounding terrain only weakly, and/or are not spatially extensive enough to have been easily visible by Earth-based observers, from which Mars has acquired a historical reputation for predominantly secular surface change.

Most commonly, regional scale darkening on Mars is sudden, or occurs as a series of discrete, brief events. Brightening is usually slow and gradual, occurring as dust settles from the atmosphere, especially subsequent to the southern spring/summer dusty season. This is modulated by the atmospheric dust load that is subject to the occurrence of large regional or "global" storms; but even in quiescent years, the redistribution of dust by seasonal, global-scale dust settling plays an important restorative role in closing the dust cycle for regions that

experience seasonal or less regular darkening. Areas that experience significant changes, especially decreases in albedo, often require multiple martian years to recover. This is especially the case for regions that darkened during the 2007 major dust storm. A few regions on Mars have undergone changes that show no or few indications of reversal, however, including in southeastern Acidalia and across the formerly dark Propontis feature. From present data, however, it is unclear if these changes have any larger significance.

The extensive record of surface changes provided by MARCI observations makes clear that the albedo of the martian surface should not be regarded as static, for either climatological or operational considerations. The observations themselves suggest that feedbacks exist between surface and atmosphere, potentially driving some of the interannual variation in local, regional, or global dust cycling. Additional multi-year coverage of Mars can be expected to shed further light on the conditions required for the genesis of global scale dust storms. The variability of the surface can also be seen as an opportunity for remote science, as new surfaces amenable to spectroscopic investigations can be revealed by large storms. We expect that continued synoptic imaging of the planet will continue to produce a valuable, multi-year dataset to better understand the time-varying nature of the surface of Mars.

2.7 Acknowledgments

We would like to thank the MRO Project for funding this research, and the MARCI/CTX team for helpful commentary and feedback over the span of several years of science team meetings. We would also like to acknowledge the hard work and dedication of the Bell group systems support staff, specifically Austin Godber, Nathan Cluff, and Ernest Cisneros, for supporting our intensive use of computational resources, sometimes against their better judgment.

CHAPTER 3

VISIBLE TO NEAR-INFRARED MSL/MASTCAM MULTISPECTRAL IMAGING: INITIAL RESULTS FROM SELECT HIGH-INTEREST SCIENCE TARGETS WITHIN GALE CRATER, MARS

This chapter was originally published in American Mineralogist (2017) 102 (6): 1202-1217 (CC-BY). It is reproduced here with the permission of the following coauthors: James F. Bell III, Jeffrey R. Johnson, Kjartan M. Kinch, Melissa S. Rice, Austin Godber, Bethany L. Ehlmann, Abigail A. Fraeman, and Craig Hardgrove. It has been reformatted to comply with the format manual of the ASU Graduate College.

3.1 Introduction

The Mars Science Laboratory (MSL) Curiosity Rover has been exploring the environment of Gale Crater since its successful landing in August 2012. The scientific payload was selected to investigate the potential for past habitable environments through a detailed investigation of the layered sedimentary units of the central mound, informally known as Mt. Sharp, and the surrounding plains (Grotzinger et al., 2012). A history of aqueous alteration within the crater is indicated by spectral and geomorphologic evidence identified from orbit (Anderson and Bell III, 2010; Milliken et al., 2010; Thomson et al., 2011) and is hypothesized to represent a global transition from clay- to sulfate-dominated alteration mineralogy that took place early in the planet's history (Bibring et al., 2006; Milliken et al., 2010). Multispectral imaging capability on Curiosity is provided by the Mast Camera (Mastcam) instrument suite (Bell III et al., 2017; Malin et al., 2010, 2017), which comprises two 1600 × 1200 pixel Bayer-patterned CCD cameras located ~2 m above the surface on the rover's remote sensing mast, along with an accompanying calibration target mounted on the rover deck. Each camera is equipped with an 8-position filter wheel designed to characterize the visible to near-infrared reflectance spectra of surface materials at up to 12 unique wavelengths from 445–1013 nm, including broadband imaging over Bayer filter red, green, and blue (RGB) wavelengths. This wavelength range includes the positions of numerous absorption features of both primary iron-bearing basaltic minerals as well as certain iron-bearing alteration products (Burns, 1993a; Clark et al., 2007; Hunt et al., 1974; Hunt and Ashley, 1979).

Multispectral observations supplement information on morphology and stratigraphic relationships provided by broadband RGB stereo Mastcam or single-band engineering stereo camera images, which together provide geologic context for other instruments. The importance of this contextual information cannot be overstated: many of the scientific instruments aboard the rover perform measurements with relatively small spot sizes (APXS, MAHLI, ChemCam) or require material to be transferred internally via the Sample Acquisition, Processing, and Handling (SA/SPaH) subsystem (CheMin, SAM) (Grotzinger et al., 2012). Mastcam multispectral observations can document compositional variability within and across geologic units on a broad scale, including distant targets that are out of range to most other rover instruments, to the extent that such variability is observable by the filter set. In the near field they can serve as reconnaissance to identify spectrally distinct materials for follow-up analyses by other instruments. Operational and data volume constraints limit the number of multispectral survey sequences that can be acquired, however, and therefore the development of imaging strategies that make use of a subset of the full pixel array, or of the full filter set, is an ongoing consideration.

As was the case for similar limited-filter visible to near-infrared multispectral imaging on the prior Mars Pathfinder, Mars Exploration Rover, and Phoenix Lander missions (Bell III et al., 2000, 2004a, 2004b; Blaney et al., 2009; Farrand et al., 2007, 2008, 2016), even complete Mastcam 12-point spectra are generally not sufficiently diagnostic to provide unique mineralogical interpretations, at least not without separate supporting information. Fortunately, analyses by other on-board instruments can help to constrain the interpretation of Mastcam spectral features. For this reason, we focus in this paper on a subset of multispectral observations acquired in conjunction with multiple other instruments to better understand the mineralogy underlying the observed spectral characteristics. Of most relevance to the interpretation of Mastcam multispectral data are elemental and mineralogic analyses by ChemCam (Maurice et al., 2012; Wiens et al., 2012), elemental analyses by the Alpha Particle X-ray Spectrometer (APXS; (Gellert et al., 2009)), and mineralogic analyses by the CheMin X-ray diffraction (XRD) instrument (Blake et al., 2012). In the case of the ChemCam instrument, Johnson et al. (2015) have shown that

ChemCam passive observations (acquired when the LIBS laser is not active) can be used to generate relative reflectance spectra in the 400–840 nm wavelength range. This range overlaps significantly with that of the Mastcam filter set, and hence inter-comparisons between the two data sets can provide an important check on the identification of spectral features within the range of overlap (as well as important cross-calibration information for both instrument investigations). Many of the observations presented herein are also the subject of ChemCam passive observations, and detailed interpretations of those data are presented by Johnson et al. (2016).

Because the most diagnostic information on mineralogy is provided by the CheMin XRD instrument, the set of Mastcam spectra presented here primarily focuses on multispectral observations of soil scoops and drill fines that have also been examined by CheMin. While drilling has been the predominant method of sample acquisition, several scoops of soil were processed early in the mission at the Rocknest location (Anderson et al., 2015b; Blake et al., 2013), uncovering fresh material for multispectral analysis in an aeolian sand ripple. The drill, part of the Powder Acquisition Drill System (PADS) portion of the SA/SPaH subsystem, produces a 1.6 cm diameter hole in the surface of up to approximately 5 cm depth (Anderson et al., 2012). The upper ~1.5 cm of material is not collected by the sampling subsystem but is instead distributed on the surface as a tailings pile. Multispectral image sequences of these drill fines allow Mastcam to observe surfaces largely uncontaminated by reddish, Fe^{3+}-bearing dust, which influences the visible to near-infrared spectra of practically all surfaces to a varying degree [including, to a lesser extent, surfaces brushed by the Dust Removal Tool (DRT)]. In addition, drill fines are typically subject to analyses by ChemCam and APXS as well, providing a comparatively comprehensive multiple-instrument data set for these targets.

3.2 Background

The Mastcam left (M-34, 34 mm focal length) and right (M-100, 100 mm focal length, thus ~3× better spatial resolution than the M-34) cameras each possess a filter wheel holding eight different optical filters for multispectral imaging. One position on each camera is occupied by a broadband infrared-cutoff filter (“filter zero”) for RGB color imaging, making use of the 2 × 2 unit-

cell Bayer pattern bonded directly to the detector to acquire three broadband visible wavelength channels. A second filter slot is taken by a narrow-band, 10-5 neutral-density-coated filter designed for direct solar imaging. The remaining 12 filter positions are occupied by narrow-band filters selected to characterize the visible to near-infrared reflectance spectra of rock, soil, and other targets in the wavelength range of 445–1013 nm (see Table 3.1 and Fig. 3.1 for filter bandpass characteristics). The combination of filters between the two cameras provides 12 unique (differing by more than a few nanometers; (Bell III et al., 2017)) center wavelengths for multispectral analysis, including the three RGB Bayer bands. Owing to the presence of the Bayer pattern, filters below 850 nm have different throughput between nonequivalent Bayer pixels (Bell III et al., 2017, 2012; Malin et al., 2010). When lossy JPEG compression is used for downlink of observations made with these narrow-band filters (which it is for most cases), the flight software produces the full-size image by bilinear interpolation from the Bayer color pixel with a wavelength response closest to that of the filter itself, discarding the other Bayer pixels [see also the Software Interface Specification (SIS) document for the instrument, (Malin et al., 2013)]. For filters L2 and R2 the Bayer blue pixels are used, for L1 and R1 the greens, and for L3, L4, and R3 the red pixels, effectively decreasing the spatial resolution at these wavelengths by a factor of about 1.4 (for L1/R1) or 2 (for the other short-wavelength filters). The broadband filters L0 and R0 are demosaicked by the algorithm of Malvar et al. (2004) to produce the individual red, green, and blue color images.

TABLE 1. Mastcam RGB Bayer and geology filters effective center wavelengths (λ_{eff}) and half-widths at half maximum (HWHM), listed in order of increasing center wavelength

Mastcam Left (M-34)		Mastcam Right (M-100)	
Filter	λ_{eff} ± HWHM (nm)	Filter	λ_{eff} ± HWHM (nm)
L2	445 ± 10	R2	447 ± 10
L0B	495 ± 37	R0B	493 ± 38
L1	527 ± 7	R1	527 ± 7
L0G	554 ± 38	R0G	551 ± 39
L0R	640 ± 44	R0R	638 ± 44
L4	676 ± 10		
L3	751 ± 10		
		R3	805 ± 10
L5	867 ± 10		
		R4	908 ± 11
		R5	937 ± 11
L6	1012 ± 21	R6	1013 ± 21

Notes: Filters that are (nearly) equivalent between the two cameras are listed on one line; for these filters, reflectance data as shown in subsequent plots are combined to one value. Adapted from Bell et al. (2012).

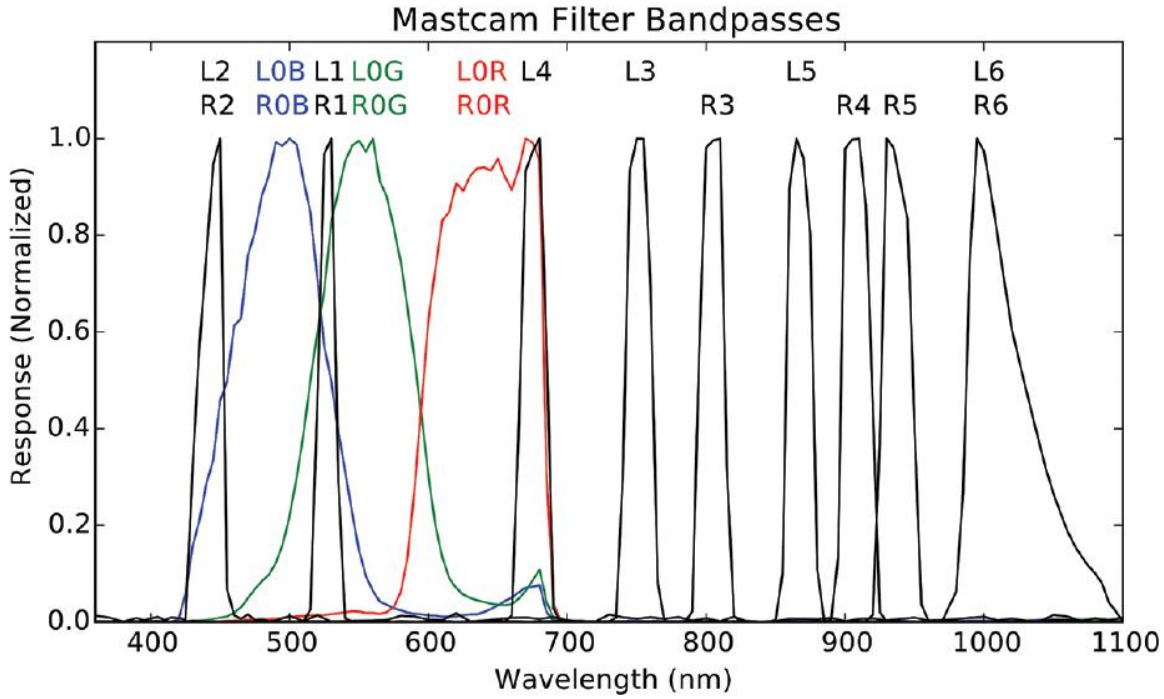

Figure 3.1: Mastcam Bayer and narrowband normalized filter profiles for the left and right cameras. The Bayer filter bandpasses (filter 0) are shown in color. For stereo filters, only the left M-34 camera filter profile is plotted, for clarity; the corresponding M-100 profiles are very similar.

Spectral features in the wavelength range of the camera are predominantly due to the crystal-field and charge-transfer absorptions of iron-bearing minerals (e.g., (Burns, 1993a), while most vibrational features lie beyond the sensitivity range of the cameras' silicon CCD detectors. One exception is a narrow H_2O vibrational overtone/combination band that, in certain hydrated minerals, coincides approximately with the longest wavelength Mastcam filter. Detection of this feature has been reported in Mars Exploration Rover (MER) Pancam observations (e.g., (Rice et al., 2010; Wang et al., 2008)) and its detection in Mastcam spectra is being explored by Rice et al. (2013a, 2013b). Broad electronic absorption bands that have been identified on Mars in this wavelength region are attributed to the presence of iron-bearing silicate, oxide, and sulfate minerals (e.g., (Bell III, 2008, 1996)). Ferrous silicates such as iron-bearing pyroxenes and olivines possess an absorption band near 1000 nm, a result of a spin-allowed transition of Fe^{2+} in octahedral coordination (e.g., (Hunt, 1977)). Reflectance spectra of pyroxenes vary systematically with composition (e.g., (Adams, 1974)), with the 900–1000 nm absorption band tending to shorter wavelengths with lower calcium content. Ferric minerals generally have several crystal-field bands in this range, as well as a strong charge-transfer band extending from the ultraviolet into the visible (e.g., (Hunt and Ashley, 1979)). As an example, hematite has a distinct band near 860 nm, a shoulder near 630 nm, and an intense absorption wing extending from the ultraviolet into the visible to about 550 nm, formed from overlapping crystal-field and charge-transfer bands (Morris et al., 1985). Nanophase hematite, an X-ray amorphous material in which the particle size is less than approximately 10 nm, lacks distinct crystal-field bands but still possesses a strong iron-oxygen charge transfer absorption edge through the visible wavelengths (Morris et al., 1989). Such nanophase oxides are believed to be primarily responsible for the reddish color of martian dust and soil (Morris et al., 1997, 1993). Representative library spectra of several of these and other iron-bearing minerals that will be mentioned below are shown in Figure 3.2, along with their values as convolved to the Mastcam filter bandpasses.

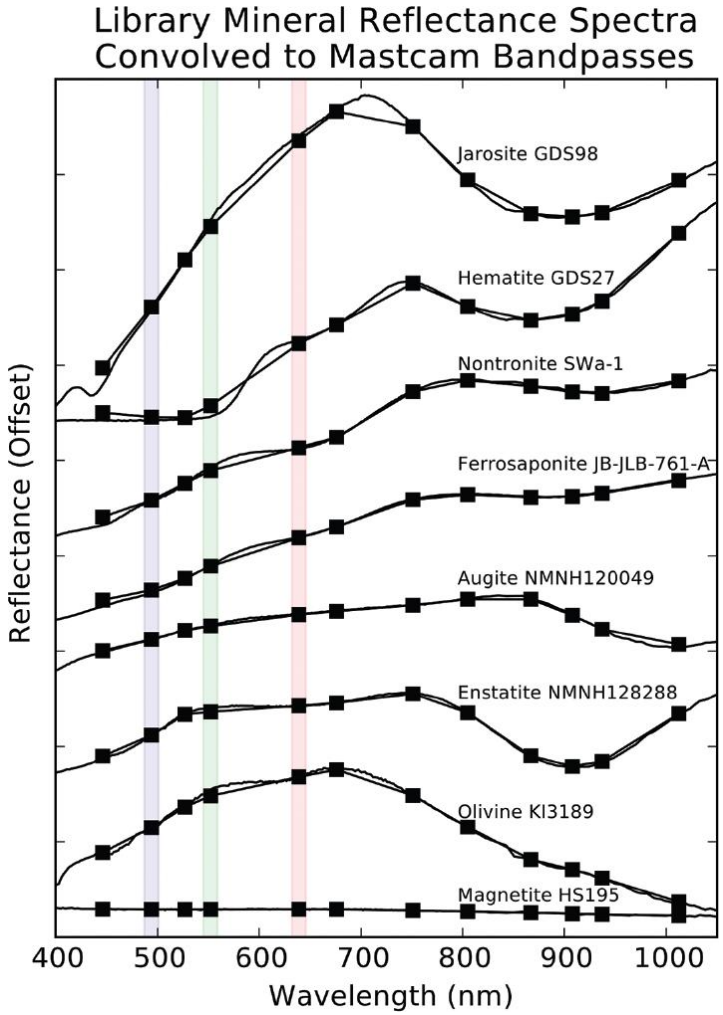

Figure 3.2: Mineral spectra from existing spectra libraries are plotted over the Mastcam wavelength range. Reflectance values convolved to Mastcam bandpasses are overlain (points are averaged at overlapping wavelengths). With the exception of magnetite, the spectra are offset vertically for clarity; y-axis tick marks are in intervals of 0.2. See text for discussion of Mastcam reflectance spectra with spectral features similar to those annotated on the plot. The ferrosaponite spectrum is from the RELAB spectral database (acquired by Janice Bishop); the others are drawn from the USGS Digital Spectral Library [splib06a, (Clark et al., 2007)**].**

Variability in Mastcam spectral data acquired within Gale Crater was anticipated on the basis of orbital observations. Specifically, previous analyses of orbital spectral data have shown evidence for the existence of nontronite, magnesium sulfates, and crystalline hematite in the lowermost layers of Mt. Sharp (Milliken et al., 2010; Thomson et al., 2011). A hematite-rich layer near the base of the mound has been mapped to the uppermost stratum of an erosion-resistant ridge (Fraeman et al., 2013) and should be easily identifiable by Mastcam, whose 867 nm filter is

located near the center of a crystalline hematite absorption band. Nontronite possesses features similar to other Fe^{3+}-rich minerals, but is distinct from hematite by the longer wavelength position of its broad near-infrared band, centered around 950 nm (Bishop et al., 2008; Singer, 1982). Magnesium sulfates, on the other hand, lack broad absorption features at Mastcam wavelengths (although hydrous varieties possess an H_2O vibrational band near 1000 nm (e.g., (Drake, 1995)) that may be detectable by the cameras). Iron-bearing varieties of sulfate were not detected from orbit, although this does not preclude the presence of minor or small-scale occurrences that may exist below the detection limit or spatial resolution of orbital instruments. Indeed ferric sulfates have been identified previously at other locations on Mars, both in situ at Meridiani Planum (Christensen et al., 2004; Klingelhöfer et al., 2004) and Gusev Crater (Arvidson et al., 2006; Johnson et al., 2007; Klingelhöfer et al., 2004) and from orbit at multiple other sites (e.g., (Bishop et al., 2009; Farrand et al., 2009; Milliken et al., 2008)). Their presence as a minor component of certain bedrock units within Gale Crater has recently been confirmed by the CheMin instrument (Cavanagh et al., 2015; Rampe et al., 2016).

3.3 Methodology

The conversion of raw Data Number (DN) values of Mastcam multispectral observations to meaningful radiometric quantities involves the use of both pre-flight calibration measurements as well as near-in-time imaging of the onboard Mastcam calibration target during data acquisition (Bell III et al., 2017, 2006). The calibration pipeline is described in detail by Bell et al. (2017), but a brief summary is presented here. Raw observations in the form of Experimental Data Records (EDRs) are decompanded from downlinked 8-bit data back to their original 11-bit dynamic range. For most observations, interpolation over unused Bayer pixels in specific shorter wavelength filters is a step handled by the on-board software, as mentioned in the section above; however, for certain observations in which the full pixel array is returned, this step must be done by the user. In these cases we follow the same debayering method as the flight software. Observations are flat-fielded using normalized relative responsivity arrays derived from sky observations acquired on Curiosity mission sols 36–38. Bias and shutter-smear corrections are not yet implemented but are insignificant components of the measured signal for all but the most extreme

observational circumstances (not the case for the observations described here). The average dark current, as measured from masked regions of the detector array, was found to be negligible at the operating temperatures and exposure times of the data reported here, and accordingly these pixel columns are excluded by subframing in most observations. Pixels that possess an 8-bit value of 240 or larger in the raw data are considered saturated on the basis of both pre-flight and in-flight observations, and are ignored as "missing data" in subsequent downstream processing. Flatfielded 11-bit DN values are converted to radiance ($W/m^2/nm/sr$) using pre-flight observations of a NIST-calibrated integrating sphere and monochrometer measurements of individual filter bandpasses.

TABLE 2. Observations discussed in the paper along with the calibration target observations used to calibrate each sequence to reflectance

Observation							Corresponding caltarget		
Sol	SeqID[a]	Target	LTST	Solar elevation	Emission angle	Phase angle	Sol	SeqID[a]	LTST
0084	000372	Rocknest (scoop 2)	14:11	57.0	35.5	66.9	0084	000371	14:09
0084	000373	Rocknest (scoops 3 & 4)	14:14	56.5	30.9	64.1	0084	000371	14:09
0183	000993	John Klein	12:45	66.9	38.8	57.9	0181	000988	12:29
0281	001202	Cumberland	11:10	74.1	41.0	47.6	0281	001201	11:05
0475	001888	Mt. Sharp layers	13:31	55.5	88.0	70.0	0475	001889	13:35
0626	002676	Windjana	12:02	66.1	54.9	69.4	0626	002677	12:07
0721	003084	Perdido	14:13	56.3	31.3	54.3	0721	003085	14:15
0726	003101	Bonanza King	13:39	64.9	34.5	46.6	0725	003097	12:57
0762	003273	Confidence Hills	13:20	69.3	44.6	40.7	0762	003274	13:22
0868	003812	Mojave	12:38	67.5	44.1	45.9	0868	003813	12:40
0883	003851	Mojave (2)	12:06	69.9	41.7	45.5	0883	003852	12:09
0909	003977	Telegraph Peak	11:36	71.7	46.6	62.3	0909	003978	11:39

Notes: Calibration target observations generally immediately precede or follow multispectral sequences, but due to operational or data volume constraints a previously acquired caltarget observation may be considered sufficient. Local true solar time (LTST) and photometric angles are listed for the first observation in the sequence; a single-pointing full-filter multispectral observation may take up to four-and-a-half minutes to run. Photometric angles listed here do not account for local topography, which is especially relevant for the sol 475 multispectral that targets the mound. [a] The seqID is the 6-digit sequence ID that occurs in product file names following the four-digit sol number and the two-digit instrument identifier.

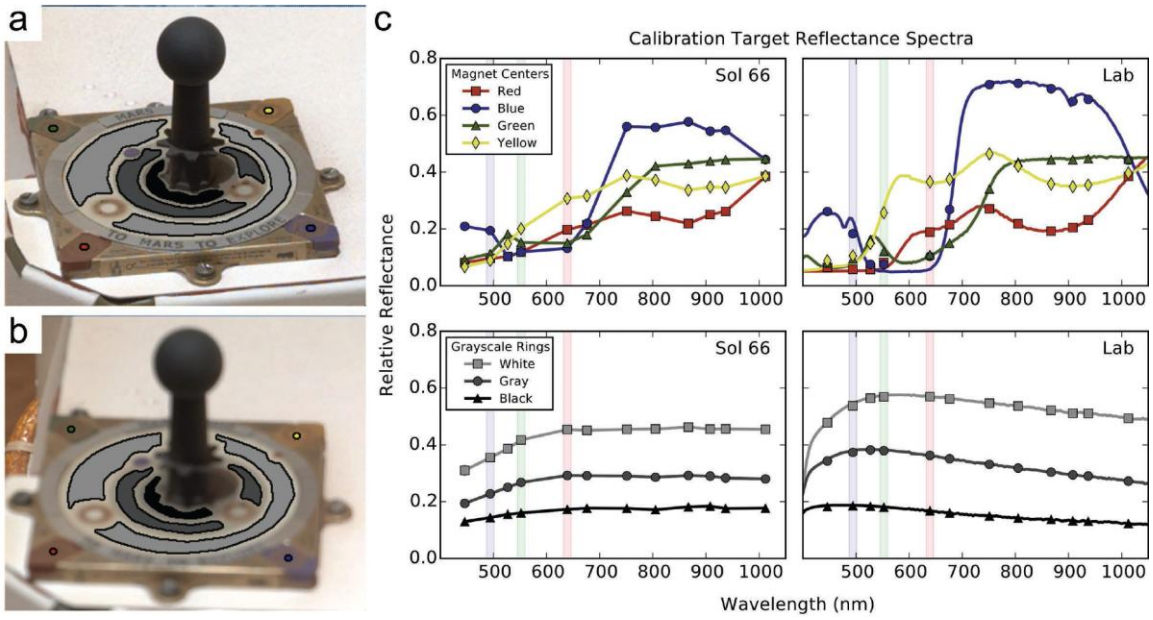

Figure 3.3: The Mastcam calibration target as imaged on sol 66 by (a) the left (M-34) and (b) the right (M-100) Mastcam cameras. The M-100 camera cannot focus at the close distance of the calibration target, and therefore ROIs made on right-eye caltarget images carefully avoid edges of caltarget regions within the approximate radius of blur. Rings of magnetic dust surround the location of the six sweep magnets underlying each of the color chips and the white and gray rings. Reflectance calibration makes use of average radiance values extracted from ROIs made on each of the three grayscale rings. Colored regions highlight the source of the data plotted in the accompanying graph. (c) Reflectance spectra from each of the rings and the less dusty color chip magnet region centers, compared with laboratory measured values. Note that lab values are directional-hemispherical reflectances made of the clean substrate material, whereas in-flight data are obtained under different conditions of illumination and with reddish airfall dust as a spectral contaminant. Despite these factors, the sol 66 color chip reflectance curves reproduce the approximate spectral shape of the pigmented substrate materials. The portion of the grayscale rings unaffected by the magnet regions show evidence for a thin layer of deposited dust; caltargets from later sols (not shown) have more substantial dust coatings.

To convert from radiance to radiance factor (unitless *I/F*, where *I* is the measured radiance and p*F* is the incident solar irradiance), multispectral observations are typically immediately followed or preceded by a sequence of images of the on-board calibration target acquired using the same filter set. In cases where they are not, a calibration target observation from another sol imaged within an hour of the appropriate time of day is used (see Table 3.2). The Mastcam calibration target is located on the right side of the rover deck approximately 1.2 m from the front windows of the cameras, on top of the Rover Pyro Firing Assembly control box. This calibration target or “caltarget,” which is nearly identical to the Pancam caltarget (Bell III et al., 2006, 2003), consists of a ball-and-stick central post (gnomon) surrounded by three grayscale rings and four color chips (Fig. 3.3). Unlike the MER design, the Mastcam calibration target includes six cylindrical magnets embedded just underneath the surface of the color chips and white and gray rings, which keep the center of the magnet regions comparatively clean while attracting a surrounding ring of magnetic dust (cf., (Goetz et al., 2008; Madsen et al., 2003)). These “clean spots” provide additional information for assessing the performance of the calibration procedure but are not directly utilized in the calibration pipeline.

Radiance values are extracted from region-of-interest (ROI) selections drawn on the grayscale calibration target rings (avoiding the rings of concentrated dust near the magnet locations). These values are plotted against the laboratory-measured directional-hemispherical

reflectance values for the caltarget materials, corrected for illumination and viewing geometry by means of a modified He-Torrance model (Bell III et al., 2003; He et al., 1991), and corrected for dust deposition (discussed below). The bidirectional reflectance distribution function model, developed on the basis of prior measurements of the caltarget substrate materials at MER/Pancam wavelengths, was judged to be adequate for Mastcam calibration, which uses parameters determined for a nearby Pancam wavelength to model the directional scattering behavior of the calibration target materials. To determine the coefficient for conversion to radiance factor, we assume that the average ROI radiance values for the three grayscale rings, when plotted against their modeled reflectance values, should fall along a straight line passing through the origin (zero radiance at zero reflectance). The coefficient is derived from the slope of the best-fit line.

A significant complication to this procedure is the deposition of martian dust on the calibration target, even early in the mission owing to material raised during the rover's "sky crane" landing, as well as subsequent gradual deposition of airfall dust from the atmosphere. To account for the influence of the dust on the caltarget reflectance values, a two-layer radiative transfer model (Hapke (1993) section 9.D.3) is employed assuming a uniform layer of dust over the selected caltarget ROIs. The model treats single-scattering events in full detail and uses a two-stream formalism (e.g., (Zdunkowski et al., 2007)) to treat multiple-scattering events. The dust model and procedure follows very closely the one described in full detail in Kinch et al. (2015), which was developed for dust correction on MER as an improvement to the two-stream model (Kinch et al., 2007) presently implemented for the MER Pancam data sets. The utility of this model for analysis of dusty caltarget surfaces was demonstrated by Johnson et al. (2006b) in laboratory studies. Preliminary work on employing the dust model for the MSL Mastcam was presented in Kinch et al. (2013), and the model as employed on Mastcam is described in Bell et al. (2017).

The dust correction procedure fits the scattering model to the three observed caltarget radiances (which are averages of black, gray, and white ring ROI values). The model requires that the dust single-scattering albedo at each wavelength be specified. The spectrum of dust

single-scattering albedo values is found from an analysis of all caltarget images over the first 816 sols of the mission. The scattering model, which has two free parameters, is run on all images using many different values for single-scattering albedo. The free parameters are the incoming irradiance and the extinction optical depth of the dust layer on the caltarget. The “correct” albedo value for each filter is the one that results in stable values for the incoming irradiance, given the known variation in Sun-Mars distance and atmospheric dust loading. If the dust was assumed to be too dark, the derived incoming irradiances would drift to higher values as the caltarget gets dustier, and vice versa for dust assumed to be too bright. This procedure as employed on MER Pancam is described in full detail in Kinch et al. (2015). When employed on MSL Mastcam the procedure results in a dust spectrum that is very similar to the spectra derived for the two MERs.

Once the single-scattering albedo spectrum for the dust is determined, the model can be run with those values on every caltarget sequence, returning the best-fit values for the incoming irradiance and dust optical depth. Dusty caltarget reflectance values for each filter can be determined from the model-derived incoming irradiance and radiances. To find the coefficients to convert the images to reflectance, these corrected reflectance values can then be plotted against the measured radiances for the three grayscale rings, and fit with a line passing through the origin, as described above for a clean caltarget.

Observations calibrated to radiance factor (*I/F*) through the above procedure are divided by the cosine of the solar incidence angle to a quantity referred to as “relative reflectance,” an approximation of the reflectance factor defined in Hapke section 10.B (1993). Relative reflectance spectra of calibrated observations are presented as the mean values derived from manually defined regions-of-interest (ROIs) made in each camera’s field of view and plotted against the filter’s effective band-center wavelength. The ROIs from which the values are determined are carefully selected by the following criteria: to include only pixels from a spectrally uniform region, to avoid edges, to be as spatially identical as possible between the two cameras, and to avoid sloping, shadowed, or highly textured regions, to the extent feasible. Saturation sometimes occurs in Mastcam observations, especially in the shortest wavelength filters, as a result of the high contrast between strongly absorbing dust and soil, and less dusty disturbed materials. Pixels

within an ROI with saturation in any filter of a multispectral sequence are ignored in others from the same camera to prevent biasing some filter values relative to the others. Right-eye filter values are scaled by the ratio of L6/R6 (these filters are less affected by uncertainties in the dust correction than other, shorter-wavelength stereo filters), to remove any offset between the two cameras, and averaged with the left-eye values at overlapping wavelengths to produce one merged spectrum. The vertical error bars at each point represent the standard deviation of the selected pixels within each ROI. Note that, therefore, these error bars do not represent the absolute or filter-to-filter uncertainty of the radiometric calibration, but instead represent the variation of the data values within each ROI, which is largely due to small-scale differences in solar incidence angle as a result of the surface texture. Owing to the smaller spatial resolution of the M-34 camera, the standard deviations may be smaller than the M-100 values. The absolute radiometric accuracy for Mastcam has been estimated at 10–20% (Bell III et al., 2013). Relative uncertainties are likely similar to values derived for Pancam, for which a filter-to-filter uncertainty of <5% and pixel-to-pixel variation of <1% were reported (Bell III et al., 2006).

3.4 Results and Analysis

Mastcam has acquired hundreds of multispectral observations of science targets along the rover's traverse. In the sections below, we describe in detail the reflectance spectra from the soil scoop marks, drill tailings piles, and a few additional targets for which inferences on specific spectral features can be made on the basis of comparisons with other rover or orbital data sets. A map showing the position of the rover along the traverse path where each included multispectral observation was acquired is shown in Figure 3.4, while details of the Mastcam observations are listed in Table 3.2. These spectra are also available as supplemental material published online.

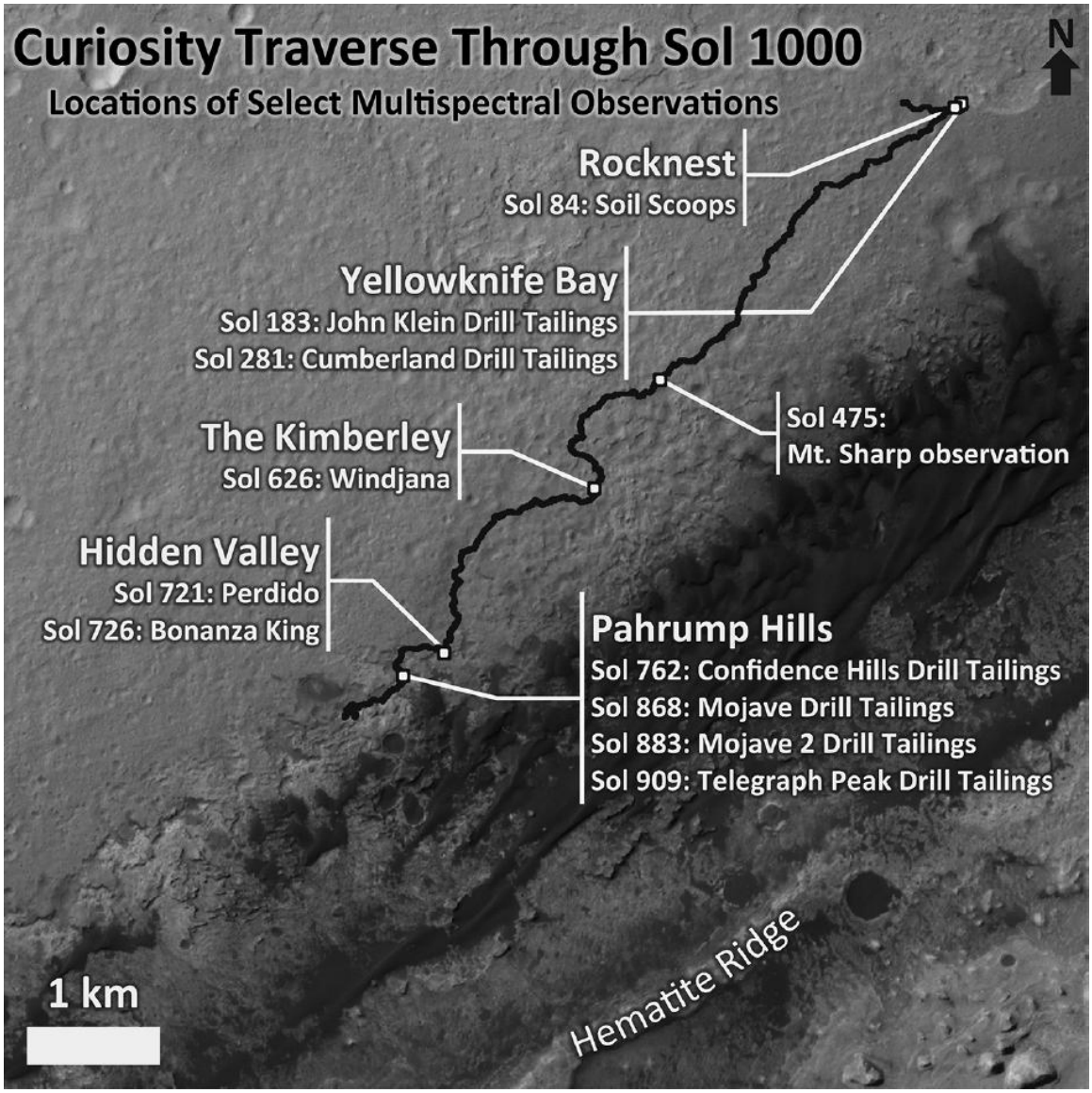

Figure 3.4: The MSL/Curiosity rover's traverse path from Bradbury Landing through sol 1000. The rover locations at which each multispectral observation discussed in the text was acquired are marked on the map. Also labeled is a feature referred to as the "Hematite Ridge" that possesses spectral features consistent with crystalline hematite and is visible in long-distance Mastcam observations targeted toward the base of the mound, including the sol 475 multispectral observation. Base map: CTX D22_035917_1733_XN_06S222W.

3.4.1 Rocknest

Curiosity's initial traverse took it in the direction of the "Glenelg" site approximately 450 m to the east of the landing site, where three units identified by orbital mapping adjoin (Anderson and Bell III, 2010; Grotzinger et al., 2014). En route, the rover spent several tens of sols (martian

days) studying an aeolian deposit at a site called “Rocknest,” where five scoops of material were collected and processed by the Collection and Handling for Interior Martian Rock Analysis (CHIMRA) unit to remove any residual contamination and to provide initial sand-sized samples for analysis to the internally housed CheMin and SAM instruments (Anderson et al., 2012; Blake et al., 2013). The soil scooping operation at Rocknest provided a fresh view of the interior of the sand shadow (Figs. 3.5a–c). Multispectral observations were acquired on sol 84 in the M-100 filters only (Fig. 3.5d), owing to operational constraints. Though CheMin analyses of the basaltic soil revealed >40 wt% mafic silicates (olivines and pyroxenes) as crystalline components (Bish et al., 2013), the reflectance spectra of the sub-surface soils exhibit at best only a weak near-infrared absorption feature. Together with the reddish slope in the visible wavelengths, this result suggests that the reflectance is dominated by an amorphous component with strongly wavelength-varying optical properties in the visible, which may include nanophase and/or poorly crystalline ferric oxides. Indeed, the presence of a substantial iron-bearing amorphous component is supported by mass balance considerations from CheMin and APXS data (Blake et al., 2013). The overall reflectance of the material inside the scoop mark is considerably lower than the dusty surface (Fig. 3.5a), although some vertical heterogeneity exists in the form of a lighter-toned layer visible in the side wall of each scoop (Figs. 3.5b–c), perhaps reflecting dust deposition during a past interlude in sand accumulation. Spectra from neighboring scoop marks in Figure 3.5 are very similar to each other, with minor differences in reflectance likely attributable to a variation in photometric angles from the relative orientation of walls of the troughs.

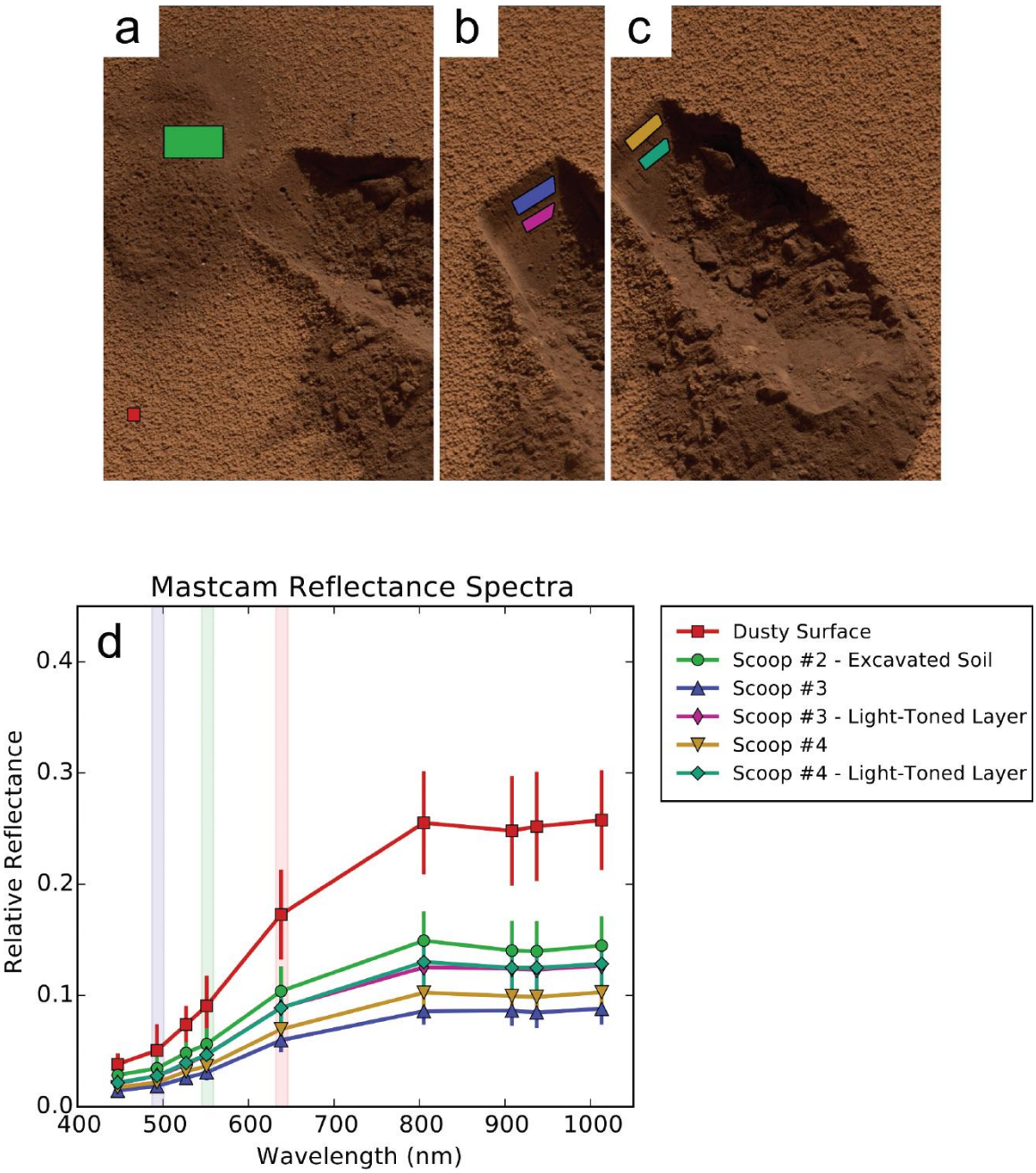

Figure 3.5: (a–c) M-100 (R0) reflectance-calibrated color images from sol 84 of soil scoop marks in the Rocknest sand drift, with colored ROIs showing regions whose mean and standard deviation are plotted in d. (a) This R0 image shows the second scoop trough made by the rover. ROIs are placed on the excavated soil material and the dusty undisturbed surface (the latter ROI is small, in the lower left of the image). The third (b) and fourth (c) scuffs, both cropped from the same observation, show a lighter-toned layer (lower ROIs) just below darker exposed soil (upper ROIs). For scale, the scuffs are about 4 cm wide. (d) A plot of spectra derived from the pictured ROIs. The two light-toned scoop-layer spectra plot as almost identical. The large standard deviation in the red spectrum values results from small-scale shadows cast on the granular surface, which is illuminated at a relatively low sun angle. Note that there is a difference in solar incidence angles

between the material lying on the surface of the aeolian deposit and the material on the walls of the troughs. These spectra are all taken from non-horizontal surfaces and therefore are less comparable, especially in magnitude, to other reflectance values presented in later plots.

3.4.2 Yellowknife Bay

Curiosity departed the Rocknest location on sol 102 and continued eastward to Glenelg, where it conducted an extensive scientific campaign in and around a topographic depression known as Yellowknife Bay. The strata of the Yellowknife Bay Formation are interpreted to have been deposited in a fluvial-lacustrine setting (Grotzinger et al., 2014), and it is from the stratigraphically lowest member of this formation, the Sheepbed Mudstone unit, that the first two drill samples were obtained on sols 182 and 279, with accompanying Mastcam multispectral observations [for a detailed stratigraphy of this and other Gale Crater units, see Grotzinger et al. (2015)]. The first of these, "John Klein," was preceded by a "mini" drill hole on sol 180, a shallow-depth drilling performed to assess the suitability of the target material for the full-depth drill activity. Figure 3.6a is a reflectance-calibrated color M-100 RGB image from a multispectral sequence acquired on sol 183 and shows both the mini drill hole (nearer the top of the frame) and full drill hole. Reflectance spectra were derived from an ROI positioned on the mini drill tailings pile, which is distributed more evenly on the surface than the full drill tailings pile. In almost all cases (the one exception being Confidence Hills, as mentioned below), spectra drawn from the tailings of adjacent full and mini drill holes reveal no substantial differences in reflectance. Figure 3.6b shows the Cumberland full drill hole and tailings pile, located just a few meters from John Klein, and the region of interest from which the mean spectrum was taken. Reflectance spectra for these two sets of drill fines are plotted in Figure 3.6e, together with spectra derived from other drill targets as well as a dust-covered surface near the John Klein target. Differences between the Sheepbed drill fines and other materials are readily apparent from the plot. Compared to the undisturbed, dusty surface, the Sheepbed drill tailings are substantially less "red" (possess a lesser reflectance slope across the visible wavelength range), as indeed are all of the drill fines. The John Klein and Cumberland tailings possess a clear reflectance maximum near 805 nm, with a broad near-infrared absorption band that appears to be centered shortward of 1000 nm. These

VNIR characteristics are consistent with a significant contribution to the spectral shape from the high abundance of smectite (~20 wt% of total sample) and/or low-Ca pyroxenes (~10 wt%) detected by the CheMin instrument (Vaniman et al., 2014). The library mineral spectra plotted in Figure 3.2 include a sample of both trioctahedral saponite and Fe^{3+}-rich, dioctahedral nontronite, in addition to several other reflectance spectra of mineral species similar to those detected by CheMin in these or subsequent drill samples. The shoulder near 650 nm in the two smectite laboratory spectra does not appear in the multispectral data, suggesting it is either too weak to be apparent at the spectral sampling provided by the filters, or else it is not present (perhaps suppressed by other phases). The ChemCam passive data show an absence of such a band, as well as the beginning of a band in the near-infrared [Fig. 3.7 and Johnson et al. (2015)], consistent with the multispectral data. It can be seen from the convolved spectra in Figure 3.2 that this near-infrared spectral band, which is centered around 950 nm, could be reproduced with either a smectite spectrum or a pyroxene with features intermediate between the augite and enstatite spectra shown. Unlike the library mineral spectra, the Sheepbed material is a complex mixture of multiple mineral and amorphous phases, and the inherently nonlinear nature of such spectral mixtures makes it not straightforward to evaluate quantitatively the relative contribution of each to the overall spectra shape. Compared to the other drill tailings (which do not possess a band at this position), the Sheepbed samples are distinct in possessing significantly more smectite, which may suggest that it is the clay mineral that is contributing substantially to the unique spectral shape.

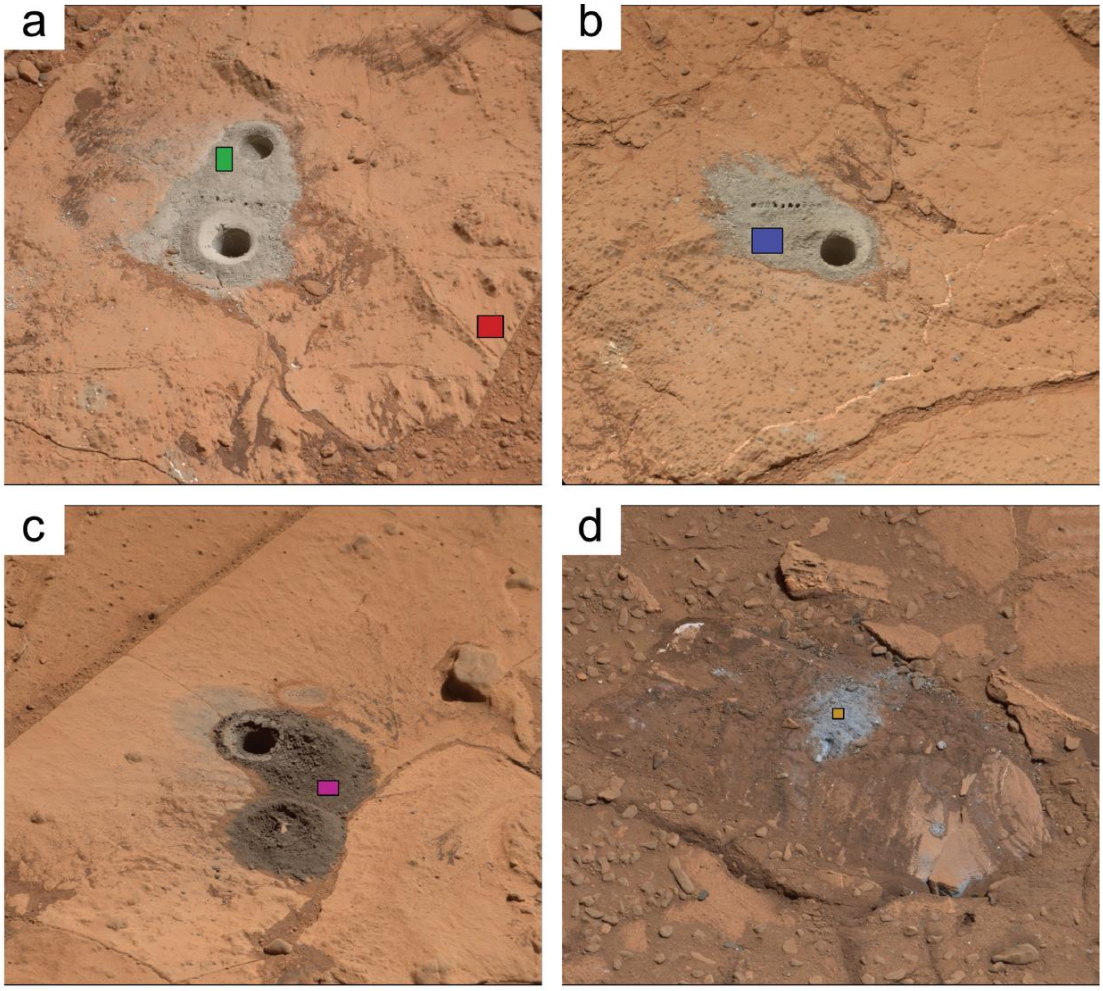
a
b
c
d

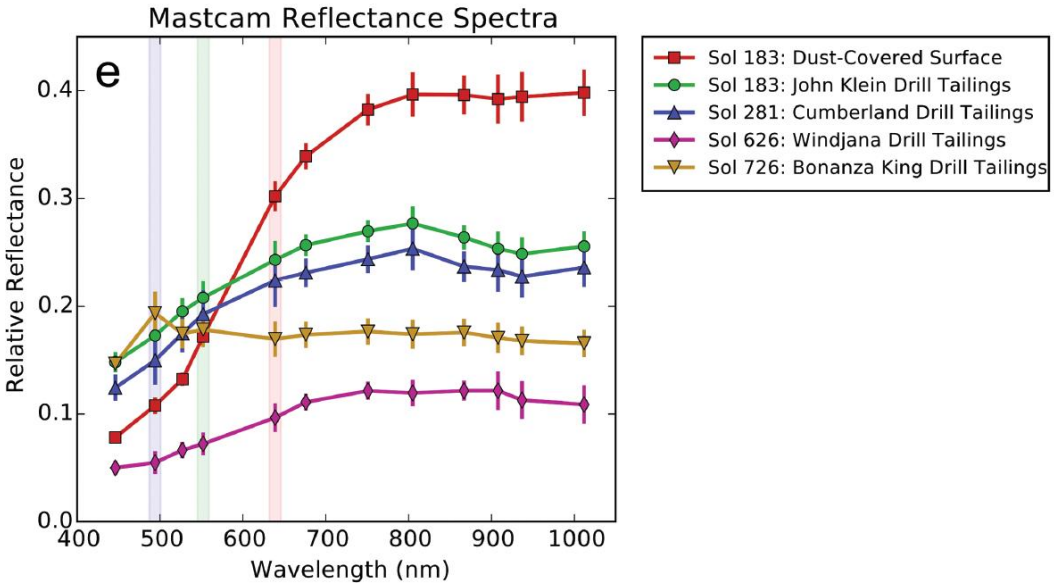
Mastcam Reflectance Spectra
e
Relative Reflectance
Wavelength (nm)
0.0
0.1
0.2
0.3
0.4
400
500
600
700
800
900
1000
Sol 183: Dust-Covered Surface
Sol 183: John Klein Drill Tailings
Sol 281: Cumberland Drill Tailings
Sol 626: Windjana Drill Tailings
Sol 726: Bonanza King Drill Tailings

Figure 3.6: Drill tailings from Yellowknife Bay (John Klein, sol 183, and Cumberland, sol 281), the Kimberley (Windjana, sol 626), and Hidden Valley (Bonanza King, sol 726) are shown in relative reflectance calibrated M-100 RGB color (a–d), with colored ROIs marking the pixels from which the reflectance spectra values plotted in e are derived. Also shown for comparison with the disturbed materials is the spectrum of a dust-covered surface near the John Klein drill hole. The anomalously high Bayer blue filter in the Bonanza King spectrum may be an artifact introduced by the broad Bayer bandpass. For scale, the drill holes are about 1.6 cm in diameter.

3.4.3 The Kimberley

Curiosity did not depart the Yellowknife Bay region until sol 324, and the subsequent emphasis on driving placed nearly 5 km between the Yellowknife Bay drill locations and the next drill hole. The rover arrived at the Kimberley drill location on sol 609 and performed full-depth drilling on sol 621 on a cross-bedded sandstone target in the Dillinger unit (Deit et al., 2015; Treiman et al., 2016) named “Windjana,” with an accompanying Mastcam multispectral observation on sol 626. The Windjana drill target produced mini and full drill tailings that are very different from the Sheepbed targets. The observation acquired on sol 626 (Fig. 3.6c) shows the mini (nearer the bottom of the frame) and full drill holes, the former of which is largely filled in with tailings vibrated back into the hole by the action of the subsequent full drill operation. Spectra derived from the full drill tailings exhibit the lowest overall reflectance of drilled material observed in the mission to date. These low reflectance values are consistent with the relatively higher abundance of strongly absorbing phases, especially higher magnetite (~12 wt% of total sample), reported by the CheMin team (Treiman et al., 2016, 2015). In addition, the reported phyllosilicate abundance in the Windjana drill materials is significantly lower (~10 wt%) than in the Sheepbed drill materials, which may also contribute to the substantially flatter spectral shape near 800 nm as compared to the previous two tailings piles. The general decrease in reflectance at the longest wavelength filters is consistent with absorptions due to mafic minerals.

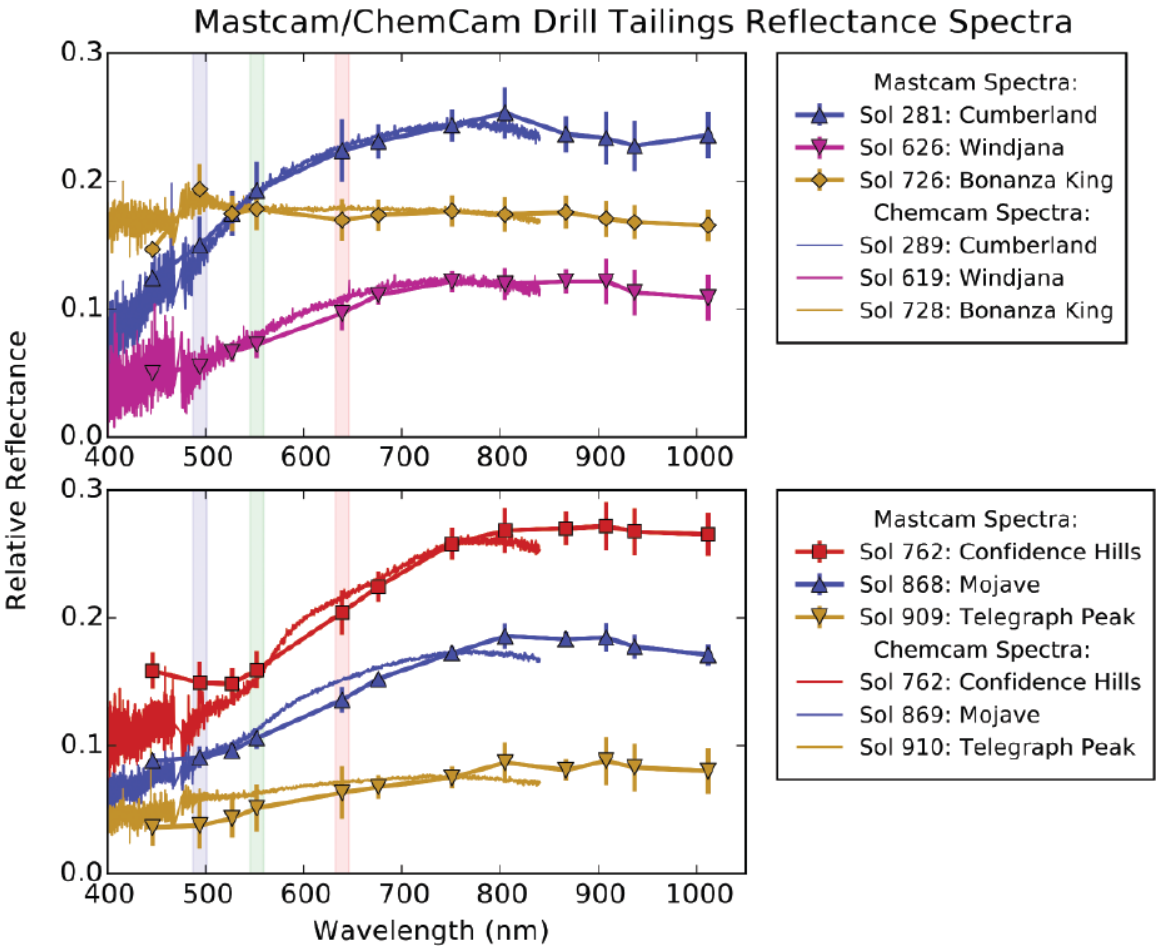

Figure 3.7: Mastcam multispectral and ChemCam passive reflectance spectra for six drill tailing targets are shown here for comparison. The top plot includes Mastcam spectra from Figure 3.6 and ChemCam passive spectra targeting similar drill material; the bottom does likewise for specific Mastcam spectra from Figure 3.8. The ChemCam data are scaled to the Mastcam filter L3 value in the neighborhood of 751 nm for each spectrum. The spectra pairs in the bottom plot are offset by +0.03, –0.02, and –0.06 (in order of top to bottom) for clarity. ChemCam passive spectra are those from Figure 10 of Johnson et al. (2016); see also Table 1 of that publication for additional details on the ChemCam observations. Note that while the Mastcam ROIs and ChemCam observations target similar material in these observations, they do not have identical spatial coverage; in particular, ChemCam has a very small (0.65 mrad) FOV while the Mastcam spectra are averages over regions shown in preceding figures. The two sets of spectra agree well with each other despite differences in spatial coverage, phase angles, and calibration approach.

3.4.4 Hidden Valley

After the Kimberley, the rover continued driving south and southwest, reaching the boundary of the landing ellipse on sol 672. Near an untraversable patch of sand ripples within a topographic low dubbed “Hidden Valley,” a fourth drill attempt was made on sol 724 on what

proved to be an unstable rock slab (“Bonanza King”). Images acquired after the failed mini-drill attempt into the target revealed that the rock had shifted during the drill activity (Anderson et al., 2015a), and thus the decision was made not to reattempt drilling on this or a nearby rock. Although no XRD data exist for this target, the mini-drill did produce a small pile of fresh tailings suitable for multispectral analysis (Fig. 3.6d). The resulting spectrum (Fig. 3.6e) is distinctly different from both the Sheepbed (John Klein and Cumberland) and Windjana spectra. Compared to those previous tailings piles, Bonanza King is intermediate in overall reflectance and extremely flat over the wavelength range sampled by Mastcam filters. (The unreasonably high value for the blue Bayer filter at 494 nm should be considered an artifact, perhaps resulting from the combination of the broad Bayer bandpass with a spectral radiance curve possessing a different shape than that of most other materials observed.) By analogy with other drill tailings spectra, we can make inferences about the mineralogy of Bonanza King despite the lack of X-ray diffraction data from CheMin. The higher overall reflectance as compared to Windjana implies that Bonanza King either has a smaller percentage of the strongly absorbing species such as magnetite that are present in the Windjana sample, or else also possesses a spectrally neutral species with relatively high reflectance, such as a silica phase. From the nearly featureless spectrum of Bonanza King we can also say, qualitatively, that the percentage of other iron-bearing minerals with strong features in these wavelengths, such as hematite, Fe-saponite, and the Fe-sulfate detected nearby (see the discussion of the “Perdido2” target in Johnson et al. (2016) and below), are likely either absent or lower in abundance compared to targets that show these features more clearly. APXS data show that the Mg/Si and Al/Si ratios are quite low for Bonanza King as compared to most other analyses, which may reflect a history of open-system aqueous alteration (Yen et al., 2015). The lack of distinct reflectance features in the multispectral data is broadly consistent with the breakdown of primary mafic minerals as in such a weathering environment.

3.4.5 Pahrump Hills

After an additional ~600 m of driving, Curiosity began a detailed investigation of basal Mt. Sharp units at Pahrump Hills, where it observed a sequence of predominantly fine-grained mudstones and siltstones that form the lowermost units of the Murray Formation (Stack et al.,

2015). Three additional drill samples (“Confidence Hills,” “Mojave 2,” and “Telegraph Peak”) were obtained in these layers on sols 759, 882, and 908 (respectively), with accompanying Mastcam multispectral observations. The first attempt at the Mojave site on sol 867 resulted in only a partial drill hole, which nevertheless produced clean material for multispectral analysis. This target is referred to below as “Mojave”, whereas “Mojave 2” refers to the second, successful drilling that produced a sample for CheMin analysis.

The Confidence Hills drill site was the stratigraphically lowest of the three Pahrump drill locations. Figure 3.8a shows the mini (lower) and full drill holes and drill tailings. The tailings to the lower left of the drill holes have a slightly higher reflectance (~0.02 higher) than the drill tailings closer to the full drill hole. Unfortunately, the full drill activity significantly disturbed soil from the surrounding surface as well as the tailings pile that previously surrounded the mini drill hole, making it difficult to ascertain the extent to which the tailings piles and soil have been mixed together. The difference in reflectance may be a result of such mixing. An alternative is that differences in composition and/or grain size exist over spatial scales and/or drill depths as small as that sampled here. Besides this small difference in overall reflectance, the tailings are spectrally similar and show a strong absorption in the shorter wavelength filters (around 550 nm) not present in any of the previous drill tailings spectra (cf. Fig. 3.6). The CheMin X-ray diffraction data revealed that a significant quantity of crystalline hematite (~8 wt% of total sample; (Cavanagh et al., 2015)) was present in the sieved sample, compared to <1 wt% in prior samples (Bish et al., 2013; Treiman et al., 2016, 2015; Vaniman et al., 2014). Interestingly, the Mastcam spectra do not show any evidence for a band near 860 nm that is typically associated with fine-grained crystalline hematite (e.g., (Morris et al., 1985)), nor do they show a downturn beyond about 785 nm as is present in the longest wavelengths of ChemCam passive spectra [Fig. 3.7 and Johnson et al. (Johnson et al., 2016)], suggesting that such a band, if present, must be very shallow. The 860 nm band may be largely masked by other constituent minerals. Alternatively, the hematite may be present as a combination of nanophase and crystalline phases, mixtures of which have been shown to vary with respect to the strength of either spectral feature mentioned above (Morris et al., 1989).

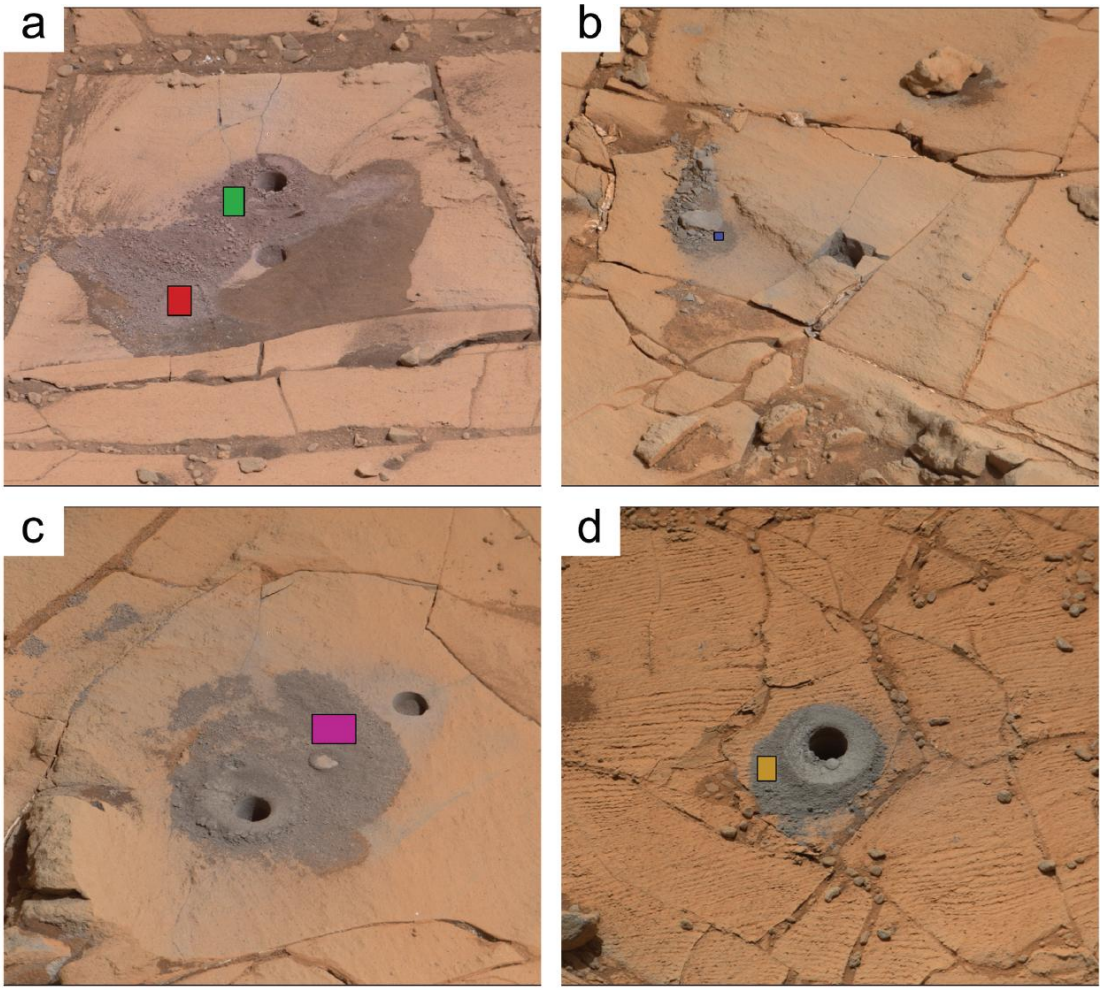
a
b
c
d

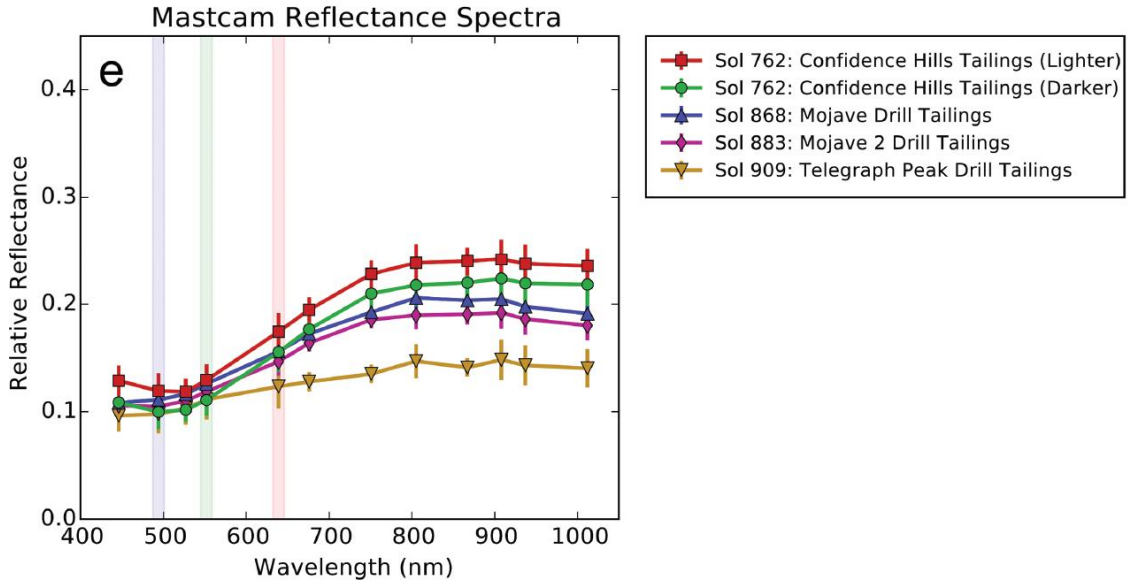
Mastcam Reflectance Spectra
e
Relative Reflectance
Wavelength (nm)
0.0
0.1
0.2
0.3
0.4
400
500
600
700
800
900
1000
Sol 762: Confidence Hills Tailings (Lighter)
Sol 762: Confidence Hills Tailings (Darker)
Sol 868: Mojave Drill Tailings
Sol 883: Mojave 2 Drill Tailings
Sol 909: Telegraph Peak Drill Tailings

Figure 3.8: Drill tailings from the Pahrump Hills drill targets are shown in M-100 RGB color (a–d), with colored ROIs marking the pixels from which the reflectance spectra values plotted in e are derived. Respectively, these drill holes are (a) Confidence Hills (sol 762), (b) Mojave (sol 868), (c) Mojave 2 (sol 883), and (d) Telegraph Peak (sol 909). The Confidence Hills full drill activity disturbed both the reddish soil, which pooled around the drill holes, as well as the drill tailings from a prior "mini" drill hole. Portions of the tailings piles were displaced as a result of the drill vibrations and may have been subject to mixing between themselves and the reddish soil, and so here are labeled only as "lighter" and "darker." The original target for the second Pahrump drilling, "Mojave," resulted in a dislodged block (b), but a second attempt (c) was successful.

Two further full drill holes were acquired in strata of the Pahrump Hills. A mini drill attempt into the original Mojave target resulted in a dislodged block and fines (Fig. 3.8b). The attempt was repeated successfully a few meters away (Fig. 3.8c). Spectra from both Mojave targets exhibit essentially identical Mastcam spectra (Fig. 3.8e). Both spectra have a reddish spectral slope with an inflection near the 527 nm filter consistent with the presence of crystalline hematite, although this feature is weaker than in the Confidence Hills spectrum. By contrast, the Telegraph Peak drill tailings (shown in Fig. 3.8d) possess a spectrum that is flatter and exhibits little evidence of an absorption near 527 nm. We compute a 527 nm band depth using the relative reflectance values at 446 and 676 nm as BD527 = 1 – R527/[0.648R446 + 0.352R676]. The 527 nm band depths for the three Pahrump drill targets are 0.23, 0.13, and 0.04 for Confidence Hills, Mojave 2, and Telegraph Peak, respectively. This parameter correlates well with the measured abundances of crystalline hematite, which were determined by the CheMin team to be ~8, ~4, and ~1 wt%, respectively (Cavanagh et al., 2015; Rampe et al., 2016). Spectral parameters such as these are also influenced by the other constituent minerals; however, within the range of mineralogies sampled by the Pahrump drill holes, such a trend in spectral shape appears to correlate reasonably well with actual hematite abundances.

3.4.6 Observations of select float rocks and distant mound layers

In addition to the previous spectra of drill powders and scoop marks, several other observations display noteworthy and unique features over the spectral range of the Mastcam filter set and are included to further document the spectral diversity observed by the cameras along first 1000 sols of the rover's traverse. Here we show near-infrared absorption features consistent with iron oxides and iron sulfates in Mastcam spectra, the former in observations targeted at a

feature approximately 5 km away that was known from orbital spectral data, and the latter as a spatially heterogeneous feature observed over generally small (~millimeters) spatial scales at certain locations in rock units explored by the rover near the basal Mt. Sharp stratigraphy. Each of these observations are discussed in turn below, beginning with a feature observed in several small rock fragments in Hidden Valley.

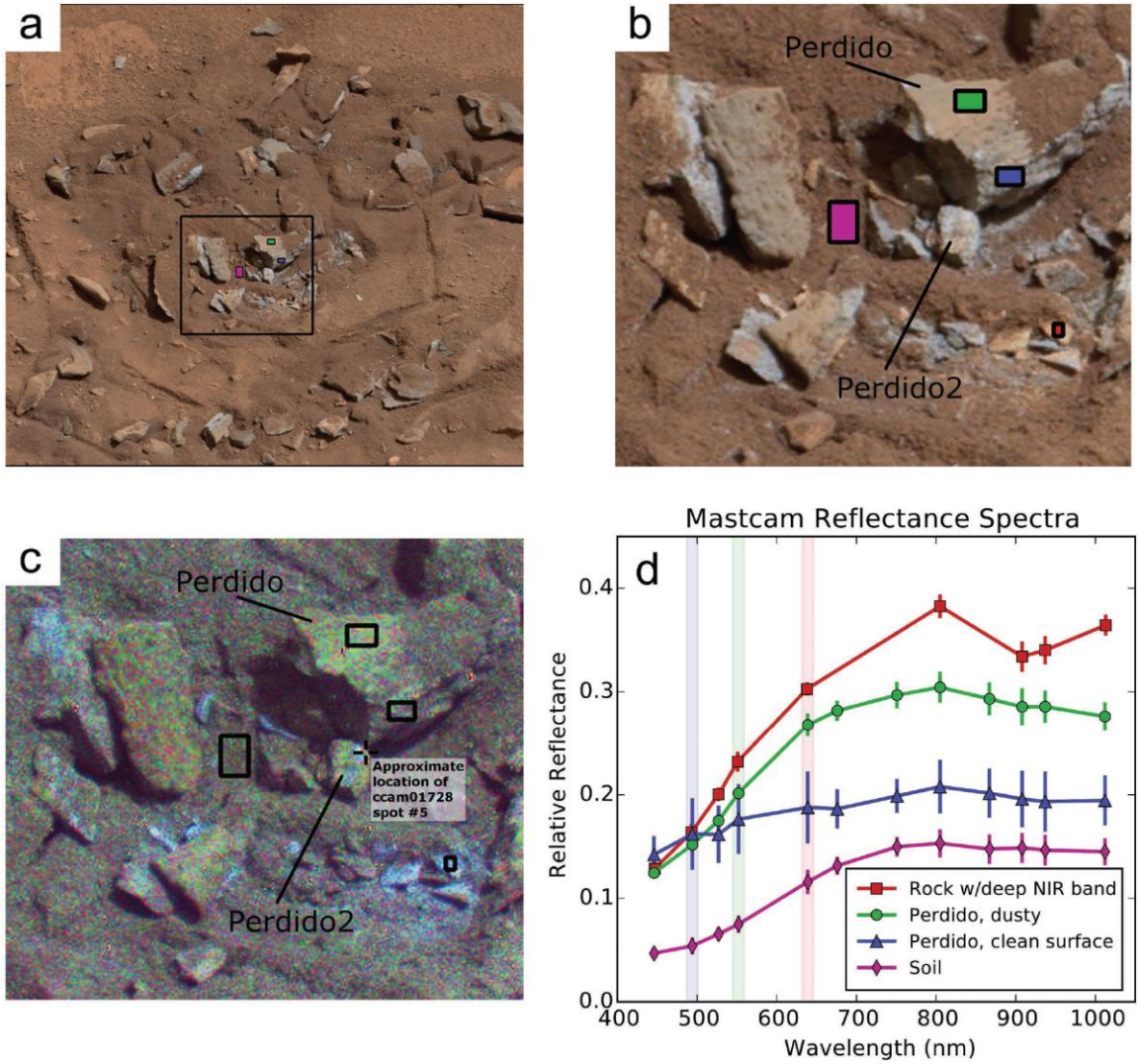

Figure 3.9: The M-100 color image (a) from a multispectral observation of the "Perdido" target on sol 721 shows numerous rock fragments broken by the rover wheels. The rocks are float pieces but several clean surfaces are similar to the Bonanza King spectrum, suggesting that they may be sourced from the local bedrock. The black box surrounds a region enlarged in b to show detail. (c) This decorrelation stretch of filters R4, R5, and R6 (908, 937, 1013 nm) shows the small-scale regions with a near-infrared feature (bluish colors). ROIs are shown here as outlines only, to show the underlying DCS colors. It can be seen that small regions of the Perdido2 fragment appear to be consistent with such a feature, although extracting reliable spectra from such a small region is problematic. (d)

Spectra from several broken rock fragments, as well as other nearby materials, are shown in the graph. The red ROI covers a region too small to define a corresponding ROI in the M-34; for this reason, only right-eye values are presented. Several of the smaller fragments, including the fragment bearing the red ROI, exhibit spectral features in the near-infrared that may be indicative of a ferric sulfate (see text). The fresh surface of Perdido (blue ROI and spectrum) is spectrally quite flat compared to the dustier top surface and the reddish soil. The spectrum is similar to the nearby Bonanza King drill tailings, although slightly redder, perhaps owing to the surface being slightly less "clean" than the tailings.

Fresh surfaces of rocks broken by the rover wheels have been very rewarding targets for multispectral observations. One such observation acquired on sol 721 targeted several broken rocks, including the ChemCam target "Perdido" (Fig. 3.9). Johnson et al. (2016) report numerous detections of a 430 nm band that suggests the presence of a ferric sulfate mineral such as jarosite, particularly when paired with a near-infrared reflectance downturn at wavelengths greater than about 700 nm (e.g., (Cloutis et al., 2006; Rossman, 1976)), with "Perdido2" (a passive ChemCam raster pointed just below the original LIBS Perdido target) expressing this feature most strongly. The 430 nm band is not detectable with Mastcam's filters, but portions of the rock fragment Perdido2 and the surrounding rocks do possess a strong, distinctive absorption in the near-infrared at 900 nm, consistent with a ferric mineral such as jarosite. Unfortunately, the rock fragments are so small (centimeter scale and smaller) that the selection of an appropriate ROI is very difficult in the M-34 images. Figure 3.9c shows a decorrelation stretch of filters R4, R5, and R6 (908, 937, and 1013 nm), in which bluish colors correspond to material possessing the near-infrared feature. Close examination of the Perdido2 target in this false-color image suggests that the rock may show this feature strongly only on a small portion of its surface. For this reason, the red spectrum in Figure 3.9d is derived from a nearby fragment expressing this feature in more pixels than the Perdido2 target itself and includes only values from the higher spatial resolution right-camera (M-100) filters. The strongest detection of a 430 nm feature in ChemCam was from the final spot of a 5 × 1 dedicated passive observation (Johnson et al., 2016), whose pointing was extremely close to the portion of the Perdido2 fragment that the decorrelation stretch image suggests may have strong near-infrared Mastcam features as well. A jarosite spectrum from the USGS spectral library (Clark et al., 2007) is shown in Figure 3.2, depicting the long-wavelength

absorption that corresponds favorably with the Mastcam data. While this feature is not uniquely indicative of jarosite, the combination of the Mastcam and ChemCam passive data as well as the subsequent identification of jarosite by CheMin in nearby drill samples (Cavanagh et al., 2015; Rampe et al., 2016) strongly suggests that this ferric sulfate is responsible for this spectral feature.

Long-distance multispectral observations targeting the lower layers of the mound were acquired on sols 468 and 475 (the latter is shown in Fig. 3.10a), in a coordinated effort with ChemCam passive observations. The field of view included a ridge referred to as the “hematite ridge” from CRISM observations identifying a layer bearing a spectral signature consistent with that oxide (Fraeman et al., 2013; Milliken et al., 2010). Mastcam spectra show that portions of a layer bear a weak but clearly present absorption feature near the 867 nm filter, consistent with crystalline hematite, as well as a weak inflection near 527 nm (Fig. 3.10c). These observations are consistent with the enhanced 535 band depths and stronger near-infrared downturns observed by ChemCam (Johnson et al., 2016). The presence of the long-wavelength spectral feature as a characteristic of a spatially coherent region of the ridge is most obvious in the decorrelation stretch image of three near-infrared bands shown in Figure 3.10b, in which the bluish-purple false color corresponds to the region exhibiting this feature. The other layers of the mound visible from this vantage point do not show any distinguishing spectral features. The dunes show a generally low reflectance and broad long-wavelength decrease consistent with a mafic mineralogy, likely with some influence from a thin dust layer. Brighter material appears to lie in a “fan” of material just above the dunes, but both this material and the topographically higher layers lack any strong or distinctive spectral features aside from the obvious influence of reddish dust at the shorter wavelengths.

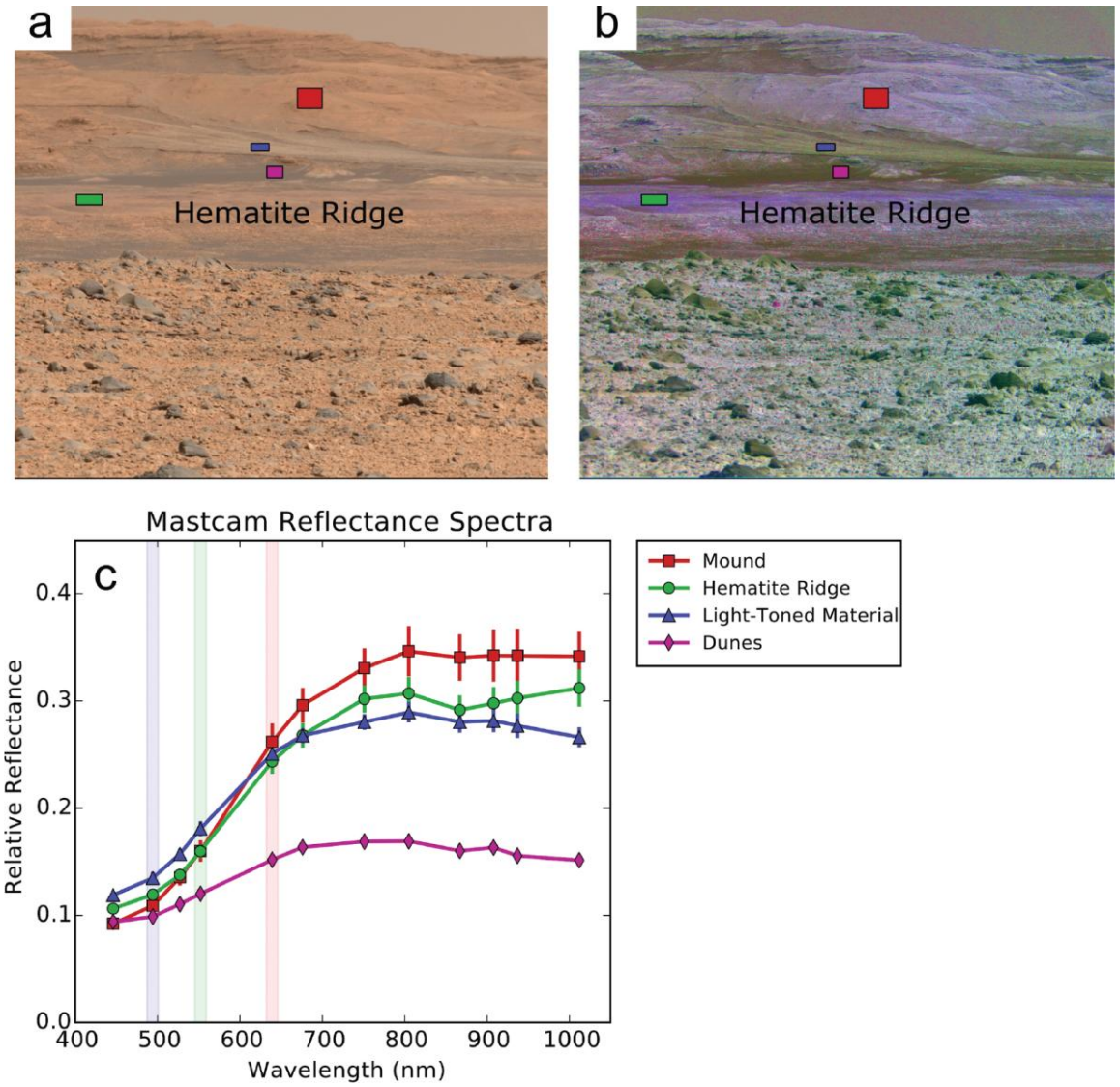

Figure 3.10: (a) This M-100 image from sol 475 was aimed toward the layers of the central mound. (b) A false-color decorrelation stretch (using bands at 805, 908, and 1013 nm) demonstrates some of the spectral diversity visible to Mastcam in the lower units of the mound. The spatial extent of the hematite-bearing region associated with the green ROI, which parallels the base of the mound, can be seen in this view. (c) Average Mastcam reflectance spectra of the colored regions. The green spectrum is from the "hematite ridge" and shows features consistent with crystalline hematite. Also shown are spectra of the dunes (purple) and the lighter-toned material (blue) that appears to lie on the sloping surface above the dune field, as well as an average spectrum of the mound (red). This upper mound is spectrally similar to average martian dust, while the other two regions possess a spectral downturn toward longer wavelengths.

3.5 Implications

Mastcam has observed an impressive diversity of reflectance spectra within Gale crater.

Tailings from each lithologic unit drilled by the rover have distinctive spectral properties, as do

certain small-scale materials observed in broken rock fragments and long distance observations of specific layers of Mt. Sharp. The multispectral data, which track changes in Fe mineralogy, are in good general agreement with mineralogical and elemental analyses conducted by other instruments on Curiosity's payload, which corroborate the detection of discrete compositional units. Clear correlations can be drawn between the mineralogy inferred from CheMin X-ray diffraction data and the visible/near-infrared spectral features identified in calibrated Mastcam spectra, further supported by results from geochemical instruments. Mastcam multispectral and ChemCam passive observations provide two independently calibrated measurements of reflectance and display equivalent features within the wavelength range where they overlap.

The drill tailings observed at Yellowknife Bay possess an 800 nm spectral peak and minimum near 930 nm, apparently deriving from Fe-bearing phyllosilicates and pyroxenes. Saponite can accommodate a range of iron content and redox state (Kodama et al., 1988; Treiman et al., 2014), which should be manifested by changes in the visible/near-infrared reflectance. Further study may permit using Mastcam VNIR data to resolve between the ferrian saponites studied by Treiman et al. (2014) and high-Mg ferrosaponites studied by Chemtob et al. (2015) as candidate compositions that fit the 02*l* diffraction peak measured by CheMin at Yellowknife Bay.

On the basis of data from other instruments, the identity of other minerals producing distinct spectral features in the Mastcam data set can be reasonably ascertained. The presence of magnetite serves to suppress reflectance across the entire VNIR range, which is most apparent in spectra of the Windjana drill tailings. The Pahrump Hills targets of Confidence Hills and Mojave possess a spectral absorption or inflection near the 527 nm filter consistent with the presence of crystalline hematite and stronger than that in surface dust spectra. The strength of this parameter appears to correlate well with hematite abundances measured by X-ray diffraction. A longer wavelength hematite feature near the 867 nm filter is not apparent in the drill fines spectra, but does appear weakly in long-distance observations targeted toward the hematite-bearing ridge, whose hematite signature was detected from orbit (Fraeman et al., 2013; Milliken et al., 2010). The ridge, therefore, may possess a greater relative abundance of crystalline hematite than has yet been sampled. A broad 900 nm near-infrared feature observed in Mastcam

spectra is consistent with a ferric sulfate mineral, likely jarosite, found in broken rock near the Perdido target, and is correlated with a ~430 nm feature in ChemCam passive data. Detection of the 900 nm feature to date has been limited to material at small spatial scales close to the rover rather than within an extensive bedrock unit. This limited detection is consistent with the lack of detection in orbital CRISM data as well, which have spatial resolutions of 18 m/pixel. Overall, the Mastcam observations are strongly consistent with the results of ChemCam passive spectra observations on the same targets (Johnson et al., 2016).

Through sol 1000 of the Curiosity mission, the lower mound layers bearing the strongest CRISM signatures of phyllosilicate, sulfate, and iron oxide minerals still lie ahead of the rover. Work by Fraeman et al. (Fraeman et al., 2015) in differentiating CRISM units on the basis of thermophysical and spectral parameters provides a forecast for promising future sites of potential multispectral investigation. Mastcam multispectral observations have demonstrated the ability to identify diversity not readily apparent in RGB color images or orbital spectra. Understanding the mineralogical implications of Mastcam spectral features based on inferences drawn from previous instrument collaborations provides the ability to interpret as well as to distinguish distinct spectral units. The rover's continued ascent up the slopes of Mt. Sharp is expected to bring it into contact with more of the mound's diverse iron mineralogies and associated spectral diversity, including arriving at the hematite ridge itself and the exposures of nontronite expected just beyond (Fraeman et al., 2013; Milliken et al., 2010; Thomson et al., 2011). Further analyses should be able to not only assist reconnaissance spectral imaging for the Curiosity mission, but also provide insight into multispectral analysis of martian materials and imaging strategies relevant for the high-heritage Mastcam-Z instrument (Bell III et al., 2014) aboard the upcoming Mars2020 mission, and the similar ExoMars PanCam investigation (Coates et al., 2015) as well.

3.6 Acknowledgments

This work was supported by Mars Science Laboratory Project grants and contracts from NASA, JPL/Caltech, and Malin Space Science Systems, Inc. We heartily thank the MSL/Curiosity science and operations team, who made these results possible. The authors also acknowledge specific funding sources, as follows: the MSL Participating Scientist program (J.R. Johnson, JPL

contract 1350588, and B.L. Ehlmann), the W.M. Keck Institute for Space Studies and Caltech GPS Division Texaco postdoctoral fellowships (A.A. Fraeman), the NASA Postdoctoral Program (M.S. Rice), and the Danish Council for Independent Research/Natural Sciences (K.M. Kinch, FNU Grant 12-127126). A portion of this research was carried out at the Jet Propulsion Laboratory, California Institute of Technology, under a contract with the National Aeronautics and Space Administration. Finally, the authors thank reviewers Edward Guiness and Jack Mustard for greatly appreciated feedback that allowed us to significantly improve upon the initial manuscript.

CHAPTER 4

MSL/MASTCAM MULTISPECTRAL IMAGING OF GALE CRATER, MARS: THE DISTRIBUTION AND SPECTRAL VARIABILITY OF FLOAT AND BEDROCK MATERIAL

This chapter is a rough draft of a manuscript that will eventually incorporate the contributions of a number of MSL science team colleagues; however, the work presented here represents the work of this author.

4.1 Introduction

The Mars Science Laboratory (MSL) Curiosity rover has traversed a complex assemblage of clastic sedimentary rock units and igneous clasts and float rock that reflect a diverse lithologic environment within and around Gale Crater, Mars. Textural and compositional information acquired from the onboard science instruments have provided the means to describe and classify bedrock and float encountered along the rover's path (Cousin et al., 2017; Mangold et al., 2017); however, geochemical information is necessarily constrained by the limited sampling and small instrument footprints characterized by the ChemCam (Maurice et al., 2012) and APXS (Gellert et al., 2009) instruments. Detailed scoop or drill sampling and accompanying mineralogical analyses are even more sparsely performed, as these operations require significant time and investment of operational resources. Imaging allows for a broader characterization of the properties of surface materials. Curiosity is equipped with numerous science and engineering cameras designed to provide context and operational support; of these, only the Mastcam stereo cameras possess multi-filter imaging capabilities that are designed to provide compositional discrimination across the entire sensitivity range of the CCD detector. Previous work provided a description of select multispectral imaging targets (Wellington et al., 2017); here, we aim to expand upon that work to include all spectral classes of rock surfaces and alteration features to more fully describe the spectral variability of the lower units and the transitions between depositional and alteration environments as imaged by the Curiosity rover.

4.2 Methods

The calibration of raw Mastcam data to calibrated reflectance values is described in Bell et al. (2017), with respect to both the pre-flight tactical pipeline and improvements based on in-

flight data. Here, we use a version of the latter as described by Wellington et al. (2017). We have gone through the full-filter Mastcam observations (i.e., sequences obtained in all filters intended for surface imaging, designated L0-6, R0-6; see Table 1 and Figure 3.1 in Section 3.2 above) and extracted regions of interest (ROI) mean values from the surfaces of rock faces, both bedrock and float (including disturbed and drilled materials), as well as some diagenetic features and alteration surfaces to characterize both the variations in primary mineralogy and the often localized and small but resolvable features resulting from post-depositional fluid interactions. These mean values are extracted from each filter image in the sequence and averaged over stereo filter positions for a total of twelve spectral mean values for each ROI (including each RGB Bayer channel as a separate value). Variations in local incidence angles are not dealt with directly; however, outside of near-shadowing and observations acquired far from local noon, the spectral shapes can be compared directly (by spectral parameters, for example); differences in overall reflectance may be expected to be significant, but relatively unbiased, for undisturbed rock facets, but less substantial for surfaces that will tend to be near-horizontal (such as DRT spots). Since our analysis does not depend on minor differences in overall reflectances, we do not expect these differences in viewing geometry to be a major source of uncertainty.

By relatively simple spectral analysis techniques, we have identified the most significant variations that are exhibited by all full filter multispectral sequences acquired by the rover up to sol 1160 (November 2015). We use this sol as a cutoff point because further observations show that since that time the stratigraphy at the base of Mt. Sharp underwent a significant change in spectral character (i.e., from exhibiting predominantly ferrous features in bedrock, to pervasively ferric spectral features) and represents some variety of compositional change that the rover is still actively investigating at the time of this writing.

4.3 Data

Example spectra for each spectral “class” are shown in Figure 4.1. We will use the following sections to describe, in greater detail, the spectral features that define the difference between these materials,

4.3.1 Spectral Class 1

Loose float rock encountered from the beginning of the traverse as well as bedrock material from the Stimson unit, a sandstone that unconformably overlies the Murray (Banham et al., 2018), have reflectance spectra characterized by relatively low overall values, a reflectance peak near 800 nm, and a subtle falloff towards longer wavelengths. These features are consistent with a generally mafic composition that includes the presence of olivine and/or pyroxene phases. The peak reflectance favors a comparatively higher percentage of high-calcium versus low-calcium pyroxene. This spectral shape may represent a range of broadly similar mafic compositions and chemical variations that may not be apparent in the spectral data.

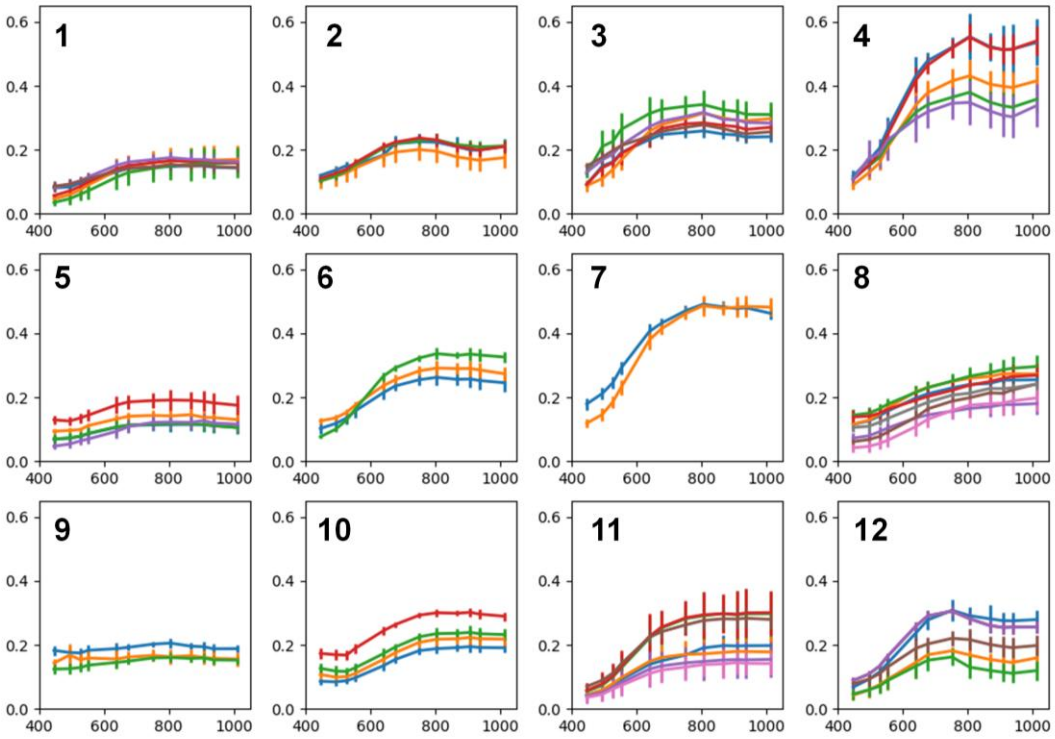

Figure 4.1: Spectral variability (reflectance vs. wavelength in nm) across Gale bedrock, float, and other materials encountered before the pervasively oxidized portion of the Upper Murray.

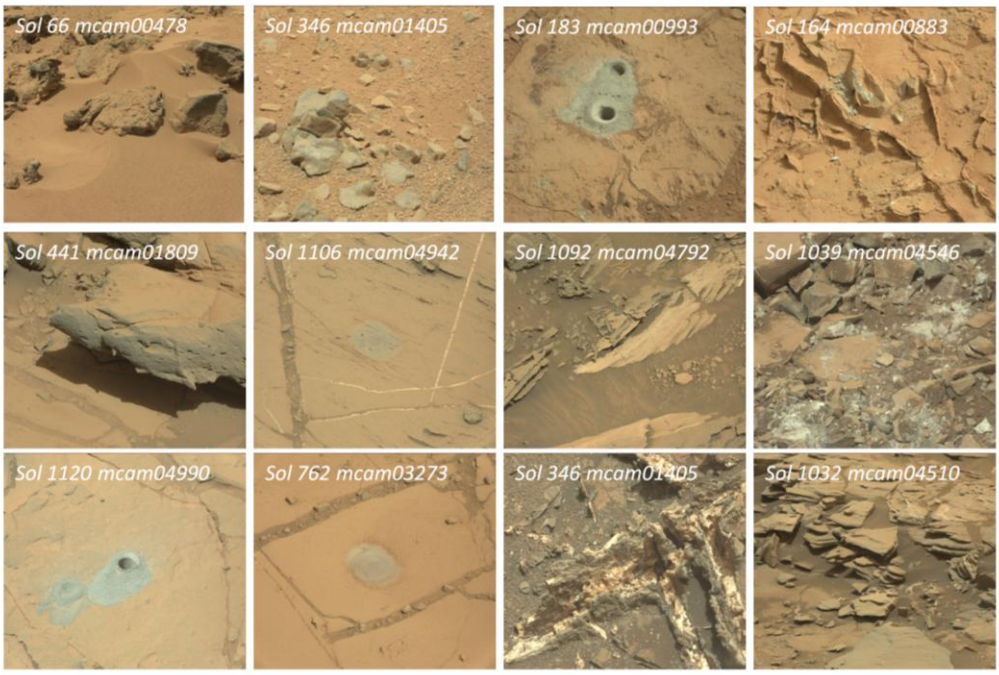

Figure 4.2: Examples of materials and context for each of the spectral types plotted in Figure 4.1, shown in the same order as above.

4.3.2 Spectral Class 2

Loose float rocks and clasts contained in conglomerates encountered early in the rover's traverse exhibited early near-infrared falloffs and shorter wavelength reflectance peaks relative to Spectral Class 1. Because of the absence of matching bedrock spectra, and the proximity of float rocks and clasts to the Peace Vallis alluvial fan feature, we interpret these materials as likely representative of units located within the watershed of the fan system, sourced either from the crater walls or outside of the crater itself. A notable example of this material was the "La Reine" target, imaged in all Mastcam filters on sol 346; it was also a ChemCam RMI target (Cousin et al., 2017), revealing a crystalline texture, and the target of a ChemCam passive spectral observation (Johnson et al., 2015). Assuming, on the basis of the RMI observation, that this rock and similar float and clasts are igneous in origin, the change of peak reflectance to shorter wavelengths (near the 751 nm filter) is most likely due to a higher percentage of low-calcium pyroxene. A slightly reddish trend in the visible wavelengths may be a result of a coarser texture, which may retain

dust better than finer-grained rocks, or may be innate. These materials were not sampled by the internal analysis suite, so definitive mineralogy is not available.

4.3.3 Spectral Class 3

The mudstones of the Yellowknife Bay Sheepbed unit, stratigraphically, the lowest formation explored by the rover (Grotzinger et al., 2015), have higher average reflectance values compared to many of the loose float material encountered in the surrounding areas, consistent with the lighter-toned appearance observed from orbit (Grotzinger et al., 2014). Flat-lying surfaces are strongly dust covered, but surfaces cleaned by the DRT or freshly broken or ground by the drill bit provide minimally contaminated spectral values. The peak reflectance is near 800 nm, with a moderate absorption band with a band center that falls just shortward of 1000 nm. Both the John Klein and Cumberland drill holes sampled this material. As discussed by Wellington et al. (2017), the spectral features are likely a combination of the measured primary mafic phases and the relatively high phyllosilicate abundance. The visible wavelength slope may indicate either some spectral contribution from admixed dust (for the tailings) or weak dust coating, or some amount of oxidation of the iron in the smectite component, the latter of which may be consistent with the CheMin diffraction pattern (Treiman et al., 2014).

4.3.4 Spectral Class 4

A number of surfaces in the Yellowknife Bay area exhibit modestly different spectral shapes compared to the drill tailings from the bulk of the unit itself. This material still exhibits the 800 nm reflectance peak and near-infrared absorption feature of ”spectral class 3”, but the band center is shifted to slightly shorter wavelengths, nearer to the 937 filter, and the upturn towards the longest wavelengths is stronger. The relationship of this material to the tailings is best shown by observations of diagenetic features termed “raised ridges”. Several of these features were driven over by the rover’s wheels, breaking them to expose the interiors. Resistant surfaces show the strong NIR upturn, while the inside is most similar to the drill piles. This suggests that the outer surface of the Sheepbed unit is variably oxidized, which may be related to the erosional resistance of these surfaces.

4.3.5 Spectral Class 5

Dark-toned sandstones encountered near the Kimberley, a sandstone outcrop waypoint selected from orbital images (Rice et al., 2017), have spectral features similar to Spectral Class 1, although the spectra are flatter between 676 and 867 nm, and without an obvious spectral peak wavelength in less dusty targets. The drill target Windjana was of this spectral class, from which CheMin measurements revealed a relatively higher magnetite abundance (Treiman et al., 2016). Magnetite in spectral mixtures has a strong effect on overall reflectance and spectral relief even at relatively minor concentrations (Singer, 1981), and may be principally responsible for the lower reflectance and grayer spectral characteristics of these materials.

4.3.6 Spectral Class 6

With even a minor dust coating, the spectral reflectance of a surface over a dark-toned substrate gains a significantly more reddish spectral slope. Stronger forward scattering by fine-grained dust at longer wavelengths may gave the near-infrared a modest spectral peak near 800 nm, consistent with laboratory spectra of coated dark-toned materials (Johnson and Grundy, 2001a). Sandstone surfaces retain dust well due to their coarse textures; therefore, perhaps it is not surprising that both the sandstones near the Kimberley and the Stimson exhibit similar spectra over dusty undisturbed surfaces.

4.3.7 Spectral Class 7

At several points across the Stimson unit, the rover encountered patches and haloes of material with uncommonly high overall reflectance, consistent with fewer mafic, iron-bearing components. The spectra of these materials varies, likely a result of the combination of initial bedrock composition and the degree of leaching experienced by these bleached rock units. Dust cover is overwhelmingly responsible for the visible spectral shape in Figure 1; drill tailings into this material are exceedingly flat over these wavelengths. CheMin analyses of drill holes Buckskin, Greenhorn, and Lubango show depletions of iron-bearing phases, and enrichments in silicic phases like opal-CT and, for Buckskin, tridymite (Morris et al., 2016). Each of these samples exhibits a high proportion of amorphous material relative to the crystalline component. Mastcam spectra are consistent with a depletion in iron minerals and/or amorphous Fe phases.

4.3.8 Spectral Class 8

Material with strongly positive NIR slopes may be indicative of Fe-Ni meteorites when exhibited by the bulk rock (Gaffey, 1976), although some secondary phases may show similar spectra (e.g., Hardgrove et al., 2015) and have been observed as well. Spectra from the Aeolus Palus meteorite fragments (e.g., Johnson et al., 2014) are included in Figure 4.1(8). Two instances were identified where small exposures of similar spectral features were seen, both in broken rock surfaces: one in Marias Pass (sol 1039 observations) and another near the beginning of the traverse, on sol 160. These are similar to spectra observed in Meridiani Planum by Opportunity (Farrand et al., 2016), and may likewise indicate the presence of manganese oxides.

4.3.9 Spectral Class 9

Very clean surfaces produced by the drill in Hidden Valley and on the Stimson unit show very flat, relatively low reflectance surfaces that may reflect some combination of higher magnetite and/or the lack of ferrous phases that would otherwise contribute to the ~1 μm band. Dust on these substrates quickly makes these materials difficult to distinguish from other mildly altered, basaltically derived materials (e.g., Spectral Class 6).

4.3.10 Spectral Class 10

Pahrump Hills materials exhibit a range of spectral features whose variations from previous units is most apparent over low-dust surfaces. Drill tailings from the Confidence Hills and Mojave targets show a relatively featureless near-infrared spectrum, but a pronounced absorption near 527 nm that we attribute to the presence of hematite in the sample. This is confirmed by CheMin analyses (Rampe et al., 2017). As reported by Wellington et al. (2017), there appears to be a correlation between the strength of this features and the measured abundance of crystalline hematite, albeit there are only three drill samples with comparable mineralogy from which to draw such comparisons. Variably abundant magnetite can be expected to decrease the overall reflectance.

4.3.11 Spectral Class 11

A subtle spectral difference showed up in certain dark-toned regions of the Garden City outcrop. Distinct portions of the outcrop show spectra that are not consistent with the rest of the bedrock. The spectra have relatively flat to weakly positive near-infrared slopes. It is unclear what

these features signify, but the outcrop contains extensive fracture-filling veins and so the spectral variations may represent either a leaching of host rock cations, or else the deposition of a minor amount of a secondary phase. Either way, the lack of features is not diagnostic of any particular phase and the spectral features seem to be restricted to the Garden City outcrop.

4.3.12 Spectral Class 12

At Hidden Valley, Garden City and Marias Pass, small-scale features were identified with strong near-infrared absorptions. These were accompanied by a variable, short wavelength (430 nm) feature detectable by ChemCam passive observations (Johnson et al., 2016). In the Garden City outcrop, spectra with these features varied significantly in overall reflectance in a way that correlates with the reflectance of the surrounding material (i.e., light-toned vein or dark bedrock), suggesting that the exposure is a coating that incompletely hides the underlying material. The best example of this material was imaged in a sol 1032 observation with one of the strongest near-infrared band depths measured to date by the camera. Follow-on ChemCam observations strongly indicated an iron sulfate (Chemcam team, personal comm.unication), which we suspect is jarosite.

4.4 Discussion

The surface reflectances of materials encountered by the rover exhibit several different modes of variation, some of which represent categorical compositional or grain size differences, while others appear to represent relative degrees of alteration. Coatings of surfaces by fine-grained particles can alter spectra considerably even with thin coatings; some surfaces may retain such particles better. Over the first approximately 1000 sols of the mission, the bedrock spectra varied significantly between the Yellowknife Bay mudstone unit and other Bradbury group units. The mudstone shows evidence for surface alteration, which could represent a change in the oxidation state of the smectite. Sandstones and float rocks of uncertain grain size tend to be lower in overall reflectance, but the spectral shape exhibits variations that may be due to compositional differences as well as dust cover, although pervasive dust coverage in especially the Stimson unit makes direct comparisons difficult. Nevertheless, Bradbury and Stimson bedrock exhibit subtle differences in redness and peak reflectances, that could reflect changing

abundances of strongly absorbing phases like magnetite and the relative abundances of ferrous phases. In the Stimson, bleaching along fracture zones (c.f. Yen et al., 2017) significantly raises the reflectance of the material but results in at best only weak changes to spectral shape. In the Pahrump section, sampled more regularly by both the drill and the DRT, it is clear that spectral variations are gradual, and are accompanied by the stronger or weaker short-wavelength ferric features.

Several regions along this portion of the traverse show unique and often small-scale regions of unusual spectral properties, often associated with either obvious diagnetic features, or interior surfaces exposed when rocks or bedrock were broken apart, presumably along planes of weakness created by the alteration. Near Hidden Valley and Marias Pass, an iron sulfate identified by ChemCam is suspected to be jarosite exposed over cm-scale surfaces, identifiable by its very strong 900 nm absorption feature and the strongly negative L3-L5 slope (751-867 nm). Very tiny surface areas, <1 cm^2, show strongly positive near-infrared slopes that may indicate a manganese oxide. These are spectrally similar to, though morphologically very distinct from, the iron meteorites encountered on occasion along the traverse. At Marias Pass, the occurrence of these potential oxide phases with nearby jarosite over small exposures may indicate deposition from fluids following contact with surface oxidants, as suggested for Mn-rich material discovered by Opportunity near Endeavor Crater (Arvidson et al., 2016).

4.5 Summary

- Mastcam multi-filter imaging reveals that float and bedrock surfaces exhibit significant variability over the traverse to the Upper Murray; in many cases, this diversity was not detectable from orbit.
- Differences in source region, such as contributed different clast and float rock to the base of the Peace Vallis alluvial fan, can account for some of the spectral variability
- Some of the variability may represent gradually changing depositional environments, which may include changes with cm-scale depth (e.g., the Pahrump Hills area).
- Post-depositional processes produced secondary minerals that are limited in spatial extent, but detectable by strong or unusual spectral features; these are likely

manganese and iron sulfate minerals. Cation movement from diagnetic processes may explain some changes in overall reflectance along fracture margins. Changes in band strength and position in the Yellowknife Bay area is consistent with iron oxidation, perhaps within clay minerals, on more resistant surfaces.

CHAPTER 5

IRON METEORITE CANDIDATES WITHIN GALE CRATER, MARS FROM MSL/MASTCAM MULTISPECTRAL OBSERVATIONS

This chapter is an early draft of a manuscript in preparation for eventual submission to Meteoritics & Planetary Science. The final manuscript will include edits and contributions from coauthors; the version presented here is work by this author.

5.1 Introduction

Meteorite finds on Mars presently number over two dozen suspected or confirmed individual rocks that were recognized in rover datasets on the basis of their distinctive morphological, chemical, and/or spectrophotometric properties. The first meteorite recognized on Mars was “Heat Shield Rock”, imaged by the MER rover Opportunity on sol 346 of its mission (Squyres et al., 2006). The unusual morphology prompted an in-situ investigation that confirmed a metallic composition on the basis of Mössbauer (Morris et al., 2006), Mini-TES (Ruff et al., 2008), APXS (Schröder et al., 2008), and Pancam results (Johnson et al., 2006a; Schröder et al., 2008). Since that find, numerous additional likely candidates have been recognized in Meridiani Planum and Gusev Crater by the MER rovers (Fairén et al., 2011; Fleischer et al., 2010a; Schröder et al., 2008, 2010; Weitz et al., 2010), and more recently within Gale Crater by the Mars Science Laboratory (MSL) Curiosity rover (Johnson et al., 2014; Meslin et al., 2017; Wellington et al., 2018; Wiens et al., 2017). Meteorites are serendipitous discoveries by rover missions whose unusual nature may be obvious or subtle in imaging data, depending on the morphology and variety of meteorite. Applications of meteorite studies to investigate past environmental conditions have been demonstrated for several terrestrial sites (Bland et al., 2000), and with the growing inventory of meteorite finds by rovers, for Mars as well (Ashley et al., 2011; Schröder et al., 2016). The presence of reactive metallic iron in these meteorites serves as a sensitive tracer of minor amounts of chemical alteration, including aqueous alteration, that these rocks experienced over the span of their residence time on Mars. Of suspected meteorites on Mars, the overwhelming majority appear to be iron-nickel or stony iron in composition, which make up only a small fraction of documented terrestrial falls (Ashley and Herkenhoff, 2017). This may be due to

some combination of a true higher proportion of fragments relative to other meteorites, as a result of impact or weathering processes preferentially filtering out and/or eroding chondritic meteorites, or else an observational bias due to the relative ease of identification. Iron meteorites, especially larger ones, are relatively easy to detect in rover imaging data due to their unusual morphology, their smooth, specular surfaces, and, in instances when multi-filter observations were acquired, their unusual near-infrared spectral slopes (Johnson et al., 2014; Schröder et al., 2008; Weitz et al., 2010; Wellington et al., 2018). Such multispectral imaging datasets can be used to identify iron meteorites during the course of a rover mission and to better understand their abundance and their degree of chemical alteration across multiple different landing site locations, with implications for the history of martian weathering environments.

Reflectance spectra over the wavelength range of the MER Pancam and MSL Mastcam instruments' filter complement (400-1100 nm; Bell et al., 2003; Malin et al., 2017) sample broad electronic absorption features whose position and strength depends on the mineralogy, crystallinity, and grain size of constituent phases within rock, soil, and other surface materials on Mars. Native martian materials have a variety of reflectance properties depending on composition. Unweathered mafic igneous rocks such as basalts and sedimentary rocks derived from them typically possess an absorption feature near 1-um. This feature stems from the presence of ferrous (Fe^{2+}) iron in six-fold coordination in the common mafic minerals olivine and pyroxene (Adams, 1974; Burns, 1993a), which incorporate iron in solid solution with Mg^{2+} and (for pyroxene) Ca^{2+}. Feldspars may similarly contribute a weak feature in this region, from the presence of minor amounts of Fe^{2+} in the mineral structure (Adams, 1975; Bell and Mao, 1973). Magnetite, if present, significantly decreases the reflectance of a mixture even at minor abundances, due to strong intervalence charge transfer between the mixed valence (Fe^{2+}/Fe^{3+}) iron cations (Singer, 1981). Fully oxidized iron species, such as hematite, goethite, or jarosite, have a strongly reddish visible wavelength slope from charge transfer absorptions and possess multiple absorption bands in the visible and near-infrared, including near 900 nm (Sherman et al., 1982; Sherman and Waite, 1985). Poorly crystalline but oxidized iron that is a component of martian dust also possesses the strong visible wavelength charge transfer absorption, but lacks

other distinct bands; as a thin layer over a dark substrate, it produces a reflectance spectrum that is flat to weakly negative-sloping into the near-infrared (Johnson and Grundy, 2001b).

5.2 Background

Early quantitative investigations of the influence of the martian atmosphere on impactors date to at least 1969 (Dycus, 1969), following Mariner IV's flyby of Mars, which returned both images of a heavily cratered terrain and a measurement of the planet's atmospheric density. More recent calculations of meteorite accumulations, carried out by Bland and Smith (2000) and based on estimates of meteoroid flux, atmospheric ablation and impact survivability, and oxidative and erosional weathering of meteoritic material have given rise to estimates of $5x10^2$-$5x10^5$ meteorites larger than 10 g per square kilometer. However, this estimate was conducted for stony meteorites; iron impactors would be significantly less numerous, and have different density, material strength, and scaling of bulk strength with size than stony impactors (Popova et al., 2003). Simulations of cratering and meteorite production by Chappelow and Sharpton (2006, 2005) suggest that, in fact, the proportion of surviving stony meteorites may not be significantly different from irons (in their 2006 study, slightly more stony meteorites survive passage through a 6 mbar atmosphere); although, as those authors state, the threshold survivable impact velocity they use for iron (2.0 km/s, Chappelow and Sharpton, 2006) may be quite conservative. In that simulation, most iron material capable of surviving to the surface in the present atmosphere had an initial mass of <10 kg, but the result was found to be strongly sensitive to variations in atmospheric density that are expected to have occurred over the planet's history.

These studies assume that incoming material traveling above a certain velocity cannot produce surviving meteorite fragments, although it is likely that at least a small number of exceptions must occur, because tiny (millimeter to sub-millimeter size) meteorites were recovered from the Moon by Apollo astronauts (Jolliff et al., 1993; McSween, 1976; Quaide et al., 1970; Rubin, 1997). It is possible that some material could survive an impact by stress-wave interference (Melosh, 1989, 1985) or perhaps a small number of impactors produced the surviving lunar fragments in uncommonly low velocity impacts (Bland et al., 2001; Zook, 1975).

However, the lack of any finds of substantial size reported from the Moon suggests that these processes are a minor contribution for larger size fractions.

Once on the surface, meteorites could be expected to survive on Mars for a significant amount of time. For much of the planet's history since the Noachian, chemical weathering rates are expected to have been quite low, due to cold temperatures and low water activity (e.g., Burns, 1993b; Hurowitz and McLennan, 2007). The rate of oxidation of iron in terrestrial meteorites has been shown to vary considerably between collection sites as a result of the local climate conditions (Al-Kathiri et al., 2005; Bland et al., 1998a, 1996; Freundel et al., 1986; Jull, 2001; Jull et al., 1993). It also varies over time as weathering progresses, with initially rapid oxidation of iron followed by significantly slower rates as weathering products form around primary minerals and reduce porosity within the sample (Bland et al., 1998b; Lee and Bland, 2004). Meteorite residence ages, determined from the abundance of cosmogenic radionuclides, have been measured to be as high as ~2 Ma from samples recovered from Antarctic ice fields (Scherer et al., 1997; Welten et al., 1997) and as much as ~0.5 Ma in hot deserts (Nishiizumi et al., 2002; Nishiizumi and Caffee, 2001). Most terrestrial residence times are much shorter, however, with up to only tens of thousands of years in hot deserts and up to only a few hundreds of thousands of years in Antarctica representing more typical ages (Jull, 2001).

A ground-based estimate of the statistics of martian finds must consider the possibility of pairings between individual meteorites, which have the potential to inflate a count meant to represent unique falls. Atmospheric fragmentation could result in significant separation of paired meteorites, i.e., the creation of a strewn field. Repeat imaging of the surface of Mars by the Mars Global Surveyor Mars Orbiter Camera (MOC) and the Mars Reconnaissance Orbiter Context Camera (CTX) instruments have captured modern day impact events, including small clusters of craters believed to be the result of breakup of the original impactor (Daubar et al., 2013; Hartmann et al., 2018; Malin et al., 2006). These are commonly separated by 10s of meters and sometimes up to a few hundred – distances that, for impacts that may have landed surviving meteorites, could leave behind widely separated fragments. These observations of primary clusters in modern observations, however, will necessarily represent the weakest impactors, and

hence significantly more likely to be stony. The fragmentation of a large iron meteoroid depends on properties of the individual body, such as internal fracturing, that influence the effective bulk strength (Popova et al., 2003); this value could vary significantly for impactors of different sizes and past impact histories. Fragmentation of different compositions of impactors than what may have been observed in the imaging record of primary clusters, and the action of this process under differing atmospheric densities of Mars' past, could produce different separation distances.

5.3 Datasets and Methods

A description of the MSL/Mastcam instrument has been provided in previous chapters; however, to allow this chapter to stand alone, and to provide an easier comparison to the MER/Pancam instruments, we will describe it and the calibration pipeline once more for readers who may be interested in this chapter only.

The Mastcam instrument suite comprises two fixed focal length stereo cameras located atop the Curiosity rover's remote sensing mast (RSM). The cameras were designed to document not only morphology, texture, stratigraphy, and other contextual properties, but also to provide some compositional discrimination by means of an eight-position filter wheel on each instrument (Bell III et al., 2017; Malin et al., 2017). The left, 34-mm focal length camera (the M-34) has a 20° x 15° field of view and narrowband geology filters (filters 1-6) positioned at effective band centers of, in filter wheel position order, 527, 447, 751, 676, 867, and 1012 nm. The right or M-100 (100-mm focal length) camera has a 6.8° x 5.1° field of view, with narrowband filters positioned at 527, 445, 805, 908, 937, and 1013 nm. Each camera has a CCD detector with a microfilter Bayer array that allows the cameras to acquire RGB images with either instrument's "filter 0", the broadband near-infrared cutoff filter. While the cameras are frequently used to acquire only broadband visible imaging, image sequences are also sometimes requested using the full filter complement or some subset (minus the last position, which is a solar filter on each camera). In most of these cases, matching filter observations of the on-board calibration target mounted on the rover deck are acquired near in time to the observation of the science target, allowing near-simultaneous characterization of the incoming solar radiance to achieve accurate reflectance calibration.

System-level radiometric response coefficients (i.e., camera- and filter-specific constants in $(W/m^2/nm/sr)/(DN/s)$ units) derived from pre-flight measurements of an NIST-certified integrating sphere were published by Bell et al. (2017), along with other pre-flight and in-flight calibration information. Images of the Mastcam calibration target (the “caltarget”) are converted to radiance and mean radiance values are extracted from the light, mid-toned, and dark rings to generate coefficients for calibration to I/F. This method relies on a pre-flight characterization of the bidirectional reflectance of the caltarget substrate materials, which had already been performed long before Mastcam pre-flight testing for the MER Pancam investigations; these used a nearly identical caltarget (Bell III, 2003). The effect of dust deposition on the caltarget reflectance during the surface mission is accounted for by means of two-layer radiative transfer model with wavelength-dependent dust single scattering values derived from in-flight observations (Bell III et al., 2017; Kinch et al., 2015, 2013). The calibration pipeline as employed here is described more fully by Wellington et al. (2017) (see also 5.3.6 of Bell et al. (2017)). A correction by the cosine of the solar incidence angle is used to convert I/F values to “relative reflectance” or “R*”, although it should be noted that we do not correct for local incidence angle (due to, e.g., rock surface orientation), and that the reflectance of iron meteorites may be expected to vary significantly with viewing geometry.

The Pancam instruments employed on the MER-A and MER-B missions are similar CCD cameras with a rotating filter wheel designed to document the spectral reflectance properties of the surface. Unlike Mastcam, both Pancam cameras on each rover have an identical focal length (43 mm), with a field-of-view of 16°x16° (Bell III et al., 2003). The distribution of filters between the camera pair is likewise different from MSL-Mastcam; shorter wavelength filters are concentrated in the left camera, with filter positions 2-7 as 753, 673, 601, 535, 482, and 432 nm, and right camera filters 1-7 as 436, 754, 803, 864, 904, 934, and 1009 nm (position 8 is a solar filter on each camera; position L1 is empty). It should also be noted that Pancam does not image through a Bayer microfilter array as Mastcam does. Calibration of Pancam observations to reflectance through the use of in-flight images acquired of the Pancam calibration target is very

similar to the methodology employed for Mastcam, and is described by (Bell III et al., 2006; Kinch et al., 2015, 2007).

The most detailed information about the reflectance properties of an imaging target is provided when the full filter set is acquired; however, due to operational or data volume constraints, sometimes only a subset were commanded. For Mastcam, it should also be noted that the differing focal lengths of the camera have two important implications for meteorite hunting: First, it can frequently be the case that a potential meteorite captured by the M-34 may not be within the field-of-view of the corresponding M-100 frame(s), since it is often the case that a single M-100 pointing is acquired on the most promising target, rather than the nine separate M-100 pointings that it would take to cover the entire M-34 field-of-view. Second, for small meteorites, the M-34 may lack sufficient spatial resolution to provide spectral data for rocks if they are barely resolvable by the M-100. For the purposes of identifying candidate iron-nickel meteorites, we investigate Mastcam multispectral observations using as few as four filters. We examined multispectral observations fitting these criteria up to sol 1869 to identify candidate iron meteorites imaged along Curiosity's traverse within Gale Crater. In addition, we re-examined the MER-A and MER-B Pancam multispectral datasets to search for unrecognized iron meteorite candidates in order to ensure an accurate comparison to the Mastcam results. For these data, we used the Pancam "13F" sequences (i.e., sequences acquired with all of the narrow band geology filters).

To search these datasets efficiently, we define spectral parameters that are consistent with the characteristics of known iron meteorites and exclude the majority of material that is clearly native martian. For Mastcam, we define the parameters indicative of a potential meteorite as 1) an L6/L3 (1012/751 nm) ratio greater than 1.08 (i.e., increasing near-infrared reflectance towards longer wavelengths, (Gaffey, 1976)) and 2) an L3/L1 (751/527 nm) ratio less than 2.2 (to exclude reddish material). Using these filters has the advantage that it does not exclude photometric sequences (e.g., Johnson et al., 2018, 2017), which are commonly acquired with the L1236 filter set, and takes advantage of the M-34's wider field-of-view. We use these parameters to generate heat maps for each multispectral sequence showing the strength of the 1012/751 nm

ratio to allow a visual search through the dataset for signals that are spatially coherent and not associated with shadows, extreme viewing geometries, rover hardware, or other obvious false positives. We also produced decorrelation stretch images (as in Alley, 1996) for each multispectral sequence using filters L1-L3-L6 (527-751-1012 nm) and L3-L5-L6 (751-867-1012 nm) for the left camera, and R3-R4-R6 (805-908-1013 nm) for the right camera. The latter two sets emphasize spectral variability in the near-infrared, while the L1-L3-L6 stretch accommodates photometry filter sets. A visual search through these products is often sufficient to identify promising candidates for further investigation.

For Pancam, we define the parameters indicative of a potential meteorite as an R6/R3 (934/803 nm) ratio greater than 1.01 and an R2/R1 (754/426 nm) ratio less than 4.0. Parameter values were chosen by iterating over portions of the dataset containing known meteorites, adjusting values to exclude obvious non-meteorites while retaining detections on iron-nickel fragments known to be present. The choice of R6 as the longest near-infrared wavelength to ratio is done to avoid known issues with the R7 (1009 nm) filter (Jakobsen et al. (2016), and in prep.). As above, we also generate decorrelation stretches for each sequence, in this case using filters R2, R4, and R6 (754, 864, and 934 nm) to search for float rocks with decorrelation stretch color matching that of known meteorites. Promising candidates are then examined in full spectral detail.

5.4 Results

5.4.1 MSL/Mastcam

A number of meteorites encountered by the MSL Curiosity rover have been identified on the basis of morphology and/or chemistry (Johnson et al., 2014; Meslin et al., 2017; Wiens et al., 2017). These are the Aeolus Palus group (sols 640-641) and a handful of smaller stones sitting loose as float on top of lower Mt. Sharp units. Most of these have accompanying Mastcam multispectral observations, providing verified iron meteorite spectra for comparison to other float rocks that have been imaged by Mastcam but which do not have accompanying compositional data. As discussed below, we identified a number of additional likely meteorites in the Mastcam multi-filter dataset, approximately doubling the count of known spatially separate clusters. The list

in Table 5.1 shows a summary of both the previously recognized Gale Crater iron meteorites and new ones identified here from the Mastcam spectral data, grouping together individual stones located within a few meters. These were identified in multispectral sequences commonly acquired for a different purpose, such as the photometry experiments, that happen to catch the unusual float rocks.

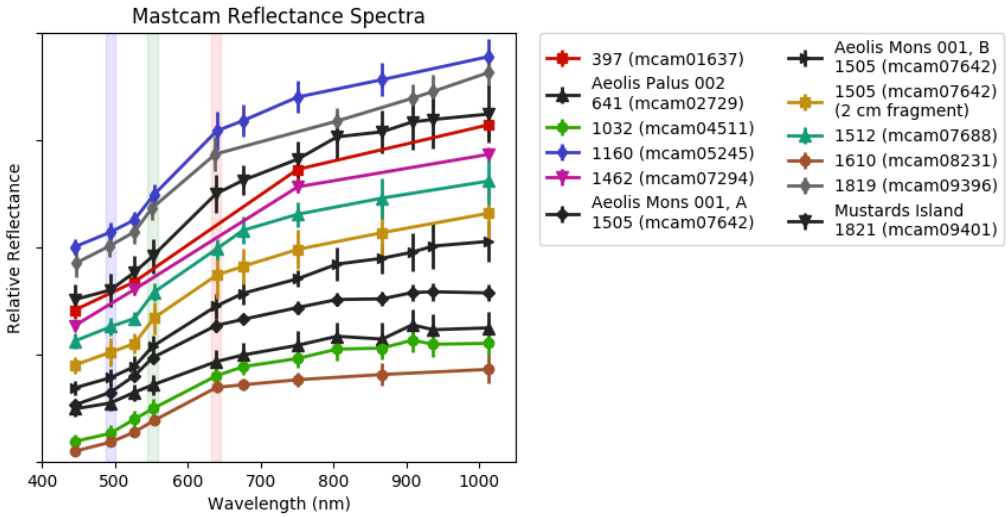

Figure 5.1: Mastcam reflectance spectra representing the numerous small and large fragments of iron meteorites identified either by Bayer color and/or morphology (the named entries), or else by multi-filter observations. Aeolis Mons 001 (“Egg Rock”) has some variability, shown by the “A” and “B” spectra.

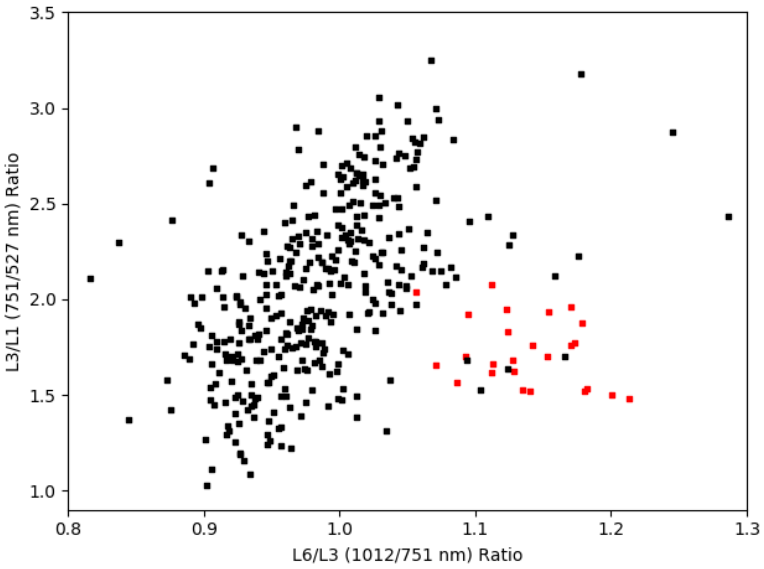

Figure 5.2: Parameter plot showing clustering of Mastcam meteorite spectral values (red) versus other float and bedrock spectra (black). Ambiguous cases and false positives are resolved through a detailed examination of the image data.

Table 5.1: Iron meteorite clusters encountered by MSL, grouped by proximity

Sol(s)	Number	Size(s)	Science Instruments	Mastcam Filters[1]	Target Name(s)
397	1	~ 6 cm	Mastcam	L1236	
640-641	3	~ 0.3-2 m	Mastcam, ChemCam RMI	L0-6, R0-6	Lebanon, Lebanon-B, Littleton
990-1032	9+	~ 3-5 cm	Mastcam	L0-6, R0-6 // L0-6 // R0-6 // L1236	Cottonwood
1160	1	~ 5 cm	Mastcam	L0-6	
1462-1463	2	~ 2-5 cm	Mastcam	L1236	
1505	2	~ 2 cm	Mastcam, ChemCam LIBS+RMI	L0-6, R0-6 // L0-6	Egg Rock
1512	1	~ 2 cm	Mastcam	L0-6	
1577	1	~ 8 cm	Mastcam, ChemCam LIBS+RMI	R0[2]	Ames Knob
1610	1	~ 1 cm	Mastcam	L0-6	
1819-1821	many	< 15 cm	Mastcam, ChemCam LIBS+RMI	R0-6 // L0-6, R0-6	Jaquish Ledge, Mustards Island

[1]Different fragments within a cluster may be covered by different filter sets, as indicated below.
[2]The Ames Knob observation was not a multispectral sequence (Bayer color only).

Table 5.2: Mastcam multi-filter observations of confirmed and candidate meteorites.

Sol	Sequence	Filters	LTST[4]	Incidence	Emission	Phase
397	mcam01634	L1236	10:44	23.5	75.6	91.2
397	mcam01637	L1236	12:15	14.8	75.6	69.3
397	mcam01642	L1236	13:46	30.2	75.6	46.9
397	mcam01645	L1236	15:19	51.8	75.6	24.0
397	mcam01648	L1236	16:24	67.6	75.6	8.0
640	mcam02718	L0-6, R0-6	12:27	22.8	79.0	59.1
641	mcam02729	L0-6, R0-6	11:39	22.2	78.4	56.2
990	mcam04372	L0-6, R0-6	10:48	17.8	43.5	60.9
994	mcam04399	L0-6, R0-6	11:45	3.7	82.8	82.8
1000	mcam04444[1]	L1236	12:46	11.6	70.4	58.8
1001	mcam04447	L1236	07:17	70.4	70.4	140.8
1001	mcam04450	L1236	10:06	28.2	70.4	98.6
1001	mcam04453	L1236	15:16	49.2	70.4	21.6
1001	mcam04456	L1236	16:16	64.1	70.4	8.3
1001	mcam04459	L1236	17:01	75.3	70.4	7.9
1000	mcam04446[2]	L1236	12:49	12.5	71.2	83.6
1001	mcam04449	L1236	07:20	69.5	71.2	3.7
1001	mcam04452	L1236	10:10	27.3	71.2	43.8
1001	mcam04455	L1236	15:20	50.0	71.2	121.2
1001	mcam04458	L1236	16:20	65.0	71.2	136.1
1001	mcam04461	L1236	17:05	76.3	71.2	147.4
1003	mcam04469	L1236	11:31	7.1	71.2	64.1
1003	mcam04477	L1236	14:28	37.0	71.2	108.2
1032	mcam04511	L0-6, R0-6	12:06	7.7	70.9	67.6
1160	mcam05245	L0-6, R0-6	12:14	27.8	65.6	49.2
1462	mcam07294[3]	L1236	11:23	15.4	73.9	71.3
1462	mcam07300	L1236	12:48	17.4	73.9	89.7
1462	mcam07304	L1236	14:35	40.3	73.8	114.1
1462	mcam07307	L1236	17:06	76.0	73.8	149.3
1463	mcam07311	L1236	08:35	51.5	73.9	42.4
1463	mcam07317	L1236	15:58	59.6	73.8	133.2
1505	mcam07642	L0-6, R0-6	12:06	19.3	50.5	68.6
1512	mcam07688	L0-6, R0-6	11:34	20.8	45.4	65.7
1610	mcam08231	L0-6, R0-6	11:17	15.8	38.7	32.5
1819	mcam09396	R0-6	12:24	27.4	93.5	66.5
1821	mcam09401	L0-6, R0-6	12:31	28.0	57.2	36.3

[1]The candidate meteorite is in the second of two pointings for this photometry observation and others of this set shown here. [2]Both pointings, potentially. [3]Second of two pointings. [4]Local true solar time.

Unnamed Target, Sol 397 Photometry Observations

A single stone captured in the anti-sunset pointing of the sol 397 photometry experiment has reflectance properties consistent with those of an iron meteorite, and is possibly the first imaged by the Mastcam instruments. Located near the right edge and vertical center of the frames of the sol 397 Mastcam sequences (see Figure 5.4a), it is a lustrous gray-toned rock that

appears to have less dust cover than other rock surfaces in the field-of-view, consistent with a smooth surface. Mastcam spectral data suggest that this float rock has a distinctly different spectral slope that is comparable to known meteorites within the dataset (Figure 5.1). The cleanest bedrock material shows a downturn between 751 and 1012 nm, consistent with a mafic composition; increasing dust cover increases both the 527-751 nm slope and the 751-1012 nm slope. The putative meteorite has a high 751-1012 slope even with a moderate slope across the visible range. This difference in emphasized in a decorrelation stretch of the 1012, 751, and 527 nm filters (Figure 5.4b)

Appearing as it does in a series of observations intended for photometric analysis, this putative meteorite was imaged in four different narrowband M-34 filters (445, 527, 751, and 1012 nm) at five different times of day (see Table 5.2). The timing of these observations for this viewing geometry favors low phase angle coverage (< 92° for a horizontal surface). A composite image of observations in the same filter acquired at different times of sol (Figure 5.4c) suggests that this rock is comparatively more forward scattering relative to other materials in the scene. Hapke scattering parameters for the MER-B meteorite Heat Shield Rock were derived quantitatively by Johnson et al. (2006a) and showed strong forward scattering relative to native martian materials, which would be consistent with what is seen here.

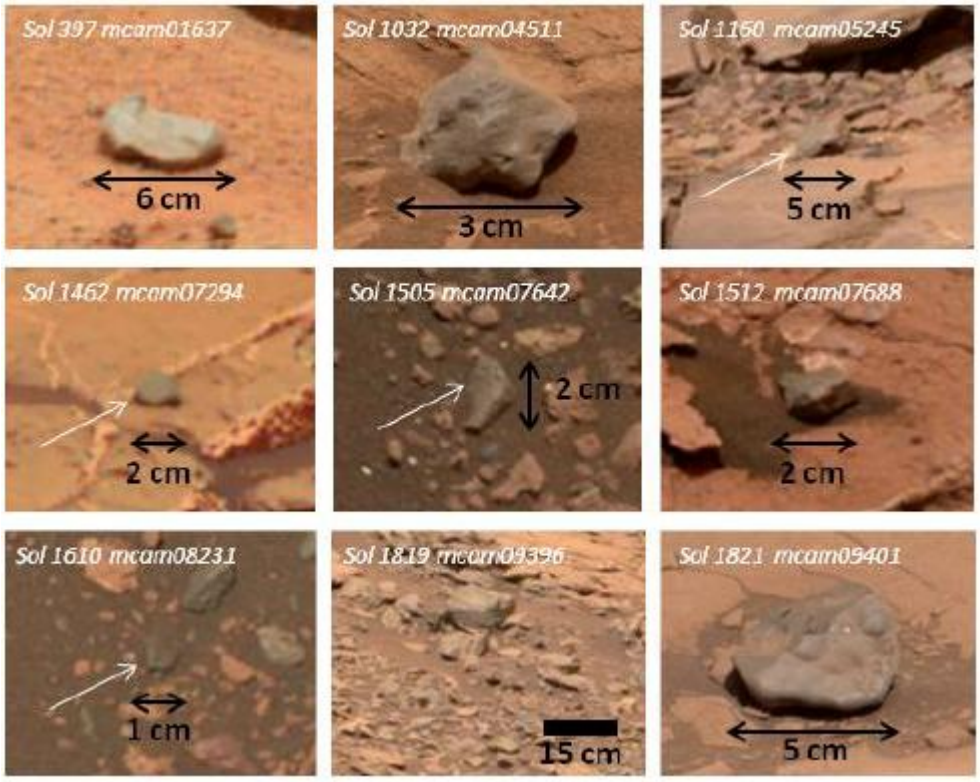

Figure 5.3: Mastcam RGB Bayer or 751-527-445 nm color images of known or candidate meteorites; see Table 5.1 and text for details.

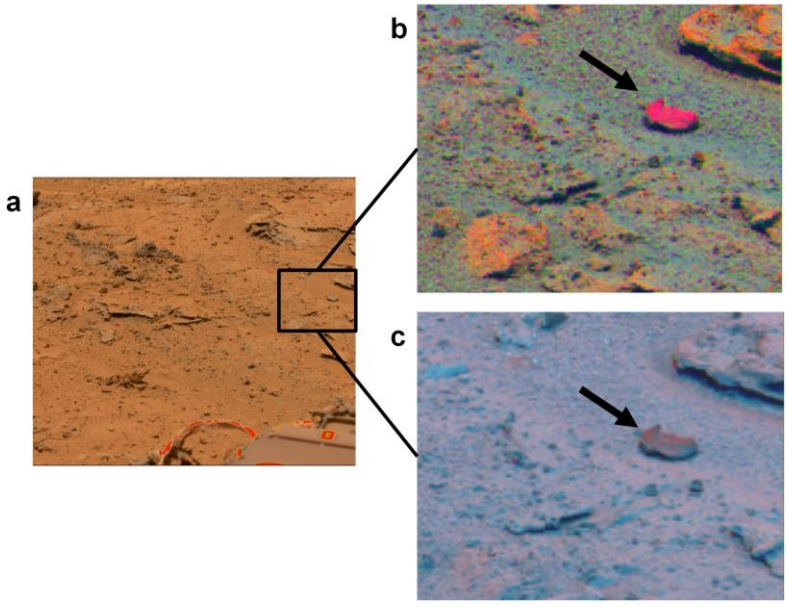

Figure 5.4: The Mastcam sol 397 mcam01637 observations, shown as a) a color composite of filter images L3 (751 nm), L1 (527 nm), and L2 (445 nm), b) a cropped decorrelation stretch image of filters L6 (1012 nm), L3 (751 nm), and L1 (527 nm), and c) a cropped color

composite of L3 (751 nm) filter images from mcam01634, mcam01645, mcam1648 (phase angles 91.2°, 24.0°, and 8.0°). In this latter, redder colors indicate a more forward scattering surface. The arrow indicates the likely meteorite.

Cottonwood & Unnamed Targets, Sols 990-1032

As the rover approached the mission's second solar conjunction, it had just navigated into a region where Stimson sandstones overlay the Murray, at a place named "Marias Pass". The last set of multispectral observations acquired before the operations stand-down included a set of four-filter photometry observations oriented to the east and west of the rover. Even this restricted filter set strongly suggested that several rock surfaces contained in the images were spectrally unusual; this included both material associated with the bedrock as well as float rock that was not a spectral match to the local bedrock. A follow-up full-filter observation acquired post-conjunction (sol 1032) confirmed that these materials were unusual and provided better spectral sampling for comparison to other materials. It was later recognized that the "Cottonwood" float rock was a very good spectral match to the meter-size Aeolis Palus iron meteorites ("Littleton", "Lebanon", and "Lebanon-B"). A number of other spectrally similar cm-sized rocks, which we interpret as likely paired fragments, can be found in other multispectral sequences around this site (Table 5.2), although only Cottonwood was imaged with the full complement of Mastcam filters.

Unnamed Target, Sol 1160 M-34 frames

A multispectral observation acquired on sol 1160 serendipitously captured an unassuming float rock in the M-34 frames (the smaller M-100 FOV did not include this rock). The local bedrock at this site shows mild ferric signatures that produce a weak near-infrared band; over the M-34 filter set, this produces a negative 751-867 nm reflectance slope and positive 867-1012 nm slope. Mean values from an ROI on this float rock show positive slopes between both these pairs of filters (i.e., a uniformly positive near-infrared slope, see Figure 5.1), a characteristic that is consistent with a metallic surface and that compares favorably to other candidate meteorites.

Unnamed Targets, Sols 1462-1463 Photometry Observations

Two rocks captured in photometry observations that spanned two sols (1462-1463) have spectral properties similar to recognized meteorites in the dataset (Figure 5.1). Because these rocks do not have sufficiently near-horizontal surfaces, the rover sees rock faces that will be poorly illuminated or shadowed in particular photometric observations; for this reason we do not attempt a qualitative comparison of scattering properties as with the sol 397 observations.

Probable Paired Fragment, Sol 1505 Egg Rock Observation

A cm-sized meteorite ("Egg Rock") recognized on the basis of its highly unusual morphology and confirmed by ChemCam analysis (Meslin et al., 2017) was targeted by a full-filter Mastcam multispectral observation to characterize its spectral properties and look for evidence of iron oxidation. The M-34 frames (but not, as is often the case, the M-100s) captured a small, partially buried pebble in the same field-of-view of as the LIBS-targeted meteorite, with spectral properties consistent with a highly similar composition. We interpret this as almost certainly a small paired fragment, located within a meter of the larger stone.

Unnamed Target, Sol 1512, Uncertain Pairing

Standard multispectral characterization of a DRT spot (target "Penobscot") captured a single rock near the bottom of the M-34 frames that is a good spectral match to other recognized meteorites. The rock is tens of meters distant from the Egg Rock meteorite and about equidistant in the opposite direction along the traverse from the Ames Knob meteorite; hence, it unclear if this rock is part of the same parent body as one of those analyzed meteorites.

Unnamed Target, Sol 1610, Ireson Hill

Multiple multispectral frames were acquired around the base and on the slopes of an isolated topographic high termed "Ireson Hill". The M-34 frames of a sol 1610 observation captured a tiny, half-buried pebble with a positive near-infrared slope. The 1012/751 nm ratio is less than that for other candidate meteorites identified here which may be a result of the viewing geometry, compositional differences, or perhaps the presence of unresolved sand grains within the ROI contributing to the mean reflectance values.

Jaquish Ledge, Sol 1819

Mid-field multispectral surveying in the L0356 filter set conducted after Curiosity crested the top of the lower Vera Rubin Ridge (VRR). One of the frames within the sol 1814 mcam09364 near-infrared filterset observation suggested spectral variability, although it was not well-resolved by the M-34 frames. A follow-on observation was requested with the M-100 filter set at approximately 30 meters away, and revealed a cluster of rocks with similar spectral signatures, and those spectra consistent with an iron-nickel composition. The rocks, the largest of which is <15 cm, grade in size down to the limit of the camera's resolution; hence, an exact count is not possible. This cluster is only a couple tens of meters from the "Mustards Island" meteorite, raising the possibility that both could be part of the same parent; we group them together in Table 5.1 although it should be noted this relationship is unclear.

5.4.2 MER-A/Pancam

The MER-A mission concluded in 2011, and hence we were able to analyze the entirety of the Pancam 13F ground target sequences acquired within Gusev Crater, including approximately 1000 individual pointings. A search through the Pancam dataset using the spectral parameters discussed in the methodology section turned up convincing meteorite candidates in Pancam multispectral observations of the McMurdo panorama (site 127-128), which included two already reported by Schröder et al. (2008) as well as two other likely paired fragments. The location of these rocks is shown in Figure 5.5, while spectra from each of these (and another float rock, for comparison) are show in the plot in Figure 5.6. Several additional smaller rocks at other sites are also under investigation but not included here. Nevertheless, the Gusev landing site turned up noticeably fewer separated clusters of potential meteorites than along the Curiosity traverse, an observation that will be explored in more detail below.

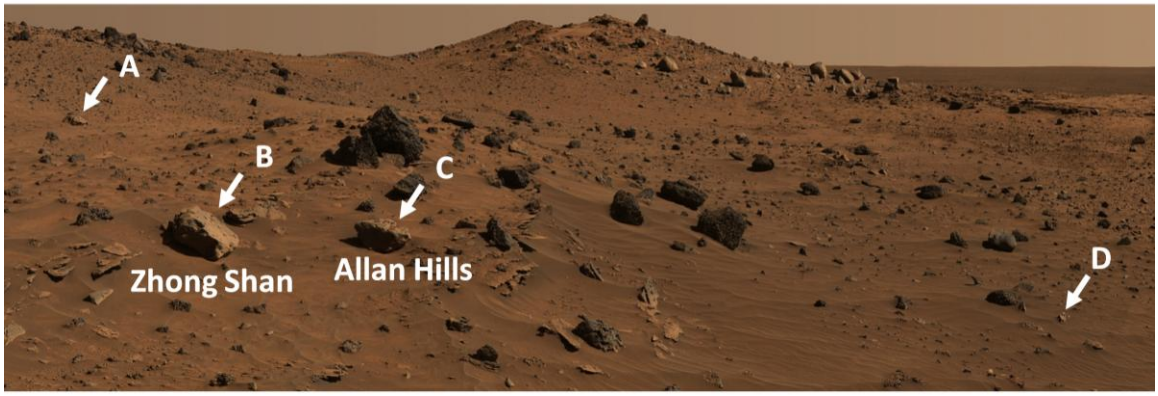

Figure 5.5: A cropped image of the McMurdo Panorama in approximate true color (Credit: NASA/JPL/Cornell), with labeled arrows (added) showing the location of iron meteorites.

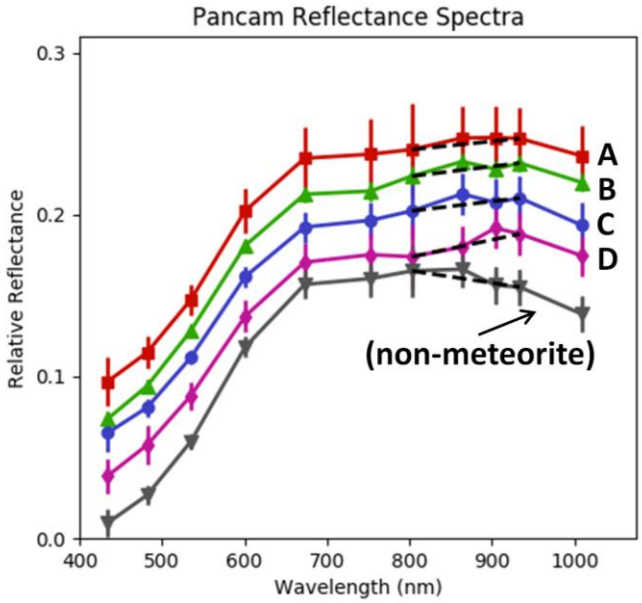

Figure 5.6: Spectra of MER-A recognized and additional candidate meteorites, offset for clarity and labeled as in 5.2, plus an example non-meteorite spectrum (gray) from P2263 on sol 872. The dashed lines connect filter positions used to search the dataset, showing the positive slope between 803 and 904 nm in the likely meteorite spectra.

Table 5.3: Iron meteorite clusters encountered by MER-A, grouped by proximity

Sol(s)	Number	Science Instruments	Pancam Filters	Target Name(s)
844-887	4	Pancam, Mini-TES	L2-7, R1-7 (13F)	Allan Hills, Zhong Shan

Table 5.4: MER-A Pancam multi-filter observations of candidate meteorites

Sol	Sequence	Filters	LTST	Incidence	Emission	Phase
844	P2293[1]	L2-7, R1-7 (13F)	12:26	36.2	71.6	86.7
872	P2263[2]	L2-7, R1-7 (13F)	12:39	39.0	87.5	77.9
887	P2266	L2-7, R1-7 (13F)	12:38	40.0	86.8	68.7

[1]Second pointing. [2]First pointing.

5.4.3 MER-B/Pancam

As an ongoing rover mission, Opportunity (MER-B) is still acquiring data along its traverse through Meridiani Planum; however, for the purposes of this study, we examined data through PDS release #55 (through sol 4860; Sept. 2017). The spectral parameterizations discussed in 5.3 highlighted the iron meteorites identified previously in the literature (Fairén et al., 2011; Schröder et al., 2008) as well as an unnamed float rock in a sol 50 sequence (see Figure 5.7). This latter was highlighted in an abstract by Nuding and Cohen (2009) based on the 934/1009 nm ratio, and we agree with the suggestion by those authors that it is an iron meteorite.

Several examples occur in this dataset of what we interpret as strong false positives – in the sense that they are good spectral mimics for meteorites and not artifacts of illumination conditions or other easily separable false signals. The Opportunity rover's investigation of its heat shield took it to an area with scattered metal debris, which our spectral parameter mapping picks up strongly. Smaller fragments of Heat Shield Rock, if there are any in the vicinity, will go undetected against the scattered artifical metal fragments. The piece of float rock known as "Pinnacle Island", imaged in Pancam multispectral on sols 3541-3557, has one of the strongest near-infrared slopes of dark-toned rocks within the dataset. Weaker examples appear to exist nearby as well; however, for both the Pinnacle Island target and other rock surfaces, the unusual spectral signature shows up only on particular rock faces, suggesting that it is a coating, and hence not a meteorite. The results of geochemical analyses indicated the presence of an Mn-oxide coating (Arvidson et al., 2016), which could explain the strongly positive near-infrared slopes (Farrand et al., 2016).

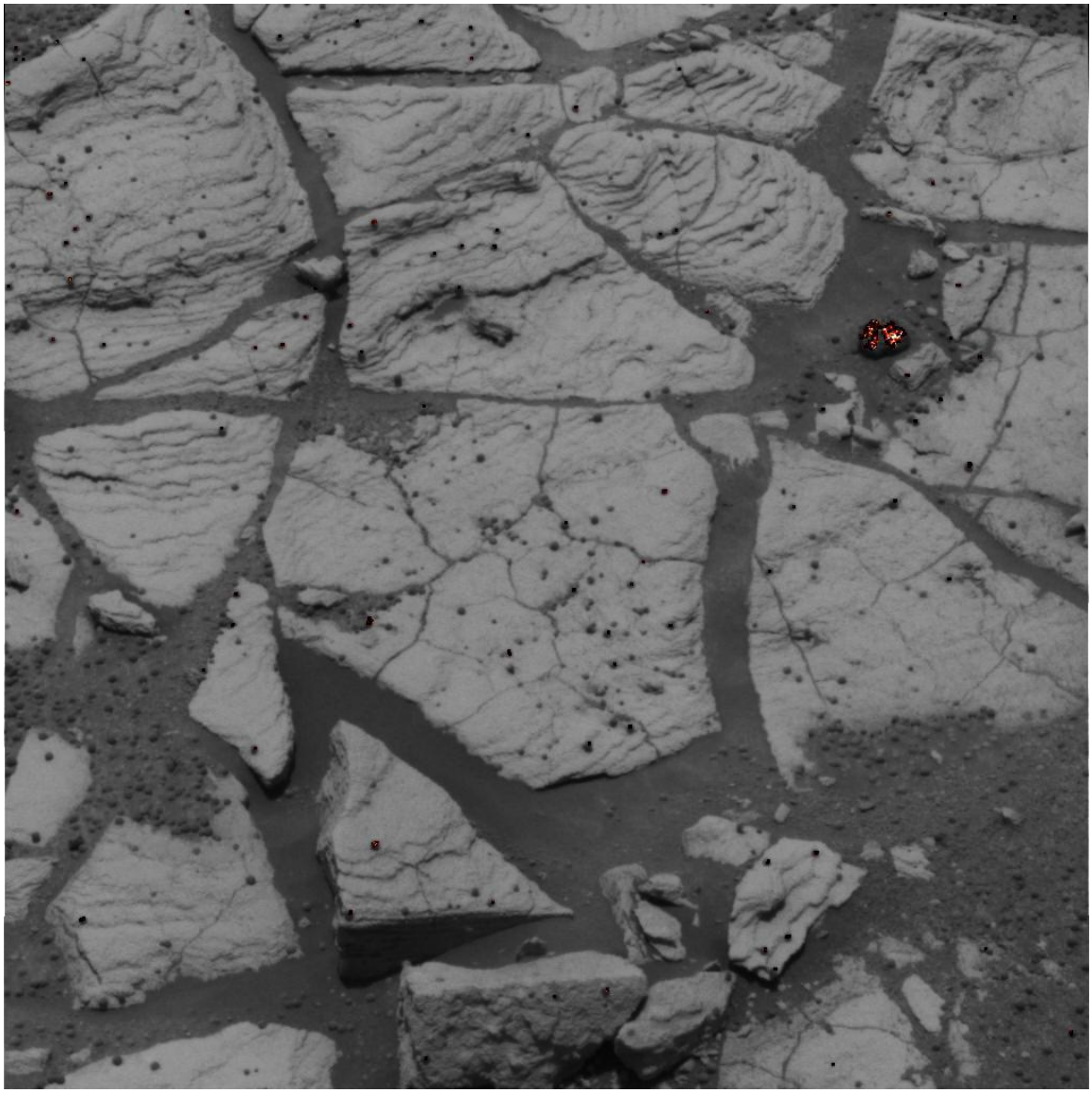

Figure 5.7: Example of a heat map highlighting surfaces with spectral parameters consistent with metallic iron. This image is a MER-B observation from sol 50 (P2574); grayscale values are from the R3 filter observation and represent values below threshold. The cobble towards the upper right is a candidate iron meteorite.

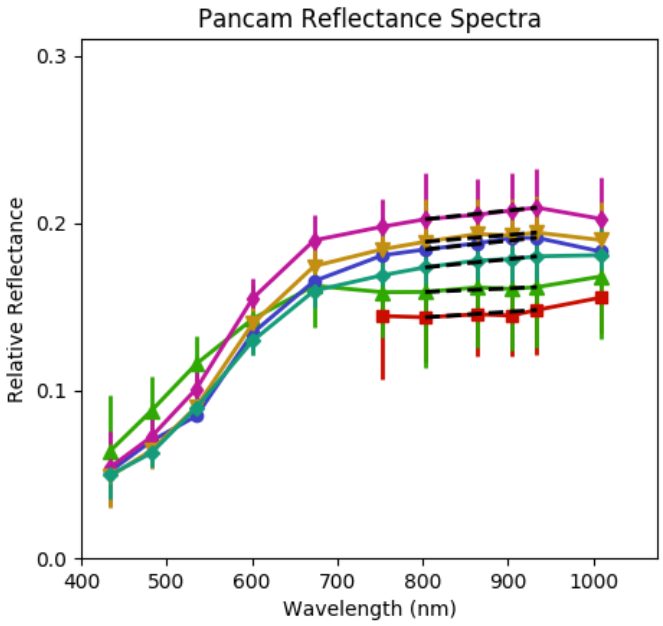

Figure 5.8: Pancam reflectance spectra of MER-B meteorites; shown are (top to bottom): Shelter Island, Mackinac Island, Block Island, Oileán Ruaidh, Heat Shield Rock, and an unnamed rock from sol 50 of the mission (saturated at shorter wavelengths, hence only the long wavelength data is shown).

Table 5.5: Iron meteorite clusters encountered by MER-B, grouped by proximity

Sol(s)	Number	Science Instruments	Pancam Filters	Target Name(s)
50	1	Pancam	L2-7, R1-7 (13F)	
339-352	1	Pancam, Mini-TES, APXS, Mössbauer	L2-7, R1-7 (13F)	Heat Shield Rock
1946-2003	1	Pancam, APXS, Mössbauer	L2-7, R1-7 (13F)	Block Island
2022-2037	2	Pancam, APXS, Mössbauer	L2-7, R1-7 (13F)	Shelter Island, Mackinac Island
2369-2371	2	Pancam	L2-7, R1-7 (13F)	Oileán Ruaidh, Ireland

Table 5.6: MER-B Pancam multi-filter observations of candidate meteorites

Sol	Sequence	Filters	LTST	Incidence	Emission	Phase
50	P2574	L2-7, R1-7 (13F)	11:34	7.5	53.4	51.8
339	P2581	L2-7, R1-7 (13F)	12:31	19.5	71.4	82.8
346	P2591	L2-7, R1-7 (13F)	12:28	18.0	50.4	58.1

352	P2596	L2-7, R1-7 (13F)	13:39	29.1	17.9	42.3
1946	P2532	L2-7, R1-7 (13F)	10:09	32.8	86.2	99.9
1961	P2390	L2-7, R1-7 (13F)	13:33	28.0	24.9	45.9
1961	P2537	L2-7, R1-7 (13F)	11:49	16.4	54.4	69.3
1975	P2549	L2-7, R1-7 (13F)	12:12	13.9	37.7	51.6
1997	P2552	L2-7, R1-7 (13F)	12:27	11.3	60.1	70.1
1998	P2553	L2-7, R1-7 (13F)	10:57	17.8	66.6	53.0
2000	P2554	L2-7, R1-7 (13F)	12:25	10.4	74.0	72.4
2001	P2555	L2-7, R1-7 (13F)	12:10	8.5	70.7	62.3
2001	P2556	L2-7, R1-7 (13F)	13:23	22.2	63.7	41.5
2002	P2557	L2-7, R1-7 (13F)	11:29	11.0	60.3	71.2
2003	P2558	L2-7, R1-7 (13F)	12:42	13.0	60.1	59.8
2022	P2561	L2-7, R1-7 (13F)	10:31	22.4	79.1	59.6
2024	P2420	L2-7, R1-7 (13F)	12:53	13.6	50.2	63.5
2024	P2563	L2-7, R1-7 (13F)	11:13	12.0	60.8	51.7
2029	P2423	L2-7, R1-7 (13F)	12:05	2.4	18.4	20.2
2031	P2565	L2-7, R1-7 (13F)	13:46	26.5	18.4	44.8
2032	P2568	L2-7, R1-7 (13F)	12:03	1.5	51.9	52.7
2033	P2424	L2-7, R1-7 (13F)	11:15	11.3	38.8	50.1
2034	P2570	L2-7, R1-7 (13F)	12:52	13.0	31.0	18.2
2037	P2571	L2-7, R1-7 (13F)	11:21	9.7	61.4	58.4
2369	P2537	L2-7, R1-7 (13F)	12:03	13.2	65.0	77.0
2371	P2539	L2-7, R1-7 (13F)	13:02	20.2	25.5	41.3

5.5 Statistics

Meteorite finds are amenable to statistical investigation because individual falls approximate independent, random events. Meteorite flux can be expected to vary only mildly over lower latitudes, on the basis of terrestrial measurements (Halliday and Griffin, 1982), and since engineering constraints have directed rover missions to date to within ±30° of the equator, landing sites investigated on Mars should receive similar amounts of meteoritic infall. Counts of iron meteorites can be combined with estimates of the area sampled by multispectral imaging footprints to derive the abundance of iron meteorites on the surface at different landing sites. For this estimate, we assume a flat horizontal surface and a rectangular footprint whose size depends on the instrument pointing and angular field-of-view, and, between missions, on the height of the camera above the surface. For MSL, the Mastcam instruments sit atop the RSM just beneath the ChemCam housing, at a height of 1.97 m (Bell et al. 2017). For Mastcam observations where both cameras imaged the surface with what we have deemed sufficient spectral coverage to detect an iron meteorite (as discussed in 5.3), we calculate the area from the M-34 footprint,

which is presumed to contain the M-100 as well. The Pancam instruments sit at the top of the PMA at 1.54 m above the surface (Bell et al. 2003), and since the filter set capable of discriminating metallic iron from native materials are all in one camera, we use that FOV for the area of each individual observation. The presence of significant topography, which we do not account for, can result in inaccurate area measurements; for this reason, and because at greater distances the cameras will not resolve smaller size fractions of meteorites, we limit observations used for this calculation to those with (site-parallel) instrument pointings of more than 18° below horizontal (i.e., the near-field). We also remove multispectral observations that image rover hardware, which is most commonly the calibration target, and, for MER, the on-board magnets. We also culled observations that contained significant overlap with previous multispectral observations, such as are occasionally acquired before and after a rover interacts with the surface (drilling, dropping sample portions on the ground, RAT grinding, etc.), for photometry observations, or for other purposes. Finally, since we intend to obtain an unbiased sampling of the abundance of meteorites, we exclude observations deliberately targeted at meteorites that were recognized on the basis of morphology alone within these or other imaging datasets, to avoid inflating the count with observations that are significantly more likely to contain a meteorite than other imaging of the near-field. Additionally, we exclude subsequent imaging after the detection of the first meteorite at a site, since further positive detections would be counted as pairs.

MSL observations that fit the criteria outlined above resulted in a total area of approximately 430 m^2. Within this same set of observations are 4 individual “clusters” of meteorites, where a cluster is defined as candidate meteorites that are sufficiently spatially proximate to each other that we consider them likely pairs. These are the Marias Pass cluster, the sol 1160 singleton, the 1512 observations, and the small 1610 rock. We estimate a 95% confidence interval for the mean abundance using a Wilson score interval, which gives abundance values of 0.30 per 100 m^2 to 2.5 per 100 m^2 for iron meteorites of approximately centimeter size or larger. The portion of the Spirit dataset that meets these conditions has an estimated areal coverage of 1210 m^2. For a single meteorite cluster, we estimate an abundance

of 0.0043 to 0.53 per 100 m^2. For Opportunity, the dataset covered approximately 1040 m^2 for observations with pointings below 18°. Drawing comparisons to the other datasets is complicated by the fact that Meridiani Planum, unlike Gale and Gusev, is a flat plain with relatively few large rocks and outcrop across significant portions of the traverse; many of the identified meteorites were noticeable in engineering camera images and deliberately targeted by Pancam, in violation of statistical assumptions that the camera pointing is an unbiased sampling of the surface. Only the sol 50 candidate was serendipitously imaged; taking this as our single detection yields 0.0050 to 0.62 per 100 m^2. Statistical testing using Fisher's exact test at $p<0.05$ suggests that, based on statistical uncertainty alone, the Gusev and Meridiani meteorite counts are less than the number of clustered fragments found in Gale Crater.

There are a number of possible ways to account for this result. One of the largest uncertainties in comparing counts between sites is that we use "clusters" (i.e., suspected fragments in close spatial proximity) as a proxy for pairing association, although chemical data suggests that this is by no means a reliable method of grouping related fragments. Nearly identical chemical compositions derived from Opportunity APXS measurements on Heat Shield Rock, Block Island, and Shelter Island suggest that these rocks, separated over kilometers of distance, are likely pairs (Fairén et al., 2011); similarly with a set of stony-iron fragments encountered by the rover (Schröder et al., 2010). These separation distances are on par with the size of rover traverses, hence it cannot be ruled out that any two suspected meteorites of a particular compositional class encountered by a rover may be related. The Gale Crater candidates could simply be the result of Curiosity's encounter with multiple pieces of the same parent body across a strewn field.

Interestingly, the variety of meteorites encountered by the rovers show markedly different weathering states, as evidenced by both their physical morphology and Mössbauer and visible/near-infrared spectra that distinguish the presence or absence of ferric oxide phases (Ashley et al., 2011; Fairén et al., 2011; Johnson et al., 2014). Cavernous weathering and iron oxides coatings were observed over a number of the Meridiani meteorites (Fairén et al., 2011; Fleischer et al., 2010b), suggesting a history of aqueous alteration. Whether these differences are

due more to the age of the meteorite and the timeline of its interaction with long-term change in the martian climate, or site-to-site differences in weathering rates and/or burial and exhumation history, is unclear. Many of the Gale Crater fragments are comparatively small in size, preventing any preservation of larger-scale morphology, but display relatively little evidence for ferric oxide formation.

Finally, different abundances of meteorites between sites may be indicative of glacial processes that are known to concentrate meteorites in certain Antarctic ice fields on Earth (Cassidy et al., 1992). Ice at equatorial latitudes would be possible only under a different obliquity state; however, large swings in Mars' obliquity are strongly indicated by modeling results. One small Gale Crater meteorite was found at the base of Ireson Hill, in the company of an unrelated cluster of float rocks capping and surrounding the base of the topographic feature. Curiosity may be traversing by chance an area of locally high meteorite abundance created by the movement of ice.

5.6 Summary

Iron meteorites are not rare finds on the surface of Mars, in the sense that they have been imaged along every major rover traverse to date. Strong candidates can be identified in rover multispectral imaging data based on spectral properties that, while not unique, are not common among native martian materials. A carefully parameterized search through Mastcam and Pancam datasets reveals potential iron meteorites in addition to those already reported by other authors, and can be used, with caveats, to produce an approximation of the abundance of these exogenous materials. Statistical testing provides some weak evidence that Curiosity has encountered a higher proportion of iron meteorites relative to other landing sites, although unknown pairing relationships are a major source of uncertainty in drawing such comparisons. Meteorites have the potential to provide some information on the environment they have experienced during their residence on the planet, although the limited data from rovers represents a challenge to such investigations.

CHAPTER 6

POSTSCRIPT

The future of Mars exploration is uncertain. Much focus has been placed on Mars Sample Return, cited as high priority in the National Research Council's Planetary Science Decadal Survey (2011) and MEPAG (Mars Exploration Program Analysis Group) reports (Carter et al., 2015; Hamilton et al., 2015). Sample return has a significant "Hail Mary" aspect to it, unfortunately, especially with respect to its stated astrobiology goals. Given that the Mars Exploration Program has managed to establish a semi-regular cadence of orbital and ground missions to the Red Planet, it makes sense to consider ways to leverage past observations to not only drive the scientific aims of future missions, but also to improve operational aspects to enhance science return. Deciphering the geologic history of Mars is demonstrably not a single mission effort; and the large investments NASA and other space agencies make into the development and operation of spacecraft and rovers only highlights the importance of better informed and better executed landing site selection and mission operations.

The individual chapters contained herein argue for their own scientific applications and future use; however, the datasets utilized in this dissertation are all remote sensing imagery with the potential to suggest more highly targeted follow-on observations. This is touched on a bit in Chapter 2 for the MARCI dataset. Mars changes every sol, sometimes in only minor ways, but sometimes dramatically. Long-lived orbiters observe the planet over numerous annual cycles, which, as Chapter 2 shows, are accompanied by waxing and waning of surface dust reservoirs. Major storms may reveal previously buried surface regions uncharacterized by orbital spectral instruments. Calibrated MARCI observations, coupled with an understanding of how albedo relates to spectral contrast, could identify such regions in a way that, when matched with previous geomorphic observations, may suggest that a promising science target has been cleaned of dust. Such an opportunity may degrade quickly following the next decline from an atmospheric opacity high as new dust settles on the surface.

For Mastcam, an instrument whose reconnaissance abilities often exceed its compositional interpretability, time is even more critical. Acquiring science measurements to

understand the formation history and post-depositional environment of the stratigraphic units within the crater is strongly limited by operational resources and the cadence of science opportunities and rover drives. Understanding how a new multispectral observation fits into the previously acquired dataset provides a framework to interpret changes between units or within alteration zones. Descriptive studies and classification efforts such as Chapters 3-4 are products of efforts to understand the spectral variability along the traverse on a more-or-less tactical timeline, parlayed into manuscript form. The ability to respond quickly to surprises in the Mastcam dataset is particularly relevant to Chapter 5; meteorite candidates without chemical data lack both any confirmation of their physical character and any hope of unraveling pairing uncertainty.

Unfortunately, these use cases often fit poorly into the framework of mission operations, mission data sharing, and scientific incentive structure. Regardless, the MEPAG NEX-SAG report (Carter et al., 2015) does identify a wide-angle, km-scale imager as well as both short-wave and thermal IR instruments as appropriate to addressing the goals laid out for the next Mars orbiter. The Mars 2020 rover will include the Mastcam-Z instrument (Bell et al., 2016); as suggested by the name, it is extremely similar in function and design to the MSL Mastcam instrument,but with paired zooming capabilities to enhance stereo and multispectral coverage. With regards to rover multi-filter imaging data, some work is being carried out by, for example, Kerner et al. (2018) to enhance automated processing of multi-band data through machine learning methods; those efforts can leverage more “manual” dataset investigations to aid in assessing model performance of novelty detection. Ultimately, recognizing and responding to opportunities falls to the respective science teams of present and future missions to the Red Planet.

REFERENCES

Adams, J.B., 1975. Interpretation of visible and near-infrared diffuse reflectance spectra of pyroxenes and other rock-forming minerals, in: Karr, C.J. (Ed.), Infrared and Raman Spectroscopy of Lunar and Terrestrial Minerals. Academic Press, New York.

Adams, J.B., 1974. Visible and near-infrared diffuse reflectance spectra of pyroxenes as applied to remote sensing of solid objects in the solar system. J. Geophys. Res. 79, 4829–4836. doi:10.1029/JB079i032p04829

Al-Kathiri, A., Hofmann, B.A., Jull, A.J.T., Gnos, E., 2005. Weathering of meteorites from Oman: Correlation of chemical and mineralogical weathering proxies with 14 C terrestrial ages and the influence of soil chemistry. Meteorit. Planet. Sci. 40, 1215–1239. doi:10.1111/j.1945-5100.2005.tb00185.x

Alley, R.E., 1996. Algorithm theoretical basis document for decorrelation stretch.

Anderson, R.B., Bell III, J.F., 2010. Geologic mapping and characterization of Gale Crater and implications for its potential as a Mars Science Laboratory landing site. Mars J. 5, 76–128. doi:10.1555/mars.2010.0004

Anderson, R.C., Beegle, L.W., Abbey, W., 2015a. Drilling on Mars: What we have learned from the Mars Science Laboratory Powder Acquisition Drill System (PADS). Lunar Planet. Sci. Conf. 46, 2417.

Anderson, R.C., Beegle, L.W., Hurowitz, J., Hanson, C., Abbey, W., Seybold, C., Liminodi, D., Kuhn, S., Jandura, L., Brown, K., Peters, G., Roumeliotis, C., Robinson, M., Edgett, K., Minitti, M., Grotzinger, J., 2015b. The Mars Science Laboratory scooping campaign at Rocknest. Icarus 256, 66–77. doi:10.1016/j.icarus.2015.03.033

Anderson, R.C., Jandura, L., Okon, a. B., Sunshine, D., Roumeliotis, C., Beegle, L.W., Hurowitz, J., Kennedy, B., Limonadi, D., McCloskey, S., Robinson, M., Seybold, C., Brown, K., 2012. Collecting samples in Gale crater, Mars; An overview of the Mars Science Laboratory sample acquisition, sample processing and handling system. Space Sci. Rev. 170, 57–75. doi:10.1007/s11214-012-9898-9

Antoniadi, E.M., 1930. The planet Mars, 1975 trans. ed. Keith Reid Limited.

Antoniadi, E.M., 1916. On the question of objective change on the surface of Mars. Mon. Not. R. Astron. Soc. 76, 413–414. doi:10.1093/mnras/76.5.413

Arvidson, R.E., Gooding, J.L., Moore, H.J., 1989. The Martian surface as imaged, sampled, and analyzed by the Viking landers. Rev. Geophys. 27, 39. doi:10.1029/RG027i001p00039

Arvidson, R.E., Squyres, S.W., Anderson, R.C., Bell III, J.F., Blaney, D., Brückner, J., Cabrol, N.A., Calvin, W.M., Carr, M.H., Christensen, P.R., Clark, B.C., Crumpler, L., Des Marais, D.J., de Souza, J.A., D'Uston, C., Economou, T., Farmer, J., Farrand, W.H., Folkner, W., Golombek, M.P., Gorevan, S., Grant, J.A., Greeley, R., Grotzinger, J., Guinness, E., Hahn, B.C., Haskin, L., Herkenhoff, K.E., Hurowitz, J.A., Hviid, S., Johnson, J.R., Klingelhöfer, G., Knoll, A.H., Landis, G., Leff, C., Lemmon, M., Li, R., Madsen, M.B., Malin, M.C., McLennan, S.M., McSween, H.Y., Ming, D.W., Moersch, J., Morris, R. V., Parker, T., Rice, J.W., Richter, L., Rieder, R., Rodionov, D.S., Schröder, C., Sims, M., Smith, M., Smith, P., Soderblom, L.A., Sullivan, R., Thompson, S.D., Tosca, N.J., Wang, A., Wänke, H., Ward, J., Wdowiak, T., Wolff, M., Yen, A., 2006. Overview of the Spirit Mars Exploration Rover

mission to Gusev Crater: Landing site to Backstay Rock in the Columbia Hills. J. Geophys. Res. E Planets. doi:10.1029/2005JE002499

Arvidson, R.E., Squyres, S.W., Morris, R. V., Knoll, A.H., Gellert, R., Clark, B.C., Catalano, J.G., Jolliff, B.L., McLennan, S.M., Herkenhoff, K.E., VanBommel, S., Mittlefehldt, D.W., Grotzinger, J.P., Guinness, E.A., Johnson, J.R., Bell III, J.F., Farrand, W.H., Stein, N., Fox, V.K., Golombek, M.P., Hinkle, M.A.G., Calvin, W.M., de Souza, P.A., 2016. High concentrations of manganese and sulfur in deposits on Murray Ridge, Endeavour Crater, Mars. Am. Mineral. 101, 1389–1405. doi:10.2138/am-2016-5599

Ashley, J.W., Golombek, M.P., Christensen, P.R., Squyres, S.W., McCoy, T.J., Schröder, C., Fleischer, I., Johnson, J.R., Herkenhoff, K.E., Parker, T.J., 2011. Evidence for mechanical and chemical alteration of iron-nickel meteorites on Mars: Process insights for Meridiani Planum. J. Geophys. Res. 116, E00F20. doi:10.1029/2010JE003672

Ashley, J.W., Herkenhoff, K.E., 2017. Meteorite weathering on Mars - Updates on exogenic iron survivability biases and micro-mapping of Meridiani Planum Block Island mosaics. Lunar Planet. Sci. Conf. 48, 2656.

Banham, S.G., Gupta, S., Rubin, D.M., Watkins, J.A., Sumner, D.Y., Edgett, K.S., Grotzinger, J.P., Lewis, K.W., Edgar, L.A., Stack-Morgan, K.M., Barnes, R., Bell III, J.F., Day, M.D., Ewing, R.C., Lapotre, M.G.A., Stein, N.T., Rivera-Hernandez, F., Vasavada, A.R., 2018. Ancient Martian aeolian processes and palaeomorphology reconstructed from the Stimson formation on the lower slope of Aeolis Mons, Gale crater, Mars. Sedimentology 65, 993–1042. doi:10.1111/sed.12469

Batson, R.M., Bridges, P.M., Inge, J.L., 1979. Atlas of Mars: The 1:5,000,000 map series. National Aeronautics and Space Administration, Washington, D.C.

Baum, W.A., 1974. Earth-based observations of Martian albedo changes. Icarus 22, 363–370. doi:10.1016/0019-1035(74)90183-3

Bell III, J.F., 2008. The Martian surface: Composition, mineralogy, and physical properties. Cambridge University Press.

Bell III, J.F., 2003. Mars Exploration Rover Athena Panoramic Camera (Pancam) investigation. J. Geophys. Res. 108. doi:10.1029/2003JE002070

Bell III, J.F., 1996. Iron, sulfate, carbonate, and hydrated minerals on Mars. Geochemical Soc. Special Pu.

Bell III, J.F., Godber, A., McNair, S., Caplinger, M.A., Maki, J.N., Lemmon, M.T., Van Beek, J., Malin, M.C., Wellington, D., Kinch, K.M., Madsen, M.B., Hardgrove, C., Ravine, M.A., Jensen, E., Harker, D., Anderson, R.B., Herkenhoff, K.E., Morris, R. V., Cisneros, E., Deen, R.G., 2017. The Mars Science Laboratory Curiosity rover Mastcam instruments: Preflight and in-flight calibration, validation, and data archiving. Earth Sp. Sci. 4, 396–452. doi:10.1002/2016EA000219

Bell III, J.F., Godber, A., Rice, M.S., Fraeman, A.A., Ehlmann, B.L., Goetz, W., Hardgrove, C., Harker, D., Johnson, J.R., Kinch, K.M., Lemmon, M.T., McNair, S., Le Mouelic, S., Madsen, M.B., Malin, M.C., 2013. Initial multispectral imaging results from the Mars Science Laboratory Mastcam investigation at the Gale Crater field site. Lunar Planet. Sci. XXXIV 1417. doi:10.1029/2005JE002544.

Bell III, J.F., Joseph, J., Sohl-Dickstein, J.N., Arneson, H.M., Johnson, M.J., Lemmon, M.T., Savransky, D., 2006. In-flight calibration and performance of the Mars Exploration Rover Panoramic Camera (Pancam) instruments. J. Geophys. Res. E Planets 111, 1–38. doi:10.1029/2005JE002444

Bell III, J.F., Maki, J.N., Mehall, G.L., Ravine, M.A., Caplinger, M.A., 2014. Mastcam-Z: A geologic, stereoscopic, and multispectral investigation on the NASA Mars-2020 rover.

Bell III, J.F., Maki, J.N., Mehall, G.L., Ravine, M.A., Caplinger, M.A., Team, M.-Z., 2016. Mastcam-Z: Designing a geologic, stereoscopic, and multispectral pair of zoom cameras for the NASA Mars 2020 rover. 3rd Int. Work. Instrum. Planet. Mission. 4126, 4126.

Bell III, J.F., Malin, M.C., Caplinger, M.A., Ravine, M.A., Godber, A.S., Jungers, M.C., Rice, M.S., Anderson, R.B., 2012. Mastcam multispectral imaging on the Mars Science Laboratory rover: Wavelength coverage and imaging strategies at the Gale Crater field site. Lunar Planet. Sci. Conf. 43, 2541.

Bell III, J.F., McSween, H.Y., Crisp, J.A., Morris, R. V., Murchie, S.L., Bridges, N.T., Johnson, J.R., Britt, D.T., Golombek, M.P., Moore, H.J., Ghosh, A., Bishop, J.L., Anderson, R.C., Brückner, J., Economou, T., Greenwood, J.P., Gunnlaugsson, H.P., Hargraves, R.M., Hviid, S., Knudsen, J.M., Madsen, M.B., Reid, R., Rieder, R., Soderblom, L., 2000. Mineralogic and compositional properties of Martian soil and dust: Results from Mars Pathfinder. J. Geophys. Res. Planets 105, 1721–1755. doi:10.1029/1999JE001060

Bell III, J.F., Rice, M.S., Johnson, J.R., Hare, T.M., 2008. Surface albedo observations at Gusev Crater and Meridiani Planum, Mars. J. Geophys. Res. 113, E06S18. doi:10.1029/2007JE002976

Bell III, J.F., Squyres, S.W., Arvidson, R.E., Arneson, H.M., Bass, D., Blaney, D., Cabrol, N., Calvin, W., Farmer, J., Farrand, W.H., Goetz, W., Golombek, M., Grant, J. a, Greeley, R., Guinness, E., Hayes, a G., Hubbard, M.Y.H., Herkenhoff, K.E., Johnson, M.J., Johnson, J.R., Joseph, J., Kinch, K.M., Lemmon, M.T., Li, R., Madsen, M.B., Maki, J.N., Malin, M., McCartney, E., McLennan, S., McSween, H.Y., Ming, D.W., Moersch, J.E., Morris, R. V, Dobrea, E.Z.N., Parker, T.J., Proton, J., Rice, J.W., Seelos, F., Soderblom, J., Soderblom, L. a, Sohl-Dickstein, J.N., Sullivan, R.J., Wolff, M.J., Wang, a, 2004a. Pancam multispectral imaging results from the Spirit Rover at Gusev Crater. Science 305, 800–806. doi:10.1126/science.1100175

Bell III, J.F., Squyres, S.W., Arvidson, R.E., Arneson, H.M., Bass, D., Calvin, W., Farrand, W.H., Goetz, W., Golombek, M., Greeley, R., Grotzinger, J., Guinness, E., Hayes, a G., Hubbard, M.Y.H., Herkenhoff, K.E., Johnson, M.J., Johnson, J.R., Joseph, J., Kinch, K.M., Lemmon, M.T., Li, R., Madsen, M.B., Maki, J.N., Malin, M., McCartney, E., McLennan, S., McSween, H.Y., Ming, D.W., Morris, R. V, Dobrea, E.Z.N., Parker, T.J., Proton, J., Rice, J.W., Seelos, F., Soderblom, J.M., Soderblom, L. a, Sohl-Dickstein, J.N., Sullivan, R.J., Weitz, C.M., Wolff, M.J., 2004b. Pancam multispectral imaging results from the Opportunity Rover at Meridiani Planum. Science 306, 1703–1709. doi:10.1126/science.1105245

Bell III, J.F., Squyres, S.W., Herkenhoff, K.E., Maki, J.N., Arneson, H.M., Brown, D., Collins, S.A., Dingizian, A., Elliot, S.T., Hagerott, E.C., Hayes, A.G., Johnson, M.J., Johnson, J.R., Joseph, J., Kinch, K., Lemmon, M.T., Morris, R. V., Scherr, L., Schwochert, M., Shepard, M.K., Smith, G.H., Sohl-Dickstein, J.N., Sullivan, R.J., Sullivan, W.T., Wadsworth, M., 2003. Mars Exploration Rover Athena Panoramic Camera (Pancam) investigation. J. Geophys. Res. Planets 108. doi:10.1029/2003JE002070

Bell III, J.F., Wolff, M.J., Daley, T.C., Crisp, D., James, P.B., Lee, S.W., Trauger, J.T., Evans, R.W., 1999. Near-Infrared Imaging of Mars from HST: Surface Reflectance, Photometric Properties, and Implications for MOLA Data. Icarus 138, 25–35. doi:10.1006/icar.1998.6057

Bell III, J.F., Wolff, M.J., Malin, M.C., Calvin, W.M., Cantor, B.A., Caplinger, M.A., Clancy, R.T., Edgett, K.S., Edwards, L.J., Fahle, J., Ghaemi, F., Haberle, R.M., Hale, A., James, P.B., Lee, S.W., McConnochie, T., Noe Dobrea, E., Ravine, M.A., Schaeffer, D., Supulver, K.D., Thomas, P.C., 2009. Mars Reconnaissance Orbiter Mars Color Imager (MARCI): Instrument description, calibration, and performance. J. Geophys. Res. 114, E08S92. doi:10.1029/2008JE003315

Bell, P.M., Mao, H.K., 1973. Optical and chemical analysis of iron in Luna 20 plagioclase. Geochim. Cosmochim. Acta 37, 755–759. doi:10.1016/0016-7037(73)90172-5

Bell, P.M., Mao, H.K., Rossman, G.R., 1975. Absorption spectroscopy of ionic and molecular units in crystals and glasses, in: Infrared and Raman Spectroscopy of Lunar and Terrestrial Minerals. Academic Press, p. 375.

Bibring, J.-P., Langevin, Y., Mustard, J.F., Poulet, F., Arvidson, R.E., Gendrin, A., Gondet, B., Mangold, N., Pinet, P., Forget, F., Berthé, M., Gomez, C., Jouglet, D., Soufflot, A., Vincendon, M., Combes, M., Drossart, P., Encrenaz, T., Fouchet, T., Merchiorri, R., Belluci, G., Altieri, F., Formisano, V., Capaccioni, F., Cerroni, P., Coradini, A., Fonti, S., Korablev, O., Kottsov, V., Ignatiev, N., Moroz, V., Titov, D., Zasova, L., Loiseau, D., Pinet, P., Douté, S., Schmitt, B., Sotin, C., Hauber, E., Hoffmann, H., Jaumann, R., Keller, U., Duxbury, T., Forget, F., Neukum, G., 2006. Global mineralogical and aqueous Mars history derived from OMEGA/Mars Express data. Science 312, 400–4. doi:10.1126/science.1122659

Bish, D.L., Blake, D.F., Vaniman, D.T., Chipera, S.J., Morris, R. V., Ming, D.W., Treiman, A.H., Sarrazin, P., Morrison, S.M., Downs, R.T., Achilles, C.N., Yen, A.S., Bristow, T.F., Crisp, J.A., Morookian, J.M., Farmer, J.D., Rampe, E.B., Stolper, E.M., Spanovich, N., 2013. X-ray diffraction results from mars science laboratory: Mineralogy of rocknest at Gale crater. Science (80-.). 341. doi:10.1126/science.1238932

Bishop, J.L., Lane, M.D., Dyar, M.D., Brown, a. J., 2008. Reflectance and emission spectroscopy study of four groups of phyllosilicates: smectites, kaolinite-serpentines, chlorites and micas. Clay Miner. 43, 35–54. doi:10.1180/claymin.2008.043.1.03

Bishop, J.L., Parente, M., Weitz, C.M., Noe Dobrea, E.Z., Roach, L.H., Murchie, S.L., McGuire, P.C., McKeown, N.K., Rossi, C.M., Brown, A.J., Calvin, W.M., Milliken, R., Mustard, J.F., 2009. Mineralogy of Juventae Chasma: Sulfates in the light-toned mounds, mafic minerals in the bedrock, and hydrated silica and hydroxylated ferric sulfate on the plateau. J. Geophys. Res. E Planets 114. doi:10.1029/2009JE003352

Blake, D., Vaniman, D., Achilles, C.N., Anderson, R.C., Bish, D., Bristow, T., Chen, C., Chipera, S., Crisp, J., Des Marais, D., Downs, R.T., Farmer, J., Feldman, S., Fonda, M., Gailhanou, M., Ma, H., Ming, D.W., Morris, R. V., Sarrazin, P., Stolper, E., Treiman, A., Yen, A., 2012. Characterization and calibration of the CheMin mineralogical instrument on Mars Science Laboratory. Space Sci. Rev. 170, 341–399. doi:10.1007/s11214-012-9905-1

Blake, D.F., Morris, R. V, Kocurek, G., Morrison, S.M., Downs, R.T., Bish, D., Ming, D.W., Edgett, K.S., Rubin, D., Goetz, W., Madsen, M.B., Sullivan, R., Gellert, R., Campbell, I., Treiman, a H., McLennan, S.M., Yen, a S., Grotzinger, J., Vaniman, D.T., Chipera, S.J., Achilles, C.N., Rampe, E.B., Sumner, D., Meslin, P.-Y., Maurice, S., Forni, O., Gasnault, O., Fisk, M., Schmidt, M., Mahaffy, P., Leshin, L. a, Glavin, D., Steele, a, Freissinet, C., Navarro-

González, R., Yingst, R. a, Kah, L.C., Bridges, N., Lewis, K.W., Bristow, T.F., Farmer, J.D., Crisp, J. a, Stolper, E.M., Des Marais, D.J., Sarrazin, P., 2013. Curiosity at Gale crater, Mars: characterization and analysis of the Rocknest sand shadow. Science 341, 1239505. doi:10.1126/science.1239505

Bland, P.A., Bevan, A.W.R., Jull, A.J.T., 2000. Ancient meteorite finds and the Earth's surface environment. Quat. Res. 53, 131–142. doi:10.1006/QRES.1999.2106

Bland, P.A., Cintala, M.J., Hörz, F., Cressey, G., 2001. Survivability of meteorite projectiles -- Results from impact experiments. 32nd Annu. Lunar Planet. Sci. Conf. March 12-16, 2001, Houston, Texas, Abstr. no.1764 32.

Bland, P.A., Conway, A., Smith, T.B., Berry, F.J., Swabey, S.E.J., Pillinger, C.T., 1998a. Calculating flux from meteorite decay rates: a discussion of problems encountered in deciphering a 10^5–10^6 year integrated meteorite flux at Allan Hills and a new approach to pairing. Geol. Soc. London, Spec. Publ. 140, 43–58. doi:10.1144/GSL.SP.1998.140.01.06

Bland, P.A., Sexton, A.S., Jull, A.J.T., Bevan, A.W.R., Berry, F.J., Thornley, D.M., Astin, T.R., Britt, D.T., Pillinger, C.T., 1998b. Climate and rock weathering: a study of terrestrial age dated ordinary chondritic meteorites from hot desert regions. Geochim. Cosmochim. Acta 62, 3169–3184. doi:10.1016/S0016-7037(98)00199-9

Bland, P.A., Smith, T.B., 2000. Meteorite accumulations on Mars. Icarus 144, 21–26. doi:10.1006/icar.1999.6253

Bland, P.A., Smith, T.B., Jull, A.J.T., Berry, F.J., Bevan, A.W.R., Cloudt, S., Pillinger, C.T., 1996. The flux of meteorites to the Earth over the last 50 000 years. Mon. Not. R. Astron. Soc. 283, 551–565. doi:10.1093/mnras/283.2.551

Blaney, D.L., Archer, D., Arvidson, R.E., Cull, S., Ellehøj, M., Fisher, D., Hecht, M., Lemmon, M., Mellon, M., Morris, R. V, Pike, T., Smith, P., Stoker, C., Team, P.S., 2009. Multi-spectral imaging of the Phoenix landing site: Characteristics of surface and subsurface ice, rocks, and soils, in: 40th Lunar and Planetary Science Conference, (Lunar and Planetary Science XL). p. 2047.

Burns, R.G., 1993a. Mineralogical applications of crystal field theory. Cambridge University Press.

Burns, R.G., 1993b. Rates and mechanisms of chemical weathering of ferromagnesian silicate minerals on Mars. Geochim. Cosmochim. Acta 57, 4555–4574. doi:10.1016/0016-7037(93)90182-V

Calvin, W.M., Cantor, B.A., James, P.B., 2017. Interannual and seasonal changes in the south seasonal polar cap of Mars: Observations from MY 28-31 using MARCI. Icarus 292, 144–153. doi:10.1016/j.icarus.2017.01.010

Calvin, W.M., James, P.B., Cantor, B.A., Dixon, E.M., 2015. Interannual and seasonal changes in the north polar ice deposits of Mars: Observations from MY 29-31 using MARCI. Icarus 251, 181–190. doi:10.1016/j.icarus.2014.08.026

Cantor, B.A., James, P.B., Caplinger, M., Wolff, M.J., 2001. Martian dust storms: 1999 Mars Orbiter Camera observations. J. Geophys. Res. Planets 106, 23653–23687. doi:10.1029/2000JE001310

Cantor, B.A., Malin, M.C., Edgett, K.S., 2014. Martian dust storms – observations by MGS-MOC and MRO, in: Eighth International Conference on Mars; LPI Contribution No. 1791.

Capen, C.F., 1976. Martian albedo feature variations with season : Data of 1971 and 1973. Icarus 28, 213–230.

Carter, L., Ehlmann, B., Jpl, C.&, Whitley, R., Wray, J., Tech, G., Heomd, E.-O., Bussey, B., Headquarters, N., Smd, M./, Meyer, M., 2015. MEPAG report from the Next Orbiter Science Analysis Group (NEX-SAG) NEX-SAG Membership.

Cassidy, W., Harvey, R., Schutt, J., Delisle, G., Yanai, K., 1992. The meteorite collection sites of Antarctica. Meteoritics 27, 490–525. doi:10.1111/j.1945-5100.1992.tb01073.x

Cavanagh, P.D., Bish, D.L., Blake, D.F., Vaniman, D.T., Morris, R. V., Ming, D.W., Rampe, E.B., Achilles, C.N., Chipera, S.J., Treiman, A.H., Downs, R.T., Morrison, S.M., Fendrich, K. V., Yen, A.S., Grotzinger, J., Crisp, J.A., Bristow, T.F., Sarrazin, P.C., Farmer, J.D., Des Marais, D.J., Stolper, E.M., Morookian, J.M., Wilson, M.A., Spanovich, N., Anderson, R.C., 2015. Confidence Hills mineralogy and CheMin results from base of Mt. Sharp, Pahrump Hills, Gale Crater, Mars. Lunar Planet. Sci. Conf. 46, 2735.

Chaikin, A.L., Maxwell, T.A., El-Baz, F., 1981. Temporal changes in the Cerberus region of Mars: Mariner 9 and Viking comparisons. Icarus 45, 167–178. doi:10.1016/0019-1035(81)90012-9

Chappelow, J.E., Sharpton, V.L., 2006. Atmospheric variations and meteorite production on Mars. Icarus 184, 424–435. doi:10.1016/j.icarus.2006.05.013

Chappelow, J.E., Sharpton, V.L., 2005. Influences of atmospheric variations on Mars's record of small craters. Icarus 178, 40–55. doi:10.1016/j.icarus.2005.03.010

Chemtob, S.M., Nickerson, R.D., Morris, R. V., Agresti, D.G., Catalano, J.G., 2015. Synthesis and structural characterization of ferrous trioctahedral smectites: Implications for clay mineral genesis and detectability on Mars. J. Geophys. Res. E Planets 120, 1119–1140. doi:10.1002/2014JE004763

Christensen, P.R., 1988. Global albedo variations on Mars: Implications for active aeolian transport, deposition, and erosion. J. Geophys. Res. 93, 7611. doi:10.1029/JB093iB07p07611

Christensen, P.R., Engle, E., Anwar, S., Dickenshied, S., Noss, D., Gorelick, N., Weiss-Malik, M., 2009. JMARS - A Planetary GIS. Am. Geophys. Union, Fall Meet. 2009, Abstr. #IN22A-06.

Christensen, P.R., Wyatt, M.B., Glotch, T.D., Rogers, A.D., Anwar, S., Arvidson, R.E., Bandfield, J.L., Blaney, D.L., Budney, C., Calvin, W.M., Fallacaro, A., Fergason, R.L., Gorelick, N., Graff, T.G., Hamilton, V.E., Hayes, A.G., Johnson, J.R., Knudson, A.T., McSween, H.Y., Mehall, G.L., Mehall, L.K., Moersch, J.E., Morris, R. V., Smith, M.D., Squyres, S.W., Ruff, S.W., Wolff, M.J., 2004. Mineralogy at Meridiani Planum from the Mini-TES experiment on the opportunity rover. Science (80-.). 306, 1733–1739. doi:10.1126/science.1104909

Clancy, R.T., Sandor, B.J., Wolff, M.J., Christensen, P.R., Smith, M.D., Pearl, J.C., Conrath, B.J., Wilson, R.J., 2000. An intercomparison of ground-based millimeter, MGS TES, and Viking atmospheric temperature measurements: Seasonal and interannual variability of temperatures and dust loading in the global Mars atmosphere. J. Geophys. Res. Planets 105, 9553–9571. doi:10.1029/1999JE001089

Clark, R.N., Swayze, G.A., Wise, R.A., Livo, K.E., Hoefen, T.M., Kokaly, R.F., Sutley, S.J., 2007. USGS Digital Spectral Library splib06a.

Cloutis, E.A., Hawthorne, F.C., Mertzman, S.A., Krenn, K., Craig, M.A., Marcino, D., Methot, M., Strong, J., Mustard, J.F., Blaney, D.L., Bell III, J.F., Vilas, F., 2006. Detection and discrimination of sulfate minerals using reflectance spectroscopy. Icarus 184, 121–157. doi:10.1016/j.icarus.2006.04.003

Coates, A.J., Jaumann, R., Schmitz, N., Leff, C.E., Josset, J.-L., Griffiths, A.D., Paar, G., Hancock, B., Barnes, D.P., Tyler, L., Gunn, M., Bauer, A., Cousins, C.R., Trauthan, F., Michaelis, H., Mosebach, H., Gutruf, S., Koncz, A., Pforte, B., Kachlicki, J., Terzer, R., 2015. PanCam on the ExoMars 2018 rover: A stereo, multispectral and high-resolution camera system to investigate the surface of Mars. Lunar Planet. Sci. Conf. 46, 1812.

Council, N.R., 2011. Vision and Voyages for Planetary Science in the Decade 2013-2022.

Cousin, A., Sautter, V., Payré, V., Forni, O., Mangold, N., Gasnault, O., Le Deit, L., Johnson, J., Maurice, S., Salvatore, M., Wiens, R.C., Gasda, P., Rapin, W., 2017. Classification of igneous rocks analyzed by ChemCam at Gale crater, Mars. Icarus 288, 265–283. doi:10.1016/J.ICARUS.2017.01.014

Daubar, I.J., McEwen, A.S., Byrne, S., Kennedy, M.R., Ivanov, B., 2013. The current martian cratering rate. Icarus 225, 506–516. doi:10.1016/j.icarus.2013.04.009

de Mottoni Y Palacios, G., 1975. The appearance of Mars from 1907 to 1971: Graphic synthesis of photographs from the I.A.U. center at Meudon. Icarus 25, 296–332. doi:10.1016/0019-1035(75)90025-1

Deit, L. Le, Mangold, N., Forni, O., Blaney, D., Cousin, A., Dromart, G., Fabre, C., Fisk, M., Gasnault, O., Lanza, N., Lasue, J., Mouélic, S. Le, Maurice, S., Nachon, M., Rapin, W., Rice, M., Sautter, V., Schröder, S., Sumner, D., Wiens, R.C., 2015. The potassic sedimentary rocks in Gale Crater, Mars as seen by ChemCam onboard Curiosity. LPSC Conf. Proc. 10–12.

Dollfus, A., 1961. Visual and photographic studies of planets at the Pic du Midi, in: Kuiper, G.P., Middlehurst, B.M. (Eds.), Planets and Satellites. The University of Chicago Press, pp. 534–571.

Drake, N.A., 1995. Reflectance spectra of evaporite minerals (400-2500 nm): Applications for remote sensing. Int. J. Remote Sens. 16, 2555–2571. doi:10.1080/01431169508954576

Dycus, R.D., 1969. The meteorite flux at the surface of Mars. Publ. Astron. Soc. Pacific. doi:10.2307/40674750

Ebisawa, S., 1960. (Map of Mars). Contr. Kwasan Obs. Kyoto 89.

Edwards, C.S., Christensen, P.R., Hill, J., 2011. Mosaicking of global planetary image datasets: 2. Modeling of wind streak thicknesses observed in Thermal Emission Imaging System (THEMIS) daytime and nighttime infrared data. J. Geophys. Res. 116, E10005. doi:10.1029/2011JE003857

Fairén, A.G., Dohm, J.M., Baker, V.R., Thompson, S.D., Mahaney, W.C., Herkenhoff, K.E., Rodríguez, J.A.P., Davila, A.F., Schulze-Makuch, D., El Maarry, M.R., Uceda, E.R., Amils, R., Miyamoto, H., Kim, K.J., Anderson, R.C., McKay, C.P., 2011. Meteorites at Meridiani

Planum provide evidence for significant amounts of surface and near-surface water on early Mars. Meteorit. Planet. Sci. 46, 1832–1841. doi:10.1111/j.1945-5100.2011.01297.x

Farrand, W.H., Bell III, J.F., Johnson, J.R., Arvidson, R.E., Crumpler, L.S., Hurowitz, J.A., Schröder, C., 2008. Rock spectral classes observed by the Spirit Rover's Pancam on the Gusev Crater Plains and in the Columbia Hills. J. Geophys. Res. E Planets 113. doi:10.1029/2008JE003237

Farrand, W.H., Bell III, J.F., Johnson, J.R., Jolliff, B.L., Knoll, A.H., McLennan, S.M., Squyres, S.W., Calvin, W.M., Grotzinger, J.P., Morris, R. V., Soderblom, J., Thompson, S.D., Watters, W.A., Yen, A.S., 2007. Visible and near-infrared multispectral analysis of rocks at Meridiani Planum, Mars, by the Mars Exploration Rover Opportunity. J. Geophys. Res. E Planets 112. doi:10.1029/2006JE002773

Farrand, W.H., Glotch, T.D., Rice, J.W., Hurowitz, J.A., Swayze, G.A., 2009. Discovery of jarosite within the Mawrth Vallis region of Mars: Implications for the geologic history of the region. Icarus 204, 478–488. doi:10.1016/j.icarus.2009.07.014

Farrand, W.H., Johnson, J.R., Rice, M.S., Wang, A., Bell III, J.F., 2016. VNIR multispectral observations of aqueous alteration materials by the Pancams on the Spirit and Opportunity Mars Exploration Rovers. Am. Mineral. 101, 2005–2019. doi:10.2138/am-2016-5627

Fenton, L.K., Toigo, A.D., Richardson, M.I., 2005. Aeolian processes in Proctor Crater on Mars: Mesoscale modeling of dune-forming winds. J. Geophys. Res. 110, E06005. doi:10.1029/2004JE002309

Flammarion, C., 1892. Camille Flammarion's The Planet Mars, 2015 trans. ed.

Fleischer, I., Brückner, J., Schröder, C., Farrand, W., Tréguier, E., Morris, R.V., Klingelhöfer, G., Herkenhoff, K., Mittlefehldt, D., Ashley, J.W., Golombek, M., Johnson, J.R., Jolliff, B., Squyres, S.W., Weitz, C., Gellert, R., de Souza, P.A., Cohen, B.A., 2010a. Mineralogy and chemistry of cobbles at Meridiani Planum, Mars, investigated by the Mars Exploration Rover Opportunity. J. Geophys. Res. 115, E00F05. doi:10.1029/2010JE003621

Fleischer, I., Klingelhöfer, G., Schröder, C., Mittlefehldt, D.W., Morris, R. V., Golombek, M., Ashley, J.W., 2010b. In situ investigation of iron meteorites at Meridiani Planum, Mars. Lunar Planet. Sci. Conf. 41, 1791.

Focas, J.H., 1962. Seasonal evolution of the fine structure of the dark areas of Mars. Planet. Space Sci. 9, 371–381. doi:10.1016/0032-0633(62)90079-X

Fraeman, a. a., Arvidson, R.E., Catalano, J.G., Grotzinger, J.P., Morris, R. V., Murchie, S.L., Stack, K.M., Humm, D.C., McGovern, J. a., Seelos, F.P., Seelos, K.D., Viviano, C.E., 2013. A hematite-bearing layer in gale crater, mars: Mapping and implications for past aqueous conditions. Geology 41, 1103–1106. doi:10.1130/G34613.1

Fraeman, A.A., Edwards, C.S., Ehlmann, B.L., Arvidson, R.E., Johnson, J.R., Rice, M., 2015. Exploring Curiosity's future path from orbit: The view of lower Mt. Sharp from integrated CRISM, HiRISE, and THEMIS datasets.

Freundel, M., Schultz, L., Reedy, R.C., 1986. Terrestrial 81Kr-Kr ages of Antarctic meteorites. Geochim. Cosmochim. Acta 50, 2663–2673. doi:10.1016/0016-7037(86)90217-6

Gaffey, M.J., 1976. Spectral reflectance characteristics of the meteorite classes. J. Geophys.

Res. 81, 905–920. doi:10.1029/JB081i005p00905

Geissler, P.E., 2005. Three decades of Martian surface changes. J. Geophys. Res. 110, E02001. doi:10.1029/2004JE002345

Geissler, P.E., Fenton, L.K., Enga, M., Mukherjee, P., 2016. Orbital monitoring of martian surface changes. Icarus 278, 279–300. doi:10.1016/j.icarus.2016.05.023

Gellert, R., Campbell, J.L., King, P.L., Leshin, L.A., Lugmair, G.W., Spray, J.G., Squyres, S.W., Yen, A.S., 2009. The Alpha-Particle-X-Ray-Spectrometer(APXS) for the Mars Science Laboratory (MSL) rover mission. Lunar Planet. Sci. Conf. 40, 2364.

Goetz, W., Leer, K., Gunnlaugsson, H.P., Bartlett, P., Basso, B., Bell III, J.F., Bertelsen, P., Binau, C.S., Chu, P.C., Gorevan, S., Hansen, M.F., Hviid, S.F., Kinch, K.M., Klingelhöfer, G., Kusack, A., Madsen, M.B., Ming, D.W., Morris, R. V., Mumm, E., Myrick, T., Olsen, M., Squyres, S.W., Wilson, J., Yen, A., 2008. Search for magnetic minerals in Martian rocks: Overview of the Rock Abrasion Tool (RAT) magnet investigation on Spirit and Opportunity. J. Geophys. Res. E Planets 113. doi:10.1029/2006JE002819

Grotzinger, J.P., Crisp, J., Vasavada, A.R., Anderson, R.C., Baker, C.J., Barry, R., Blake, D.F., Conrad, P., Edgett, K.S., Ferdowski, B., Gellert, R., Gilbert, J.B., Golombek, M., Gómez-Elvira, J., Hassler, D.M., Jandura, L., Litvak, M., Mahaffy, P., Maki, J., Meyer, M., Malin, M.C., Mitrofanov, I., Simmonds, J.J., Vaniman, D., Welch, R. V., Wiens, R.C., 2012. Mars Science Laboratory mission and science investigation, Space Science Reviews. doi:10.1007/s11214-012-9892-2

Grotzinger, J.P., Gupta, S., Malin, M.C., Rubin, D.M., Schieber, J., Siebach, K., Sumner, D.Y., Stack, K.M., Vasavada, A.R., Arvidson, R.E., Calef, F., Edgar, L., Fischer, W.F., Grant, J.A., Griffes, J., Kah, L.C., Lamb, M.P., Lewis, K.W., Mangold, N., Minitti, M.E., Palucis, M., Rice, M., Williams, R.M.E., Yingst, R.A., Blake, D., Blaney, D., Conrad, P., Crisp, J., Dietrich, W.E., Dromart, G., Edgett, K.S., Ewing, R.C., Gellert, R., Hurowitz, J.A., Kocurek, G., Mahaffy, P., McBride, M.J., McLennan, S.M., Mischna, M., Ming, D., Milliken, R., Newsom, H., Oehler, D., Parker, T.J., Vaniman, D., Wiens, R.C., Wilson, S.A., 2015. Deposition, exhumation, and paleoclimate of an ancient lake deposit, Gale crater, Mars. Science (80-.). 350. doi:10.1126/science.aac7575

Grotzinger, J.P., Sumner, D.Y., Kah, L.C., Stack, K., Gupta, S., Edgar, L., Rubin, D., Lewis, K., Schieber, J., Mangold, N., Milliken, R., Conrad, P.G., DesMarais, D., Farmer, J., Siebach, K., Calef, F., Hurowitz, J., McLennan, S.M., Ming, D., Vaniman, D., Crisp, J., Vasavada, A., Edgett, K.S., Malin, M.C., Blake, D., Gellert, R., Mahaffy, P., Wiens, R.C., Maurice, S., Grant, J.A., Wilson, S., Anderson, R.C., Beegle, L.W., Arvidson, R.E., Hallet, B., Sletten, R.S., Rice, M., Bell III, J.F., Griffes, J., Ehlmann, B., Anderson, R.B., Bristow, T.F., Dietrich, W.E., Dromart, G., Eigenbrode, J., Fraeman, A., Hardgrove, C., Herkenhoff, K., Jandura, L., Kocurek, G., Lee, S., Leshin, L.A., Leveille, R., Limonadi, D., Maki, J., McCloskey, S., Meyer, M., Minitti, M., Newsom, H., Oehler, D., Okon, A., Palucis, M., Parker, T., Rowland, S., Schmidt, M., Squyres, S., Steele, A., Stolper, E., Summons, R., Treiman, A., Williams, R., Yingst, A., 2014. A habitable fluvio-lacustrine environment at Yellowknife Bay, Gale crater, Mars. Science (80-.). 343. doi:10.1126/science.1242777

Haberle, R.M., 1986. Interannual Variability of Global Dust Storms on Mars. Science (80-.). doi:10.2307/1697342

Halliday, I., Griffin, A.A., 1982. A study of the relative rates of meteorite falls on the Earth's surface. Meteoritics 17, 31–46. doi:10.1111/j.1945-5100.1982.tb00025.x

Hamilton, V.E., Hoehler, T., Eigenbrode, J., 2015. Mars science goals, objectives, investigations, and priorities: 2015 version Mars Exploration Program Analysis Group (MEPAG) 74.

Hapke, B., 1993. Theory of reflectance and emittance spectroscopy. Cambridge University Press.

Hardgrove, C., Johnson, J., Rice, M., Bell III, J.F., Kinch, K., Wellington, D., Arvidson, R., Godber, A., 2015. Detecting high manganese phases in Curiosity Mastcam multispectral images and Chemcam passive visible to near infrared spectra. Lunar Planet. Sci. Conf. 46, 2748.

Hartmann, W.K., Daubar, I.J., Popova, O., Joseph, E.C.S., 2018. Martian cratering 12. Utilizing primary crater clusters to study crater populations and meteoroid properties. Meteorit. Planet. Sci. 53, 672–686. doi:10.1111/maps.13042

He, X.D., Torrance, K.E., Sillion, F.X., Greenberg, D.P., 1991. A comprehensive physical model for light reflection. ACM SIGGRAPH Comput. Graph. 25, 175–186. doi:10.1145/127719.122738

Hollingsworth, J.L., Haberle, R.M., Barnes, J.R., Bridger, A.F.C., Pollack, J.B., Lee, H., Schaeffer, J., 1996. Orographic control of storm zones on Mars. Nature 380, 413–416. doi:10.1038/380413a0

Hollingsworth, J.L., Haberle, R.M., Schaeffer, J., 1997. Seasonal variations of storm zones on Mars. Adv. Sp. Res. 19, 1237–1240. doi:10.1016/S0273-1177(97)00275-5

Hunt, G.R., 1977. Spectral signatures of particulate minerals in the visible and near infrared. Geophysics. doi:10.1190/1.1440721

Hunt, G.R., Ashley, R.P., 1979. Spectra of altered rocks in the visible and near infrared. Econ. Geol. 74, 1613–1629. doi:10.2113/gsecongeo.74.7.1613

Hunt, G.R., Salisbury, J.W., Lenhoff, C.J., 1974. Visible and near infrared spectra of minerals and rocks: IX. Basic and ultrabasic igneous rocks. Mod. Geol. vol. 5, p. 15-22 (1974). 5, 15–22.

Hurowitz, J.A., McLennan, S.M., 2007. A ~ 3.5 Ga record of water-limited, acidic weathering conditions on Mars. Earth Planet. Sci. Lett. 260, 432–443. doi:10.1016/J.EPSL.2007.05.043

Jakobsen, S.J., Kinch, K.M., Madsen, M.B., Bell III, J.F., Wellington, D., Godber, A., 2016. An excess signal in the tail of the PSF observed in the Pancam R7 filter on board the Mars Exploration Rovers: Characterisation and correction. Lunar Planet. Sci. Conf. 47, 2631.

James, P.B., Bell III, J.F., Clancy, R.T., Lee, S.W., Martin, L.J., Wolff, M.J., 1996. Global imaging of Mars by Hubble space telescope during the 1995 opposition. J. Geophys. Res. Planets 101, 18883–18890. doi:10.1029/96JE01605

Johnson, J.R., Bell III, J.F., Bender, S., Blaney, D., Cloutis, E., DeFlores, L., Ehlmann, B., Gasnault, O., Gondet, B., Kinch, K., Lemmon, M., Le Mouélic, S., Maurice, S., Rice, M., Wiens, R.C., 2015. ChemCam passive reflectance spectroscopy of surface materials at the Curiosity landing site, Mars. Icarus 249, 74–92. doi:10.1016/j.icarus.2014.02.028

Johnson, J.R., Bell III, J.F., Bender, S., Blaney, D., Cloutis, E., Ehlmann, B., Fraeman, A., Gasnault, O., Kinch, K., Le Mouelic, S., Maurice, S., Rampe, E., Vaniman, D., Wiens, R.C., 2016. Constraints on iron sulfate and iron oxide mineralogy from ChemCam visible/near-infrared reflectance spectroscopy of Mt. Sharp basal units, Gale Crater, Mars. Am. Mineral. 101, 1501–1514. doi:10.2138/am-2016-5553

Johnson, J.R., Bell III, J.F., Cloutis, E., Staid, M., Farrand, W.H., McCoy, T., Rice, M., Wang, A., Yen, A., 2007. Mineralogic constraints on sulfur-rich soils from Pancam spectra at Gusev crater, Mars. Geophys. Res. Lett. 34. doi:10.1029/2007GL029894

Johnson, J.R., Bell III, J.F., Gasnault, O., Le Mouelic, S., Rapin, W., Bridges, J., Wellington, D.F., 2014. First iron meteorites observed by the Mars Science Laboratory (MSL) rover Curiosity. AGU Fall Meet. Abstr. P51E.

Johnson, J.R., Bell III, J.F., Hayes, A., Liang, W., Lemmon, M.T., Grundy, W.M., Deen, R.G., 2017. Modeling of Mastcam visible/near-infrared spectrophotometric observations at Yellowknife Bay. AGU Fall Meet. Abstr. 2017, P31A–2794.

Johnson, J.R., Bell III, J.F., Lemmon, M.L., 2018. Overview of recent Mastcam and MAHLI visible/near-infrared spectrophotometric observations: Big Sky to Vera Rubin Ridge. Lunar Planet. Sci. Conf. 1354.

Johnson, J.R., Christensen, P.R., Lucey, P.G., 2002. Dust coatings on basaltic rocks and implications for thermal infrared spectroscopy of Mars. J. Geophys. Res. 107, 5035. doi:10.1029/2000JE001405

Johnson, J.R., Grundy, W.M., 2001a. Visible/near-infrared spectra and two-layer modeling of palagonite-coated basalts. Geophys. Res. Lett. 28, 2101–2104. doi:10.1029/2000GL012669

Johnson, J.R., Grundy, W.M., 2001b. Visible/near-infrared spectra and two-layer modeling of palagonite-coated basalts. Geophys. Res. Lett. 28, 2101–2104. doi:10.1029/2000GL012669

Johnson, J.R., Grundy, W.M., Lemmon, M.T., Bell III, J.F., Johnson, M.J., Deen, R., Arvidson, R.E., Farrand, W.H., Guinness, E., Hayes, A.G., Herkenhoff, K.E., Seelos, F., Soderblom, J., Squyres, S., 2006a. Spectrophotometric properties of materials observed by Pancam on the Mars Exploration Rovers: 2. Opportunity. J. Geophys. Res. Planets 111, n/a-n/a. doi:10.1029/2006JE002762

Johnson, J.R., Sohl-Dickstein, J., Grundy, W.M., Arvidson, R.E., Bell III, J.F., Christensen, P.R., Graff, T., Guinness, E. a., Kinch, K., Morris, R., Shepard, M.K., 2006b. Radiative transfer modeling of dust-coated Pancam calibration target materials: Laboratory visible/near-infrared spectrogoniometry. J. Geophys. Res. E Planets 111, 1–22. doi:10.1029/2005JE002658

Jolliff, B.L., Korotev, R.L., Haskin, L.A., 1993. An iridium-rich iron micrometeorite with silicate inclusions from the Moon. Lunar Planet. Inst., Twenty-Fourth Lunar Planet. Sci. Conf. Part 2 G-M p 729-730 (SEE N94-16173 03-91) 24.

Jull, A.J.T., 2001. Terrestrial Ages of Meteorites, in: Accretion of Extraterrestrial Matter Throughout Earth's History. Springer US, Boston, MA, pp. 241–266. doi:10.1007/978-1-4419-8694-8_14

Jull, A.J.T., Donahue, D.J., Cielaszyk, E., Wlotzka, F., 1993. Carbon-14 terrestrial ages and weathering of 27 meteorites from the southern high plains and adjacent areas (USA). Meteoritics 28, 188–195. doi:10.1111/j.1945-5100.1993.tb00756.x

Kahn, R.A., Martin, T.Z., Zurek, R.W., Lee, S.W., 1992. The martian dust cycle, in: Kieffer, H.H., Jakosky, B.M., Snyder, C.W., Matthews, M.S. (Eds.), Mars. The University of Arizona Press, Tucson, pp. 1017–1053.

Kahre, M.A., Murphy, J., Chanover, N., Africano, J., Roberts, L., Kervin, P., 2005a. Observing the martian surface albedo pattern: Comparing the AEOS and TES data sets. Icarus 179, 55–62. doi:10.1016/j.icarus.2005.06.011

Kahre, M.A., Murphy, J.R., Haberle, R.M., Montmessin, F., Schaeffer, J., 2005b. Simulating the Martian dust cycle with a finite surface dust reservoir. Geophys. Res. Lett. 32, L20204. doi:10.1029/2005GL023495

Kerner, H.R., Wellington, D.F., Wagstaff, K.L., Bell III, J.F., Amor, H.B., 2018. Novelty detection for multispectral images with application to planetary exploration, submitted, in: Neural and Information Processing Systems (NIPS).

Kerschmann, R.L., 2017. What Questions Should We Ask About The Health Effects Of Mars Dust? Lessons From The Lunar Dust Experience, in: Dust in the Atmosphere of Mars, LPI Contrib. No. 1966. p. 6034.

Kieffer, H.H., Christensen, P.R., Titus, T.N., 2006. CO2 jets formed by sublimation beneath translucent slab ice in Mars' seasonal south polar ice cap. Nature 442, 793–796. doi:10.1038/nature04945

Kieffer, H.H., Martin, T.Z., Peterfreund, A.R., Jakosky, B.M., Miner, E.D., Palluconi, F.D., 1977. Thermal and albedo mapping of Mars during the Viking primary mission. J. Geophys. Res. 82, 4249–4291. doi:10.1029/JS082i028p04249

Kinch, K.M., Bell III, J.F., Goetz, W., Johnson, J.R., Joseph, J., Madsen, M.B., Sohl-Dickstein, J., 2015. Dust deposition on the decks of the Mars Exploration Rovers: 10 years of dust dynamics on the Panoramic Camera calibration targets. Earth Sp. Sci. 2, 144–172. doi:10.1002/2014EA000073

Kinch, K.M., Madsen, M.B., Bell III, J.F., Johnson, J.R., Goetz, W., Team, M.S., 2013. Dust on the Curiosity Mast Camera calibration target. Lunar Planet. Sci. Conf. 44, 1061.

Kinch, K.M., Sohl-Dickstein, J., Bell III, J.F., Johnson, J.R., Goetz, W., Landis, G. a., 2007. Dust deposition on the Mars Exploration Rover Panoramic Camera (Pancam) calibration targets. J. Geophys. Res. E Planets 112, 1–21. doi:10.1029/2006JE002807

Klingelhöfer, G., Morris, R. V., Bernhardt, B., Schröder, C., Rodionov, D.S., De Souza, P.A., Yen, A., Gellert, R., Evlanov, E.N., Zubkov, B., Foh, J., Bonnes, U., Kankeleit, E., Gütlich, P., Ming, D.W., Renz, F., Wdowiak, T., Squyres, S.W., Arvidson, R.E., 2004. Jarosite and hematite at Meridiani Planum from opportunity's Mössbauer spectrometer. Science (80-.). 306, 1740–1745. doi:10.1126/science.1104653

Kodama, H., De Kimpe, I.C.R., Dejou, J., 1988. FERRIAN SAPONITE IN A GABBRO SAPROLITE AT MONT MI~GANTIC, QUEBEC. Clays Clay Miner. 36, 102–110.

Landis, G.A., Jenkins, P.P., 2000. Measurement of the settling rate of atmospheric dust on Mars by the MAE instrument on Mars Pathfinder. J. Geophys. Res. Planets 105, 1855–1857. doi:10.1029/1999JE001029

Lee, M.R., Bland, P.A., 2004. Mechanisms of weathering of meteorites recovered from hot and cold deserts and the formation of phyllosilicates. Geochim. Cosmochim. Acta 68, 893–916. doi:10.1016/S0016-7037(03)00486-1

Lee, S.W., Thomas, P.C., Cantor, B.A., 2014. Disappearance of the Propontis regional dark

albedo feature on Mars, in: Eighth International Conference on Mars; LPI Contribution No. 1791. p. 1426.

Madsen, M.B., Bertelsen, P., Goetz, W., Binau, C.S., Olsen, M., Folkmann, F., Gunnlaugsson, H.P., Kinch, K.M., Knudsen, J.M., Merrison, J., Nørnberg, P., Squyres, S.W., Yen, A.S., Rademacher, J.D., Gorevan, S., Myrick, T., Bartlett, P., 2003. Magnetic Properties Experiments on the Mars Exploration Rover mission. J. Geophys. Res. Planets 108. doi:10.1029/2002JE002029

Magalhães, J., Gierasch, P., 1982. A model of Martian slope winds: Implications for eolian transport. J. Geophys. Res. 87, 9975. doi:10.1029/JB087iB12p09975

Malin, M.C., Cantor, B.A., Britton, A.W., Wu, M.R., Kennedy, M.R., Shean, D.E., Harrison, T.N., Saper, L.M., 2007. MRO MARCI Weather Reports [WWW Document]. Malin Sp. Sci. Syst. Captioned Image Release Ser. URL http://www.msss.com/msss_images/subject/weather_reports.html

Malin, M.C., Caplinger, M. a, Edgett, K.S., Ghaemi, F.T., Ravine, M. a, Schaffner, J. a, Baker, J.M., Bardis, J.D., DiBiase, D.R., Maki, J.N., 2010. The Mars Science Laboratory (MSL) Mast-Mounted Cameras (Mastcams) flight instruments. 41st Lunar Planet. Sci. Conf. 8, 9–10.

Malin, M.C., Edgett, K.S., 2001. Mars Global Surveyor Mars Orbiter Camera: Interplanetary cruise through primary mission. J. Geophys. Res. Planets 106, 23429–23570. doi:10.1029/2000JE001455

Malin, M.C., Edgett, K.S., Jensen, E., Lipkaman, L., 2013. Mars Science Laboratory Project Software Interface Specification (SIS): Mast Camera (Mastcam), Mars Hand Lens Imager (MAHLI), and Mars Descent Imager (MARDI) Experimental Data Record (EDR) and Reduced Data Record (RDR) PDS Data Products.

Malin, M.C., Edgett, K.S., Posiolova, L. V, Mccolley, S.M., Dobrea, E.Z.N., 2006. Present-Day Impact Cratering Rate and Contemporary Gully Activity on Mars 314, 1573–1577. doi:10.1126/science.1135156

Malin, M.C., Ravine, M.A., Caplinger, M.A., Tony Ghaemi, F., Schaffner, J.A., Maki, J.N., Bell III, J.F., Cameron, J.F., Dietrich, W.E., Edgett, K.S., Edwards, L.J., Garvin, J.B., Hallet, B., Herkenhoff, K.E., Heydari, E., Kah, L.C., Lemmon, M.T., Minitti, M.E., Olson, T.S., Parker, T.J., Rowland, S.K., Schieber, J., Sletten, R., Sullivan, R.J., Sumner, D.Y., Aileen Yingst, R., Duston, B.M., McNair, S., Jensen, E.H., 2017. The Mars Science Laboratory (MSL) Mast cameras and Descent imager: Investigation and instrument descriptions. Earth Sp. Sci. 4, 506–539. doi:10.1002/2016EA000252

Malvar, H.S., Li-wei He, Cutler, R., 2004. High-quality linear interpolation for demosaicing of Bayer-patterned color images, in: 2004 IEEE International Conference on Acoustics, Speech, and Signal Processing. IEEE, p. iii-485-8. doi:10.1109/ICASSP.2004.1326587

Mangold, N., Loizeau, D., Poulet, F., Ansan, V., Baratoux, D., LeMouelic, S., Bardintzeff, J.M., Platevoet, B., Toplis, M., Pinet, P., Masson, P., Bibring, J.P., Gondet, B., Langevin, Y., Neukum, G., 2010. Mineralogy of recent volcanic plains in the Tharsis region, Mars, and implications for platy-ridged flow composition. Earth Planet. Sci. Lett. 294, 440–450. doi:10.1016/J.EPSL.2009.07.036

Mangold, N., Schmidt, M.E., Fisk, M.R., Forni, O., McLennan, S.M., Ming, D.W., Sautter, V.,

Sumner, D., Williams, A.J., Clegg, S.M., Cousin, A., Gasnault, O., Gellert, R., Grotzinger, J.P., Wiens, R.C., 2017. Classification scheme for sedimentary and igneous rocks in Gale crater, Mars. Icarus 284, 1–17. doi:10.1016/J.ICARUS.2016.11.005

Martin, L.J., James, P.B., Dollfus, A., Iwasaki, K., 1992. Telescopic observations: visual, photographic, polarimetric, in: Kieffer, H.H., Jakosky, B.M., Snyder, C.W., Matthews, M.S. (Eds.), Mars. The University of Arizona Press, Tucson, pp. 34–70.

Martin, L.J., Zurek, R.W., 1993. An analysis of the history of dust activity on Mars. J. Geophys. Res. Planets 98, 3221–3246. doi:10.1029/92JE02937

Maurice, S., Wiens, R.C., Saccoccio, M., Barraclough, B., Gasnault, O., Forni, O., Mangold, N., Baratoux, D., Bender, S., Berger, G., Bernardin, J., Berthé, M., Bridges, N., Blaney, D., Bouyé, M., Caïs, P., Clark, B., Clegg, S., Cousin, A., Cremers, D., Cros, A., Deflores, L., Derycke, C., Dingler, B., Dromart, G., Dubois, B., Dupieux, M., Durand, E., D'Uston, L., Fabre, C., Faure, B., Gaboriaud, A., Gharsa, T., Herkenhoff, K., Kan, E., Kirkland, L., Kouach, D., Lacour, J.L., Langevin, Y., Lasue, J., Le Mouélic, S., Lescure, M., Lewin, E., Limonadi, D., Manhès, G., Mauchien, P., McKay, C., Meslin, P.Y., Michel, Y., Miller, E., Newsom, H.E., Orttner, G., Paillet, A., Parès, L., Parot, Y., Pérez, R., Pinet, P., Poitrasson, F., Quertier, B., Sallé, B., Sotin, C., Sautter, V., Séran, H., Simmonds, J.J., Sirven, J.B., Stiglich, R., Striebig, N., Thocaven, J.J., Toplis, M.J., Vaniman, D., 2012. The ChemCam instrument suite on the Mars Science Laboratory (MSL) rover: Science objectives and mast unit description. Space Sci. Rev. 170, 95–166. doi:10.1007/s11214-012-9912-2

McSween, H.Y., 1976. A new type of chondritic meteorite found in Lunar soil. Earth Planet. Sci. Lett. 31, 193–199.

Melosh, H.J., 1989. Impact cratering : a geologic process. Oxford University Press.

Melosh, H.J., 1985. Ejection of rock fragments from planetary bodies. Geology 13, 144–148. doi:10.1130/0091-7613(1985)13<144:EORFFP>2.0.CO;2

Meslin, P.-Y., Johnson, J.R., Forni, O., Beck, P., Cousin, A., Bridges, J., Rapin, W., Cohen, B., Newsom, H., Sautter, V., Lewin, E., Nachon, M., Wiens, R.C., Payré, V., Gasnault, O., Maurice, S., Fairén, A.G., Schröder, S., Mangold, N., Thomas, N., 2017. Egg Rock Encounter: Analysis of an Iron-Nickel Meteorite Found in Gale Crater by Curiosity. Lunar Planet. Sci. Conf. 48, 2258.

Milliken, R.E., Grotzinger, J.P., Thomson, B.J., 2010. Paleoclimate of mars as captured by the stratigraphic record in gale crater. Geophys. Res. Lett. 37, 1–6. doi:10.1029/2009GL041870

Milliken, R.E., Swayze, G.A., Arvidson, R.E., Bishop, J.L., Clark, R.N., Ehlmann, B.L., Green, R.O., Grotzinger, J.P., Morris, R. V., Murchie, S.L., Mustard, J.F., Weitz, C., 2008. Opaline silica in young deposits on Mars. Geology 36, 847–850. doi:10.1130/G24967A.1

Morris, R. V., Agresti, D.G., Lauer, H. V., Newcomb, J.A., Shelfer, T.D., Murali, A. V., 1989. Evidence for pigmentary hematite on Mars based on optical, magnetic, and Mossbauer studies of superparamagnetic (nanocrystalline) hematite. J. Geophys. Res. Solid Earth 94, 2760–2778. doi:10.1029/JB094iB03p02760

Morris, R. V., Golden, D.C., Bell III, J.F., 1997. Low-temperature reflectivity spectra of red hematite and the color of Mars. J. Geophys. Res. 102, 9125. doi:10.1029/96JE03993

Morris, R. V., Klingelhöfer, G., Schröder, C., Rodionov, D.S., Yen, A., Ming, D.W., de Souza,

P.A., Wdowiak, T., Fleischer, I., Gellert, R., Bernhardt, B., Bonnes, U., Cohen, B.A., Evlanov, E.N., Foh, J., Gütlich, P., Kankeleit, E., McCoy, T., Mittlefehldt, D.W., Renz, F., Schmidt, M.E., Zubkov, B., Squyres, S.W., Arvidson, R.E., 2006. Mössbauer mineralogy of rock, soil, and dust at Meridiani Planum, Mars: Opportunity's journey across sulfate-rich outcrop, basaltic sand and dust, and hematite lag deposits. J. Geophys. Res. Planets 111, n/a-n/a. doi:10.1029/2006JE002791

Morris, R. V., Lauer, H. V., Lawson, C.A., Gibson, E.K., Nace, G.A., Stewart, C., 1985. Spectral and other physicochemical properties of submicron powders of hematite (α-Fe_2O_3), maghemite (γ-Fe_2O_3), magnetite (Fe_3O_4), goethite (α-FeOOH), and lepidocrocite (γ-FeOOH). J. Geophys. Res. 90, 3126. doi:10.1029/JB090iB04p03126

Morris, R. V, Golden, D.C., Bell III, J.F., Lauer, H. V, Adams, J.B., 1993. Pigmenting agents in Martian soils: inferences from spectral, Mossbauer, and magnetic properties of nanophase and other iron oxides in Hawaiian palagonitic soil PN-9. Geochim. Cosmochim. Acta 57, 4597–4609. doi:10.1016/0016-7037(93)90185-Y

Morris, R. V, Vaniman, D.T., Blake, D.F., Gellert, R., Chipera, S.J., Rampe, E.B., Ming, D.W., Morrison, S.M., Downs, R.T., Treiman, A.H., Yen, A.S., Grotzinger, J.P., Achilles, C.N., Bristow, T.F., Crisp, J.A., Des Marais, D.J., Farmer, J.D., Fendrich, K. V, Frydenvang, J., Graff, T.G., Morookian, J.-M., Stolper, E.M., Schwenzer, S.P., 2016. Silicic volcanism on Mars evidenced by tridymite in high-SiO2 sedimentary rock at Gale crater. Proc. Natl. Acad. Sci. U. S. A. 113, 7071–6. doi:10.1073/pnas.1607098113

Mulholland, D.P., Read, P.L., Lewis, S.R., 2013. Simulating the interannual variability of major dust storms on Mars using variable lifting thresholds. Icarus 223, 344–358. doi:10.1016/j.icarus.2012.12.003

Newman, C.E., Lewis, S.R., Read, P.L., Forget, F., 2002. Modeling the Martian dust cycle 2. Multiannual radiatively active dust transport simulations. J. Geophys. Res. Planets 107, 7-1-7–15. doi:10.1029/2002JE001920

Newman, C.E., Richardson, M.I., 2015. The impact of surface dust source exhaustion on the martian dust cycle, dust storms and interannual variability, as simulated by the MarsWRF General Circulation Model. Icarus 257, 47–87. doi:10.1016/j.icarus.2015.03.030

Nishiizumi, K., Caffee, M.W., 2001. Exposure Histories of Lunar Meteorites Dhofar 025, 026, and Northwest Africa 482. Meteorit. Planet. Sci. vol. 36, Suppl. p.A148 36, A148.

Nishiizumi, K., Okazaki, R., Park, J., Nagao, K., Masarik, J., Finkel, R.C., 2002. Exposure and Terrestrial Histories of Dhofar 019 Martian Meteorite. 33rd Annu. Lunar Planet. Sci. Conf. March 11-15, 2002, Houston, Texas, Abstr. no.1366 33.

Nuding, D.L., Cohen, B.A., 2009. Characterization of Rock Types at Meridiani Planum, Mars Using MER 13-Filter Pancam Spectra. Lunar Planet. Sci. Conf. 40, 2023.

Pankine, A.A., Ingersoll, A.P., 2004. Interannual variability of Mars global dust storms: an example of self-organized criticality? Icarus 170, 514–518. doi:10.1016/J.ICARUS.2004.04.006

Pollack, J.B., Greenberg, E.H., Sagan, C., 1967. A statistical analysis of the Martian wave of darkening and related phenomena. Planet. Sp. Sci 15, 817–824.

Popova, O., Nemtchinov, I., Hartmann, W.K., 2003. Bolides in the present and past martian

atmosphere and effects on cratering processes. Meteorit. Planet. Sci. 38, 905–925. doi:10.1111/j.1945-5100.2003.tb00287.x

Quaide, W., Bunch, T., Wrigley, R., 1970. Impact Metamorphism of Lunar Surface Materials. Science (80-.). doi:10.2307/1728801

Rampe, E.B., Ming, D.W., Blake, D.F., Bristow, T.F., Chipera, S.J., Grotzinger, J.P., Morris, R.V., Morrison, S.M., Vaniman, D.T., Yen, A.S., Achilles, C.N., Craig, P.I., Des Marais, D.J., Downs, R.T., Farmer, J.D., Fendrich, K.V., Gellert, R., Hazen, R.M., Kah, L.C., Morookian, J.M., Peretyazhko, T.S., Sarrazin, P., Treiman, A.H., Berger, J.A., Eigenbrode, J., Fairén, A.G., Forni, O., Gupta, S., Hurowitz, J.A., Lanza, N.L., Schmidt, M.E., Siebach, K., Sutter, B., Thompson, L.M., 2017. Mineralogy of an ancient lacustrine mudstone succession from the Murray formation, Gale crater, Mars. Earth Planet. Sci. Lett. 471, 172–185. doi:10.1016/J.EPSL.2017.04.021

Rampe, E.B., Ming, D.W., Morris, R. V., Blake, D.F., Bristow, T.F., Chipera, S.J., Vaniman, D.T., Yen, A.S., Grotzinger, J.P., Downs, R.T., Morrison, S.M., Peretyazhko, T., Achilles, C.N., Bish, D.L., Cavanagh, P.D., Craig, P.I., Crisp, J.A., Fairen, A.G., Des Marais, D.J., Farmer, J.D., Fendrich, K. V., Morookian, J.M., Treiman, A.H., 2016. Diagenesis in the Murray Formation, Gale Crater, Mars. Lunar Planet. Sci. Conf. 47, 2543.

Read, P.L., Lewis, S.R., Mulholland, D.P., 2015. The physics of Martian weather and climate: a review. Reports Prog. Phys. 78, 125901. doi:10.1088/0034-4885/78/12/125901

Rice, M.S., Bell III, J.F., Cloutis, E.A., Wang, A., Ruff, S.W., Craig, M.A., Bailey, D.T., Johnson, J.R., de Souza, P.A., Farrand, W.H., 2010. Silica-rich deposits and hydrated minerals at Gusev Crater, Mars: Vis-NIR spectral characterization and regional mapping. Icarus 205, 375–395. doi:10.1016/j.icarus.2009.03.035

Rice, M.S., Bell III, J.F., Godber, A., Wellington, D., Fraeman, A.A., Johnson, J.R., Kinch, K.M., Malin, M.C., Grotzinger, J.P., 2013a. Mastcam multispectral imaging results from the Mars Science Laboratory investigation in Yellowknife Bay. Eur. Planet. Sci. Congr. 8, EPSC2013.

Rice, M.S., Bell III, J.F., Wellington, D.F., Godber, A., Hardgrove, C.J., Ehlmann, B.L., Grotzinger, J.P., Kinch, K.M., Clegg, S.M., Fraeman, A.A., Johnson, J.R., Malin, M.C., Stack, K., Siebach, K.L., Kah, L.C., Team, M., 2013b. Hydrated Minerals at Yellowknife Bay, Gale Crater, Mars: Observations from Mastcam's Science Filters. AGU Fall Meet. Abstr. P23C.

Rice, M.S., Gupta, S., Treiman, A.H., Stack, K.M., Calef, F., Edgar, L.A., Grotzinger, J., Lanza, N., Le Deit, L., Lasue, J., Siebach, K.L., Vasavada, A., Wiens, R.C., Williams, J., 2017. Geologic overview of the Mars Science Laboratory rover mission at the Kimberley, Gale crater, Mars. J. Geophys. Res. Planets 122, 2–20. doi:10.1002/2016JE005200

Rossman, G.R., 1976. Spectroscopic and magnetic studies of ferric iron hydroxy sulfates: the series Fe(OH)SO4 nH2O and the jarosite. Am. Mineral. 61, 398–404.

Rubin, A.E., 1997. The Hadley Rille enstatite chondrite and its agglutinate-like rim: Impact melting during accretion to the Moon. Meteorit. Planet. Sci. 32, 135–141. doi:10.1111/j.1945-5100.1997.tb01248.x

Rucker, M.A., 2017. Dust storm impacts on human Mars mission equipment and operations, in: Dust in the Atmosphere of Mars, LPI Contrib. No. 1966. p. 6013.

Ruff, S.W., Christensen, P.R., 2002. Bright and dark regions on Mars: Particle size and

mineralogical characteristics based on Thermal Emission Spectrometer data. J. Geophys. Res. Planets 107, 2-1-2–22. doi:10.1029/2001JE001580

Ruff, S.W., Christensen, P.R., Glotch, T.D., Blaney, D.. L.., Moersch, J.. E.., Wyatt, M.B.., 2008. The mineralogy of Gusev crater and Meridiani Planum derived from the Miniature Thermal Emission Spectrometers on the Spirit and Opportunity rovers, in: Bell, J.F.I. (Ed.), The Martian Surface: Composition, Mineralogy, and Physical Properties. Cambridge Univ. Press, New York.

Sagan, C., Veverka, J., Fox, P., Dubisch, R., French, R., Gierasch, P., Quam, L., Lederberg, J., Levinthal, E., Tucker, R., Eross, B., Pollack, J.B., 1973. Variable features on Mars, 2, Mariner 9 global results. J. Geophys. Res. 78, 4163–4196. doi:10.1029/JB078i020p04163

Sagan, C., Veverka, J., Fox, P., Dubisch, R., Lederberg, J., Levinthal, E., Quam, L., Tucker, R., Pollack, J.B., Smith, B.A., 1972. Variable features on Mars: Preliminary Mariner 9 television results. Icarus 17, 346–372. doi:10.1016/0019-1035(72)90005-X

Salisbury, J.W., 1966. The light and dark areas of Mars. Icarus 5, 291–298. doi:10.1016/0019-1035(66)90039-X

Scherer, P., Schultz, L., Neupert, U., Knauer, M., Neumann, S., Leya, I., Michel, R., Mokos, J., Lipschutz, M.E., Metzler, K., Suter, M., Kubik, P.W., 1997. Allan Hills 88019: An Antarctic H-chondrite with a very long terrestrial age. Meteorit. Planet. Sci. 32, 769–773. doi:10.1111/j.1945-5100.1997.tb01567.x

Schröder, C., Bland, P.A., Golombek, M.P., Ashley, J.W., Warner, N.H., Grant, J.A., 2016. Amazonian chemical weathering rate derived from stony meteorite finds at Meridiani Planum on Mars. Nat. Commun. 7, 13459. doi:10.1038/ncomms13459

Schröder, C., Herkenhoff, K.E., Farrand, W.H., Chappelow, J.E., Wang, W., Nittler, L.R., Ashley, J.W., Fleischer, I., Gellert, R., Golombek, M.P., Johnson, J.R., Klingelhöfer, G., Li, R., Morris, R. V., Squyres, S.W., 2010. Properties and distribution of paired candidate stony meteorites at Meridiani Planum, Mars. J. Geophys. Res. 115, E00F09. doi:10.1029/2010JE003616

Schröder, C., Rodionov, D.S., McCoy, T.J., Jolliff, B.L., Gellert, R., Nittler, L.R., Farrand, W.H., Johnson, J.R., Ruff, S.W., Ashley, J.W., Mittlefehldt, D.W., Herkenhoff, K.E., Fleischer, I., Haldemann, A.F.C., Klingelhöfer, G., Ming, D.W., Morris, R. V., de Souza, P.A., Squyres, S.W., Weitz, C., Yen, A.S., Zipfel, J., Economou, T., 2008. Meteorites on Mars observed with the Mars Exploration Rovers. J. Geophys. Res. 113, E06S22. doi:10.1029/2007JE002990

Sherman, D.M., Burns, R.G., Burns, V.M., 1982. Spectral characteristics of the iron oxides with application to the Martian bright region mineralogy. J. Geophys. Res. 87, 10169. doi:10.1029/JB087iB12p10169

Sherman, D.M., Waite, T.D., 1985. Electronic spectra of Fe3+ oxides and oxide hydroxides in the near IR to near UV. Am. Mineral. 70, 1262–1269.

Singer, R.B., 1982. Spectral Evidence for the Mineralogy of High-Albedo Soils and Dust on Mars. J. Geophys. Res. 87168, 159–10. doi:10.1029/JB087iB12p10159

Singer, R.B., 1981. Near-infrared spectral reflectance of mineral mixtures: Systematic combinations of pyroxenes, olivine, and iron oxides. J. Geophys. Res. Solid Earth 86, 7967–

7982. doi:10.1029/JB086iB09p07967

Singer, R.B., McCord, T.B., Clark, R.N., Adams, J.B., Huguenin, R.L., 1979. Mars surface composition from reflectance spectroscopy: A summary. J. Geophys. Res. 84, 8415. doi:10.1029/JB084iB14p08415

Slipher, E.C., 1962. The Photographic Story of Mars, Sky Publishing Corp. Cambridge, MA.

Smith, M.D., 2004. Interannual variability in TES atmospheric observations of Mars during 1999–2003. Icarus 167, 148–165. doi:10.1016/j.icarus.2003.09.010

Spiga, A., Forget, F., 2009. A new model to simulate the Martian mesoscale and microscale atmospheric circulation: Validation and first results. J. Geophys. Res. 114, E02009. doi:10.1029/2008JE003242

Squyres, S.W., Arvidson, R.E., Bollen, D., Bell III, J.F., Brückner, J., Cabrol, N.A., Calvin, W.M., Carr, M.H., Christensen, P.R., Clark, B.C., Crumpler, L., Des Marais, D.J., D'Uston, C., Economou, T., Farmer, J., Farrand, W.H., Folkner, W., Gellert, R., Glotch, T.D., Golombek, M., Gorevan, S., Grant, J.A., Greeley, R., Grotzinger, J., Herkenhoff, K.E., Hviid, S., Johnson, J.R., Klingelhöfer, G., Knoll, A.H., Landis, G., Lemmon, M., Li, R., Madsen, M.B., Malin, M.C., McLennan, S.M., McSween, H.Y., Ming, D.W., Moersch, J., Morris, R. V., Parker, T., Rice, J.W., Richter, L., Rieder, R., Schröder, C., Sims, M., Smith, M., Smith, P., Soderblom, L.A., Sullivan, R., Tosca, N.J., Wänke, H., Wdowiak, T., Wolff, M., Yen, A., 2006. Overview of the Opportunity Mars Exploration Rover Mission to Meridiani Planum: Eagle Crater to Purgatory Ripple. J. Geophys. Res. Planets 111, n/a-n/a. doi:10.1029/2006JE002771

Stack, K.M., Grotzinger, J.P., Gupta, S., Kah, L.C., Lewis, K.W., McBride, M.J., Minitti, M.E., Rubin, D.M., Schieber, J., Sumner, D.Y., Thompson, L.M., Van Beek, J., Vasavada, A.R., Yingst, R.A., 2015. Sedimentology and Stratigraphy of the Pahrump Hills Outcrop, Lower Mount Sharp, Gale Crater, Mars. Lunar Planet. Sci. Conf. 46, 1994.

Stockstill-Cahill, K.R., Anderson, F.S., Hamilton, V.E., 2008. A study of low-albedo deposits within Amazonis Planitia craters: Evidence for locally derived ultramafic to mafic materials. J. Geophys. Res. 113, E07008. doi:10.1029/2007JE003036

Strausberg, M.J., Wang, H., Richardson, M.I., Ewald, S.P., Toigo, A.D., 2005. Observations of the initiation and evolution of the 2001 Mars global dust storm. J. Geophys. Res. 110, E02006. doi:10.1029/2004JE002361

Szwast, M.A., Richardson, M.I., Vasavada, A.R., 2006. Surface dust redistribution on Mars as observed by the Mars Global Surveyor and Viking orbiters. J. Geophys. Res. 111, E11008. doi:10.1029/2005JE002485

Thomas, P.., Gierasch, P., Sullivan, R., Miller, D.., Alvarez del Castillo, E., Cantor, B., Mellon, M.., 2003. Mesoscale linear streaks on Mars: environments of dust entrainment. Icarus 162, 242–258. doi:10.1016/S0019-1035(03)00028-9

Thomas, P., Veverka, J., 1979. Seasonal and secular variation of wind streaks on Mars: An analysis of Mariner 9 and Viking data. J. Geophys. Res. 84, 8131. doi:10.1029/JB084iB14p08131

Thomson, B.J., Bridges, N.T., Milliken, R., Baldridge, a., Hook, S.J., Crowley, J.K., Marion, G.M., de Souza Filho, C.R., Brown, a. J., Weitz, C.M., 2011. Constraints on the origin and

evolution of the layered mound in Gale Crater, Mars using Mars Reconnaissance Orbiter data. Icarus 214, 413–432. doi:10.1016/j.icarus.2011.05.002

Toigo, A.D., Richardson, M.I., Wilson, R.J., Wang, H., Ingersoll, A.P., 2002. A first look at dust lifting and dust storms near the south pole of Mars with a mesoscale model. J. Geophys. Res. 107, 5050. doi:10.1029/2001JE001592

Toyota, T., Kurita, K., Spiga, A., 2011. Distribution and time-variation of spire streaks at Pavonis Mons on Mars. Planet. Space Sci. 59, 672–682. doi:10.1016/J.PSS.2011.01.015

Treiman, A.H., Bish, D.L., Vaniman, D.T., Chipera, S.J., Blake, D.F., Ming, D.W., Morris, R. V., Bristow, T.F., Morrison, S.M., Baker, M.B., Rampe, E.B., Downs, R.T., Filiberto, J., Glazner, A.F., Gellert, R., Thompson, L.M., Schmidt, M.E., Le Deit, L., Wiens, R.C., McAdam, A.C., Achilles, C.N., Edgett, K.S., Farmer, J.D., Fendrich, K. V., Grotzinger, J.P., Gupta, S., Morookian, J.M., Newcombe, M.E., Rice, M.S., Spray, J.G., Stolper, E.M., Sumner, D.Y., Vasavada, A.R., Yen, A.S., 2016. Mineralogy, provenance, and diagenesis of a potassic basaltic sandstone on Mars: CheMin X-ray diffraction of the Windjana sample (Kimberley area, Gale Crater). J. Geophys. Res. Planets 121, 75–106. doi:10.1002/2015JE004932

Treiman, A.H., Morris, R. V., Agresti, D.G., Graff, T.G., Achilles, C.N., Rampe, E.B., Bristow, T.F., Blake, D.F., Vaniman, D.T., Bish, D.L., Chipera, S.J., Morrison, S.M., Downs, R.T., 2014. Ferrian saponite from the Santa Monica Mountains (California, U.S.A., Earth): Characterization as an analog for clay minerals on Mars with application to Yellowknife Bay in Gale Crater. Am. Mineral. 99, 2234–2250. doi:10.2138/am-2014-4763

Treiman, M.A.H., Bish, D., Ming, D.W., Grotzinger, J., Vaniman, D.T., Baker, M.B., Farmer, J., Chipera, S., Downs, R.T., Morris, R. V, Rampe, E., Blake, D.F., Berger, J., Cavanagh, P.D., Gellert, R., 2015. 46th Lunar and Planetary Science Conference (2015) 46th Lunar and Planetary Science Conference (2015) 9–10. doi:10.1111/maps.12363.

Vaniman, D.T., Bish, D.L., Ming, D.W., Bristow, T.F., Morris, R. V., Blake, D.F., Chipera, S.J., Morrison, S.M., Treiman, A.H., Rampe, E.B., Rice, M., Achilles, C.N., Grotzinger, J.P., McLennan, S.M., Williams, J., Bell III, J.F., Newsom, H.E., Downs, R.T., Maurice, S., Sarrazin, P., Yen, A.S., Morookian, J.M., Farmer, J.D., Stack, K., Milliken, R.E., Ehlmann, B.L., Sumner, D.Y., Berger, G., Crisp, J.A., Hurowitz, J.A., Anderson, R.B., Des Marais, D.J., Stolper, E.M., Edgett, K.S., Gupta, S., Spanovich, N., 2014. Mineralogy of a mudstone at Yellowknife Bay, Gale crater, Mars. Science (80-.). 343. doi:10.1126/science.1243480

Veverka, J., Thomas, P., Greeley, R., 1977. A study of variable features on Mars during the Viking primary mission. J. Geophys. Res. 82, 4167–4188. doi:10.1029/JS082i028p04167

Vincendon, M., Audouard, J., Altieri, F., Ody, A., 2015. Mars Express measurements of surface albedo changes over 2004-2010. Icarus 251, 145–163. doi:10.1016/j.icarus.2014.10.029

Wang, A., Bell III, J.F., Li, R., Johnson, J.R., Farrand, W.H., Cloutis, E.A., Arvidson, R.E., Crumpler, L., Squyres, S.W., McLennan, S.M., Herkenhoff, K.E., Ruff, S.W., Knudson, A.T., Chen, W., Greenberger, R., 2008. Light-toned salty soils and coexisting Si-rich species discovered by the Mars Explorafion Rover Spirit in Columbia Hills. J. Geophys. Res. E Planets 113. doi:10.1029/2008JE003126

Wang, H., Ingersoll, A.P., 2002. Martian clouds observed by Mars Global Surveyor Mars Orbiter Camera. J. Geophys. Res. 107, 5078. doi:10.1029/2001JE001815

Wang, H., Richardson, M.I., 2015. The origin, evolution, and trajectory of large dust storms on

Mars during Mars years 24–30 (1999–2011). Icarus 251, 112–127. doi:10.1016/j.icarus.2013.10.033

Weitz, C.M., Farrand, W.H., Johnson, J.R., Fleischer, I., Schröder, C., Yingst, A., Jolliff, B., Gellert, R., Bell III, J.F., Herkenhoff, K.E., Klingelhöfer, G., Cohen, B., Calvin, W., Rutherford, M., Ashley, J.W., 2010. Visible and near-infrared multispectral analysis of geochemically measured rock fragments at the Opportunity landing site in Meridiani Planum. J. Geophys. Res. 115, E00F10. doi:10.1029/2010JE003660

Wellington, D.F., Bell III, J.F., Johnson, J.R., Kinch, K.M., Rice, M.S., Godber, A., Ehlmann, B.L., Fraeman, A.A., Hardgrove, C., 2017. Visible to near-infrared MSL/Mastcam multispectral imaging: Initial results from select high-interest science targets within Gale Crater, Mars. Am. Mineral. 102, 1202–1217. doi:10.2138/am-2017-5760CCBY

Wellington, D.F., Johnson, J.R., Meslin, P.-Y., Bell III, J.F., 2018. Iron Meteorite Candidates Within Gale Crater, Mars, from MSL/Mastcam Multispectral Observations. Lunar Planet. Sci. Conf. 1832.

Welten, K.C., Alderliesten, C., Borg, K., Lindner, L., Loeken, T., Schultz, L., 1997. Lewis Cliff 86360: An Antarctic L-chondrite with a terrestrial age of 2.35 million years. Meteorit. Planet. Sci. 32, 775–780. doi:10.1111/j.1945-5100.1997.tb01568.x

Wiens, R.C., Maurice, S., Barraclough, B., Saccoccio, M., Barkley, W.C., Bell III, J.F., Bender, S., Bernardin, J., Blaney, D., Blank, J., Bouyé, M., Bridges, N., Bultman, N., Caïs, P., Clanton, R.C., Clark, B., Clegg, S., Cousin, A., Cremers, D., Cros, A., Deflores, L., Delapp, D., Dingler, R., D'Uston, C., Darby Dyar, M., Elliott, T., Enemark, D., Fabre, C., Flores, M., Forni, O., Gasnault, O., Hale, T., Hays, C., Herkenhoff, K., Kan, E., Kirkland, L., Kouach, D., Landis, D., Langevin, Y., Lanza, N., Larocca, F., Lasue, J., Latino, J., Limonadi, D., Lindensmith, C., Little, C., Mangold, N., Manhes, G., Mauchien, P., McKay, C., Miller, E., Mooney, J., Morris, R. V., Morrison, L., Nelson, T., Newsom, H., Ollila, A., Ott, M., Pares, L., Perez, R., Poitrasson, F., Provost, C., Reiter, J.W., Roberts, T., Romero, F., Sautter, V., Salazar, S., Simmonds, J.J., Stiglich, R., Storms, S., Striebig, N., Thocaven, J.J., Trujillo, T., Ulibarri, M., Vaniman, D., Warner, N., Waterbury, R., Whitaker, R., Witt, J., Wong-Swanson, B., 2012. The ChemCam instrument suite on the Mars Science Laboratory (MSL) rover: Body unit and combined system tests. Space Sci. Rev. 170, 167–227. doi:10.1007/s11214-012-9902-4

Wiens, R.C., Meslin, P.-Y., Wellington, D.F., Johnson, J.R., Fraeman, A., Gasnault, O., Maurice, S., Forni, O., Beck, P., Cohen, B.A., Newsom, H.E., Bridges, J.C., Sautter, V., Gasda, P., Lanza, N., Ollila, A., Johnstone, S.E., Fairen, A., 2017. Composition and Morphology of Iron Meteorites Found in Gale Crater, Mars. 80th Annu. Meet. Meteorit. Soc. 80, 6168.

Yen, A.S., Ming, D.W., Gellert, R., Clark, B.C., Mittlefehldt, D.W., Morris, R. V., Thompson, L.M., Berger, J., 2015. Silica Retention and Enrichment in Open-System Chemical Weathering on Mars. Lunar Planet. Sci. Conf. 46, 2380.

Yen, A.S., Ming, D.W., Vaniman, D.T., Gellert, R., Blake, D.F., Morris, R.V., Morrison, S.M., Bristow, T.F., Chipera, S.J., Edgett, K.S., Treiman, A.H., Clark, B.C., Downs, R.T., Farmer, J.D., Grotzinger, J.P., Rampe, E.B., Schmidt, M.E., Sutter, B., Thompson, L.M., 2017. Multiple stages of aqueous alteration along fractures in mudstone and sandstone strata in Gale Crater, Mars. Earth Planet. Sci. Lett. 471, 186–198. doi:10.1016/J.EPSL.2017.04.033

Zdunkowski, W., Trautmann, T., Bott, A., 2007. Radiation in the atmosphere: A course in theoretical meteorology, Radiation in the Atmosphere: A Course in Theoretical Meteorology.

doi:10.1017/CBO9780511535796

Zook, H.A., 1975. The State of Meteoritic Material on the Moon. Lunar Sci. Conf. 6, 1653–1672. doi:10.1016/S0009-2509(97)00081-X

Zurek, R.W., 1982. Martian great dust storms: An update. Icarus 50, 288–310. doi:10.1016/0019-1035(82)90127-0

Zurek, R.W., Smrekar, S.E., 2007. An overview of the Mars Reconnaissance Orbiter (MRO) science mission. J. Geophys. Res. 112, E05S01. doi:10.1029/2006JE002701

APPENDIX A

DISCRETE CHANGES OBSERVED BY THE MARCI INSTRUMENT

Feature	Quadrangle[1]	Mars Year[2]	"Before" Image ID[3]	"After" Image ID[3]	°N, °E[4]
N. Amazonis	02-Diacria	28	P12_005903_3392_MA_00N150W	P13_005956_3414_MA_00N157W	40, 204
N. Amazonis	02-Diacria	28	P13_006246_3532_MA_00N156W	P14_006470_0020_MA_00N151W	38, 201
N. Amazonis	02-Diacria	29	B12_014315_3220_MA_00N143W	B16_016016_0291_MA_00N141W	42, 212
N. Amazonis	02-Diacria	29	B12_014421_3266_MA_00N157W	B16_015911_0253_MA_00N154W	37, 197
Olympus A	02-Diacria	29	P15_006759_0129_MA_00N122W	P15_006825_0154_MA_00N124W	31, 228
Olympus A	02-Diacria	29	P15_006957_0203_MA_00N128W	P15_007023_0227_MA_00N130W	35, 224
Olympus A	02-Diacria	29	B11_013748_2961_MA_00N143W	B11_013761_2968_MA_00N138W	34, 216
Olympus A	02-Diacria	29	B11_013761_2968_MA_00N138W	B11_013827_2998_MA_00N140W	33, 214
Olympus A	02-Diacria	29	B11_013853_3011_MA_00N130W	B11_013932_3047_MA_00N127W	36, 225
Olympus A	02-Diacria	29	B11_014051_3102_MA_00N136W	B11_014117_3131_MA_00N138W	38, 216
Olympus A.	02-Diacria	29	P14_006614_0075_MA_00N123W	P14_006693_0105_MA_00N120W	31, 228
Olympus A.	02-Diacria	29	B12_014433_3271_MA_00N125W	B16_015910_0253_MA_00N127W	32, 228
Olympus A.	02-Diacria	30	G04_019800_1655_MA_00N129W	G04_019813_1660_MA_00N124W	31, 228
Olympus A.	02-Diacria	30	G10_022187_2781_MA_00N138W	G10_022253_2813_MA_00N140W	33, 214
Olympus A.	02-Diacria	30	G10_022253_2813_MA_00N140W	G11_022319_2845_MA_00N142W	33, 215
Olympus A.	02-Diacria	30	G11_022332_2851_MA_00N137W	G11_022385_2876_MA_00N144W	33, 214
Olympus A.	02-Diacria	30	G11_022398_2883_MA_00N139W	G11_022464_2914_MA_00N141W	33, 215
Olympus A.	02-Diacria	30	G16_024415_0138_MA_00N124W	G16_024481_0163_MA_00N126W	30, 229
Olympus A.	02-Diacria	30	G16_024481_0163_MA_00N126W	G16_024626_0216_MA_00N125W	33, 225
Olympus A.	02-Diacria	31	D10_031009_2784_MA_00N145W	D10_031022_2790_MA_00N140W	34, 216
Olympus A.	02-Diacria	31	D10_031233_2892_MA_00N141W	D10_031246_2898_MA_00N136W	32, 213
Olympus A.	02-Diacria	31	D11_031312_2929_MA_00N138W	D12_031747_3130_MA_00N135W	33, 214
Olympus A.	02-Diacria	31	D13_032340_3387_MA_00N124W	D13_032406_3415_MA_00N126W	31, 228
Olympus A.	02-Diacria	32	D15_033118_0096_MA_00N125W	D15_033184_0121_MA_00N127W	30, 229
Olympus A.	02-Diacria	32	F11_040002_2869_MA_00N133W	F11_040042_2888_MA_00N145W	33, 215
Olympus A.	02-Diacria	32	F11_040068_2900_MA_00N135W	F11_040121_2926_MA_00N142W	33, 214
Olympus A.	02-Diacria	32	F11_040160_2944_MA_00N127W	F11_040226_2975_MA_00N129W	33, 227
Olympus A.	02-Diacria	32	F12_040345_3030_MA_00N138W	F12_040411_3061_MA_00N139W	33, 214
Olympus A.	02-Diacria	32	F12_040569_3133_MA_00N133W	F12_040609_3151_MA_00N145W	32, 214
Olympus A.	02-Diacria	33	J10_048560_2744_MA_00N140W	J10_048626_2776_MA_00N142W	33, 215
Olympus A.	02-Diacria	33	J11_048916_2915_MA_00N139W	J11_048969_2940_MA_00N146W	33, 214
Olympus A.	02-Diacria	33	J11_049127_3014_MA_00N140W	J11_049193_3045_MA_00N142W	33, 214
Propontis	02-Diacria	28	P12_005706_3309_MA_00N172W	P12_005772_3337_MA_00N174W	37, 180
Propontis	02-Diacria	28	P12_005917_3398_MA_00N173W	P13_005983_3425_MA_00N175W	38, 182
Propontis	02-Diacria	28	P13_006207_3516_MA_00N171W	P13_006260_3537_MA_00N178W	39, 185
Propontis	02-Diacria	28	P13_006286_3548_MA_00N168W	P14_006484_0025_MA_00N174W	37, 185
Propontis	02-Diacria	29	B12_014316_3220_MA_00N170W	B12_014435_3272_MA_00N179W	38, 182
Propontis	02-Diacria	31	D06_029507_2051_MA_00N177W	D06_029639_2113_MA_00N181W	38, 177
Propontis	02-Diacria	31	D14_032632_3507_MA_00N176W	D14_032698_3533_MA_00N178W	38, 178
Propontis	02-Diacria	32	F07_038500_2135_MA_00N175W	F07_038566_2166_MA_00N176W	37, 178
Utopia	02-Diacria	30	G03_019471_1520_MA_00N147W	G03_019511_1536_MA_00N159W	61, 203
Utopia	02-Diacria	32	F03_036969_1466_MA_00N143W	F04_037193_1556_MA_00N139W	63, 210
Utopia	02-Diacria	33	F17_042481_0297_MA_00N135W	F17_042521_0311_MA_00N147W	56, 206
Acidalia	03-Arcadia	30	B17_016344_0407_MA_00N095W	B17_016410_0430_MA_00N097W	64, 254
Acidalia	03-Arcadia	30	G02_019099_1374_MA_00N071W	G02_019152_1394_MA_00N078W	62, 281
Acidalia	03-Arcadia	30	G04_019811_1659_MA_00N070W	G05_020022_1749_MA_00N070W	63, 280
Acidalia	03-Arcadia	31	D01_027605_1257_MA_00N093W	D01_027671_1281_MA_00N095W	61, 255
Acidalia	03-Arcadia	31	D02_027802_1331_MA_00N070W	D02_027947_1386_MA_00N068W	64, 284
Acidalia	03-Arcadia	32	F01_036348_1230_MA_00N108W	F02_036427_1259_MA_00N105W	61, 256
Acidalia	03-Arcadia	32	F04_037310_1604_MA_00N093W	F04_037429_1653_MA_00N102W	62, 253
Acidalia	03-Arcadia	33	J01_045275_1270_MA_00N090W	J01_045315_1285_MA_00N102W	61, 256
Alba Patera	03-Arcadia	28	P02_001774_1493_MA_00N104W	P02_001840_1520_MA_00N106W	40, 243
Alba Patera	03-Arcadia	28	P02_001840_1520_MA_00N106W	P02_001906_1546_MA_00N108W	38, 242
Alba Patera	03-Arcadia	28	P02_001906_1546_MA_00N108W	P02_001972_1573_MA_00N110W	40, 241
Alba Patera	03-Arcadia	28	P02_001985_1579_MA_00N105W	P03_002038_1600_MA_00N112W	36, 241
Alba Patera	03-Arcadia	28	P03_002051_1606_MA_00N107W	P03_002117_1633_MA_00N108W	33, 243
Alba Patera	03-Arcadia	28	P05_002895_1975_MA_00N109W	P05_003106_2073_MA_00N109W	38, 240
Alba Patera	03-Arcadia	28	P05_003106_2073_MA_00N109W	P05_003172_2104_MA_00N111W	37, 239
Alba Patera	03-Arcadia	28	P12_005585_3257_MA_00N109W	P12_005651_3286_MA_00N111W	40, 245
Alba Patera	03-Arcadia	28	P12_005651_3286_MA_00N111W	P12_005717_3314_MA_00N112W	42, 236
Alba Patera	03-Arcadia	28	P12_005717_3314_MA_00N112W	P12_005862_3375_MA_00N111W	40, 238
Alba Patera	03-Arcadia	28	P12_005862_3375_MA_00N111W	P13_005928_3403_MA_00N113W	42, 236
Alba Patera	03-Arcadia	28	P13_005928_3403_MA_00N113W	P13_005941_3408_MA_00N108W	33, 244
Alba Patera	03-Arcadia	28	P13_006007_3435_MA_00N110W	P13_006152_3494_MA_00N109W	38, 240
Alba Patera	03-Arcadia	28	P13_006231_3526_MA_00N106W	P14_006508_0034_MA_00N109W	38, 241
Alba Patera	03-Arcadia	29	P14_006508_0034_MA_00N109W	P15_006798_0144_MA_00N107W	31, 243
Alba Patera	03-Arcadia	29	P15_006798_0144_MA_00N107W	P15_006864_0169_MA_00N109W	31, 242
Alba Patera	03-Arcadia	29	P15_006864_0169_MA_00N109W	P16_007220_0298_MA_00N109W	31, 243
Alba Patera	03-Arcadia	29	P18_008090_0601_MA_00N106W	P18_008156_0623_MA_00N108W	31, 245
Alba Patera	03-Arcadia	29	B02_010358_1403_MA_00N111W	B02_010424_1428_MA_00N113W	38, 241
Alba Patera	03-Arcadia	29	B02_010437_1433_MA_00N108W	B02_010503_1459_MA_00N110W	32, 245
Alba Patera	03-Arcadia	29	B06_011927_2076_MA_00N107W	B06_011993_2107_MA_00N109W	38, 238
Alba Patera	03-Arcadia	29	B06_011993_2107_MA_00N109W	B07_012204_2208_MA_00N110W	38, 238
Alba Patera	03-Arcadia	29	B10_013562_2873_MA_00N105W	B10_013628_2905_MA_00N107W	37, 243
Alba Patera	03-Arcadia	29	B10_013628_2905_MA_00N107W	B11_013905_3035_MA_00N110W	42, 239
Alba Patera	03-Arcadia	29	B11_013905_3035_MA_00N110W	B11_013971_3065_MA_00N112W	43, 239
Alba Patera	03-Arcadia	29	B12_014182_3161_MA_00N112W	B12_014393_3254_MA_00N112W	42, 242
Alba Patera	03-Arcadia	29	B12_014406_3259_MA_00N107W	B16_015883_0243_MA_00N109W	36, 244

Alba Patera	03-Arcadia	30	B16_015949_0267_MA_00N111W	B16_016015_0290_MA_00N113W	32, 241
Alba Patera	03-Arcadia	30	B19_016951_0616_MA_00N107W	B19_017017_0639_MA_00N109W	32, 245
Alba Patera	03-Arcadia	30	B21_017650_0854_MA_00N111W	B21_017716_0877_MA_00N113W	30, 242
Alba Patera	03-Arcadia	30	G03_019430_1503_MA_00N108W	G03_019496_1530_MA_00N110W	38, 241
Alba Patera	03-Arcadia	30	G03_019496_1530_MA_00N110W	G03_019562_1556_MA_00N112W	35, 244
Alba Patera	03-Arcadia	30	G03_019575_1562_MA_00N107W	G04_019641_1589_MA_00N109W	36, 240
Alba Patera	03-Arcadia	30	G05_020340_1890_MA_00N112W	G06_020406_1919_MA_00N114W	40, 242
Alba Patera	03-Arcadia	30	G06_020564_1992_MA_00N107W	G06_020630_2022_MA_00N109W	38, 240
Alba Patera	03-Arcadia	30	G06_020630_2022_MA_00N109W	G06_020696_2053_MA_00N111W	38, 238
Alba Patera	03-Arcadia	30	G06_020696_2053_MA_00N111W	G06_020762_2084_MA_00N113W	34, 241
Alba Patera	03-Arcadia	30	G07_020828_2116_MA_00N115W	G07_020907_2153_MA_00N112W	43, 238
Alba Patera	03-Arcadia	30	G11_022397_2882_MA_00N111W	G11_022463_2913_MA_00N113W	41, 238
Alba Patera	03-Arcadia	30	G11_022595_2976_MA_00N117W	G11_022674_3013_MA_00N114W	43, 237
Alba Patera	03-Arcadia	30	G11_022674_3013_MA_00N114W	G12_022740_3043_MA_00N116W	44, 236
Alba Patera	03-Arcadia	30	G12_022819_3079_MA_00N113W	G12_022885_3110_MA_00N115W	44, 240
Alba Patera	03-Arcadia	30	G14_023663_3445_MA_00N115W	G14_023729_3472_MA_00N117W	37, 241
Alba Patera	03-Arcadia	30	G15_023953_3561_MA_00N112W	G15_024098_0018_MA_00N111W	40, 241
Alba Patera	03-Arcadia	31	G16_024467_0158_MA_00N104W	G16_024612_0211_MA_00N103W	31, 248
Alba Patera	03-Arcadia	31	G17_024678_0235_MA_00N105W	G17_024823_0288_MA_00N104W	31, 248
Alba Patera	03-Arcadia	31	G19_025667_0582_MA_00N106W	G19_025733_0604_MA_00N107W	31, 245
Alba Patera	03-Arcadia	31	D03_028252_1505_MA_00N115W	D04_028595_1646_MA_00N118W	39, 241
Alba Patera	03-Arcadia	31	D04_028608_1651_MA_00N113W	D04_028674_1679_MA_00N115W	36, 240
Alba Patera	03-Arcadia	31	D04_028753_1713_MA_00N112W	D04_028819_1741_MA_00N114W	38, 238
Alba Patera	03-Arcadia	31	D04_028911_1781_MA_00N105W	D05_028977_1810_MA_00N107W	40, 242
Alba Patera	03-Arcadia	31	D06_029399_2001_MA_00N109W	D06_029465_2031_MA_00N111W	38, 239
Alba Patera	03-Arcadia	31	D09_030823_2693_MA_00N107W	D10_031034_2796_MA_00N108W	37, 239
Alba Patera	03-Arcadia	31	D10_031100_2828_MA_00N110W	D10_031166_2859_MA_00N112W	41, 239
Alba Patera	03-Arcadia	31	D10_031245_2897_MA_00N108W	D11_031311_2929_MA_00N111W	42, 239
Alba Patera	03-Arcadia	31	D11_031311_2929_MA_00N111W	D12_031746_3130_MA_00N108W	43, 238
Alba Patera	03-Arcadia	31	D13_032458_3436_MA_00N106W	D14_032524_3463_MA_00N108W	40, 241
Alba Patera	03-Arcadia	31	D14_032656_3516_MA_00N112W	D14_032735_3548_MA_00N108W	37, 245
Alba Patera	03-Arcadia	32	D15_033091_0086_MA_00N108W	D15_033236_0140_MA_00N107W	31, 243
Alba Patera	03-Arcadia	32	D15_033236_0140_MA_00N107W	D16_033381_0194_MA_00N106W	31, 243
Alba Patera	03-Arcadia	32	D16_033447_0218_MA_00N108W	D16_033592_0271_MA_00N107W	31, 244
Alba Patera	03-Arcadia	32	D19_034805_0692_MA_00N104W	D20_034871_0714_MA_00N106W	32, 245
Alba Patera	03-Arcadia	32	D20_034937_0736_MA_00N108W	D20_035148_0808_MA_00N108W	30, 242
Alba Patera	03-Arcadia	32	F03_036849_1419_MA_00N107W	F03_036915_1445_MA_00N109W	39, 242
Alba Patera	03-Arcadia	32	F03_036915_1445_MA_00N109W	F04_037192_1555_MA_00N111W	39, 242
Alba Patera	03-Arcadia	32	F04_037271_1587_MA_00N108W	F04_037337_1615_MA_00N110W	39, 241
Alba Patera	03-Arcadia	32	F04_037469_1670_MA_00N113W	F05_037614_1732_MA_00N112W	35, 242
Alba Patera	03-Arcadia	32	F05_037614_1732_MA_00N112W	F05_037759_1795_MA_00N110W	40, 242
Alba Patera	03-Arcadia	32	F05_037759_1795_MA_00N110W	F05_037825_1824_MA_00N112W	36, 241
Alba Patera	03-Arcadia	32	F06_038181_1985_MA_00N109W	F06_038247_2015_MA_00N111W	40, 240
Alba Patera	03-Arcadia	32	F06_038247_2015_MA_00N111W	F06_038313_2046_MA_00N112W	37, 239
Alba Patera	03-Arcadia	32	F06_038313_2046_MA_00N112W	F07_038379_2077_MA_00N113W	38, 238
Alba Patera	03-Arcadia	32	F07_038379_2077_MA_00N113W	F07_038445_2108_MA_00N114W	38, 238
Alba Patera	03-Arcadia	32	F10_039777_2760_MA_00N110W	F11_039922_2830_MA_00N109W	41, 239
Alba Patera	03-Arcadia	32	F11_039922_2830_MA_00N109W	F11_039988_2862_MA_00N111W	42, 239
Alba Patera	03-Arcadia	32	F11_039988_2862_MA_00N111W	F11_040054_2894_MA_00N113W	37, 242
Alba Patera	03-Arcadia	32	F11_040133_2931_MA_00N110W	F11_040199_2962_MA_00N112W	43, 236
Alba Patera	03-Arcadia	32	F14_041267_3433_MA_00N109W	F14_041333_3460_MA_00N111W	36, 244
Alba Patera	03-Arcadia	33	F15_041768_0033_MA_00N108W	F16_041900_0083_MA_00N112W	37, 245
Alba Patera	03-Arcadia	33	F16_041913_0088_MA_00N107W	F16_041979_0113_MA_00N109W	31, 243
Alba Patera	03-Arcadia	33	F16_042124_0167_MA_00N108W	F16_042203_0196_MA_00N105W	32, 247
Alba Patera	03-Arcadia	33	F17_042335_0244_MA_00N109W	F17_042414_0273_MA_00N106W	30, 244
Alba Patera	03-Arcadia	33	F19_043192_0545_MA_00N107W	F19_043337_0595_MA_00N106W	31, 245
Alba Patera	03-Arcadia	33	F19_043337_0595_MA_00N106W	F20_043548_0667_MA_00N106W	31, 245
Alba Patera	03-Arcadia	33	F20_043548_0667_MA_00N106W	F20_043759_0738_MA_00N106W	30, 244
Alba Patera	03-Arcadia	33	F20_043759_0738_MA_00N106W	F21_043904_0788_MA_00N105W	30, 243
Alba Patera	03-Arcadia	33	J02_045724_1442_MA_00N108W	J03_045803_1473_MA_00N105W	38, 243
Alba Patera	03-Arcadia	33	J03_045803_1473_MA_00N105W	J03_045869_1499_MA_00N107W	39, 242; 34, 246
Alba Patera	03-Arcadia	33	J03_045948_1531_MA_00N104W	J03_046080_1584_MA_00N108W	37, 244
Alba Patera	03-Arcadia	33	J03_046080_1584_MA_00N108W	J03_046133_1606_MA_00N115W	38, 239
Alba Patera	03-Arcadia	33	J03_046133_1606_MA_00N115W	J04_046357_1700_MA_00N110W	40, 238
Alba Patera	03-Arcadia	33	J04_046357_1700_MA_00N110W	J04_046410_1723_MA_00N117W	38, 237
Alba Patera	03-Arcadia	33	J06_047056_2011_MA_00N114W	J06_047122_2042_MA_00N116W	39, 237
Alba Patera	03-Arcadia	33	J06_047122_2042_MA_00N116W	J06_047188_2073_MA_00N118W	38, 238
Alba Patera	03-Arcadia	33	J10_048691_2807_MA_00N116W	J10_048757_2839_MA_00N118W	41, 238
Alba Patera	03-Arcadia	33	J10_048902_2909_MA_00N117W	J11_048915_2915_MA_00N112W	40, 236
Alba Patera	03-Arcadia	33	J11_048915_2915_MA_00N112W	J11_048981_2946_MA_00N114W	44, 236
Alba Patera	03-Arcadia	33	J11_049060_2983_MA_00N111W	J11_049113_3008_MA_00N118W	43, 239
Alba Patera	03-Arcadia	33	J14_050326_3531_MA_00N113W	J15_050471_3589_MA_00N112W	39, 240
Tempe Terra	03-Arcadia	28	P11_005347_3152_MA_00N091W	P11_005479_3211_MA_00N095W	44, 259
Tempe Terra	03-Arcadia	28	P11_005479_3211_MA_00N095W	P12_005545_3240_MA_00N097W	44, 258
Tempe Terra	03-Arcadia	28	P12_005545_3240_MA_00N097W	P12_005558_3245_MA_00N092W	39, 263
Tempe Terra	03-Arcadia	28	P12_005557_3245_MA_00N064W	P12_005623_3273_MA_00N066W	34, 289
Tempe Terra	03-Arcadia	28	P12_005558_3245_MA_00N092W	P12_005611_3268_MA_00N099W	35, 261
Tempe Terra	03-Arcadia	28	P12_005611_3268_MA_00N099W	P12_005677_3297_MA_00N100W	35, 257
Tempe Terra	03-Arcadia	28	P12_005636_3279_MA_00N061W	P12_005689_3302_MA_00N068W	37, 287
Tempe Terra	03-Arcadia	28	P12_005702_3307_MA_00N063W	P12_005768_3336_MA_00N065W	36, 290
Tempe Terra	03-Arcadia	28	P12_005703_3308_MA_00N090W	P12_005756_3330_MA_00N097W	32, 261

Tempe Terra	03-Arcadia	28	P12_005768_3336_MA_00N065W	P12_005834_3363_MA_00N067W	36, 289
Tempe Terra	03-Arcadia	28	P12_005822_3358_MA_00N099W	P12_005835_3364_MA_00N094W	40, 257
Tempe Terra	03-Arcadia	28	P12_005834_3363_MA_00N067W	P12_005847_3369_MA_00N062W	38, 291
Tempe Terra	03-Arcadia	28	P12_005848_3369_MA_00N089W	P12_005901_3391_MA_00N096W	37, 257
Tempe Terra	03-Arcadia	28	P12_005901_3391_MA_00N096W	P13_005967_3419_MA_00N098W	38, 259
Tempe Terra	03-Arcadia	28	P12_005913_3396_MA_00N063W	P13_005979_3424_MA_00N065W	34, 288
Tempe Terra	03-Arcadia	28	P13_005979_3424_MA_00N065W	P13_006124_3483_MA_00N065W	35, 291
Tempe Terra	03-Arcadia	28	P13_006124_3483_MA_00N065W	P13_006190_3509_MA_00N067W	32, 288
Tempe Terra	03-Arcadia	28	P13_006190_3509_MA_00N067W	P13_006269_3541_MA_00N064W	35, 288
Tempe Terra	03-Arcadia	29	P14_006600_0069_MA_00N101W	P14_006679_0099_MA_00N098W	30, 253
Tempe Terra	03-Arcadia	29	B09_013310_2751_MA_00N065W	B10_013455_2822_MA_00N064W	34, 287
Tempe Terra	03-Arcadia	29	B10_013456_2822_MA_00N091W	B10_013522_2854_MA_00N093W	36, 264
Tempe Terra	03-Arcadia	29	B10_013522_2854_MA_00N093W	B10_013667_2923_MA_00N092W	37, 265
Tempe Terra	03-Arcadia	29	B10_013667_2923_MA_00N092W	B11_013733_2954_MA_00N094W	33, 262
Tempe Terra	03-Arcadia	29	B11_013733_2954_MA_00N094W	B11_013799_2985_MA_00N096W	32, 260
Tempe Terra	03-Arcadia	29	B11_013798_2985_MA_00N068W	B11_013877_3022_MA_00N065W	38, 291
Tempe Terra	03-Arcadia	29	B11_013851_3010_MA_00N075W	B11_013917_3040_MA_00N077W	36, 276
Tempe Terra	03-Arcadia	29	B11_013878_3022_MA_00N092W	B11_013944_3053_MA_00N094W	35, 256
Tempe Terra	03-Arcadia	29	B11_013944_3053_MA_00N094W	B11_014010_3083_MA_00N096W	37, 257
Tempe Terra	03-Arcadia	29	B11_013970_3065_MA_00N084W	B11_014036_3095_MA_00N086W	31, 270
Tempe Terra	03-Arcadia	29	B11_014010_3083_MA_00N096W	B11_014076_3113_MA_00N098W	34, 254
Tempe Terra	03-Arcadia	29	B12_014142_3143_MA_00N100W	B12_014287_3207_MA_00N099W	29, 252
Tempe Terra	03-Arcadia	29	B12_014181_3160_MA_00N085W	B12_014313_3219_MA_00N088W	31, 267
Tempe Terra	03-Arcadia	29	B12_014352_3236_MA_00N073W	B12_014418_3265_MA_00N075W	34, 281
Tempe Terra	03-Arcadia	30	G11_022423_2894_MA_00N101W	G11_022568_2963_MA_00N100W	34, 256
Tempe Terra	03-Arcadia	30	G11_022528_2944_MA_00N088W	G11_022594_2975_MA_00N090W	38, 265
Tempe Terra	03-Arcadia	30	G11_022647_3000_MA_00N096W	G12_022713_3031_MA_00N099W	32, 255
Tempe Terra	03-Arcadia	30	G11_022659_3006_MA_00N064W	G12_022725_3036_MA_00N066W	38, 292
Tempe Terra	03-Arcadia	30	G12_022713_3031_MA_00N099W	G12_022779_3061_MA_00N101W	31, 255
Tempe Terra	03-Arcadia	30	G12_022725_3036_MA_00N066W	G12_022791_3067_MA_00N068W	38, 290
Tempe Terra	03-Arcadia	30	G12_022779_3061_MA_00N101W	G12_022845_3091_MA_00N102W	32, 254
Tempe Terra	03-Arcadia	30	G12_022791_3067_MA_00N068W	G12_022870_3103_MA_00N065W	39, 290
Tempe Terra	03-Arcadia	30	G12_022884_3109_MA_00N087W	G12_022950_3139_MA_00N089W	33, 267
Tempe Terra	03-Arcadia	30	G13_023371_3323_MA_00N062W	G13_023437_3351_MA_00N064W	32, 285
Tempe Terra	03-Arcadia	31	D09_030783_2673_MA_00N095W	D10_030928_2744_MA_00N094W	36, 263
Tempe Terra	03-Arcadia	31	D10_031007_2783_MA_00N091W	D10_031073_2815_MA_00N093W	34, 262
Tempe Terra	03-Arcadia	31	D10_031073_2815_MA_00N093W	D10_031139_2847_MA_00N095W	35, 259
Tempe Terra	03-Arcadia	31	D10_031139_2847_MA_00N095W	D10_031271_2910_MA_00N098W	35, 259
Tempe Terra	03-Arcadia	31	D10_031257_2903_MA_00N076W	D12_031758_3135_MA_00N075W	32, 281
Tempe Terra	03-Arcadia	31	D10_031271_2910_MA_00N098W	D12_031772_3141_MA_00N097W	32, 253
Tempe Terra	03-Arcadia	31	D10_031296_2921_MA_00N061W	D12_031784_3147_MA_00N065W	39, 289
Tempe Terra	03-Arcadia	31	D12_031797_3153_MA_00N060W	D12_031863_3182_MA_00N062W	34, 290
Tempe Terra	03-Arcadia	31	D13_032194_3326_MA_00N098W	D13_032273_3359_MA_00N095W	37, 257
Tempe Terra	03-Arcadia	31	D13_032339_3387_MA_00N097W	D13_032405_3414_MA_00N099W	29, 252; 42, 252
Tempe Terra	03-Arcadia	31	D13_032405_3414_MA_00N099W	D13_032471_3442_MA_00N101W	42, 253
Tempe Terra	03-Arcadia	31	D13_032417_3419_MA_00N066W	D14_032483_3447_MA_00N068W	31, 287
Tempe Terra	03-Arcadia	31	D13_032471_3442_MA_00N101W	D14_032550_3474_MA_00N098W	42, 253
Tempe Terra	03-Arcadia	31	D14_032550_3474_MA_00N098W	D14_032616_3500_MA_00N100W	42, 253
Tempe Terra	03-Arcadia	31	D14_032628_3505_MA_00N067W	D14_032694_3532_MA_00N069W	32, 285
Tempe Terra	03-Arcadia	32	D15_033142_0105_MA_00N061W	D15_033195_0125_MA_00N068W	34, 290
Tempe Terra	03-Arcadia	32	F10_039816_2779_MA_00N095W	F11_039961_2849_MA_00N094W	35, 259
Tempe Terra	03-Arcadia	32	F11_039973_2855_MA_00N061W	F11_040118_2924_MA_00N060W	34, 284; 35, 291
Tempe Terra	03-Arcadia	32	F11_040027_2881_MA_00N096W	F11_040106_2918_MA_00N093W	32, 260
Tempe Terra	03-Arcadia	32	F11_040106_2918_MA_00N093W	F11_040172_2950_MA_00N095W	34, 256
Tempe Terra	03-Arcadia	32	F11_040172_2950_MA_00N095W	F11_040238_2981_MA_00N097W	33, 255
Tempe Terra	03-Arcadia	32	F11_040185_2956_MA_00N090W	F12_040330_3024_MA_00N088W	31, 268
Tempe Terra	03-Arcadia	32	F11_040238_2981_MA_00N097W	F12_040304_3011_MA_00N098W	32, 254
Tempe Terra	03-Arcadia	32	F12_040304_3011_MA_00N098W	F12_040370_3042_MA_00N100W	31, 254
Tempe Terra	03-Arcadia	32	F12_040329_3023_MA_00N061W	F12_040395_3054_MA_00N063W	39, 290
Tempe Terra	03-Arcadia	32	F12_040330_3024_MA_00N088W	F12_040409_3060_MA_00N085W	31, 271
Tempe Terra	03-Arcadia	32	F12_040369_3042_MA_00N073W	F12_040435_3072_MA_00N075W	37, 278
Tempe Terra	03-Arcadia	32	F12_040370_3042_MA_00N100W	F12_040436_3072_MA_00N102W	30, 253
Tempe Terra	03-Arcadia	32	F12_040436_3072_MA_00N102W	F12_040581_3138_MA_00N100W	30, 253
Tempe Terra	03-Arcadia	32	F12_040540_3120_MA_00N061W	F12_040606_3149_MA_00N063W	39, 288
Tempe Terra	03-Arcadia	32	F12_040541_3120_MA_00N088W	F12_040620_3156_MA_00N085W	30, 272
Tempe Terra	03-Arcadia	32	F13_040936_3294_MA_00N073W	F13_041002_3323_MA_00N075W	35, 277
Tempe Terra	03-Arcadia	32	F13_040962_3305_MA_00N063W	F13_041028_3334_MA_00N065W	32, 284
Tempe Terra	03-Arcadia	32	F14_041359_3471_MA_00N101W	F15_041504_3529_MA_00N100W	41, 250
Tempe Terra	03-Arcadia	32	F14_041384_3481_MA_00N063W	F15_041529_3539_MA_00N063W	34, 290
Tempe Terra	03-Arcadia	33	J10_048532_2730_MA_00N095W	J10_048677_2801_MA_00N094W	34, 258
Tempe Terra	03-Arcadia	33	J10_048677_2801_MA_00N094W	J10_048822_2870_MA_00N093W	32, 264
Tempe Terra	03-Arcadia	33	J10_048821_2870_MA_00N066W	J11_048966_2939_MA_00N065W	35, 284; 38, 291
Tempe Terra	03-Arcadia	33	J11_048980_2946_MA_00N087W	J11_049059_2983_MA_00N084W	30, 272
Tempe Terra	03-Arcadia	33	J11_049033_2971_MA_00N094W	J11_049099_3001_MA_00N096W	33, 255
Tempe Terra	03-Arcadia	33	J11_049059_2983_MA_00N084W	J11_049125_3014_MA_00N085W	31, 267
Tempe Terra	03-Arcadia	33	J11_049099_3001_MA_00N096W	J11_049165_3032_MA_00N097W	32, 253
Tempe Terra	03-Arcadia	33	J11_049165_3032_MA_00N097W	J12_049442_3158_MA_00N099W	35, 257
Tempe Terra	03-Arcadia	33	J11_049243_3068_MA_00N067W	J12_049322_3104_MA_00N064W	34, 284
Tempe Terra	03-Arcadia	33	J12_049322_3104_MA_00N064W	J12_049388_3134_MA_00N065W	34, 290
Tempe Terra	03-Arcadia	33	J12_049388_3134_MA_00N065W	J12_049454_3164_MA_00N067W	33, 290

Tempe Terra	03-Arcadia	33	J12_049454_3164_MA_00N067W	J12_049533_3199_MA_00N064W	34, 290
Tempe Terra	03-Arcadia	33	J12_049454_3164_MA_00N067W	J12_049546_3204_MA_00N058W	40, 289
Tempe Terra	03-Arcadia	33	J14_050141_3457_MA_00N102W	J14_050220_3489_MA_00N099W	43, 256
Tempe Terra	03-Arcadia	33	J14_050220_3489_MA_00N099W	J14_050286_3516_MA_00N101W	42, 252
M. Acidalium	04-Acidalium	28	P12_005886_3385_MA_00N046W	P13_006163_3499_MA_00N049W	35, 308
M. Acidalium	04-Acidalium	29	P17_007809_0504_MA_00N353W	P18_007875_0527_MA_00N355W	61, 2
M. Acidalium	04-Acidalium	31	G18_025307_0458_MA_00N358W	G18_025373_0481_MA_00N000W	62, 355
M. Acidalium	04-Acidalium	33	F20_043440_0630_MA_00N038W	F20_043519_0657_MA_00N034W	67, 329
Ismenius L.	05-Ismenius	28	P12_005540_3237_MA_00N320W	P12_005606_3266_MA_00N322W	43, 28
Ismenius L.	05-Ismenius	28	P12_005606_3266_MA_00N322W	P12_005672_3295_MA_00N324W	43, 28
Ismenius L.	05-Ismenius	28	P12_005672_3295_MA_00N324W	P12_005751_3328_MA_00N321W	43, 35
Utopia	05-Ismenius	28	P12_005539_3237_MA_00N293W	P12_005605_3266_MA_00N295W	44, 63
Utopia	05-Ismenius	28	P12_005618_3271_MA_00N290W	P12_005671_3294_MA_00N297W	42, 60
Utopia	05-Ismenius	28	P13_006251_3534_MA_00N292W	P14_006462_0016_MA_00N293W	46, 62
Utopia	06-Casius	28	P03_002163_1652_MA_00N284W	P03_002189_1663_MA_00N274W	66, 69
Utopia	06-Casius	28	P12_005867_3377_MA_00N248W	P13_005933_3405_MA_00N249W	46, 109
Utopia	06-Casius	28	P13_006157_3496_MA_00N246W	P13_006223_3523_MA_00N248W	48, 112
Utopia	06-Casius	28	P13_006223_3523_MA_00N248W	P13_006236_3528_MA_00N243W	46, 111
Utopia	06-Casius	29	B02_010574_1487_MA_00N248W	B03_010640_1514_MA_00N250W	67, 94
Utopia	06-Casius	29	B12_014411_3261_MA_00N244W	B16_015888_0245_MA_00N246W	47, 104
Utopia	06-Casius	29	B12_014425_3268_MA_00N266W	B16_015889_0245_MA_00N273W	42, 81
Utopia	06-Casius	30	B17_016430_0437_MA_00N283W	B18_016496_0460_MA_00N285W	66, 69
Utopia	06-Casius	30	G05_019990_1735_MA_00N276W	G05_020069_1770_MA_00N273W	64, 75
Utopia	07-Cebrenia	33	J03_046150_1613_MA_00N219W	J04_046163_1618_MA_00N214W	67, 141
W. Propontis	07-Cebrenia	28	P12_005891_3387_MA_00N183W	P13_005957_3415_MA_00N185W	34, 169
W. Propontis	07-Cebrenia	28	P13_006247_3532_MA_00N183W	P14_006524_0040_MA_00N186W	32, 170
Amazonis	08-Amazonis	28	P07_003648_2335_MA_00N146W	P07_003714_2367_MA_00N148W	27, 207
Amazonis	08-Amazonis	28	P08_004334_2673_MA_00N155W	P10_004980_2984_MA_00N151W	26, 205
Amazonis	08-Amazonis	28	P13_006246_3532_MA_00N156W	P14_006470_0020_MA_00N151W	29, 205
Amazonis	08-Amazonis	29	B02_010531_1470_MA_00N154W	B02_010597_1496_MA_00N156W	26, 201
Amazonis	08-Amazonis	29	B06_011942_2083_MA_00N157W	B07_012232_2222_MA_00N154W	29, 200
Amazonis	08-Amazonis	29	B07_012311_2260_MA_00N151W	B07_012443_2324_MA_00N155W	29, 200
Amazonis	08-Amazonis	29	B07_012443_2324_MA_00N155W	B08_012588_2396_MA_00N153W	27, 202
Amazonis	08-Amazonis	29	B09_012957_2578_MA_00N148W	B09_013102_2650_MA_00N146W	26, 205
Amazonis	08-Amazonis	29	B12_014263_3197_MA_00N163W	B12_014329_3226_MA_00N165W	27, 194
Amazonis	08-Amazonis	29	B12_014289_3208_MA_00N153W	B12_014368_3243_MA_00N150W	28, 201; 28, 209
Amazonis	08-Amazonis	29	B12_014289_3208_MA_00N153W	B16_015885_0244_MA_00N164W	28, 196; 23, 200
Amazonis	08-Amazonis	30	G07_020922_2161_MA_00N161W	G08_021489_2437_MA_00N162W	28, 197
Amazonis	08-Amazonis	30	G07_020948_2173_MA_00N151W	G07_021014_2205_MA_00N153W	28, 207
Amazonis	08-Amazonis	30	G09_021634_2509_MA_00N160W	G09_021700_2542_MA_00N162W	25, 198
Amazonis	08-Amazonis	30	G11_022517_2939_MA_00N147W	G11_022570_2964_MA_00N154W	28, 205
Amazonis	08-Amazonis	30	G12_022794_3068_MA_00N150W	G12_022860_3098_MA_00N152W	28, 205
Amazonis	08-Amazonis	30	G12_022979_3152_MA_00N161W	G13_023190_3245_MA_00N161W	26, 196
Amazonis	08-Amazonis	30	G13_023427_3347_MA_00N151W	G14_023493_3375_MA_00N153W	30, 204
Amazonis	08-Amazonis	31	D07_030060_2317_MA_00N155W	D08_030337_2453_MA_00N158W	26, 201
Amazonis	08-Amazonis	31	D11_031313_2930_MA_00N165W	D12_031814_3160_MA_00N164W	30, 194
Amazonis	08-Amazonis	32	F07_038460_2115_MA_00N163W	F07_038671_2217_MA_00N161W	27, 195
Amazonis	08-Amazonis	32	F08_039014_2384_MA_00N159W	F09_039159_2456_MA_00N159W	27, 199
Amazonis	08-Amazonis	32	F12_040504_3103_MA_00N158W	F12_040649_3169_MA_00N157W	29, 199
Amazonis	08-Amazonis	32	F13_040860_3262_MA_00N158W	F13_041005_3324_MA_00N157W	31, 199
Amazonis	08-Amazonis	33	J07_047440_2193_MA_00N158W	J07_047585_2264_MA_00N157W	27, 197
Amazonis	08-Amazonis	33	J07_047638_2290_MA_00N164W	J07_047717_2328_MA_00N162W	22, 196
Amazonis	08-Amazonis	33	J14_050130_3452_MA_00N161W	J14_050196_3479_MA_00N164W	30, 193
Ascraeus Mons	09-Tharsis	28	P01_001576_1416_MA_00N103W	P02_001655_1446_MA_00N098W	10.5, 256.5
Ascraeus Mons	09-Tharsis	28	P02_001853_1525_MA_00N101W	P02_001998_1584_MA_00N100W	13.0, 255.0; 11.5, 256.0
Ascraeus Mons	09-Tharsis	28	P12_005888_3386_MA_00N101W	P13_005967_3419_MA_00N098W	10.5, 256.5; 13.0, 255.0
Ascraeus Mons	09-Tharsis	28	P13_005967_3419_MA_00N098W	P13_006112_3478_MA_00N097W	10.5, 256.5; 13.0, 255.0
Ascraeus Mons	09-Tharsis	28	P13_006112_3478_MA_00N097W	P13_006178_3505_MA_00N099W	12.0, 256.5
Ascraeus Mons	09-Tharsis	28	P13_006178_3505_MA_00N099W	P13_006244_3531_MA_00N101W	12.5, 255.5
Ascraeus Mons	09-Tharsis	28	P13_006244_3531_MA_00N101W	P14_006468_0019_MA_00N097W	13.0, 255.5; 12.0, 257.0; 10.0, 256.0
Ascraeus Mons	09-Tharsis	29	P14_006534_0044_MA_00N099W	P14_006600_0069_MA_00N101W	10.5, 255.5
Ascraeus Mons	09-Tharsis	29	P14_006679_0099_MA_00N098W	P15_006745_0124_MA_00N100W	12.0, 255.5
Ascraeus Mons	09-Tharsis	29	P15_006824_0154_MA_00N097W	P15_006890_0178_MA_00N099W	11.5, 253.5
Ascraeus Mons	09-Tharsis	29	P15_006890_0178_MA_00N099W	P15_007035_0231_MA_00N098W	11.5, 253.5; 9.5, 255.5
Ascraeus Mons	09-Tharsis	29	P16_007246_0307_MA_00N099W	P16_007391_0359_MA_00N099W	10.5, 255.0
Ascraeus Mons	09-Tharsis	29	P16_007391_0359_MA_00N099W	P17_007536_0410_MA_00N098W	10.5, 255.0
Ascraeus Mons	09-Tharsis	29	P17_007536_0410_MA_00N098W	P17_007602_0433_MA_00N101W	10.5, 254.0
Ascraeus Mons	09-Tharsis	29	P17_007681_0460_MA_00N098W	P18_007892_0533_MA_00N099W	11.5, 254.0
Ascraeus Mons	09-Tharsis	29	P18_007892_0533_MA_00N099W	P18_007958_0556_MA_00N101W	11.5, 254.0; 10.5, 254.5
Ascraeus Mons	09-Tharsis	29	P18_007958_0556_MA_00N101W	P18_008037_0583_MA_00N099W	10.5, 254.5
Ascraeus Mons	09-Tharsis	29	P19_008459_0726_MA_00N102W	P20_008749_0825_MA_00N102W	10.0, 254.5
Ascraeus Mons	09-Tharsis	29	P20_008749_0825_MA_00N102W	P20_008894_0875_MA_00N101W	10.5, 255.5
Ascraeus Mons	09-Tharsis	29	P20_008894_0875_MA_00N101W	P20_008973_0902_MA_00N099W	10.5, 255.5; 11.5, 254.5

Ascraeus Mons	09-Tharsis	29	P20_008973_0902_MA_00N099W	P20_009039_0925_MA_00N101W	10.5, 256.0
Ascraeus Mons	09-Tharsis	29	P21_009105_0947_MA_00N103W	P21_009184_0975_MA_00N099W	11.0, 256.0; 11.5, 255.0
Ascraeus Mons	09-Tharsis	29	B02_010239_1357_MA_00N102W	B02_010450_1438_MA_00N103W	13.0, 255.0; 10.0, 257.0
Ascraeus Mons	09-Tharsis	29	B03_010885_1613_MA_00N099W	B04_011241_1764_MA_00N099W	12.0, 255.5
Ascraeus Mons	09-Tharsis	29	B11_013852_3010_MA_00N103W	B11_013997_3077_MA_00N101W	13.0, 254.5
Ascraeus Mons	09-Tharsis	29	B12_014142_3143_MA_00N100W	B12_014353_3236_MA_00N100W	12.5, 255.0
Ascraeus Mons	09-Tharsis	29	B12_014353_3236_MA_00N100W	B16_015896_0248_MA_00N104W	11.5, 253.5; 10.5, 256.5
Ascraeus Mons	09-Tharsis	30	B16_015975_0276_MA_00N101W	B17_016120_0328_MA_00N100W	10.5, 254.5
Ascraeus Mons	09-Tharsis	30	B18_016608_0498_MA_00N103W	B18_016674_0521_MA_00N104W	11.0, 254.0
Ascraeus Mons	09-Tharsis	30	B19_016898_0598_MA_00N100W	B19_016964_0620_MA_00N102W	11.0, 254.0
Ascraeus Mons	09-Tharsis	30	B19_016964_0620_MA_00N102W	B20_017610_0840_MA_00N099W	11.0, 254.0
Ascraeus Mons	09-Tharsis	30	B20_017610_0840_MA_00N099W	B21_017676_0863_MA_00N101W	10.5, 255.5
Ascraeus Mons	09-Tharsis	30	B21_017676_0863_MA_00N101W	B21_017742_0886_MA_00N103W	11.5, 255.5
Ascraeus Mons	09-Tharsis	30	B21_017742_0886_MA_00N103W	B21_017821_0913_MA_00N100W	10.5, 255.5
Ascraeus Mons	09-Tharsis	30	B21_017821_0913_MA_00N100W	B21_017887_0936_MA_00N102W	11.5, 254.5
Ascraeus Mons	09-Tharsis	30	B22_018098_1009_MA_00N102W	B22_018177_1037_MA_00N099W	11.5, 255.0
Ascraeus Mons	09-Tharsis	30	B22_018243_1060_MA_00N101W	B22_018309_1083_MA_00N103W	12.0, 255.0
Ascraeus Mons	09-Tharsis	30	B22_018322_1088_MA_00N098W	B22_018388_1111_MA_00N100W	11.5, 255.5
Ascraeus Mons	09-Tharsis	30	G02_019021_1344_MA_00N102W	G02_019100_1374_MA_00N099W	10.0, 256.0
Ascraeus Mons	09-Tharsis	30	G02_019166_1399_MA_00N101W	G03_019311_1456_MA_00N099W	13.0, 254.5; 9.5, 256.0
Ascraeus Mons	09-Tharsis	30	G03_019311_1456_MA_00N099W	G03_019377_1482_MA_00N101W	12.5, 256.0
Ascraeus Mons	09-Tharsis	30	G03_019588_1567_MA_00N102W	G04_019799_1654_MA_00N102W	13.0, 256.0; 11.5, 257.5
Ascraeus Mons	09-Tharsis	30	G13_023346_3313_MA_00N100W	G13_023491_3374_MA_00N099W	12.0, 256.5
Ascraeus Mons	09-Tharsis	30	G13_023491_3374_MA_00N099W	G14_023847_3519_MA_00N098W	12.5, 256.5
Ascraeus Mons	09-Tharsis	30	G14_023847_3519_MA_00N098W	G15_023913_3546_MA_00N100W	11.0, 257.0; 9.5, 255.0
Ascraeus Mons	09-Tharsis	30	G15_023913_3546_MA_00N100W	G15_023992_3577_MA_00N097W	12.0, 257.0
Ascraeus Mons	09-Tharsis	30	G15_023992_3577_MA_00N097W	G15_024058_0003_MA_00N099W	10.0, 256.0
Ascraeus Mons	09-Tharsis	30	G15_024058_0003_MA_00N099W	G15_024203_0058_MA_00N097W	13.0, 256.0
Ascraeus Mons	09-Tharsis	31	G15_024203_0058_MA_00N097W	G15_024269_0084_MA_00N099W	10.5, 255.5
Ascraeus Mons	09-Tharsis	31	G16_024401_0133_MA_00N102W	G16_024480_0163_MA_00N099W	11.0, 253.5
Ascraeus Mons	09-Tharsis	31	G16_024546_0187_MA_00N101W	G16_024625_0216_MA_00N098W	9.5, 255.5
Ascraeus Mons	09-Tharsis	31	G17_024691_0240_MA_00N100W	G17_024836_0292_MA_00N099W	10.0, 257.0
Ascraeus Mons	09-Tharsis	31	G18_025403_0491_MA_00N099W	G19_025469_0514_MA_00N101W	10.5, 254.5
Ascraeus Mons	09-Tharsis	31	G19_025469_0514_MA_00N101W	G19_025535_0537_MA_00N102W	11.5, 254.0
Ascraeus Mons	09-Tharsis	31	G19_025535_0537_MA_00N102W	G19_025614_0564_MA_00N099W	10.5, 254.0
Ascraeus Mons	09-Tharsis	31	G21_026313_0802_MA_00N102W	G21_026392_0829_MA_00N099W	10.5, 255.0
Ascraeus Mons	09-Tharsis	31	G21_026392_0829_MA_00N099W	G21_026458_0851_MA_00N101W	11.5, 256.0
Ascraeus Mons	09-Tharsis	31	G21_026458_0851_MA_00N101W	G21_026524_0874_MA_00N103W	10.5, 255.5
Ascraeus Mons	09-Tharsis	31	G21_026603_0901_MA_00N099W	G22_026669_0924_MA_00N101W	10.5, 255.0
Ascraeus Mons	09-Tharsis	31	G22_026669_0924_MA_00N101W	G22_026814_0974_MA_00N100W	11.0, 256.0
Ascraeus Mons	09-Tharsis	31	D02_027935_1381_MA_00N101W	D02_028146_1463_MA_00N101W	12.5, 254.0; 10.0, 257.0
Ascraeus Mons	09-Tharsis	31	D02_028001_1407_MA_00N103W	D02_028067_1432_MA_00N104W	12.5, 254.0
Ascraeus Mons	09-Tharsis	31	D03_028225_1495_MA_00N098W	D03_028568_1634_MA_00N101W	12.0, 256.0; 10.0, 255.5
Ascraeus Mons	09-Tharsis	31	D10_031258_2903_MA_00N103W	D12_031759_3136_MA_00N103W	12.5, 255.0
Ascraeus Mons	09-Tharsis	31	D13_032194_3326_MA_00N098W	D13_032260_3354_MA_00N100W	12.0, 256.5
Ascraeus Mons	09-Tharsis	31	D13_032326_3382_MA_00N102W	D13_032405_3414_MA_00N099W	12.0, 256.5
Ascraeus Mons	09-Tharsis	31	D13_032471_3442_MA_00N101W	D14_032550_3474_MA_00N098W	10.5, 256.5
Ascraeus Mons	09-Tharsis	31	D14_032682_3527_MA_00N101W	D14_032761_3558_MA_00N098W	12.0, 256.5; 9.5, 255.5
Ascraeus Mons	09-Tharsis	31	D14_032827_3584_MA_00N100W	D15_032893_0010_MA_00N102W	9.0, 255.5
Ascraeus Mons	09-Tharsis	32	D15_032906_0015_MA_00N097W	D15_032972_0040_MA_00N099W	11.5, 253.5;
Ascraeus Mons	09-Tharsis	32	D17_033671_0299_MA_00N104W	D17_033750_0327_MA_00N100W	10.5, 254.5
Ascraeus Mons	09-Tharsis	32	D17_033750_0327_MA_00N100W	D18_034172_0475_MA_00N101W	11.5, 253.5
Ascraeus Mons	09-Tharsis	32	D18_034172_0475_MA_00N101W	D18_034238_0498_MA_00N103W	11.5, 254.0
Ascraeus Mons	09-Tharsis	32	D18_034238_0498_MA_00N103W	D18_034304_0520_MA_00N104W	11.5, 254.0
Ascraeus Mons	09-Tharsis	32	D18_034383_0548_MA_00N102W	D19_034449_0570_MA_00N104W	11.5, 254.0
Ascraeus Mons	09-Tharsis	32	D20_034950_0741_MA_00N103W	D20_035029_0768_MA_00N099W	11.5, 254.5
Ascraeus Mons	09-Tharsis	32	D21_035240_0840_MA_00N100W	D21_035306_0862_MA_00N102W	11.0, 255.0
Ascraeus Mons	09-Tharsis	32	D21_035385_0889_MA_00N099W	D21_035451_0912_MA_00N101W	10.5, 256.0
Ascraeus Mons	09-Tharsis	32	D21_035517_0935_MA_00N103W	D22_035596_0962_MA_00N099W	11.0, 256.0
Ascraeus Mons	09-Tharsis	32	D22_035596_0962_MA_00N099W	D22_035662_0985_MA_00N101W	11.5, 255.0
Ascraeus Mons	09-Tharsis	32	F02_036717_1368_MA_00N103W	F03_036862_1424_MA_00N102W	12.0, 254.0; 10.5, 256.5
Ascraeus Mons	09-Tharsis	32	F03_036862_1424_MA_00N102W	F03_036928_1450_MA_00N104W	12.0, 254.0
Ascraeus Mons	09-Tharsis	32	F05_037851_1835_MA_00N101W	F06_038062_1930_MA_00N101W	11.5, 256.0
Ascraeus Mons	09-Tharsis	32	F11_039935_2837_MA_00N104W	F11_040014_2875_MA_00N101W	12.5, 255.5
Ascraeus Mons	09-Tharsis	32	F14_041214_3412_MA_00N102W	F14_041359_3471_MA_00N101W	12.5, 256.5
Ascraeus Mons	09-Tharsis	32	F14_041359_3471_MA_00N101W	F15_041504_3529_MA_00N100W	10.5, 256.0
Ascraeus Mons	09-Tharsis	32	F15_041504_3529_MA_00N100W	F15_041794_0043_MA_00N098W	10.5, 256.6; 9.5, 255.5; 13.0, 255.5
Ascraeus Mons	09-Tharsis	33	F16_041860_0068_MA_00N100W	F16_041926_0093_MA_00N102W	10.0, 255.0; 13.0, 254.5
Ascraeus Mons	09-Tharsis	33	F16_041926_0093_MA_00N102W	F16_042071_0147_MA_00N101W	11.0, 253.5
Ascraeus Mons	09-Tharsis	33	F16_042071_0147_MA_00N101W	F17_042572_0329_MA_00N100W	10.0, 255.5

Ascraeus Mons	09-Tharsis	33	F17_042572_0329_MA_00N100W	F17_042638_0352_MA_00N102W	10.0, 254.0
Ascraeus Mons	09-Tharsis	33	F18_042994_0477_MA_00N101W	F19_043060_0500_MA_00N103W	11.0, 254.0
Ascraeus Mons	09-Tharsis	33	F19_043060_0500_MA_00N103W	F19_043139_0527_MA_00N100W	11.0, 254.0
Ascraeus Mons	09-Tharsis	33	F19_043205_0549_MA_00N102W	F19_043350_0599_MA_00N101W	11.0, 254.0
Ascraeus Mons	09-Tharsis	33	F19_043416_0622_MA_00N102W	F20_043561_0671_MA_00N101W	10.5, 254.0
Ascraeus Mons	09-Tharsis	33	F20_043627_0693_MA_00N103W	F20_043772_0743_MA_00N101W	11.0, 254.0
Ascraeus Mons	09-Tharsis	33	F21_043917_0792_MA_00N100W	F21_043983_0815_MA_00N101W	11.5, 254.0
Ascraeus Mons	09-Tharsis	33	F21_043983_0815_MA_00N101W	F21_044049_0837_MA_00N103W	11.0, 254.5
Ascraeus Mons	09-Tharsis	33	F21_044194_0887_MA_00N101W	F22_044471_0982_MA_00N103W	11.0, 255.0
Ascraeus Mons	09-Tharsis	33	J02_045605_1395_MA_00N099W	J02_045750_1452_MA_00N098W	12.0, 254.0; 10.5, 256.5
Ascraeus Mons	09-Tharsis	33	J02_045750_1452_MA_00N098W	J03_045816_1478_MA_00N100W	11.0, 257.0
Ascraeus Mons	09-Tharsis	33	J03_045816_1478_MA_00N100W	J03_045882_1504_MA_00N102W	12.5, 256.0
Ascraeus Mons	09-Tharsis	33	J03_046093_1590_MA_00N102W	J04_046238_1650_MA_00N101W	13.0, 254.5
Ascraeus Mons	09-Tharsis	33	J14_050141_3457_MA_00N102W	J14_050286_3516_MA_00N101W	10.5, 256.0; 10.0, 254.5
Ascraeus Mons	09-Tharsis	33	J14_050286_3516_MA_00N101W	J14_050431_3573_MA_00N100W	11.5, 256.6; 10.5, 254.0
Ascraeus Mons	09-Tharsis	33	J14_050431_3573_MA_00N100W	J15_050497_3599_MA_00N102W	9.5, 254.0; 12.5, 254.0
Tharsis Plateau	09-Tharsis	28	P03_002249_1689_MA_00N112W	P03_002394_1751_MA_00N111W	13, 247
Tharsis Plateau	09-Tharsis	28	P12_005901_3391_MA_00N096W	P13_005967_3419_MA_00N098W	1, 257; 29, 253
Tharsis Plateau	09-Tharsis	28	P13_005967_3419_MA_00N098W	P13_006112_3478_MA_00N097W	4, 256; 5, 250; 29, 255; 19, 255
Tharsis Plateau	09-Tharsis	28	P13_006112_3478_MA_00N097W	P13_006178_3505_MA_00N099W	6, 259
Tharsis Plateau	09-Tharsis	28	P13_006178_3505_MA_00N099W	P13_006244_3531_MA_00N101W	7, 258; 6, 250; 18, 255; 15, 250
Tharsis Plateau	09-Tharsis	28	P13_006244_3531_MA_00N101W	P14_006468_0019_MA_00N097W	8, 260; 18, 256
Tharsis Plateau	09-Tharsis	29	P14_006481_0024_MA_00N092W	P14_006560_0054_MA_00N089W	10, 265
Tharsis Plateau	09-Tharsis	29	P14_006560_0054_MA_00N089W	P14_006626_0079_MA_00N091W	9, 260
Tharsis Plateau	09-Tharsis	29	P14_006587_0065_MA_00N106W	P14_006653_0090_MA_00N108W	13, 247
Tharsis Plateau	09-Tharsis	29	P14_006626_0079_MA_00N091W	P14_006692_0104_MA_00N093W	11, 261
Tharsis Plateau	09-Tharsis	29	P14_006692_0104_MA_00N093W	P14_006705_0109_MA_00N088W	13, 265
Tharsis Plateau	09-Tharsis	29	P14_006705_0109_MA_00N088W	P15_006771_0134_MA_00N090W	12, 261
Tharsis Plateau	09-Tharsis	29	P15_006719_0114_MA_00N110W	P15_006785_0139_MA_00N112W	8, 243; 23, 240
Tharsis Plateau	09-Tharsis	29	P15_006771_0134_MA_00N090W	P15_006837_0159_MA_00N092W	10, 260
Tharsis Plateau	09-Tharsis	29	P15_006798_0144_MA_00N107W	P15_006864_0169_MA_00N109W	14, 247; 22, 239
Tharsis Plateau	09-Tharsis	29	P15_006864_0169_MA_00N109W	P15_007009_0222_MA_00N108W	15, 247; 21, 239
Tharsis Plateau	09-Tharsis	29	P15_007009_0222_MA_00N108W	P15_007075_0246_MA_00N110W	20, 239
Tharsis Plateau	09-Tharsis	29	P16_007141_0270_MA_00N112W	P16_007207_0293_MA_00N114W	19, 240
Tharsis Plateau	09-Tharsis	29	B02_010437_1433_MA_00N108W	B02_010516_1464_MA_00N105W	14, 249
Tharsis Plateau	09-Tharsis	29	B02_010516_1464_MA_00N105W	B02_010582_1490_MA_00N107W	14, 248
Tharsis Plateau	09-Tharsis	29	B02_010542_1475_MA_00N095W	B02_010608_1501_MA_00N097W	2, 258
Tharsis Plateau	09-Tharsis	29	B11_013918_3041_MA_00N105W	B11_013984_3071_MA_00N106W	11, 248
Tharsis Plateau	09-Tharsis	29	B11_014116_3131_MA_00N110W	B12_014261_3196_MA_00N109W	10, 248; 6, 250
Tharsis Plateau	09-Tharsis	29	B12_014142_3143_MA_00N100W	B12_014287_3207_MA_00N099W	2, 258; 5, 250; 19, 255
Tharsis Plateau	09-Tharsis	29	B12_014261_3196_MA_00N109W	B12_014340_3231_MA_00N105W	12, 249
Tharsis Plateau	09-Tharsis	29	B12_014287_3207_MA_00N099W	B12_014432_3271_MA_00N097W	5, 257
Tharsis Plateau	09-Tharsis	29	B12_014406_3259_MA_00N107W	B16_015883_0243_MA_00N109W	8, 243; 13, 247; 25, 238
Tharsis Plateau	09-Tharsis	29	B12_014432_3271_MA_00N097W	B16_015909_0252_MA_00N099W	6, 258; 20, 255
Tharsis Plateau	09-Tharsis	30	B16_015962_0271_MA_00N106W	B16_016028_0295_MA_00N108W	16, 248
Tharsis Plateau	09-Tharsis	30	G04_019707_1616_MA_00N110W	G04_019786_1649_MA_00N107W	15, 247
Tharsis Plateau	09-Tharsis	30	G04_019786_1649_MA_00N107W	G04_019852_1676_MA_00N109W	15, 248; 18, 240
Tharsis Plateau	09-Tharsis	30	G04_019852_1676_MA_00N109W	G04_019918_1704_MA_00N111W	11, 246
Tharsis Plateau	09-Tharsis	30	G13_023109_3210_MA_00N110W	G13_023188_3244_MA_00N107W	6, 251
Tharsis Plateau	09-Tharsis	30	G13_023135_3221_MA_00N100W	G13_023201_3250_MA_00N102W	1, 257
Tharsis Plateau	09-Tharsis	30	G13_023188_3244_MA_00N107W	G13_023254_3273_MA_00N108W	6, 251
Tharsis Plateau	09-Tharsis	30	G13_023214_3256_MA_00N096W	G13_023280_3284_MA_00N098W	4, 257
Tharsis Plateau	09-Tharsis	30	G13_023280_3284_MA_00N098W	G13_023346_3313_MA_00N100W	1, 260; 28, 253
Tharsis Plateau	09-Tharsis	30	G14_023715_3466_MA_00N095W	G14_023781_3493_MA_00N097W	1, 262
Tharsis Plateau	09-Tharsis	30	G14_023781_3493_MA_00N097W	G14_023847_3519_MA_00N098W	1, 260
Tharsis Plateau	09-Tharsis	30	G14_023847_3519_MA_00N098W	G15_023926_3551_MA_00N095W	7, 257
Tharsis Plateau	09-Tharsis	30	G15_023926_3551_MA_00N095W	G15_023992_3577_MA_00N097W	8, 262; 18, 256
Tharsis Plateau	09-Tharsis	30	G15_024005_3582_MA_00N092W	G15_024071_0008_MA_00N094W	11, 264
Tharsis Plateau	09-Tharsis	31	G15_024071_0008_MA_00N094W	G15_024137_0033_MA_00N095W	9, 261
Tharsis Plateau	09-Tharsis	31	G15_024137_0033_MA_00N095W	G15_024203_0058_MA_00N097W	8, 260
Tharsis Plateau	09-Tharsis	31	G15_024216_0063_MA_00N092W	G16_024282_0088_MA_00N094W	12, 262

Tharsis Plateau	09-Tharsis	31	G15_024243_0074_MA_00N109W	G16_024309_0099_MA_00N111W	13, 246
Tharsis Plateau	09-Tharsis	31	G16_024309_0099_MA_00N111W	G16_024388_0128_MA_00N107W	16, 247
Tharsis Plateau	09-Tharsis	31	G16_024362_0119_MA_00N118W	G16_024428_0143_MA_00N119W	25, 238
Tharsis Plateau	09-Tharsis	31	G16_024388_0128_MA_00N107W	G16_024454_0153_MA_00N109W	12, 246
Tharsis Plateau	09-Tharsis	31	G16_024441_0148_MA_00N114W	G16_024507_0173_MA_00N116W	23, 237
Tharsis Plateau	09-Tharsis	31	G16_024586_0202_MA_00N113W	G16_024652_0226_MA_00N115W	19, 240
Tharsis Plateau	09-Tharsis	31	G16_024625_0216_MA_00N098W	G17_024691_0240_MA_00N100W	20, 255
Tharsis Plateau	09-Tharsis	31	G17_024678_0235_MA_00N105W	G17_024823_0288_MA_00N104W	16, 252
Tharsis Plateau	09-Tharsis	31	G17_024823_0288_MA_00N104W	G17_024902_0316_MA_00N101W	17, 253
Tharsis Plateau	09-Tharsis	31	G18_025219_0427_MA_00N115W	G18_025298_0455_MA_00N112W	19, 241
Tharsis Plateau	09-Tharsis	31	D10_031258_2903_MA_00N103W	D12_031759_3136_MA_00N103W	5, 251; 2, 256
Tharsis Plateau	09-Tharsis	31	D12_031772_3141_MA_00N097W	D12_031825_3165_MA_00N104W	2, 258
Tharsis Plateau	09-Tharsis	31	D13_032194_3326_MA_00N098W	D13_032273_3359_MA_00N095W	3, 258
Tharsis Plateau	09-Tharsis	31	D13_032273_3359_MA_00N095W	D13_032418_3420_MA_00N094W	6, 258; 29, 252; 28, 262
Tharsis Plateau	09-Tharsis	31	D13_032418_3420_MA_00N094W	D14_032484_3447_MA_00N096W	7, 257; 18, 255
Tharsis Plateau	09-Tharsis	31	D13_032458_3436_MA_00N106W	D14_032524_3463_MA_00N108W	11, 248
Tharsis Plateau	09-Tharsis	31	D14_032484_3447_MA_00N096W	D14_032550_3474_MA_00N098W	6, 259
Tharsis Plateau	09-Tharsis	31	D14_032524_3463_MA_00N108W	D14_032669_3522_MA_00N107W	6, 248
Tharsis Plateau	09-Tharsis	31	D14_032550_3474_MA_00N098W	D14_032616_3500_MA_00N100W	6, 255
Tharsis Plateau	09-Tharsis	31	D14_032629_3506_MA_00N095W	D14_032695_3532_MA_00N096W	9, 262; 19, 257
Tharsis Plateau	09-Tharsis	31	D14_032669_3522_MA_00N107W	D14_032735_3548_MA_00N108W	12, 246
Tharsis Plateau	09-Tharsis	31	D14_032695_3532_MA_00N096W	D14_032761_3558_MA_00N098W	9, 260
Tharsis Plateau	09-Tharsis	31	D14_032735_3548_MA_00N108W	D14_032814_3579_MA_00N105W	7, 251
Tharsis Plateau	09-Tharsis	31	D14_032774_3563_MA_00N093W	D14_032840_3589_MA_00N095W	7, 260
Tharsis Plateau	09-Tharsis	31	D14_032814_3579_MA_00N105W	D15_032880_0005_MA_00N107W	14, 247
Tharsis Plateau	09-Tharsis	31	D14_032840_3589_MA_00N095W	D15_032906_0015_MA_00N097W	10, 261
Tharsis Plateau	09-Tharsis	32	D15_032906_0015_MA_00N097W	D15_032985_0045_MA_00N094W	11, 263
Tharsis Plateau	09-Tharsis	32	D15_032946_0030_MA_00N109W	D15_033012_0056_MA_00N111W	10, 245; 8, 240
Tharsis Plateau	09-Tharsis	32	D15_032985_0045_MA_00N094W	D15_033051_0071_MA_00N096W	11, 261
Tharsis Plateau	09-Tharsis	32	D15_033012_0056_MA_00N111W	D15_033091_0086_MA_00N108W	15, 247
Tharsis Plateau	09-Tharsis	32	D15_033051_0071_MA_00N096W	D15_033130_0100_MA_00N093W	10, 262
Tharsis Plateau	09-Tharsis	32	D15_033091_0086_MA_00N108W	D15_033157_0111_MA_00N110W	15, 247; 25, 237
Tharsis Plateau	09-Tharsis	32	D15_033130_0100_MA_00N093W	D15_033196_0125_MA_00N095W	12, 263
Tharsis Plateau	09-Tharsis	32	D15_033157_0111_MA_00N110W	D15_033236_0140_MA_00N107W	11, 246
Tharsis Plateau	09-Tharsis	32	D15_033196_0125_MA_00N095W	D15_033262_0150_MA_00N097W	10, 260
Tharsis Plateau	09-Tharsis	32	D15_033196_0125_MA_00N095W	D16_033341_0179_MA_00N094W	2, 263
Tharsis Plateau	09-Tharsis	32	D15_033236_0140_MA_00N107W	D16_033302_0165_MA_00N109W	15, 247
Tharsis Plateau	09-Tharsis	32	D16_033302_0165_MA_00N109W	D16_033381_0194_MA_00N106W	11, 247; 19, 240
Tharsis Plateau	09-Tharsis	32	D16_033605_0275_MA_00N102W	D17_033671_0299_MA_00N104W	16, 252
Tharsis Plateau	09-Tharsis	32	D17_033829_0355_MA_00N097W	D17_033895_0378_MA_00N099W	3, 255
Tharsis Plateau	09-Tharsis	32	F04_037192_1555_MA_00N111W	F04_037205_1560_MA_00N106W	15, 247
Tharsis Plateau	09-Tharsis	32	F04_037205_1560_MA_00N106W	F04_037271_1587_MA_00N108W	13, 247
Tharsis Plateau	09-Tharsis	32	F04_037258_1582_MA_00N113W	F04_037337_1615_MA_00N110W	18, 240; 5, 242
Tharsis Plateau	09-Tharsis	32	F04_037337_1615_MA_00N110W	F04_037403_1642_MA_00N112W	6, 242; 8, 243; 2, 239; 14, 248; 23, 237
Tharsis Plateau	09-Tharsis	32	F04_037350_1620_MA_00N105W	F04_037416_1648_MA_00N107W	15, 248; 5, 250; 1, 252
Tharsis Plateau	09-Tharsis	32	F04_037363_1625_MA_00N100W	F04_037429_1653_MA_00N102W	7, 252; 1, 258; 17, 252
Tharsis Plateau	09-Tharsis	32	F12_040647_3168_MA_00N102W	F13_040792_3232_MA_00N101W	5, 250; 3, 256
Tharsis Plateau	09-Tharsis	32	F13_040871_3266_MA_00N098W	F13_040937_3295_MA_00N100W	1, 257
Tharsis Plateau	09-Tharsis	32	F14_041293_3444_MA_00N099W	F14_041438_3503_MA_00N098W	5, 257
Tharsis Plateau	09-Tharsis	32	F14_041438_3503_MA_00N098W	F15_041504_3529_MA_00N100W	2, 259
Tharsis Plateau	09-Tharsis	32	F15_041478_3519_MA_00N110W	F15_041768_0033_MA_00N108W	6, 249
Tharsis Plateau	09-Tharsis	32	F15_041504_3529_MA_00N100W	F15_041794_0043_MA_00N098W	8, 260
Tharsis Plateau	09-Tharsis	32	F15_041530_3540_MA_00N090W	F15_041741_0022_MA_00N091W	8, 261
Tharsis Plateau	09-Tharsis	32	F15_041531_3540_MA_00N117W	F15_041742_0022_MA_00N118W	3, 237; 1, 240
Tharsis Plateau	09-Tharsis	33	F15_041807_0047_MA_00N093W	F16_041886_0078_MA_00N090W	8, 263
Tharsis Plateau	09-Tharsis	33	F16_041886_0078_MA_00N090W	F16_041952_0103_MA_00N092W	12, 263; 7, 266
Tharsis Plateau	09-Tharsis	33	F16_041887_0078_MA_00N117W	F16_041953_0103_MA_00N119W	28, 234; 25, 237
Tharsis Plateau	09-Tharsis	33	F16_041952_0103_MA_00N092W	F16_042031_0132_MA_00N089W	8, 266; 14, 266; 12, 261
Tharsis Plateau	09-Tharsis	33	F16_041979_0113_MA_00N109W	F16_042124_0167_MA_00N108W	12, 247; 21, 243
Tharsis Plateau	09-Tharsis	33	F16_042071_0147_MA_00N101W	F16_042150_0176_MA_00N098W	19, 258
Tharsis Plateau	09-Tharsis	33	F16_042097_0157_MA_00N091W	F16_042163_0181_MA_00N093W	2, 262

Tharsis Plateau	09-Tharsis	33	F16_042216_0201_MA_00N100W	F17_042361_0253_MA_00N099W	17, 251; 20, 255
Tharsis Plateau	09-Tharsis	33	F17_042309_0235_MA_00N119W	F17_042388_0263_MA_00N116W	24, 236; 16, 237
Tharsis Plateau	09-Tharsis	33	F17_042388_0263_MA_00N116W	F17_042454_0287_MA_00N118W	26, 234; 19, 240
Tharsis Plateau	09-Tharsis	33	J04_046370_1705_MA_00N105W	J04_046436_1734_MA_00N107W	12, 246
Tharsis Plateau	09-Tharsis	33	J04_046409_1722_MA_00N090W	J04_046475_1751_MA_00N092W	11, 265
Tharsis Plateau	09-Tharsis	33	J04_046410_1723_MA_00N117W	J04_046489_1757_MA_00N114W	18, 240; 23, 238
Tharsis Plateau	09-Tharsis	33	J12_049376_3129_MA_00N098W	J12_049442_3158_MA_00N099W	3, 257
Tharsis Plateau	09-Tharsis	33	J12_049640_3246_MA_00N104W	J13_049706_3274_MA_00N106W	5, 250; 2, 251
Tharsis Plateau	09-Tharsis	33	J12_049653_3251_MA_00N099W	J13_049719_3280_MA_00N101W	2, 256
Tharsis Plateau	09-Tharsis	33	J14_050075_3430_MA_00N100W	J14_050154_3462_MA_00N097W	2, 257
Tharsis Plateau	09-Tharsis	33	J14_050154_3462_MA_00N097W	J14_050220_3489_MA_00N099W	4, 259
Tharsis Plateau	09-Tharsis	33	J14_050233_3494_MA_00N094W	J14_050299_3521_MA_00N096W	1, 263
Tharsis Plateau	09-Tharsis	33	J14_050260_3505_MA_00N111W	J14_050339_3537_MA_00N108W	11, 248
Tharsis Plateau	09-Tharsis	33	J14_050299_3521_MA_00N096W	J14_050378_3552_MA_00N093W	6, 264; 1, 260
Tharsis Plateau	09-Tharsis	33	J14_050405_3563_MA_00N110W	J15_050471_3589_MA_00N112W	11, 246; 5, 242
Tharsis Plateau	09-Tharsis	33	J14_050418_3568_MA_00N105W	J15_050484_3594_MA_00N107W	6, 248; 11, 248
Tharsis Plateau	09-Tharsis	33	J14_050431_3573_MA_00N100W	J15_050497_3599_MA_00N102W	6, 255
Nilokeras	10-Lunae	28	P12_005570_3250_MA_00N059W	P12_005636_3279_MA_00N061W	29, 296; 25, 297
Nilokeras	10-Lunae	28	P12_005636_3279_MA_00N061W	P12_005702_3307_MA_00N063W	28, 296; 25, 298
Nilokeras	10-Lunae	28	P12_005794_3347_MA_00N055W	P12_005847_3369_MA_00N062W	28, 298
Nilokeras	10-Lunae	28	P13_005926_3402_MA_00N058W	P13_005992_3429_MA_00N060W	30, 299; 23, 305
Nilokeras	10-Lunae	29	B12_014286_3207_MA_00N071W	B12_014365_3241_MA_00N068W	29, 289
Nilokeras	10-Lunae	30	G12_022817_3079_MA_00N058W	G12_022962_3144_MA_00N057W	29, 297; 6, 301
Nilokeras	10-Lunae	30	G13_023358_3318_MA_00N067W	G13_023424_3346_MA_00N070W	27, 287; 31, 284
Nilokeras	10-Lunae	31	D13_032417_3419_MA_00N066W	D14_032483_3447_MA_00N068W	28, 290
Nilokeras	10-Lunae	32	F13_040949_3300_MA_00N068W	F14_041081_3356_MA_00N071W	27, 282
Nilokeras	10-Lunae	32	F13_040949_3300_MA_00N068W	F14_041094_3361_MA_00N066W	27, 292
Nilokeras	10-Lunae	32	F15_041463_3513_MA_00N061W	F15_041503_3529_MA_00N073W	28, 291
Nilokeras	10-Lunae	33	J12_049322_3104_MA_00N064W	J12_049375_3128_MA_00N070W	28, 289
Nilokeras	10-Lunae	33	J12_049533_3199_MA_00N064W	J13_049678_3262_MA_00N062W	14, 293
Niliacus L.	11-Oxia	28	P05_002839_1949_MA_00N020W	P05_003050_2047_MA_00N020W	28, 335
Niliacus L.	11-Oxia	28	P08_004263_2638_MA_00N016W	P10_004909_2950_MA_00N013W	15, 345
Niliacus L.	11-Oxia	28	P12_005543_3239_MA_00N042W	P12_005609_3267_MA_00N044W	28, 319
Niliacus L.	11-Oxia	28	P12_005609_3267_MA_00N044W	P12_005688_3301_MA_00N041W	29, 320
Niliacus L.	11-Oxia	28	P12_005754_3330_MA_00N043W	P12_005820_3357_MA_00N044W	25, 320
Niliacus L.	11-Oxia	28	P12_005820_3357_MA_00N044W	P12_005899_3391_MA_00N041W	28, 316
Niliacus L.	11-Oxia	28	P12_005899_3391_MA_00N041W	P13_005978_3423_MA_00N038W	26, 320
Niliacus L.	11-Oxia	29	B02_010368_1406_MA_00N024W	B02_010566_1484_MA_00N030W	29, 333
Niliacus L.	11-Oxia	29	B02_010381_1411_MA_00N019W	B02_010526_1468_MA_00N018W	19, 339
Niliacus L.	11-Oxia	29	B11_013915_3039_MA_00N023W	B11_013981_3070_MA_00N025W	27, 334
Niliacus L.	11-Oxia	29	B11_013955_3058_MA_00N035W	B12_014166_3153_MA_00N035W	25, 320
Niliacus L.	11-Oxia	30	G14_023620_3427_MA_00N021W	G14_023686_3454_MA_00N023W	28, 340
Niliacus L.	11-Oxia	30	G14_023699_3460_MA_00N018W	G14_023778_3492_MA_00N015W	26, 342
Niliacus L.	11-Oxia	30	G14_023699_3460_MA_00N018W	G14_023844_3518_MA_00N016W	17, 340
Niliacus L.	11-Oxia	31	D02_028143_1462_MA_00N019W	D03_028209_1488_MA_00N021W	27, 335
Niliacus L.	11-Oxia	31	D12_031756_3134_MA_00N021W	D12_031822_3164_MA_00N022W	12, 338
Niliacus L.	11-Oxia	31	D14_032600_3494_MA_00N023W	D14_032679_3526_MA_00N020W	27, 335
Niliacus L.	11-Oxia	32	F07_038534_2151_MA_00N022W	F08_038877_2317_MA_00N021W	12, 338; 7, 337
Niliacus L.	11-Oxia	32	F11_040183_2955_MA_00N035W	F12_040394_3053_MA_00N035W	27, 320
Niliacus L.	11-Oxia	33	J06_047158_2059_MA_00N019W	J06_047290_2122_MA_00N023W	28, 338
Niliacus L.	11-Oxia	33	J11_049031_2970_MA_00N039W	J11_049097_3001_MA_00N041W	25, 317
Niliacus L.	11-Oxia	33	J12_049637_3244_MA_00N023W	J13_049848_3335_MA_00N022W	13, 339
Oxia	12-Arabia	28	P09_004473_2741_MA_00N350W	P10_004829_2913_MA_00N349W	10, 9
E Syrtis	13-Syrtis	28	P09_004378_2695_MA_00N276W	P11_005512_3225_MA_00N276W	11, 83
E Syrtis	13-Syrtis	29	B07_012197_2205_MA_00N278W	B07_012276_2243_MA_00N275W	13, 83
E Syrtis	13-Syrtis	29	B11_013911_3037_MA_00N273W	B11_014056_3104_MA_00N272W	12, 84
E Syrtis	13-Syrtis	30	G13_023392_3332_MA_00N276W	G13_023458_3360_MA_00N278W	15, 80
E Syrtis	13-Syrtis	31	D06_029458_2028_MA_00N279W	D06_029603_2096_MA_00N278W	14, 81
E Syrtis	13-Syrtis	32	F07_038517_2143_MA_00N279W	F07_038596_2180_MA_00N274W	11, 83
NW Syrtis	13-Syrtis	28	P01_001530_1398_MA_00N288W	P02_001662_1449_MA_00N289W	21, 61; 23, 69
NW Syrtis	13-Syrtis	29	B02_010510_1462_MA_00N301W	B02_010576_1488_MA_00N303W	19, 60; 20, 59
NW Syrtis	13-Syrtis	30	G02_019028_1347_MA_00N293W	G02_019081_1367_MA_00N300W	20, 60; 17, 59
NW Syrtis	13-Syrtis	30	G02_019173_1402_MA_00N292W	G03_019252_1433_MA_00N288W	24, 68; 22, 63
NW Syrtis	13-Syrtis	32	F03_036948_1458_MA_00N290W	F03_036961_1463_MA_00N285W	25, 69
W Syrtis	13-Syrtis	28	P09_004379_2695_MA_00N303W	P09_004458_2734_MA_00N300W	6, 60
Alcyonius	14-Amenthes	28	P08_004338_2675_MA_00N264W	P11_005261_3113_MA_00N263W	24, 92
Alcyonius	14-Amenthes	29	B11_013937_3049_MA_00N263W	B11_013990_3074_MA_00N270W	25, 92

Alcyonius	14-Amenthes	29	B12_014425_3268_MA_00N266W	B16_015889_0245_MA_00N273W	22, 93
Alcyonius	14-Amenthes	31	D06_029497_2046_MA_00N264W	D07_029787_2184_MA_00N262W	24, 93
Hyblaeus	14-Amenthes	28	P05_003071_2057_MA_00N234W	P06_003348_2189_MA_00N236W	21, 122
Hyblaeus	14-Amenthes	28	P07_003638_2330_MA_00N233W	P07_003651_2336_MA_00N228W	23, 129
Hyblaeus	14-Amenthes	28	P08_004324_2668_MA_00N242W	P10_005036_3010_MA_00N240W	5, 120
Hyblaeus	14-Amenthes	30	G10_022309_2840_MA_00N229W	G11_022375_2872_MA_00N231W	24, 126
Hyblaeus	14-Amenthes	30	G13_023377_3326_MA_00N226W	G14_023496_3376_MA_00N235W	25, 124
Hyblaeus	14-Amenthes	31	D10_031289_2918_MA_00N230W	D12_031856_3179_MA_00N231W	25, 126
Hyblaeus	14-Amenthes	32	F13_040889_3274_MA_00N230W	F13_040942_3297_MA_00N237W	25, 126
Cerberus	15-Elysium	28	P08_004283_2648_MA_00N202W	P11_005206_3088_MA_00N201W	13, 158
Cerberus	15-Elysium	29	B12_014383_3249_MA_00N199W	B12_014436_3272_MA_00N206W	11, 159
Elysium Mons	15-Elysium	28	P13_006261_3538_MA_00N205W	P14_006472_0020_MA_00N206W	25.0, 146.5
Elysium Mons	15-Elysium	29	P14_006472_0020_MA_00N206W	P14_006538_0046_MA_00N208W	25.5, 146.5
Elysium Mons	15-Elysium	29	P14_006538_0046_MA_00N208W	P14_006617_0076_MA_00N205W	24.5, 147.0
Elysium Mons	15-Elysium	29	P14_006617_0076_MA_00N205W	P14_006683_0101_MA_00N207W	24.5, 147.0
Elysium Mons	15-Elysium	29	P14_006683_0101_MA_00N207W	P15_006749_0126_MA_00N209W	24.5, 146.0
Elysium Mons	15-Elysium	29	P15_006736_0121_MA_00N214W	P15_006815_0150_MA_00N211W	27, 142
Elysium Mons	15-Elysium	29	P15_006749_0126_MA_00N209W	P15_007039_0233_MA_00N207W	24.0, 146.5; 25.5, 146.5
Elysium Mons	15-Elysium	29	P15_007039_0233_MA_00N207W	P16_007184_0285_MA_00N206W	24.5, 147.0
Elysium Mons	15-Elysium	29	P16_007250_0309_MA_00N209W	P16_007395_0360_MA_00N208W	25.5, 146.5; 24.0, 146.5
Elysium Mons	15-Elysium	29	P18_008041_0584_MA_00N208W	P18_008120_0611_MA_00N205W	25.5, 146.0
Elysium Mons	15-Elysium	29	P18_008120_0611_MA_00N205W	P19_008331_0683_MA_00N207W	25.0, 146.5; 24.5, 146.5
Elysium Mons	15-Elysium	29	P19_008331_0683_MA_00N207W	P19_008476_0732_MA_00N207W	23.5, 146.5
Elysium Mons	15-Elysium	29	P19_008476_0732_MA_00N207W	P19_008621_0781_MA_00N206W	24.5, 146.5
Elysium Mons	15-Elysium	29	B12_014436_3272_MA_00N206W	B16_015913_0254_MA_00N209W	25.0, 146.5; 27, 142
Elysium Mons	15-Elysium	30	B16_015913_0254_MA_00N209W	B16_015992_0282_MA_00N205W	25.5, 147.0
Elysium Mons	15-Elysium	30	B16_015992_0282_MA_00N205W	B16_016058_0306_MA_00N207W	24.5, 147.0
Elysium Mons	15-Elysium	30	B16_016058_0306_MA_00N207W	B17_016203_0357_MA_00N206W	24.0, 147.0
Elysium Mons	15-Elysium	30	B17_016480_0454_MA_00N208W	B18_016559_0482_MA_00N205W	25.5, 146.5
Elysium Mons	15-Elysium	30	B18_016770_0554_MA_00N205W	B19_016981_0626_MA_00N206W	25.5, 146.0; 24.0, 146.5
Elysium Mons	15-Elysium	30	B19_017047_0649_MA_00N208W	B19_017192_0698_MA_00N207W	24.5, 146.5
Elysium Mons	15-Elysium	30	G14_023838_3516_MA_00N213W	G15_023983_3573_MA_00N211W	27, 142; 26, 144; 28, 144
Elysium Mons	15-Elysium	31	G16_024339_0110_MA_00N210W	G16_024352_0115_MA_00N205W	25.0, 146.5; 24.5, 146.5
Elysium Mons	15-Elysium	31	G16_024352_0115_MA_00N205W	G16_024418_0140_MA_00N206W	25.0, 147.0; 24.5, 147.0
Elysium Mons	15-Elysium	31	G17_024695_0241_MA_00N209W	G17_024840_0294_MA_00N208W	25.0, 147.0; 24.5, 147.0
Elysium Mons	15-Elysium	31	G17_024906_0317_MA_00N210W	G17_024985_0345_MA_00N207W	25.5, 147.0; 24.0, 147.0
Elysium Mons	15-Elysium	31	G19_025552_0542_MA_00N206W	G19_025618_0565_MA_00N208W	25.5, 146.5
Elysium Mons	15-Elysium	31	G19_025763_0615_MA_00N207W	G19_025829_0637_MA_00N208W	24.0, 146.5
Elysium Mons	15-Elysium	31	D13_032119_3294_MA_00N210W	D13_032264_3356_MA_00N209W	27, 142
Elysium Mons	15-Elysium	31	D13_032264_3356_MA_00N209W	D13_032330_3383_MA_00N211W	29, 145; 26, 144
Elysium Mons	15-Elysium	32	D15_033108_0092_MA_00N212W	D15_033187_0122_MA_00N209W	27, 142
Elysium Mons	15-Elysium	32	D15_033121_0097_MA_00N207W	D15_033187_0122_MA_00N209W	24.5, 146.5; 25.0, 146.5
Elysium Mons	15-Elysium	32	D15_033187_0122_MA_00N209W	D15_033266_0151_MA_00N206W	24.5, 146.5; 25.0, 146.5
Elysium Mons	15-Elysium	32	D16_033332_0176_MA_00N208W	D16_033411_0205_MA_00N205W	25.0, 147.0; 24.5, 147.0
Elysium Mons	15-Elysium	32	D16_033543_0253_MA_00N209W	D16_033609_0277_MA_00N211W	26, 142
Elysium Mons	15-Elysium	32	D16_033543_0253_MA_00N209W	D16_033622_0281_MA_00N206W	24.5, 147.0
Elysium Mons	15-Elysium	32	D16_033622_0281_MA_00N206W	D17_033688_0305_MA_00N208W	25.5, 146.5
Elysium Mons	15-Elysium	32	D18_034189_0481_MA_00N205W	D19_034466_0576_MA_00N208W	25.5, 146.5
Elysium Mons	15-Elysium	32	D19_034466_0576_MA_00N208W	D19_034545_0603_MA_00N205W	25.0, 146.0
Elysium Mons	15-Elysium	32	D19_034677_0648_MA_00N209W	D19_034756_0675_MA_00N206W	24.5, 146.5
Elysium Mons	15-Elysium	32	F15_041508_3531_MA_00N209W	F16_041864_0069_MA_00N209W	27, 142
Elysium Mons	15-Elysium	33	F16_041864_0069_MA_00N209W	F16_041943_0099_MA_00N206W	25.0, 147.0; 24.5, 146.5
Elysium Mons	15-Elysium	33	F16_042009_0124_MA_00N208W	F16_042088_0153_MA_00N205W	25.5, 146.5; 24.0, 146.5
Elysium Mons	15-Elysium	33	F16_042088_0153_MA_00N205W	F16_042154_0178_MA_00N207W	24.0, 146.5
Elysium Mons	15-Elysium	33	F16_042220_0202_MA_00N209W	F17_042299_0231_MA_00N206W	25.0, 147.0; 24.5, 147.0
Elysium Mons	15-Elysium	33	F17_042431_0279_MA_00N210W	F17_042510_0307_MA_00N207W	25.5, 147.0
Elysium Mons	15-Elysium	33	F18_042866_0432_MA_00N207W	F18_042932_0455_MA_00N209W	25.5, 146.5; 24.0, 146.5
Elysium N.	15-Elysium	28	P13_005958_3415_MA_00N212W	P13_006169_3501_MA_00N213W	31, 144
Elysium N.	15-Elysium	29	B11_013843_3006_MA_00N217W	B11_013922_3042_MA_00N214W	30, 143
Elysium N.	15-Elysium	30	G11_022414_2890_MA_00N216W	G11_022559_2959_MA_00N214W	30, 142
Elysium N.	15-Elysium	30	G11_022625_2990_MA_00N216W	G12_022770_3057_MA_00N215W	30, 142
Elysium N.	15-Elysium	31	D10_031183_2868_MA_00N216W	D10_031262_2905_MA_00N213W	31, 142
Elysium N.	15-Elysium	32	F11_039939_2839_MA_00N213W	F11_040005_2870_MA_00N215W	30, 143
Elysium N.	15-Elysium	33	J11_049011_2960_MA_00N213W	J11_049077_2991_MA_00N215W	31, 142
M. Sirenum	16-Memnonia	28	P02_001895_1542_MA_00N168W	P03_002040_1601_MA_00N166W	-24, 198
M. Sirenum	16-Memnonia	28	P03_002079_1617_MA_00N151W	P03_002132_1639_MA_00N158W	-28, 209

M. Sirenum	16-Memnonia	28	P03_002343_1729_MA_00N158W	P03_002409_1757_MA_00N160W	-25, 203
M. Sirenum	16-Memnonia	29	B03_010742_1555_MA_00N155W	B03_010808_1582_MA_00N157W	-23, 205
M. Sirenum	16-Memnonia	30	G04_019735_1627_MA_00N155W	G04_019880_1688_MA_00N153W	-24, 209
M. Sirenum	16-Memnonia	30	G04_019815_1661_MA_00N179W	G04_019947_1717_MA_00N182W	-25, 179
M. Sirenum	16-Memnonia	31	D03_028201_1485_MA_00N162W	D04_028623_1657_MA_00N162W	-22, 198
M. Sirenum	16-Memnonia	31	D03_028227_1495_MA_00N152W	D03_028570_1635_MA_00N155W	-25, 209
M. Sirenum	16-Memnonia	32	F04_037299_1599_MA_00N153W	F04_037431_1654_MA_00N156W	-24, 209
M. Sirenum	16-Memnonia	32	F04_037339_1616_MA_00N165W	F04_037484_1676_MA_00N163W	-22, 200
M. Sirenum	16-Memnonia	33	J03_046042_1569_MA_00N150W	J03_046095_1590_MA_00N157W	-24, 209
M. Sirenum	16-Memnonia	33	J04_046386_1712_MA_00N182W	J04_046531_1775_MA_00N181W	-22, 181
M. Sirenum	16-Memnonia	33	J05_046635_1821_MA_00N140W	J05_046701_1850_MA_00N142W	-29, 219
Solis Lacus	17-Phoenicis	28	P05_002789_1926_MA_00N095W	P05_002855_1956_MA_00N097W	-21 270
Solis Lacus	17-Phoenicis	28	P05_002947_1999_MA_00N089W	P05_003066_2054_MA_00N097W	-23 270
Solis Lacus	17-Phoenicis	28	P05_003079_2060_MA_00N092W	P05_003145_2092_MA_00N094W	-24 268
Solis Lacus	17-Phoenicis	28	P05_003145_2092_MA_00N094W	P06_003211_2123_MA_00N096W	-24 269
Solis Lacus	17-Phoenicis	28	P06_003422_2224_MA_00N096W	P06_003488_2256_MA_00N098W	-22 266
Solis Lacus	17-Phoenicis	28	P06_003488_2256_MA_00N098W	P07_003633_2327_MA_00N097W	-24 267
Solis Lacus	17-Phoenicis	28	P07_003844_2431_MA_00N097W	P07_003923_2470_MA_00N094W	-25 269; -20 268
Solis Lacus	17-Phoenicis	28	P07_003923_2470_MA_00N094W	P08_003989_2503_MA_00N096W	-25 270
Solis Lacus	17-Phoenicis	29	B02_010278_1372_MA_00N087W	B02_010318_1387_MA_00N099W	-26 270
Solis Lacus	17-Phoenicis	29	B04_011281_1782_MA_00N111W	B04_011347_1811_MA_00N113W	-24 256
Solis Lacus	17-Phoenicis	29	B04_011360_1817_MA_00N108W	B05_011426_1846_MA_00N109W	-25 256
Solis Lacus	17-Phoenicis	29	B05_011637_1941_MA_00N110W	B05_011703_1971_MA_00N112W	-24 257
Solis Lacus	17-Phoenicis	29	B08_012586_2395_MA_00N099W	B08_012639_2421_MA_00N106W	-23 260
Solis Lacus	17-Phoenicis	29	B08_012876_2538_MA_00N096W	B08_012942_2571_MA_00N098W	-24, 270
Solis Lacus	17-Phoenicis	29	B09_013087_2642_MA_00N097W	B09_013140_2668_MA_00N104W	-24, 262
Solis Lacus	17-Phoenicis	29	B10_013364_2778_MA_00N099W	B10_013496_2842_MA_00N103W	-24, 263
Solis Lacus	17-Phoenicis	29	B11_013957_3059_MA_00N089W	B11_013984_3071_MA_00N106W	-24, 268
Solis Lacus	17-Phoenicis	30	B21_017966_0963_MA_00N099W	B21_018019_0981_MA_00N106W	-26, 263
Solis Lacus	17-Phoenicis	30	B22_018111_1014_MA_00N097W	B22_018164_1032_MA_00N104W	-27, 264
Solis Lacus	17-Phoenicis	30	G01_018612_1192_MA_00N095W	G01_018678_1216_MA_00N097W	-25, 267
Solis Lacus	17-Phoenicis	30	G04_019812_1660_MA_00N097W	G04_019878_1687_MA_00N099W	-26, 267
Solis Lacus	17-Phoenicis	30	G09_021803_2593_MA_00N095W	G09_021843_2612_MA_00N107W	-25, 265
Solis Lacus	17-Phoenicis	30	G11_022647_3000_MA_00N096W	G12_022713_3031_MA_00N099W	-26, 265
Solis Lacus	17-Phoenicis	30	G12_022792_3067_MA_00N095W	G12_022845_3091_MA_00N102W	-26, 266
Solis Lacus	17-Phoenicis	30	G12_022858_3097_MA_00N097W	G12_022924_3127_MA_00N099W	-24, 262; -26, 268
Solis Lacus	17-Phoenicis	31	D06_029451_2025_MA_00N088W	D06_029491_2043_MA_00N101W	-20, 270
Solis Lacus	17-Phoenicis	31	D06_029504_2050_MA_00N095W	D06_029570_2081_MA_00N097W	-24, 265; -23, 270
Solis Lacus	17-Phoenicis	31	D08_030229_2400_MA_00N090W	D08_030348_2459_MA_00N099W	-24, 268
Solis Lacus	17-Phoenicis	31	D09_030638_2602_MA_00N096W	D09_030704_2634_MA_00N098W	-26, 269
Solis Lacus	17-Phoenicis	31	D09_030783_2673_MA_00N095W	D09_030836_2699_MA_00N102W	-25, 267
Solis Lacus	17-Phoenicis	31	D09_030836_2699_MA_00N102W	D09_030849_2706_MA_00N097W	-25, 265
Solis Lacus	17-Phoenicis	31	D10_031047_2802_MA_00N103W	D10_031113_2834_MA_00N105W	-26, 265
Solis Lacus	17-Phoenicis	31	D10_031139_2847_MA_00N095W	D10_031192_2872_MA_00N102W	-26, 266
Solis Lacus	17-Phoenicis	31	D10_031284_2916_MA_00N093W	D12_031785_3147_MA_00N092W	-28, 270
Solis Lacus	17-Phoenicis	32	D22_035886_1064_MA_00N096W	D22_035952_1087_MA_00N098W	-27, 270
Solis Lacus	17-Phoenicis	32	F01_036097_1139_MA_00N096W	F01_036242_1191_MA_00N095W	-22, 265
Solis Lacus	17-Phoenicis	32	F01_036308_1215_MA_00N096W	F01_036374_1239_MA_00N098W	-28, 267
Solis Lacus	17-Phoenicis	32	F04_037508_1686_MA_00N098W	F05_037574_1714_MA_00N100W	-27, 268
Solis Lacus	17-Phoenicis	32	F07_038352_2064_MA_00N096W	F07_038418_2096_MA_00N097W	-23, 271
Solis Lacus	17-Phoenicis	32	F08_039038_2396_MA_00N095W	F08_039104_2429_MA_00N097W	-24, 269
Solis Lacus	17-Phoenicis	32	F08_039104_2429_MA_00N097W	F09_039170_2461_MA_00N099W	-25, 269
Solis Lacus	17-Phoenicis	32	F09_039170_2461_MA_00N099W	F09_039315_2533_MA_00N098W	-26, 266
Solis Lacus	17-Phoenicis	32	F10_039539_2644_MA_00N093W	F10_039605_2676_MA_00N095W	-26, 270
Solis Lacus	17-Phoenicis	32	F11_040159_2944_MA_00N100W	F11_040238_2981_MA_00N097W	-25, 265
Solis Lacus	17-Phoenicis	32	F11_040251_2987_MA_00N091W	F12_040317_3018_MA_00N093W	-26, 268
Solis Lacus	17-Phoenicis	32	F12_040607_3150_MA_00N090W	F12_040673_3179_MA_00N092W	-21, 271
Solis Lacus	17-Phoenicis	32	F13_041029_3334_MA_00N092W	F14_041095_3362_MA_00N094W	-27, 268
Solis Lacus	17-Phoenicis	33	J02_045539_1370_MA_00N097W	J02_045605_1395_MA_00N099W	-22, 265
Solis Lacus	17-Phoenicis	33	J06_047108_2036_MA_00N094W	J06_047187_2073_MA_00N091W	-23, 271
Solis Lacus	17-Phoenicis	33	J08_047886_2411_MA_00N096W	J08_048031_2483_MA_00N095W	-23, 268
Solis Lacus	17-Phoenicis	33	J08_048097_2516_MA_00N097W	J09_048163_2548_MA_00N099W	-24, 270
Solis Lacus	17-Phoenicis	33	J09_048163_2548_MA_00N099W	J09_048387_2659_MA_00N096W	-22, 270
Solis Lacus	17-Phoenicis	33	J09_048387_2659_MA_00N096W	J09_048453_2691_MA_00N098W	-26, 271
Solis Lacus	17-Phoenicis	33	J10_048743_2833_MA_00N096W	J10_048888_2902_MA_00N095W	-27, 271
Solis Lacus	17-Phoenicis	33	J10_048888_2902_MA_00N095W	J11_048954_2933_MA_00N097W	-27, 270
Solis Lacus	17-Phoenicis	33	J11_049033_2971_MA_00N094W	J11_049086_2995_MA_00N101W	-22, 271
Solis Lacus	17-Phoenicis	33	J11_049099_3001_MA_00N096W	J11_049165_3032_MA_00N097W	-22, 270
Solis Lacus	17-Phoenicis	33	J12_049587_3222_MA_00N098W	J12_049653_3251_MA_00N099W	-27, 264
Tharsis Plateau	17-Phoenicis	28	P04_002460_1780_MA_00N113W	P04_002526_1808_MA_00N115W	-2, 242
Tharsis Plateau	17-Phoenicis	28	P13_005994_3430_MA_00N115W	P13_006139_3489_MA_00N114W	-6, 241; -1, 242
Tharsis Plateau	17-Phoenicis	28	P13_006007_3435_MA_00N110W	P13_006165_3499_MA_00N104W	-2, 252
Tharsis Plateau	17-Phoenicis	28	P13_006139_3489_MA_00N114W	P13_006205_3515_MA_00N116W	-3, 240
Tharsis Plateau	17-Phoenicis	28	P13_006165_3499_MA_00N104W	P13_006244_3531_MA_00N101W	0, 254
Tharsis Plateau	17-Phoenicis	28	P13_006192_3510_MA_00N121W	P15_006825_0154_MA_00N124W	-11, 234
Tharsis Plateau	17-Phoenicis	28	P13_006205_3515_MA_00N116W	P13_006284_3547_MA_00N113W	-7, 242; -2, 244
Tharsis Plateau	17-Phoenicis	28	P13_006284_3547_MA_00N113W	P14_006495_0029_MA_00N114W	-4, 243
Tharsis Plateau	17-Phoenicis	29	P14_006614_0075_MA_00N123W	P15_006746_0125_MA_00N127W	-5, 231

Tharsis Plateau	17-Phoenicis	29	P14_006614_0075_MA_00N123W	P14_006693_0105_MA_00N120W	-5, 233; -3, 236
Tharsis Plateau	17-Phoenicis	29	P15_006825_0154_MA_00N124W	P15_006970_0207_MA_00N123W	-1, 234
Tharsis Plateau	17-Phoenicis	29	P15_006878_0174_MA_00N131W	P15_007023_0227_MA_00N130W	-10, 226
Tharsis Plateau	17-Phoenicis	29	P16_007247_0308_MA_00N127W	P16_007458_0382_MA_00N128W	-15, 231
Tharsis Plateau	17-Phoenicis	29	P17_007682_0460_MA_00N125W	P17_007748_0483_MA_00N127W	-1, 232
Tharsis Plateau	17-Phoenicis	29	P17_007735_0479_MA_00N132W	P17_007814_0506_MA_00N129W	-8, 228
Tharsis Plateau	17-Phoenicis	29	B02_010503_1459_MA_00N110W	B02_010582_1490_MA_00N107W	-3, 253
Tharsis Plateau	17-Phoenicis	29	B02_010556_1480_MA_00N117W	B03_010622_1506_MA_00N119W	-2, 239
Tharsis Plateau	17-Phoenicis	29	B03_010846_1597_MA_00N114W	B03_010912_1625_MA_00N116W	-3, 241
Tharsis Plateau	17-Phoenicis	29	B10_013602_2892_MA_00N117W	B10_013681_2930_MA_00N114W	-1, 243
Tharsis Plateau	17-Phoenicis	29	B11_014063_3107_MA_00N103W	B12_014129_3137_MA_00N105W	-2, 253
Tharsis Plateau	17-Phoenicis	29	B12_014129_3137_MA_00N105W	B12_014274_3201_MA_00N104W	-1, 253
Tharsis Plateau	17-Phoenicis	29	B12_014182_3161_MA_00N112W	B12_014314_3219_MA_00N116W	-1, 242
Tharsis Plateau	17-Phoenicis	29	B12_014446_3277_MA_00N119W	B16_015936_0262_MA_00N116W	-4, 241
Tharsis Plateau	17-Phoenicis	31	B16_015897_0248_MA_00N132W	B16_016042_0300_MA_00N130W	-10, 226
Tharsis Plateau	17-Phoenicis	31	B17_016174_0347_MA_00N134W	B17_016319_0398_MA_00N133W	-9, 226
Tharsis Plateau	17-Phoenicis	31	B17_016332_0403_MA_00N128W	B17_016411_0430_MA_00N124W	0, 232
Tharsis Plateau	17-Phoenicis	31	B17_016332_0403_MA_00N128W	B17_016477_0453_MA_00N126W	-11, 228
Tharsis Plateau	17-Phoenicis	30	B17_016345_0407_MA_00N123W	B17_016411_0430_MA_00N124W	0, 232
Tharsis Plateau	17-Phoenicis	30	B17_016451_0444_MA_00N136W	B18_016530_0472_MA_00N133W	-9, 226
Tharsis Plateau	17-Phoenicis	31	B17_016451_0444_MA_00N136W	B18_016530_0472_MA_00N133W	-8, 226
Tharsis Plateau	17-Phoenicis	31	B18_016688_0526_MA_00N127W	B19_016899_0598_MA_00N127W	-11, 232
Tharsis Plateau	17-Phoenicis	30	B18_016754_0549_MA_00N128W	B19_016899_0598_MA_00N127W	-11, 234
Tharsis Plateau	17-Phoenicis	30	G04_019839_1671_MA_00N114W	G04_019905_1699_MA_00N116W	-3, 241
Tharsis Plateau	17-Phoenicis	30	G12_023056_3186_MA_00N103W	G13_023122_3215_MA_00N105W	-1, 253
Tharsis Plateau	17-Phoenicis	30	G13_023122_3215_MA_00N105W	G13_023188_3244_MA_00N107W	-2, 253
Tharsis Plateau	17-Phoenicis	30	G13_023267_3279_MA_00N103W	G13_023333_3307_MA_00N105W	-1, 255
Tharsis Plateau	17-Phoenicis	30	G14_023768_3488_MA_00N102W	G14_023834_3514_MA_00N103W	-2, 253
Tharsis Plateau	17-Phoenicis	30	G14_023795_3499_MA_00N119W	G14_023874_3530_MA_00N115W	-4, 241
Tharsis Plateau	17-Phoenicis	30	G14_023834_3514_MA_00N103W	G15_023900_3541_MA_00N105W	-2, 252
Tharsis Plateau	17-Phoenicis	31	G15_024204_0059_MA_00N124W	G15_024270_0084_MA_00N126W	-5, 231
Tharsis Plateau	17-Phoenicis	31	D10_031219_2885_MA_00N119W	D10_031232_2891_MA_00N114W	-1, 243
Tharsis Plateau	17-Phoenicis	31	D10_031232_2891_MA_00N114W	D10_031298_2922_MA_00N116W	-1, 243
Tharsis Plateau	17-Phoenicis	31	D12_031746_3130_MA_00N108W	D12_031759_3136_MA_00N103W	0, 254
Tharsis Plateau	17-Phoenicis	31	D12_031759_3136_MA_00N103W	D12_031825_3165_MA_00N104W	-2, 253
Tharsis Plateau	17-Phoenicis	31	D12_032036_3258_MA_00N104W	D13_032181_3320_MA_00N103W	0, 255
Tharsis Plateau	17-Phoenicis	31	D13_032181_3320_MA_00N103W	D13_032247_3348_MA_00N105W	0, 255
Tharsis Plateau	17-Phoenicis	31	D13_032260_3354_MA_00N100W	D13_032326_3382_MA_00N102W	0, 255
Tharsis Plateau	17-Phoenicis	31	D13_032458_3436_MA_00N106W	D14_032537_3469_MA_00N103W	-2, 254
Tharsis Plateau	17-Phoenicis	31	D14_032511_3458_MA_00N113W	D14_032577_3485_MA_00N115W	-1, 241
Tharsis Plateau	17-Phoenicis	31	D14_032603_3495_MA_00N105W	D14_032669_3522_MA_00N107W	-2, 252
Tharsis Plateau	17-Phoenicis	31	D14_032695_3532_MA_00N096W	D14_032774_3563_MA_00N093W	-2, 263
Tharsis Plateau	17-Phoenicis	31	D14_032709_3538_MA_00N119W	D14_032788_3569_MA_00N115W	-2, 240
Tharsis Plateau	17-Phoenicis	32	D15_032973_0041_MA_00N126W	D15_033039_0066_MA_00N128W	-6, 230
Tharsis Plateau	17-Phoenicis	32	D16_033527_0247_MA_00N132W	D16_033606_0276_MA_00N129W	-11, 229
Tharsis Plateau	17-Phoenicis	32	D17_033975_0406_MA_00N123W	D17_034041_0429_MA_00N125W	0, 233
Tharsis Plateau	17-Phoenicis	32	D17_034015_0420_MA_00N135W	D18_034160_0471_MA_00N133W	-10, 225
Tharsis Plateau	17-Phoenicis	32	D18_034318_0525_MA_00N127W	D18_034397_0552_MA_00N124W	-11, 232
Tharsis Plateau	17-Phoenicis	32	D18_034397_0552_MA_00N124W	D19_034463_0575_MA_00N126W	-13, 234
Tharsis Plateau	17-Phoenicis	32	F04_037324_1609_MA_00N115W	F04_037390_1637_MA_00N117W	-2, 242; -2, 235
Tharsis Plateau	17-Phoenicis	32	F04_037350_1620_MA_00N105W	F04_037416_1648_MA_00N107W	0, 251
Tharsis Plateau	17-Phoenicis	32	F05_037812_1818_MA_00N117W	F06_037957_1883_MA_00N115W	-1, 243
Tharsis Plateau	17-Phoenicis	32	F11_039975_2856_MA_00N116W	F11_040120_2925_MA_00N115W	-1, 243
Tharsis Plateau	17-Phoenicis	32	F12_040647_3168_MA_00N102W	F13_040792_3232_MA_00N101W	-1, 254
Tharsis Plateau	17-Phoenicis	32	F13_040858_3261_MA_00N103W	F13_040924_3289_MA_00N105W	-1, 254
Tharsis Plateau	17-Phoenicis	32	F14_041346_3466_MA_00N106W	F14_041425_3498_MA_00N103W	-2, 254
Tharsis Plateau	17-Phoenicis	32	F14_041451_3508_MA_00N093W	F15_041517_3534_MA_00N095W	-2, 263
Tharsis Plateau	17-Phoenicis	32	F15_041465_3514_MA_00N115W	F15_041531_3540_MA_00N117W	-2, 241
Tharsis Plateau	17-Phoenicis	32	F15_041491_3524_MA_00N105W	F15_041781_0038_MA_00N103W	-3, 253
Tharsis Plateau	17-Phoenicis	32	F15_041517_3534_MA_00N095W	F15_041807_0047_MA_00N093W	-2, 263
Tharsis Plateau	17-Phoenicis	32	F15_041518_3535_MA_00N122W	F15_041808_0048_MA_00N120W	0, 236
Tharsis Plateau	17-Phoenicis	32	F15_041531_3540_MA_00N117W	F15_041742_0022_MA_00N118W	-1, 241
Tharsis Plateau	17-Phoenicis	33	F17_042415_0273_MA_00N133W	F17_042560_0325_MA_00N132W	-10, 225
Tharsis Plateau	17-Phoenicis	33	F17_042639_0353_MA_00N129W	F18_042784_0404_MA_00N128W	-10, 230
Tharsis Plateau	17-Phoenicis	33	F18_042850_0427_MA_00N130W	F18_042916_0450_MA_00N132W	-7, 226
Tharsis Plateau	17-Phoenicis	33	F18_042902_0445_MA_00N109W	F18_042981_0472_MA_00N106W	-2, 249
Tharsis Plateau	17-Phoenicis	33	J10_048836_2877_MA_00N115W	J10_048902_2909_MA_00N117W	-1, 242
Tharsis Plateau	17-Phoenicis	33	J10_048902_2909_MA_00N117W	J11_048981_2946_MA_00N114W	0, 242
Tharsis Plateau	17-Phoenicis	33	J12_049561_3211_MA_00N108W	J13_049706_3274_MA_00N106W	-2, 252
Tharsis Plateau	17-Phoenicis	33	J14_050141_3457_MA_00N102W	J14_050207_3484_MA_00N104W	0, 255
Tharsis Plateau	17-Phoenicis	33	J14_050207_3484_MA_00N104W	J14_050352_3542_MA_00N103W	-2, 253
Tharsis Plateau	17-Phoenicis	33	J14_050299_3521_MA_00N096W	J14_050378_3552_MA_00N093W	-2, 263
Tharsis Plateau	17-Phoenicis	33	J14_050313_3526_MA_00N118W	J14_050392_3558_MA_00N115W	-3, 240
Tharsis Plateau	17-Phoenicis	33	J14_050326_3531_MA_00N113W	J14_050392_3558_MA_00N115W	0, 242
Tharsis Plateau	17-Phoenicis	33	J14_050392_3558_MA_00N115W	J15_050458_3584_MA_00N117W	-1, 241
Tharsis Plateau	17-Phoenicis	33	J14_050418_3568_MA_00N105W	J15_050497_3599_MA_00N102W	-3, 254
Solis Lacus	18-Coprates	28	P05_002815_1938_MA_00N085W	P05_002881_1968_MA_00N087W	-20, 276
Solis Lacus	18-Coprates	28	P05_002881_1968_MA_00N087W	P05_003092_2067_MA_00N087W	-22, 273
Solis Lacus	18-Coprates	28	P06_003461_2243_MA_00N081W	P06_003527_2275_MA_00N083W	-24, 282
Solis Lacus	18-Coprates	28	P06_003514_2269_MA_00N088W	P07_003580_2301_MA_00N090W	-23, 273

Solis Lacus	18-Coprates	28	P07_003804_2411_MA_00N085W	P07_003870_2444_MA_00N087W	-22, 273
Solis Lacus	18-Coprates	28	P08_004160_2587_MA_00N084W	P08_004226_2620_MA_00N086W	-17, 273; -24, 276
Solis Lacus	18-Coprates	28	P10_004991_2989_MA_00N091W	P10_005057_3020_MA_00N093W	-24, 269
Solis Lacus	18-Coprates	29	P15_007008_0221_MA_00N081W	P16_007153_0274_MA_00N080W	-27, 281
Solis Lacus	18-Coprates	29	B02_010265_1367_MA_00N092W	B02_010344_1397_MA_00N089W	-26, 270
Solis Lacus	18-Coprates	29	B05_011689_1965_MA_00N090W	B05_011755_1995_MA_00N091W	-24, 273
Solis Lacus	18-Coprates	29	B05_011755_1995_MA_00N091W	B06_011821_2026_MA_00N093W	-23, 271
Solis Lacus	18-Coprates	29	B06_011834_2032_MA_00N088W	B06_011979_2100_MA_00N087W	-20, 275
Solis Lacus	18-Coprates	29	B07_012401_2304_MA_00N088W	B08_012612_2408_MA_00N089W	-25, 275
Solis Lacus	18-Coprates	29	B08_012889_2544_MA_00N091W	B09_012955_2577_MA_00N093W	-24, 271
Solis Lacus	18-Coprates	29	B09_013034_2616_MA_00N090W	B09_013100_2649_MA_00N092W	-25, 272
Solis Lacus	18-Coprates	29	B10_013601_2892_MA_00N090W	B10_013680_2929_MA_00N087W	-21, 274
Solis Lacus	18-Coprates	29	B11_013957_3059_MA_00N089W	B11_014089_3119_MA_00N093W	-24, 270
Solis Lacus	18-Coprates	30	G01_018704_1226_MA_00N087W	G01_018770_1250_MA_00N089W	-12, 274
Solis Lacus	18-Coprates	30	G02_018915_1304_MA_00N088W	G02_018981_1329_MA_00N090W	-13, 274
Solis Lacus	18-Coprates	30	G03_019284_1445_MA_00N082W	G03_019350_1471_MA_00N084W	-16, 276
Solis Lacus	18-Coprates	30	G03_019350_1471_MA_00N084W	G03_019482_1524_MA_00N088W	-15, 275
Solis Lacus	18-Coprates	30	G04_019746_1632_MA_00N095W	G04_019957_1721_MA_00N095W	-26, 269
Solis Lacus	18-Coprates	30	G04_019970_1727_MA_00N090W	G05_020049_1761_MA_00N087W	-15, 275
Solis Lacus	18-Coprates	30	G06_020695_2053_MA_00N084W	G06_020761_2084_MA_00N086W	-22, 277
Solis Lacus	18-Coprates	30	G07_021051_2223_MA_00N083W	G08_021473_2429_MA_00N085W	-22, 279
Solis Lacus	18-Coprates	30	G09_021737_2560_MA_00N093W	G09_021882_2632_MA_00N091W	-24, 274
Solis Lacus	18-Coprates	30	G12_022805_3073_MA_00N090W	G12_022871_3103_MA_00N092W	-25, 269
Solis Lacus	18-Coprates	30	G12_022897_3115_MA_00N082W	G12_022963_3145_MA_00N084W	-25, 279
Solis Lacus	18-Coprates	30	G12_023042_3180_MA_00N081W	G13_023108_3209_MA_00N083W	-19, 278
Solis Lacus	18-Coprates	31	D05_029319_1964_MA_00N084W	D06_029385_1994_MA_00N086W	-23, 274
Solis Lacus	18-Coprates	31	D06_029372_1988_MA_00N091W	D06_029438_2019_MA_00N093W	-23, 272
Solis Lacus	18-Coprates	31	D06_029438_2019_MA_00N093W	D06_029517_2056_MA_00N090W	-21, 270
Solis Lacus	18-Coprates	31	D06_029517_2056_MA_00N090W	D06_029583_2087_MA_00N092W	-23, 270
Solis Lacus	18-Coprates	31	D08_030216_2393_MA_00N095W	D08_030361_2465_MA_00N094W	-24, 271
Solis Lacus	18-Coprates	31	D09_030638_2602_MA_00N096W	D09_030704_2634_MA_00N098W	-25, 271
Solis Lacus	18-Coprates	31	D09_030783_2673_MA_00N095W	D09_030849_2706_MA_00N097W	-24, 270
Solis Lacus	18-Coprates	31	D10_031297_2922_MA_00N088W	D12_031798_3153_MA_00N087W	-21, 275
Solis Lacus	18-Coprates	32	F02_036729_1373_MA_00N070W	F03_036861_1424_MA_00N074W	-19, 287
Solis Lacus	18-Coprates	32	F04_037455_1664_MA_00N091W	F05_037587_1720_MA_00N095W	-26, 269
Solis Lacus	18-Coprates	32	F06_038299_2040_MA_00N090W	F07_038365_2071_MA_00N091W	-21, 275
Solis Lacus	18-Coprates	32	F08_039051_2402_MA_00N090W	F08_039117_2435_MA_00N092W	-24, 271
Solis Lacus	18-Coprates	32	F08_039117_2435_MA_00N092W	F09_039183_2468_MA_00N094W	-25, 270
Solis Lacus	18-Coprates	32	F09_039473_2611_MA_00N092W	F10_039605_2676_MA_00N095W	-26, 271
Solis Lacus	18-Coprates	32	F11_040198_2962_MA_00N084W	F11_040264_2993_MA_00N086W	-25, 275
Solis Lacus	18-Coprates	32	F12_040409_3060_MA_00N085W	F12_040475_3090_MA_00N087W	-26, 274
Solis Lacus	18-Coprates	32	F12_040620_3156_MA_00N085W	F13_040765_3220_MA_00N084W	-19, 280
Solis Lacus	18-Coprates	32	F13_041029_3334_MA_00N092W	F14_041161_3390_MA_00N095W	-28, 269
Solis Lacus	18-Coprates	33	J05_046831_1908_MA_00N091W	J05_046897_1938_MA_00N093W	-22, 272
Solis Lacus	18-Coprates	33	J05_046897_1938_MA_00N093W	J06_046963_1968_MA_00N095W	-22, 274
Solis Lacus	18-Coprates	33	J06_047108_2036_MA_00N094W	J06_047174_2067_MA_00N096W	-24, 272
Solis Lacus	18-Coprates	33	J08_047899_2418_MA_00N091W	J08_048044_2490_MA_00N090W	-24, 269
Solis Lacus	18-Coprates	33	J09_048321_2626_MA_00N094W	J09_048466_2698_MA_00N093W	-26, 271
Solis Lacus	18-Coprates	33	J10_048822_2870_MA_00N093W	J10_048901_2908_MA_00N090W	-27, 271
Solis Lacus	18-Coprates	33	J11_049046_2977_MA_00N089W	J11_049099_3001_MA_00N096W	-26, 273
Solis Lacus	18-Coprates	33	J11_049046_2977_MA_00N089W	J11_049112_3007_MA_00N091W	-22, 271
Solis Lacus	18-Coprates	33	J12_049560_3211_MA_00N081W	J13_049692_3268_MA_00N084W	-19, 278
Thaumasia	18-Coprates	28	P06_003447_2236_MA_00N059W	P06_003513_2269_MA_00N061W	-25, 304
Thaumasia	18-Coprates	28	P06_003513_2269_MA_00N061W	P07_003579_2301_MA_00N062W	-28, 303
Thaumasia	18-Coprates	28	P07_003579_2301_MA_00N062W	P07_003724_2372_MA_00N061W	-28, 303
Thaumasia	18-Coprates	28	P08_004067_2541_MA_00N065W	P08_004212_2613_MA_00N064W	-30, 298
Thaumasia	18-Coprates	28	P11_005201_3086_MA_00N065W	P11_005267_3116_MA_00N067W	-20, 297
Thaumasia	18-Coprates	28	P11_005254_3110_MA_00N072W	P11_005320_3140_MA_00N074W	-30, 288
Thaumasia	18-Coprates	28	P11_005267_3116_MA_00N067W	P11_005412_3181_MA_00N066W	-24, 297
Thaumasia	18-Coprates	28	P11_005320_3140_MA_00N074W	P11_005386_3169_MA_00N076W	-30, 285
Thaumasia	18-Coprates	28	P11_005452_3199_MA_00N078W	P11_005518_3228_MA_00N080W	-29, 283
Thaumasia	18-Coprates	28	P11_005478_3210_MA_00N067W	P12_005544_3239_MA_00N069W	-26, 293
Thaumasia	18-Coprates	28	P11_005478_3210_MA_00N067W	P12_005544_3239_MA_00N069W	-19, 296
Thaumasia	18-Coprates	28	P11_005518_3228_MA_00N080W	P12_005584_3257_MA_00N081W	-30, 281
Thaumasia	18-Coprates	28	P12_005557_3245_MA_00N064W	P12_005636_3279_MA_00N061W	-17, 299
Thaumasia	18-Coprates	28	P12_005623_3273_MA_00N066W	P12_005689_3302_MA_00N068W	-23, 294
Thaumasia	18-Coprates	28	P12_005636_3279_MA_00N061W	P12_005702_3307_MA_00N063W	-16, 299
Thaumasia	18-Coprates	28	P12_005689_3302_MA_00N068W	P12_005768_3336_MA_00N065W	-21, 294
Thaumasia	18-Coprates	28	P12_005702_3307_MA_00N063W	P12_005768_3336_MA_00N065W	-17, 298
Thaumasia	18-Coprates	28	P12_005741_3324_MA_00N048W	P12_005807_3352_MA_00N050W	-11, 309
Thaumasia	18-Coprates	28	P12_005768_3336_MA_00N065W	P12_005834_3363_MA_00N067W	-19, 294
Thaumasia	18-Coprates	28	P12_005768_3336_MA_00N065W	P12_005847_3369_MA_00N062W	-17, 298
Thaumasia	18-Coprates	28	P12_005795_3347_MA_00N082W	P12_005874_3380_MA_00N079W	-29, 281
Thaumasia	18-Coprates	28	P12_005847_3369_MA_00N062W	P12_005913_3396_MA_00N063W	-17, 298
Thaumasia	18-Coprates	28	P12_005873_3380_MA_00N051W	P13_006163_3499_MA_00N049W	-10, 309
Thaumasia	18-Coprates	28	P13_005979_3424_MA_00N065W	P13_006124_3483_MA_00N065W	-19, 294; -18, 296
Thaumasia	18-Coprates	28	P13_006005_3434_MA_00N055W	P13_006150_3493_MA_00N054W	-30, 303
Thaumasia	18-Coprates	28	P13_006006_3435_MA_00N083W	P13_006151_3494_MA_00N082W	-28, 280
Thaumasia	18-Coprates	28	P13_006269_3541_MA_00N064W	P14_006480_0023_MA_00N065W	-6, 297
Thaumasia	18-Coprates	29	P14_006467_0018_MA_00N070W	P14_006612_0074_MA_00N069W	-28, 293

Thaumasia	18-Coprates	29	P14_006612_0074_MA_00N069W	P14_006678_0099_MA_00N071W	-28, 294
Thaumasia	18-Coprates	29	P14_006678_0099_MA_00N071W	P15_006757_0129_MA_00N068W	-28, 294
Thaumasia	18-Coprates	29	P15_006731_0119_MA_00N078W	P15_006876_0173_MA_00N077W	-28, 283
Thaumasia	18-Coprates	29	P15_006757_0129_MA_00N068W	P15_006836_0158_MA_00N065W	-30, 297; -28, 295
Thaumasia	18-Coprates	29	P15_006902_0183_MA_00N067W	P15_006968_0207_MA_00N069W	-27, 295
Thaumasia	18-Coprates	29	P15_006968_0207_MA_00N069W	P16_007113_0259_MA_00N068W	-30, 300
Thaumasia	18-Coprates	29	P15_007007_0221_MA_00N054W	P16_007152_0274_MA_00N053W	-25, 309
Thaumasia	18-Coprates	29	P16_007113_0259_MA_00N068W	P16_007179_0283_MA_00N070W	-29, 299
Thaumasia	18-Coprates	29	P16_007126_0264_MA_00N063W	P16_007271_0316_MA_00N062W	-9, 300
Thaumasia	18-Coprates	29	P16_007179_0283_MA_00N070W	P16_007390_0358_MA_00N072W	-28, 291
Thaumasia	18-Coprates	29	P16_007429_0372_MA_00N056W	P17_007574_0423_MA_00N056W	-20, 308
Thaumasia	18-Coprates	29	P17_007482_0391_MA_00N064W	P17_007548_0414_MA_00N066W	-26, 296
Thaumasia	18-Coprates	29	B06_012057_2137_MA_00N056W	B07_012202_2207_MA_00N055W	-25, 309
Thaumasia	18-Coprates	29	B07_012400_2303_MA_00N060W	B08_012756_2479_MA_00N060W	-28, 303
Thaumasia	18-Coprates	30	G07_020971_2184_MA_00N059W	G07_021037_2216_MA_00N061W	-28, 303
Thaumasia	18-Coprates	30	G07_021037_2216_MA_00N061W	G08_021459_2423_MA_00N063W	-29, 302
Thaumasia	18-Coprates	30	G12_022725_3036_MA_00N066W	G12_022936_3133_MA_00N067W	-23, 295
Thaumasia	18-Coprates	31	G16_024584_0201_MA_00N059W	G17_024874_0306_MA_00N056W	-19, 306
Thaumasia	18-Coprates	31	G18_025085_0381_MA_00N057W	G18_025151_0404_MA_00N059W	-17, 304
Thaumasia	18-Coprates	31	D06_029740_2162_MA_00N059W	D07_029806_2193_MA_00N061W	-28, 302
Thaumasia	18-Coprates	31	D07_030017_2296_MA_00N061W	D08_030162_2367_MA_00N060W	-29, 302
Thaumasia	18-Coprates	31	D08_030228_2399_MA_00N062W	D08_030373_2471_MA_00N061W	-30, 301
Thaumasia	18-Coprates	31	D10_031283_2915_MA_00N066W	D12_031784_3147_MA_00N065W	-30, 296
Thaumasia	18-Coprates	32	D15_033195_0125_MA_00N068W	D16_033274_0154_MA_00N065W	-28, 295
Thaumasia	18-Coprates	32	D16_033445_0217_MA_00N053W	D16_033511_0241_MA_00N055W	-21, 304
Thaumasia	18-Coprates	32	D16_033577_0265_MA_00N057W	D17_033722_0317_MA_00N056W	-21, 306
Thaumasia	18-Coprates	32	D17_033722_0317_MA_00N056W	D17_033867_0368_MA_00N055W	-20, 308
Thaumasia	18-Coprates	32	F07_038509_2139_MA_00N060W	F08_038918_2337_MA_00N060W	-28, 302
Thaumasia	18-Coprates	32	F09_039129_2441_MA_00N060W	F09_039195_2474_MA_00N062W	-29, 302
Thaumasia	18-Coprates	32	F09_039261_2506_MA_00N064W	F09_039406_2578_MA_00N062W	-30, 302
Thaumasia	18-Coprates	32	F09_039327_2539_MA_00N066W	F09_039472_2611_MA_00N064W	-30, 299
Thaumasia	18-Coprates	32	F13_040975_3311_MA_00N058W	F14_041186_3400_MA_00N058W	-27, 304
Thaumasia	18-Coprates	33	F16_042043_0137_MA_00N056W	F16_042109_0161_MA_00N058W	-26, 303
Thaumasia	18-Coprates	33	F17_042399_0267_MA_00N056W	F17_042544_0319_MA_00N055W	-17, 305
Thaumasia	18-Coprates	33	J05_046764_1878_MA_00N062W	J05_046909_1944_MA_00N060W	-30, 303
Thaumasia	18-Coprates	33	J07_047476_2211_MA_00N061W	J07_047542_2243_MA_00N063W	-28, 302
Thaumasia	18-Coprates	33	J07_047621_2281_MA_00N060W	J07_047687_2314_MA_00N062W	-29, 302
Thaumasia	18-Coprates	33	J08_047753_2346_MA_00N065W	J08_047832_2385_MA_00N062W	-29, 301
Thaumasia	18-Coprates	33	J08_047766_2352_MA_00N059W	J08_047911_2424_MA_00N059W	-29, 302
Thaumasia	18-Coprates	33	J08_047911_2424_MA_00N059W	J08_048056_2495_MA_00N058W	-30, 302
Thaumasia	18-Coprates	33	J08_048109_2522_MA_00N065W	J09_048254_2593_MA_00N064W	-30, 302
Thaumasia	18-Coprates	33	J09_048320_2626_MA_00N066W	J09_048465_2697_MA_00N066W	-31, 298
Margaritifer Sinus	19-Margaritifer	30	G02_018899_1298_MA_00N011W	G02_018978_1328_MA_00N008W	-14, 355
Margaritifer Sinus	19-Margaritifer	30	G02_019202_1413_MA_00N003W	G03_019268_1439_MA_00N005W	-23, 358
Margaritifer Sinus	19-Margaritifer	30	G03_019545_1549_MA_00N008W	G04_019611_1576_MA_00N010W	-19, 357
Margaritifer Sinus	19-Margaritifer	31	D02_028037_1421_MA_00N005W	D02_028103_1446_MA_00N007W	-21, 359
Margaritifer Sinus	19-Margaritifer	31	D02_028090_1441_MA_00N012W	D02_028169_1472_MA_00N009W	-15, 355
Margaritifer Sinus	19-Margaritifer	32	F03_036819_1407_MA_00N008W	F03_036885_1433_MA_00N010W	-21, 358
Margaritifer Sinus	19-Margaritifer	32	F03_036951_1459_MA_00N012W	F03_037030_1490_MA_00N008W	-15, 355
Margaritifer Sinus	19-Margaritifer	33	J02_045628_1404_MA_00N007W	J02_045707_1435_MA_00N004W	-16, 0
M. Serpentis	20-Sabaeus	28	P02_001822_1513_MA_00N334W	P02_001875_1534_MA_00N341W	-26, 23
M. Serpentis	20-Sabaeus	28	P05_003140_2089_MA_00N318W	P06_003272_2152_MA_00N321W	-22, 42
M. Serpentis	20-Sabaeus	28	P06_003418_2222_MA_00N347W	P06_003431_2229_MA_00N342W	-25, 22
M. Serpentis	20-Sabaeus	28	P08_004143_2579_MA_00N340W	P08_004209_2611_MA_00N342W	-23, 20
M. Serpentis	20-Sabaeus	29	B02_010432_1431_MA_00N331W	B02_010485_1452_MA_00N338W	-30, 24
M. Serpentis	20-Sabaeus	29	B04_011342_1809_MA_00N336W	B05_011421_1844_MA_00N333W	-26, 28
M. Serpentis	20-Sabaeus	29	B04_011355_1814_MA_00N331W	B04_011368_1820_MA_00N326W	-17, 37
M. Serpentis	20-Sabaeus	29	B04_011368_1820_MA_00N326W	B05_011434_1849_MA_00N328W	-23, 36
M. Serpentis	20-Sabaeus	29	B07_012331_2270_MA_00N337W	B07_012397_2302_MA_00N339W	-29, 24
M. Serpentis	20-Sabaeus	29	B07_012463_2334_MA_00N341W	B07_012529_2367_MA_00N343W	-17, 19; -23, 20; -27, 23
M. Serpentis	20-Sabaeus	29	B11_014032_3093_MA_00N337W	B11_014072_3111_MA_00N349W	-29, 18
M. Serpentis	20-Sabaeus	30	G02_019161_1398_MA_00N324W	G03_019227_1423_MA_00N326W	-18, 38
M. Serpentis	20-Sabaeus	30	G02_019162_1398_MA_00N351W	G03_019228_1423_MA_00N353W	-22, 6
M. Serpentis	20-Sabaeus	30	G03_019544_1549_MA_00N340W	G04_019610_1576_MA_00N342W	-25, 25
M. Serpentis	20-Sabaeus	30	G03_019583_1565_MA_00N325W	G04_019728_1625_MA_00N324W	-24, 39
M. Serpentis	20-Sabaeus	30	G03_019584_1565_MA_00N352W	G04_019729_1625_MA_00N351W	-24, 5
M. Serpentis	20-Sabaeus	30	G07_020796_2101_MA_00N321W	G07_020862_2132_MA_00N323W	-22, 42
M. Serpentis	20-Sabaeus	30	G09_021574_2479_MA_00N322W	G09_021640_2512_MA_00N324W	-20, 37
M. Serpentis	20-Sabaeus	31	D02_028036_1420_MA_00N338W	D02_028089_1441_MA_00N345W	-29, 22
M. Serpentis	20-Sabaeus	31	D02_028102_1446_MA_00N340W	D02_028168_1472_MA_00N341W	-29, 22
M. Serpentis	20-Sabaeus	31	D06_029566_2079_MA_00N348W	D06_029592_2091_MA_00N338W	-22, 24
M. Serpentis	20-Sabaeus	31	D12_031755_3134_MA_00N353W	D12_031821_3163_MA_00N355W	-27, 5
M. Serpentis	20-Sabaeus	32	F02_036725_1371_MA_00N321W	F02_036738_1376_MA_00N316W	-18, 38
M. Serpentis	20-Sabaeus	32	F03_036792_1397_MA_00N350W	F03_036858_1422_MA_00N352W	-22, 6
M. Serpentis	20-Sabaeus	32	F03_036804_1401_MA_00N318W	F03_036870_1427_MA_00N320W	-22, 42
M. Serpentis	20-Sabaeus	32	F05_037859_1839_MA_00N320W	F06_037991_1898_MA_00N323W	-19, 35
M. Serpentis	20-Sabaeus	32	F07_038611_2188_MA_00N323W	F07_038677_2220_MA_00N324W	-18, 37
M. Serpentis	20-Sabaeus	33	J03_045785_1466_MA_00N333W	J03_045851_1492_MA_00N335W	-29, 28
M. Serpentis	20-Sabaeus	33	J03_046036_1566_MA_00N346W	J03_046102_1593_MA_00N348W	-24, 13

M. Serpentis	20-Sabaeus	33	J06_047301_2127_MA_00N323W	J07_047367_2158_MA_00N325W	-21, 36
M. Serpentis	20-Sabaeus	33	J07_047367_2158_MA_00N325W	J07_047446_2196_MA_00N322W	-17, 32
M. Tyrrhenum	22-Tyrrhenum	28	P09_004390_2700_MA_00N244W	P09_004654_2829_MA_00N251W	-3, 105; 0, 108
M. Tyrrhenum	22-Tyrrhenum	32	F03_036973_1467_MA_00N252W	F04_037250_1579_MA_00N255W	-3, 105
M. Cimmerium	23-Aeolis	28	P02_001896_1542_MA_00N195W	P03_002107_1629_MA_00N195W	-23, 169
M. Cimmerium	23-Aeolis	29	P16_007223_0299_MA_00N191W	P16_007355_0346_MA_00N196W	-25, 170
M. Cimmerium	23-Aeolis	29	B03_010625_1508_MA_00N201W	B03_010770_1566_MA_00N200W	-21, 162; -23, 167; -19, 164
M. Cimmerium	23-Aeolis	29	B03_010664_1523_MA_00N185W	B03_010796_1577_MA_00N189W	-22, 169; -15, 175
M. Cimmerium	23-Aeolis	29	B03_010678_1529_MA_00N208W	B03_010744_1556_MA_00N210W	-18, 153
M. Cimmerium	23-Aeolis	30	G04_019736_1628_MA_00N182W	G04_019802_1655_MA_00N184W	-24, 179
M. Cimmerium	23-Aeolis	30	G04_019855_1678_MA_00N191W	G04_019921_1706_MA_00N193W	-17, 169; -17, 167
M. Cimmerium	23-Aeolis	30	G04_019868_1683_MA_00N186W	G04_019934_1711_MA_00N188W	-15, 175
M. Cimmerium	23-Aeolis	31	D02_028150_1465_MA_00N210W	D03_028572_1636_MA_00N210W	-19, 154
M. Cimmerium	23-Aeolis	32	F03_036945_1456_MA_00N208W	F04_037222_1567_MA_00N211W	-20, 153
M. Cimmerium	23-Aeolis	32	F04_037327_1611_MA_00N197W	F04_037393_1638_MA_00N199W	-19, 164; -19, 167
M. Cimmerium	23-Aeolis	33	J04_046307_1679_MA_00N185W	J04_046373_1707_MA_00N187W	-23, 175

[1]Supplementary animation files include twenty-eight separately projected mosaic sequences numbered by and covering each of the nonpolar USGS mapping quadrangles. [2]Martian years are numbered following the convention of Clancy et al. (2000). [3]The third underscore-separated segment of the image ID contains the areocentric longitude (L_s) of the observation to a tenth of a degree. See Appendix A of Bell et al. (2009) for a complete description of the file-naming convention. [4]Because the affected regions are of various sizes and sometimes irregular and discontinuous, these locations are necessarily approximate. See text for details on the extent of individual changes.

159